POLISH ACADEMY OF SCIENCES
COMMITTEE OF METALLURGY
INSTITUTE OF METALLURGY
AND MATERIALS SCIENCE

ARCHIVES OF METALLURGY AND MATERIALS

QUARTERLY

Volume 49 · Issue 3

This issue is devoted to presentations during Calphad XXXIII in Kraków May 30 to June 4, 2004 (papers 1 to 13), while papers 14 to 20 are the regular research papers.

WARSZAWA — KRAKÓW 2004

The Archives of Metallurgy and Materials is covered in the following Institute for Scientific Information® products: SciSearch (the Science Citation Index® — Expanded), Research Alert®, Materials Science Citation Index®, and Current Contents® / Engineering, Computing and Technology. Articles published in the Archives of Metallurgy and Materials are also indexed or abstracted by Cambridge Scientific Abstracts.

EDITORIAL ADDRESS
M. Bitner al. Mickiewicza 30, AGH, paw. A-4, III p., pok. 312b
30-059 Kraków, Poland
Tel. +48 (12) 6173425
e-mail: archives@imim-pan.krakow.pl

Skład, łamanie druk i oprawa: Warszawska Drukarnia Naukowa PAN
Warszawa, ul. Śniadeckich 8, tel./fax 628-87-77

Ark. wyd. 21,25 Ark. druk. 17,0
Nakład: 200 egz.
Druk ukończono w 2004 r.

SUMMARY OF THE CALPHAD XXXIII MEETING

An International Conference on Phase Diagram Calculation and Computational Thermochemistry

May 30 – June 4, 2004
KRAKOW, POLAND

Organized by: Prof. **Zbigniew Moser** (Chairman), Institute of Metallurgy and Materials Science, Polish Academy of Sciences
Prof. **Rafał Kozubski** (V-Chairman), Jagiellonian University
Prof. **Krzysztof Fitzner** (V-Chairman), AGH University of Science and Technology
Dr **Wojciech Zakulski** (Secretary), Institute of Metallurgy and Materials Science, Polish Academy of Sciences
Dr **Ewa Bełtowska-Lehman** (Office), Institute of Metallurgy and Materials Science, Polish Academy of Sciences

Sponsored by: Calphad Inc.
Thermo-Calc Software
Thermfact
GTT Technologies
CompuTherm LLC
JMatPro

1. Introduction

The thirty third CALPHAD meeting was held from 30 May to 4th June in Kraków. It was the first time the Calphad conference had taken place in the former East European country, which is now the part of the United Europe. One hundred and 48 participants from all over the world took part and 16 accompanying persons. 162 technical papers, posters and software demonstrations were presented. Aljette Ansara was with us and Her presence somehow compensated Himo's absence. The Conference took place in the building of one of the oldest European Universities, the Jagiellonian University, established in the year 1364 and located in the Old City area. Perhaps, due to the Pope John Paul II blessing, which the participants received just in the opening day, the weather was good during the time of the Conference and everybody was able to enjoy the beauty of the former capital of Poland.

2. Summary of the Conference

In the oral sessions, 98 papers were given during the meeting including plenary, invited and regular presentations. In this brief summary, we discuss the main topics and point out new, interesting emerging trends.

The essence of the so-called Calphad modeling is obtaining the parameters of the thermodynamic models for the Gibbs energies of respective phases existing in the considered system in terms of known thermodynamic and phase equilibrium data. Then, this description can be extrapolated to obtain the Gibbs energies of multicomponent alloy phases, which often enable us to make reliable prediction of multicomponent phase diagram.

Two lectures vividly stressed this point of view. **Larry Kaufman** pointed out that development of Calphad Thermodynamics (CT) to describe the all possible phases in the system over the wide range of conditions and supported by powerful computational methods (and fast PC's) had resulted in efficient calculations of phase diagrams. Still, the success depends on the explicit description of the stability of the unstable and metastable phases as well as the functional description of p,T,X dependencies of the Gibbs energy and entropy of such phases in binary systems. Thus, the knowledge of relative phase stability and the proper description of binary systems are of principal importance. **Ted Massalski** gave a talk on plutonium, which is a metal of great interest because of its unusual metallurgical, electronic and nuclear properties. It exhibits six solid allotropic changes at ordinary pressure and it undergoes virtually every type of known phase transformation. It was interesting to listen to the story of how the knowledge of the conditions stabilizing one particular plutonium phase changed the balance of power in the 20 century.

It is taken for granted that the phase diagram optimization has to start with a set of experimental information. **Jean-Claude Gachon** remained us that even these techniques, which are not specifically devoted to determination of a phase diagram, can give very interesting details about its constitution. In turn, application of Knudsen effusion mass spectrometry to the determination of partial and integral thermodynamic properties of ordered intermetallic phases was discussed by **Klaus Hilpert**. Mass spectrometry provides the most complete information on vaporization processes since it allows the indentification of the vapor species and the determination of the partial pressures over the wide temperature range. Chemical activities, Gibbs energies and enthalpies of mixing are obtained for the alloy components in the binary and ternary solid solutions.

Experimental information obtained from different sources needs a flexible model description. The need for model compatibility when extending thermodynamic description from lower order to higher order multicomponent systems was pointed out in several presentations. Thermodynamic models currently used for ordered phases are to some extent connected with the software used for calculations. Probably, the most commonly used formalism is the compound energy formalism (CEF) developed by Hillert's school in Stockholm. Since it is adopted in Thermo-Calc software it has became the general way for describing the thermodynamics of the ordered phases due to the widespread popularity of this software system throughout the world. However, **Sergei Decterov** pointed out that

when working with oxide systems one may end up with an unbalanced model that gives unreasonable extrapolation of lower order subsystem to a multicomponent solution. Also, **Austin Chang** claimed that the application of cluster site approximation (CSA) to account for the configuration dependent term in the Gibbs free energy of the ordered intermetallic phase greatly simplifies the calculations.

Combination of ab initio total energy calculations including the magnetic contributions were presented in a number of papers. This powerful computational technique was not only used for calculations of lattice stability difference; it was shown by **Tetsuo Mohri** how Cluster Variation Method via Cluster Expansion Method can be applied to simulation of microstructure evolution processes. **Didier de Fontaine** demonstrated how temperature effect on oxygen ordering in YBCO supercondutor can be simulated with Monte Carlo method. Generally, very interesting trend emerged, which concentrates more and more on dynamic phenomena in alloys.

This new trend was seen in presentations such as the DICTRA simulation of precipitation reactions in ferritic steel (**Gerhard Inden**), the kinetics of precipitate-nucleation at the edge of the miscibility gap (**Toru Miyazaki et al.**) and computer simulations of the Kirkendall effect in binary and multicomponent alloys (**Henrik Strandlund** and **Henrik Larsson**). Since the growth of stable and metastable phases begins with nucleation process, its dependence on chemical driving force and the interfacial energy should be known. Thus, it is not surprising that a number of research groups have devoted their efforts to the investigations of physical properties among which the most important seems to be the determination of the interfacial energy. Another interesting problem is the departure from conditions which are usually assumed as standard. More and more calculations are devoted to problems of the modeling of the equilibrium under high pressure or the interaction between the chemical and magnetic ordering. As examples, a few works can be mentioned. A new semi-empirical equation of state that is used to describe the pressure-volume-temperature dependence, which can be integrated to yield explicit, analytic expression of G(T, p) was applied to the available experimental data on uranium by **Eli Brosh et al.** In turn, results of calculations of the Al-Si-Mg system, including pressure dependence for condensed phases in the Gibbs energy expression for each phase, were given by **Bengt Hallstedt** and **Jochen M. Schneider**. Thermodynamic analysis of Fe-Al and Fe-Ga binary systems showed that stability of the ordered phase may be enhanced or depressed due to the interaction between chemical and magnetic ordering. **Ikuo Ohnuma et al.** demonstrated that two-phase separation in these systems is caused by this kind of depressive interaction.

An excellent example of the usefulness of the experimental studies and thermodynamic calculations based on CALPHAD method was given by **Kiyohito Ishida**. By utilizing the information on phase diagrams, development of databases on microalloying steels, ADAMIS, Cu-base alloys as well as experimental information on the following advanced material has been archived:

- a new type of high speed steels,
- new Pb-free machinable stainless steels,
- new Pb-free solder,

- shape memory alloys,
- Invar alloys,
- egg-type powders.

Herbert Ipser reported on European Research Action on lead – free soldering, which was initiated in 2002 under the COST Program of the European Union. The goal of this program is the establishment of a database that contain the relevant knowledge on possible lead free solder materials and providing expertise for selecting particular materials for specific soldering purposes. One of the tendencies in modeling of Pb-free soldering materials is the investigation of quaternary and quinary systems on the basis of Sn-Ag and Sn-Ag-Cu eutectics. The results of experimental wettability studies of these alloys were discussed by **Zbigniew Moser et al.** Other studies were concerned with the phase evolution, phase equilibria, surface tension, viscosity as well as to the modeling of those phenomena. The development of thermodynamic databases was lectured on by **Alan Dinsdale**. Scientific Group Thermodata Europe (SGTE) is a part of broader international effort to unify thermodynamic data and the assessment methods. Activities undertaken within SGTE started from the well established Substance, Solution and UNARY Databases and there are plans to release of a number of new materials specific databases as well as plans for the next generation of database.

Some papers deal with the industrial applications of the knowledge of the phase equilibria and alloys thermodynamics. It seems that the potential of the CALPHAD method may also consist in its various applications.

3. Next meeting

As the next Chairman of the Organizing Committee, **Harry Oonk** advertised "the place in the middle of the nowhere". Maastricht, the small town in the Netherlands, will be the host of the next Calphad Meeting in 2005. Let's hope that most of us will be able to get together there.

Editorial

From Aleksander Krupkowski's Ideas to Associated Phase Diagram and Thermodynamics Committee and XXXIII Calphad in Kraków

Dedicated to Professor Aleksander Krupkowski in His 110 years anniversary of the birth

Aleksander Krupkowski was the dominating scientist who put the foundations in the thermodynamic theory of the metallurgical processes. In 1950, A. Krupkowski proposed a binary formalism for the thermodynamics description of metallic alloys [1]. This formalism is particulary applicable to systems with positive deviations from ideality. The utility of this formalism has been verified by studies in real systems with alloying components numbering anywhere from two to five mainly by means of high temperature electrochemical methods.

A broadened utilization of the Krupkowski formalism has resulted from its presentation at the symposium on "Thermodynamics of Alloys" that was organized in Münster, Germany in 1972. Participants in the symposium were a worldwide mix. A majority of those participants have developed into what might be considered an interactive "thermodynamic family" with active participation of Polish scientists. In the series of my Editorials published in *the Journal of Phase Equilibria* in 1992, 1994, 1996, 1998 and 2002 I subsequently presented the most important features of this "thermodynamic family" and in the shortened form they are presented here as regards the Polish contribution.

In 1976 a program began at the Institute for Metal Research (next renamed as Aleksander Krupkowski Institute of Metallurgy and Materials Science) to coordinate research on problems of basic interest to the utilization and production of metals in Poland. In addition to our Insitute, a number of others were involved. These include the AGH University of Science and Technology, the Jagiellonian University in Kraków, and technical universities in Silesia, Warsaw, as well as a number of industrial research institutes.

In 1978 Polish centers joined the program undertaken by the National Bureau of Standards and American Society for Metals (in the frame of Maria Curie-Skłodowska funds) to combine thermodynamic data with existing information on phase equilibria to produce critically evaluated phase diagrams for industrial application. As a result, numerous evaluations of zinc, cadmium and mercury binary systems were published in *Bulletin of Alloy Phase Diagrams*, in monographs edited by ASM International and next in the *Journal of Phase Equilibria*. This enabled the Polish contribution to Calphad group, to participations in regular "Thermodynamics of Alloys" conferences and initiated the idea to organize one of future Calphad meeting in Poland, recently held in Kraków May 30—June 4, 2004. Though the real history of phase diagram evaluation is more complicated, the points is that the calculations showed one very interesting and important feature of available experimental data. It would not be possible to derive the complete phase diagram even for the binary system if the data used for calculation were taken from only one experimental source. Basing on international co-operation, step by step our Institute initiated the calorimetric studies, being an important contribution in parallel to experimental high-temperature galvanic cells and vapor pressure measurements.

Calorimetry provides the way of the determination of the heat effects by means of a suitably device. In several previous studies we have measured heats effects accompanying the formation of liquid alloys, but in the recent years, we have followed the actual trends in thermodynamics of solid intermetallics to make the comparison between experiment and theoretical predictions of the enthalpies of formation in co-operation with Brookhaven National Laboratory in USA [2]. Experimental studies were concentrated on phases of Al-Ni, Al-Ti and Al-Fe systems combining two techniques: solution calorimetry in liquid aluminium or observing the heat effects accompanying reaction of powder components directly in the calorimeter realized within the co-operation with Nancy University in France (direct reaction method). These two calorimetric methods were used for the determination of the enthalpies of formation of advanced aluminides: Al_3Ni_2, AlNi and $AlNi_3$ as the main candidates for the high-temperature application on blades of turbines in electric power stations and in engines of helicopters [3].

Discussions of the specific details of the experimental thermodynamic efforts throughout Poland is beyond the scope of this presentation. Suffice is to say that Poland is one of the few places in the world where basic thermodynamic research continues. In this respect our position is very important because as noted by P. Nash from Illinois Institute of Technology [4] "there are so few centers in the United States that a critical mass barely exists to ensure continued competence in the measurement of thermodynamic data in the future".

Transformation of PPDC into international committee

In 1994 our Institute celebrated the one hundredth anniversary of the birth of its founder, Aleksander Krupkowski, which occured concurrently with the acceptance of the Polish Phase Diagram Committee (PPDC) into the Alloy Phase Diagram International Commission (APDIC) comprising the leading world centers working in phase equilibria studies in the broad context. This was a recognition of the experimental thermodynamic research of several groups within Poland that are directed toward the calculation of phase equilibria.

We are still trying to perform experimental studies within the members of PPDC and even we are feeling responsible for other European countries, which have gone through political and democratic changes. This problem has been undertaken many times during the period from 1995 to 1998 at each annual meeting of APIDC. It was mentioned that variety of scientific centers exist in these countries where experimental thermodynamics and phase equilibria are studied. Due to these facts, it was strongly recommended by APDIC that the authorities of the Polish Phase Diagram Committee should encourage the integration of partners from Central European countries. It took nearly four years of discussions during joint work-shops together with presentations of different countries activities at annual meetings of APDIC to accept in 2002 as a member of APDIC the new committee: "Associated Phase Diagram and Thermodynamics Committee" (Poland, Bulgaria, the Czech Republic, Hungary, Slovakia and Yugoslavia). It should be added, that during the work-shop of the new Committee in November 2003 in Kraków, Slovenia and Romania became the new members and instead of Yugoslavia now are Slovenia and Montenegro.

The future of the new Committee from 2002 to 2004 acting as the international net-work is connected with joint research, the exchange of our experience, and the attempts to prepare proposals of projects financed by EU.

The research carried out by Polish centers in the field of experimental thermodynamics of alloys and the organization of the XXXIII Calphad Congress in Kraków are all associated with the late eminent Professor Aleksander Krupkowski, whose 110th birthday was commemorated this May.

[1] Z. M o s e r, Thermodynamic Behaviour in Binary Metallic Solutions, Metall. Trans. B **6B**, 1975, 653-659.
[2] K. R z y m a n, Z. M o s e r, R.E. W a t s o n, M. W e i n e r t, Enthalpies of Formation of Ni_3Al: Experiment Versus Theory, J. Phase Equilibria **17**, 1996, 173-178.
[3] K. R z y m a n, Z. M o s e r, Calorimetric studies of the enthalpies of formation of Al_3Ni_2, AlNi and $AlNi_3$, Progress in Materials Science, A Festschrift Issue in Honor of T.B. Massalski **49**, 2004, 581-606.
[4] U.R. K a t t n e r, J.E. M o r r a l, W.J. B o e t t i n g e r, Databases for Computational Thermodynamics and Diffusion Modeling, J. Phase Equilibria **24**, 2003, 418.

Zbigniew Moser
Editor of Archives of Metallurgy and Materials

A R C H I V E S O F M E T A L L U R G Y A N D M A T E R I A L S
Volume 49 2004 Issue 3

G. AURELIO *, A.F. GUILLERMET*, P.B. BOZZANO**, G.J. CUELLO***

HIGH-TEMPERATURE ISOTHERMAL NUCLEATION OF THE METASTABLE Ω PHASE IN Zr-Nb ALLOYS

WYSOKOTEMPERATUROWE IZOTERMICZNE ZARODKOWANIE METASTABILNEJ FAZY Ω W STOPACH Zr-Nb

This paper presents an experimental study and an analysis of the isothermal nucleation of the metastable omega (Ω) phase in a high-Nb Zr-Nb alloy. The work combines *in situ* neutron thermodiffraction (NTD) with transmission electron microscopy (TEM) observations at room temperature in quenched/aged/quenched alloys. The NTD data are interpreted on the basis of a rather general lattice parameter *vs.* composition systematics established very recently by ourselves. The results of the present study yield strong support to a picture of the isothermal bcc→Ω phase transformation which involves the initial formation of significantly Nb-depleted Ω nuclei.

W pracy przedstawiono wyniki badań eksperymentalnych oraz analizy przebiegu izotermicznego zarodkwania metastabilnej fazy omega (Ω) w bogatych w Nb stopach Zr-Nb. Wyniki obserwacji *in situ* z metody rozpraszania neutronów termicznych (NTD) połączono z wynikami badań transmisyjnym mikroskopem elektronowym (TEM) prowadzonych w temperaturze pokojowej na stopach szybko schładzanych, starzonych i ponownie szybko schładzanych. Dane otrzymane metodą NTD zostały zinterpretowane w oparciu o własne, uzyskane niedawno, uogólnione parametry sieciowe w funkcji zmiany składu. Wyniki przeprowadzonych badań pozwalają zobrazować przebieg izotermicznej transformacji fazowej bcc→Ω z uwzględnieniem początkowego formowania się zarodków fazy Ω, znacznie zubożonych w Nb.

1. Introduction

The phase stability trends in the periodic table, particularly in the transition metals, has been a matter of continuous theoretical interest [1]. The early studies focused on the

* CENTRO ATÓMICO BARILOCHE AND CONSEJO NACIONAL DE INVESTIGACIONES CIENTIFICAS Y TECNICAS, AV. BUSTILLO 9500. BARILOCHE (RN), 8400, ARGENTINA
** COMISIÓN NACIONAL DE ENERGIÁ ATÓMICA, CENTRO ATÓMICO CONSTITUYENTES, AV. GRAL. PAZ 1499, SAN MARTIN, BUENOS AIRES, 1650, ARGENTINA
*** INSTITUT LAUE LANGEVIN, BP 156, F-38042 GRENOBLE CEDEX 9, FRANCE

structural sequence hcp→bcc→hcp→fcc which is observed from left to right across the non-magnetic transition metals (TM). Later, there was a growing interest in studying the stability of progressively more complex phases [2] in particular, those which form in alloys through structural transitions of one of the key phases mentioned above. This is the case of the Ω phase, which is observed experimentally at high pressure in pure Zr, Ti and Hf. This phase also forms by quenching alloys of these elements with other transition metals [3]. More recently, the interest in a detailed account of the structural properties and the relative stability of the Ω and bcc phases in the TM elements has been renewed [4–8]. In the present work we focus on the high-temperature reactions of the Ω phase in a key TM alloy system, *viz.*, the Zr-Nb system.

The Zr-Nb system has traditionally been considered a prototype of the binary Ω forming alloys on the 4d TM series. The phase diagram [9] shows a stable high-temperature bcc (β) phase which forms various metastable structures upon quenching ("q") to room temperature (T_R), *viz.*, the martensitically formed hcp (α^q) phase, the "athermal" Ω phase (Ω^q) and the untransformed β^q phase [3, 7]. In addition, under isothermal heat treatments ("aging") at an aging temperature, $T_A > T_R$, diffusion-controlled reactions occur in the quenched alloys. In particular, the Ω phase might be induced by aging the quenched β^q phase in alloys with an appropriate Nb content [10–12]. However, the relative stability and structural properties of the "isothermal" β^a and Ω^a phases involved in the aging phenomenon have traditionally been poorly known from direct measurements [4, 5]. In view of this problem, we are currently carrying out a long-term research project aimed at developing a picture of the structural properties and relative stability of the athermal and isothermal metastable phases in Zr-Nb and Ti-V alloys [4–7, 13–15]. In order to introduce the specific type of problems dealt with in our previous and present work, we shall briefly review the account of the occurrence of the Ω phase in terms of the usual Ω_s *vs.* composition diagram, where Ω_s represents the so-called Ω-start temperature.

Figure 1 shows a schematic plot of the Ω_s line applicable to alloys with $6 \leq x_{Nb} \leq 20$, which is based on experimental data by Cometto [6], Perkins [17] and ourselves [7]. For lower Nb contents, the Ω formation is suppressed because of the competing α^q transformation [6, 7]. The arrows in Fig. 1 indicate the sequence of transformations that occur in alloys with representative compositions x_{Nb} = 10 and 18 at.%. For an alloy with 10 at.% Nb, rapid cooling from the high temperature β field (vertical arrows) causes a crossing of the Ω_s temperature at ≈ 650 K leading to the partial transformation of β into Ω^q. At T_R the transformation is still not complete and the alloy consists of a two-phase mixture of β^q and Ω^q with 10 at.% Nb [7, 15]. Alternatively, for alloys with $x_{Nb} > 18$ at.%, the Ω_s temperature is lower than T_R. Therefore, no Ω^q phase is formed by quenching. In the latter case, the as-quenched state consists of a single-phase β^q alloy [7].

When the as-quenched alloys are subjected to aging treatments, diffusion- controlled reactions occur, which are represented in Fig. 1 by horizontal arrows. When the quenched 10 at.% alloy is aged at a temperature lower than Ω_s, the as-quenched two-phase alloy evolves into a Nb-depleted Ω^a phase coexisting with a Nb-enriched β^a phase [8]. Eventually, the alloy reaches a stationary two-phase state where Ω^a and β^a coexist, which is metastable with respect to the formation of the α phase.

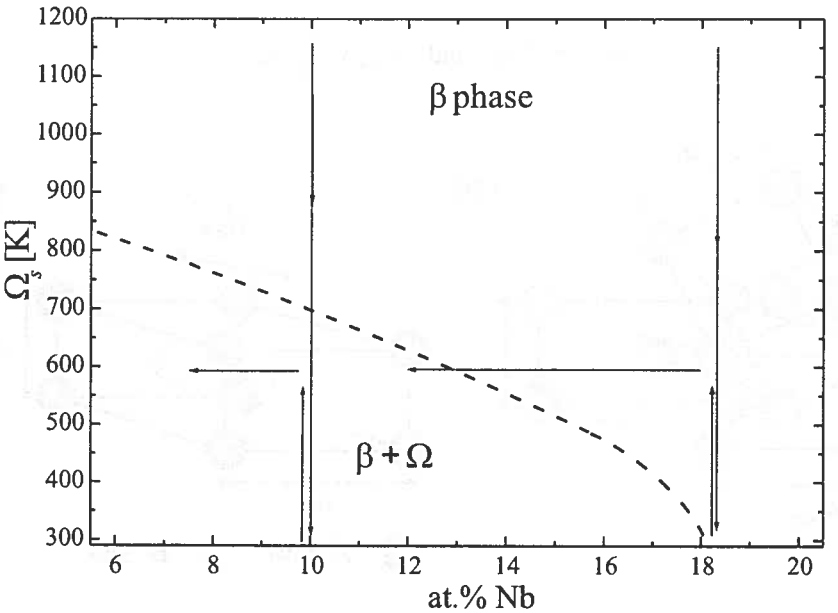

Fig. 1. Schematic $\beta \rightarrow \Omega$ athermal reaction start temperature as a function of alloy composition in the Zr-Nb system. The arrows represent the quenching and aging heat treatments considered in the text.

Finally, as an introduction to the question which motivates the present study, let us consider the possible evolution of a quenched alloy with 18 at.% Nb aged at high temperature. According to the scheme in Fig. 1, the alloy should remain single-phase when heated to any temperature above T_R. However, during an aging treatment it is feasible that composition fluctuations might cause the formation of Nb depleted regions which fall on the left-hand side of the Ω_s line. In such case, as described by the horizontal arrow in Fig. 1, the $\beta \rightarrow \Omega$ transformation would be induced, and a Zr-rich Ω^a phase might, in principle, nucleate. The purpose of the present study is to explore experimentally the possible isothermal formation and the subsequent evolution of the Ω^a phase in a Zr-Nb alloy with a high Nb content. The work combines *in situ* neutron thermodiffraction (NTD) experiments with transmission electron microscopy (TEM) observations at T_R of alloys quenched, aged and quenched again.

2. Crystallographic basis and structural relations

The $\beta \rightarrow \Omega$ transformation occurring on quenching Zr-rich Zr-Nb alloys may be described by referring to an hexagonal representation of the parent β phase, which is shown schematically in Fig. 2(a). There, the β phase, with a lattice parameter (LP) a_β, has been represented by means of an hexagonal cell with LPs a_{bcc} and c_{bcc}, which are related to a_β as follows

$$a_{bcc} = \sqrt{2}\, a_\beta \quad \text{and} \quad c_{bcc} = \frac{\sqrt{3}}{2} a_\beta \tag{1}$$

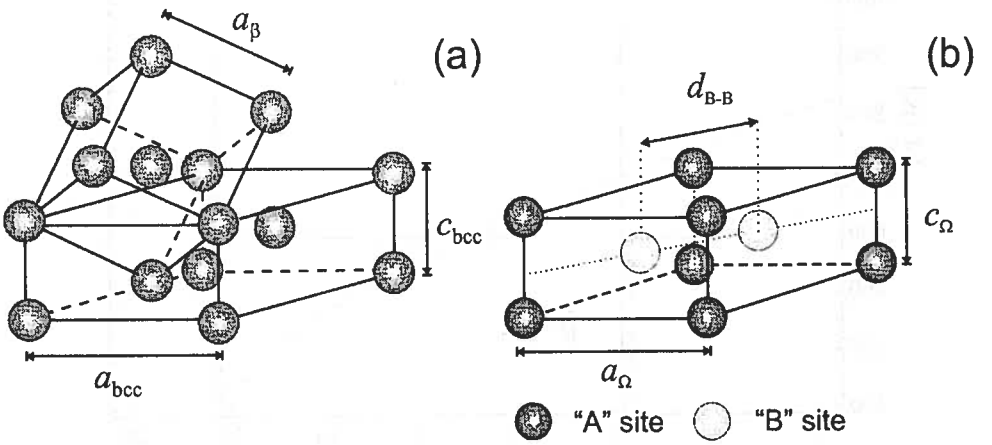

Fig. 2. (a) Geometrical relations between the hexagonal representation of the bcc structure and the traditional cubic cell. (b) The unit cell of the hexagonal Ω phase.

The athermal $\beta \rightarrow \Omega$ transformation involves a change in the position of the inner atoms of the hexagonal cell. The magnitude of this change depends upon the composition of the alloy [7]. The so-called ideal Ω phase, which has hexagonal symmetry, is described by space group P6/*mmm* and is formed in pure Zr [18–20] and Zr-rich Zr-Nb alloys [7, 21, 22]. In more concentrated alloys the symmetry is trigonal, described by the space group $P\bar{3}m1$ [7, 22]. The β structure corresponds to space group $Im\bar{3}m$.

Changes in the LPs of the hexagonal cell may also occur during the athermal $\beta \rightarrow \Omega$ transformation. In Zr-Nb alloys, this transformation does not reach completion on quenching, *i.e.*, there always remains some untransformed β^q phase coexisting with Ω^q [7]. These structures have been shown to present well-defined orientation relationships, *viz.*, the $[0001]_\Omega$ hexagonal axis is parallel to the $[111]_\beta$ cubic direction, and the $[11\bar{2}0]_\Omega$ hexagonal direction is parallel to the $[1\bar{1}0]_\beta$ cubic direction [23]. There is, in general, a misfit between the β and Ω lattices, which can be expressed by means of the relative differences $\Delta a/a = (a_\Omega - a_{bcc})/a_{bcc}$ and $\Delta c/c = (c_\Omega - c_{bcc})/c_{bcc}$.

3. Experimental methods and results

3.1 Alloys, samples and heat-treatments

The measurements discussed in this paper were performed on alloys with a nominal Nb content of 18 at.% Nb. Two sets of alloys were prepared from Zr and Nb of 99.9% and

99.8% purity, respectively, in an arc furnace, on a water-cooled copper hearth, using non-consumable electrodes in a 350-Torr Ar atmosphere, and were remelted at least six times to favor homogeneity. For NTD experiments, the alloy was cut into shavings of about 2 mm side length in order to approach the conditions of a powder. The shavings were wrapped up in Ta foils, doubly- encapsulated in quartz under high-purity Ar, annealed 1 h at 1273 K, and quenched in water by breaking the outer capsule. The global Nb content of this NTD alloy, *viz.*, 18.6 ± 0.5 at.% Nb, was determined using a Cameca SX100 EPMA equipped with five wavelength-dispersive spectrometers at the Max- Plank Institut, Stuttgart. For TEM studies, a second alloy was spark-machined to a 3 mm diameter cilinder, encapsulated in quartz under high-purity Ar, annealed 1 h at 1273 K, and quenched in water by breaking the capsule. This quenched cilinder was cut into 4 samples, each one encapsulated in Vycor glass and annealed at 600 K for 2, 10, 20 and 30 h. These annealings were interrupted by a quenching in water with breaking the capsules. The composition of the samples was determined by EDS during the TEM experiments.

3.2 Neutron thermodiffractometry and data processing

The neutron thermodiffraction experiments were performed in the D1B two-axes diffractometer at the Institute Laue-Langevin, Grenoble, France. The neutron spectra were collected placing the ^{3}He multidetector of 400 cells in a cylindrical geometry centered at the sample. The angular span was of 80°, with steps of 0.2°. A Ge monochromator in the (311) reflection was used, obtaining a wavelength $\lambda \approx 1.28$ Å. This wavelength and the zero-shift were calibrated using a standard Al_2O_3 sample, which yielded $\lambda = 1.2899 \pm 0.0001$ Å. The samples were aged in a standard Vanadium furnace under vacuum of $1.8\ 10^{-4}$ mbar in order to prevent oxidation, which was verified after the aging treatment. The neutron flux on the sample was of about 10^6 n/(s cm^2), which allowed us to monitor the evolution during aging by diffraction patterns collected in 5 minutes. The sample was first kept for some minutes at $T = T_R$ and a long aging treatment at $T = 600$ K was performed. The diffraction data, which amount to 24 diffractograms, were processed using the full-pattern analysis Rietveld method, with the program Fullprof [24].

3.3 Transmission Electron Microscopy

The quenched/aged/quenched samples for TEM studies were cut into 3 mm discs and mechanically grinded to a thickness of 0.1 mm. For the final thinning, the discs were electropolished at 243 K in a 10% perchloric acid, 55% methanol and 35% buthanol mixture using a current of 25–30 mA. The TEM observations were performed in a Phillips CM200 transmission electron microscope operating at 200 kV with an energy dispersive X-ray spectrometer EDAX DX- 4. The energy dispervive spectrometry (EDS) data were converted to relative at.% values using the M o t t and M a s s e y model [25].

4. Discussion and Conclusions

4.1 Neutron Thermodiffractometry

Figure 3 shows the evolution during aging of the neutron diffractograms collected at $T = 600$ K. The arrows indicate the position of peaks corresponding to a second structure present in the sample after 250 min. These peaks can be well accounted for in the Rietveld refinements by adding a second phase with hexagonal symmetry, corresponding to the Ω phase.

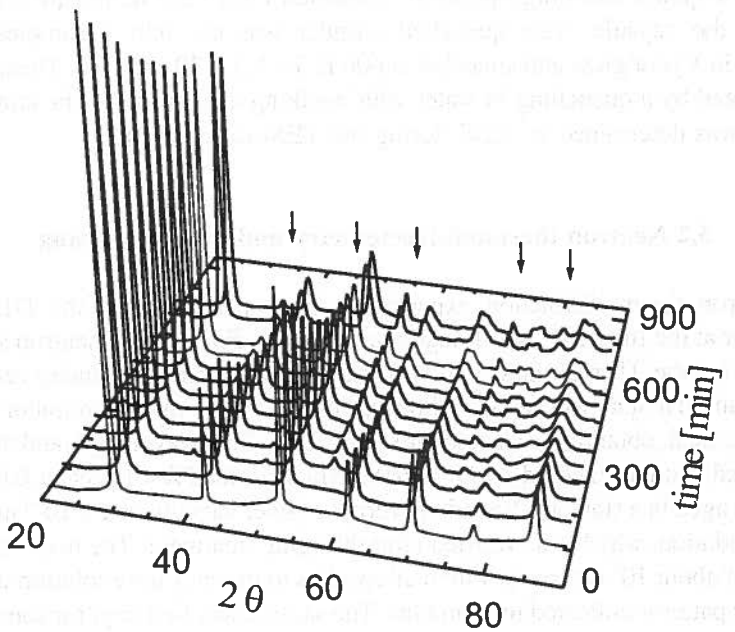

Fig. 3. Neutron diffractograms as a function of aging time. The data were collected at ILL's D1B diffractometer for an alloy with 18.6 at.% Nb aged at 600 K.

In Fig. 4 we present the temperature *vs.* time data corresponding to the heat-treatment applied to the sample. The solid line in (a) represents the temperature of the sample, measured in 5-minute time steps. The symbols represent series of 5-minute neutron diffractograms at a given temperature which were added up to enhance the statistics for the Rietveld refinements. Figure 4 shows with filled symbols the LPs determined for the sample as functions of aging time for the β phase (b) and the Ω phase (c-d). Open symbols in Fig. 4 correspond to the LPs a_{bcc} and c_{bcc} of the β phase in its hexagonal representation, calculated inserting the a_β values in Fig. 4(b) into Eq. (1).

The results in Figs. 3 and 4 indicate that in the as-quenched state the alloy with 18.6 at.% Nb consists of a single β^q phase. Upon aging, the original β^q single-phase state transforms to a $\beta^a + \Omega^a$ mixture, more specifically, the Ω^a phase was observed to form in co-existence with β^a after 4 h at 600 K. In addition, Fig. 4(c) reveals a striking feature of the LPs

behaviour. The LP a_Ω in the first detectable embryos of Ω^a in exactly the same as the a_{bcc} value of the β phase, which is indicative of the high degree of coherency between both phases in the a_Ω-axis direction. The c_Ω parameter of the Ω^a embryos, on the other hand, suggests that there are no significant coherency Ω/β strains in the c_Ω-axis direction. These results will be further discussed below.

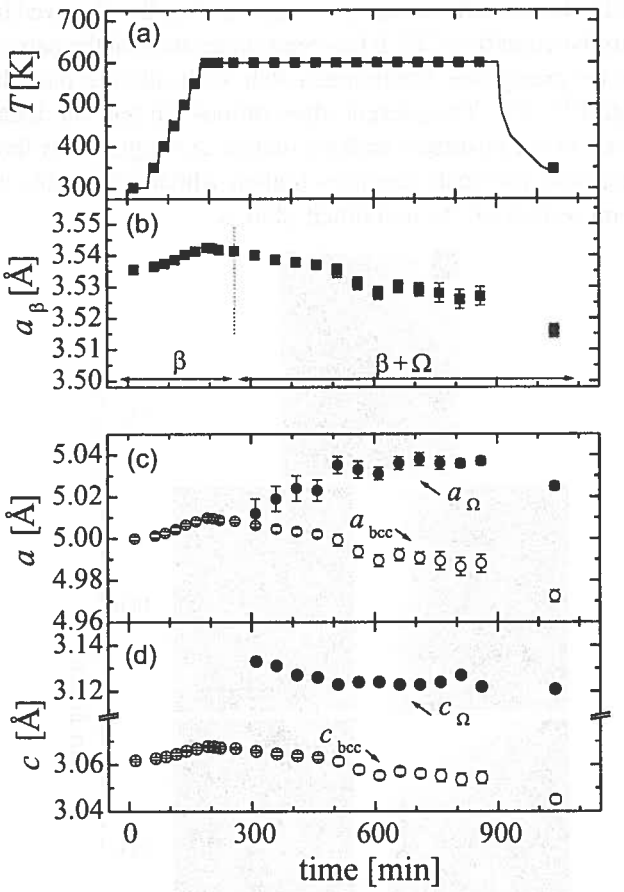

Fig. 4. (a) Heat-treatment applied to an alloy with 18.6 at.% Nb. The solid line represents the temperature of the sample, measured in 5-minute time steps. Symbols represent series of 5-minute neutron diffractograms at a given temperature, which were added up to enhance the statistics. (b) The experimental LP of the β phase determined as function of time during the heat-treatment presented in (a). (c-d) The experimental LPs of the Ω phase, a_Ω and c_Ω, respectively (filled symbols). Open symbols represent the LPs a_{bcc} (c) and c_{bcc} (d) of the β phase in its hexagonal representation

4.2 Microstructure of aged alloys

In Fig. 5 we present the microstructure of samples corresponding to an alloy with 18.0 ± 0.3 at.% Nb aged at 600 K for 2 h (a), 10 h (b-c), 20 h (d-e) and 30 h (f-g). Dark field

micrographs (Fig.5 (c), (e) and (g)) were obtained using Ω reflections from the electron diffraction pattern. For short aging times no Ω particles are detected (Fig.5 (a)), whereas after 10h at 600 K there is a change in the microstructure, consisting of very small Ω particles in a β matrix. The sequence of micrographs shows that as aging time is increased the particles seem to align and adopt the cuboidal shape characteristic of the aged Ω phase in other Zr-Nb alloys [8], although the cubes size is smaller than the observed in Zr-10 at.% Nb alloys aged under similar conditions [8]. It has been suggested that the particle morpholgy is highly dependent on the precipitate- matrix mismatch, with cuboidal particles formed when the mismatch is high [27, 28]. The present observations support the idea that the initial Ω particles form with a lower mismatch with the matrix, as suggested by the LP data, and as the aging time is increased the misfit becomes higher, which is probably connected to the evolution of the composition of the individual phases.

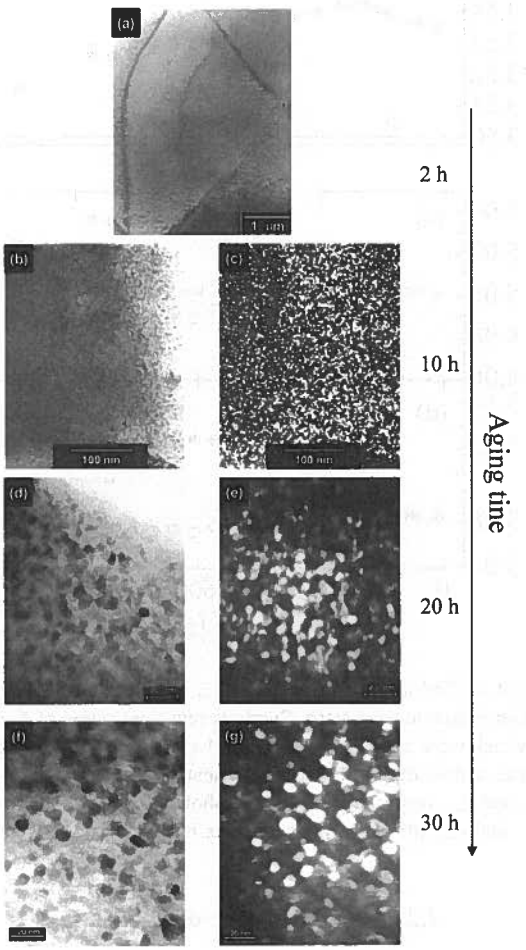

Fig. 5. TEM micrographs of an alloy with 18 at.% Nb aged at 600 K. (a) After 2 h aging. (b, c) After 10 h aging. (d, e) After 20 h aging. (f, g) After 30 h aging. Dark field images (c, e, g) were obtained using an Ω reflection from the electron diffraction pattern

4.3 Final remarks on the isothermal Wa nucleation processes

In Fig. 6 we show the c_Ω parameter in quenched (open symbols) and aged (filled symbols) alloys at $T = 600$ K as function of the Nb content according to various sources [4–7, 10, 11, 13, 16, 18, 23, 29–32]. For aged alloys, the composition was estimated using the method of analysis described in references [8] and [15]. The horizontal dotted lines represent the c_Ω values determined in the present work for the Ω phase which forms isothermally at the initial stages of the aging treatment (upper line) and after the longest aging time (lower Wline). These lattice parameter values are consistent with a picture of the nucleation of an isothermal Ω phase significantly depleted in Nb.

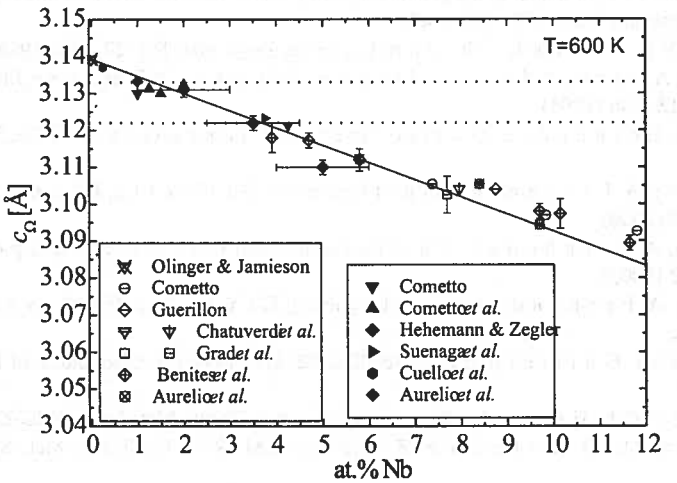

Fig. 6. Composition dependence of the lattice parameter c_Ω in quenched (open symbols) and aged (filled symbols) Zr-Nb alloys at T_R. The Nb content in the Ω^a phase was determined using the estimation procedure described in Refs. 8 and 15. The solid line represents the reference behaviour proposed for the c_Ω parameter. The horizontal dotted lines represent the c_Ω values determined in the present work for the aged Ω phase formed at the initial stages of the aging treatment (upper line) and after the longest aging time (lower line)

We have shown in previous studies [8, 15] that the isothermal Ω phase, characterized by relatively high c_Ω values as compared with the parent athermal Ω^q phase, is actually depleted in Nb. The present results indicate that this feature holds not only for an Ω^a phase in which the already formed Ω particles exchange Nb with the matrix, but that this Nb depletion is necessary for the nucleation of the Ω^a phase in single-phase β alloys with a relatively high Nb content.

Acknowledgments

The alloys and samples were prepared by C. Ayala at the Metals Physics Division (Centro Atómico Bariloche, Argentina). We appreciate the support of the Spanish Cooperation Research Group at the Institut Laue-Langevin,

which allowed us to use the D1B neutron diffractometer, and in particular we thank Dr. J. Campo for his help and assistance during the experiments at D1B. This work is part of a research project supported by Agencia Nacional de Promoción Cientfica y Tecnológica (Argentina), under grant No. 03-00000-00688 and by CONICET (Argentina) under grant PIP 02612.

REFERENCES

[1] R.A. Deegan, J.Phys. C **1**, 763 (1968); N.W. Dalton, R.A. Deegan, J.Phys. C **2**, 2369 (1969); J. Friedel, in The Physics of Metals, edited by J.M. Ziman (Cambridge, UK, 1969); D.G. Pettifor, J. Phys. C **3**, 367 (1970); J.C. Duthie, D.G. Pettifor, Phys. Rev. Lett. **38**, 564 (1977); D.G. Pettifor, J. Chem. Phys. **69**, 2930 (1978); H.L. Skriver, Phys. Rev. B **31**, 1909 (1985).

[2] A.P. Miodownik, in Statics and Dynamics of Alloy Phase Transformations, edited by P.E.A. Turchi and A. Gonis (Plenum Press, NY, 1994), 45.

[3] S.K. Sikka, Y.K. Vohra, R. Chidambaram, Prog. Mat. Sci. **27**, 245 (1982).

[4] G.J. Cuello, A. Fernández Guillermet, G.B. Grad, R.E. Mayer, J.R. Granada, J. Nucl. Mat. **218**, 236 (1995).

[5] G.B. Grad, A. Fernández Guillermet, J.J. Pieres, G.J. Cuello, Z. Metallkd. **87**, 721 (1996).

[6] G.M. Benites, A. Fernández Guillermet, G.J. Cuello, J. Campo, J. Alloys and Comp. **299**, 183 (2000).

[7] G. Aurelio, A. Fernández Guillermet, G.J. Cuello, J. Campo, J. Alloys and Comp. **335**, 132 (2002).

[8] G. Aurelio, A. Fernández Guillermet, G.J. Cuello, P.B. Bozzano, Mat. Sci. Forum, in press.

[9] A. Fernández Guillermet, Z. Metallkd. **82**, 478 (1991); H. Okamoto, J. of Phase Equilibria **13**, 577 (1992).

[10] D.J. Cometto, G.L. Houze Jr., R.F. Hehemann, Trans. Met. Soc. AIME **233**, 30 (1965).

[11] M. Suenaga, J.L. O'Brien, V.F. Zackay, K.M. Ralls, Trans. Met. Soc. AIME **239**, 992 (1967).

[12] N.A. Vanderpuye, A.P. Miodownik, in The Science Technology and Applications of Titanium, edited by Jaffee and Promisel (1970), p. 719.

[13] G. Aurelio, A. Fernández Guillermet, G.J. Cuello, J. Campo, Met. & Mat. Trans. **32A**, 1903 (2001).

[14] G. Aurelio, A. Fernández Guillermet, G.J. Cuello, J. Campo, Met. & Mat. Trans. **34A**, 2771 (2003).

[15] G. Aurelio, A. Fernández Guillermet, G.J. Cuello, J. Campo, to be published.

[16] D.J. Cometto, PhD Thesis (Case Institut of Technology, 1962).

[17] A.J. Perkins, P.E. Yaffe, R.F. Hehemann, Met. Trans. **1**, 2225 (1970).

[18] B. Olinger, J.C. Jamieson, High Temp. High Press. **5**, 123 (1973).

[19] E.N. Kaufmann, D.B. McWhan, Phys. Rev. B **8**, 1390 (1973).

[20] T. Butz, G.M. Kalvius, H. Göbel, W.B. Holzapfel, Hyperfine Interactions **1**, 1 (1975).

[21] G.B. Grad, A. Fernández Guillermet, J.R. Granada, Z. Metallkd. **87**, 726 (1996).

[22] G.M. Benites, A. Fernández Guillermet, J. Alloys and Comp. **302**, 192 (2000).

[23] J.P. Guérillon, Metaux, Corrosion, Industrie **557**, 21 (1972).

[24] J. Rodríguez-Carvajal, *FULLPROF*: A Program for Rietveld Refinement and Pattern Matching Analysis, Abstracts of the Satellite Meeting on Powder Diffraction of the XV Congress of the IUCr, 127, Toulouse, France (1990).

[25] Principles of analytical electron microscopy, D. Joy, A. Romig y J. Goldstein Eds., Plenum Press, NY, 1986.

[26] G. Aurelio, Ph.D. thesis, Instituto Balseiro – Universidad Nacional de Cuyo, Bariloche, Argentina, 2003.

[27] B.S. H i c k m a n, Trans. Met. Soc. AIME **245** 1329, (1969).
[28] A.J. P e r k i n s, P.E. Y a f f e, R.F. H e h e m a n n: Metallography **4** 303, (1971).
[29] G.B. G r a d, J.J. P i e r e s, A. F e r n á n d e z G u i l l e r m e t, G.J. C u e l l o, J.R. G r a n a d a, R.E. M a y e r, Physica B **213**, 433 (1995).
[30] M. C h a t u r v e d i, K. T a n g r i, Trans. Met. Soc. AIME **245**, 259 (1969).
[31] M. C h a t u v e r d i, R.N. S i n g h, J. L e s s - C o m m. Metals **18**, 71 (1969).
[32] R.F. H e h e m a n n, S.T. Z e g l e r, Trans. Met. Soc. AIME **236**, 1594 (1966).

Received: 15 June 2004.

A R C H I V E S O F M E T A L L U R G Y A N D M A T E R I A L S
Volume 49 2004 Issue 3

V. JAN *, J. SOPOUŠEK**, R. FORET*

WELD JOINT SIMULATIONS OF HEAT-RESISTANT STEELS

SYMULACJE SPAWÓW STALI WYSOKOTEMPERATUROWYCH

Knowledge of microstructure stability is essential for reliable estimations of lifetime limitations of materials and welded joints at higher temperatures. The CALPHAD method complemented with appropriate diffusion approach can help us to simulate phase and element profile evolutions inside diffusion-affected zone of weld joint. The different heat-resistant steels (alloying base: Cr, Ni, Mo, V, C, N) and their weld joints are objects of our study. The particular results of the equilibrium calculations are presented as phase diagram cross-sections and element activities of the selected heat-resistant steels. The temperature dependences of carbon and nitrogen activities were calculated for individual steels. The difference in these activities in two different steels (at given temperature) indicates diffusion flow direction, which can be opposite to that deduced from the element content (up-hill diffusion). The simulations respect the coexistence of different carbide phases in the materials and they are conducted with the assumption that local phase equilibrium holds and that diffusion is the control process of phase transformation. The phase diagram calculations and diffusion couple simulations involving time-distance dependences for phase and element redistributions in diffusion-affected zones enabled us to obtain basic information, which allow to estimate thermodynamic and diffusion stabilities of the studied heat-resistant steels and their weld joints.
Keywords: phase profile, carbon redistribution, electrode, weld.

Znajomość stabilności mikrostruktur jest kluczowa dla wiarygodnego szacowania trwałości materiałów i ich spawów w wysokich temperaturach. Metoda CALPHAD uzupełniona odpowiednimi rozważaniami z dziedziny dyfuzji umożliwia symulację ewolucji profilów zawartości faz i składników wewnątrz strefy dyfuzji w obrębie spawu. Przedmiotem prezentowanych badań są różnego rodzaju stale wysokotemperaturowe (zawierające Cr, Ni, Mo, V, C, N) oraz ich spawy. Wyniki obliczeń równowagowych przedstawione są w postaci izotermicznych przekrojów wykresów równowagi oraz aktywności pierwiastków w wybranych stalach wysokotemperaturowych. Zależności temperaturowe aktywności węgla i azotu zostały obliczone dla poszczególnych

* DEPT. OF MATERIALS SCIENCE, FACULTY OF MECHANICAL ENGINEERING, BRNO UNIVERSITY OF TECHNOLOGY, TECHNICKÁ 2, BRNO CZ-61669 BRNO, CZECH REPUBLIK
** MASARYK UNIVERSITY-BRNO, FACULTY OF SCIENCE, DEPARTMENT OF THEORETICAL AND PHYSICAL CHEMISTRY, KOTLÁŘSKA 2, CZ-61137 BRNO, CZECH REPUBLIC

stali. Różnica pomiędzy takimi aktywnościami określonymi dla dwóch różnych stali w danej temperaturze określa kierunek strumienia dyfuzji, który może okazać się przeciwny w stosunku do kierunku wynikającego z gradientu koncentracji (dyfuzja "up-hill"). Przeprowadzone symulacje uwzględniają współistnienie w materiałach różnych faz węglikowych i prowadzone są przy założeniu lokalnych równowag fazowych oraz dyfuzyjnego charakteru przemian fazowych. Obliczanie wykresów równowag fazowych oraz symulacje par dyfuzyjnych przy uwzględnieniu czasowo przestrzennych zależności rozkładu faz i pierwiastków w strefie dyfuzji pozwoliły na uzyskanie podstawowych informacji, na podstawie których można było oszacować termodynamiczną i dyfuzyjną stabilność stali wysokotemperaturowych i ich spawów.

1. Introduction

Introducing new and improving the existing technologies and applications can be solved either by an entirely new technological unit or by a reconstruction involving a part of the unit being replaced with another while keeping the satisfactory part of the unit. Here, in the last mantioned ease, we usually are faced with the necessity of joining different materials.

A common way for joining different materials is the weld joint, which has many advantages that make it suitable for use at elevated temperatures. Frequently used materials are in this case various types of heat-resistant steels, which are usually used at temperatures of up to 500–700°C. Most of these weld joints are exposed to creep and low-cycle fatigue. The basic demand on these joints is therefore long-term mechanical stability, which is frequently decisive for the overall service life of the whole design solution.

The changes in creep strength are usually accompanied by microstructural changes in the material [1–4], which are driven by the natural tendency of material to reduce the total energy of the system. These changes include also diffusion of components in the direction of chemical potential gradient. Kinetics of diffusion-controlled transformations primarily depends on temperature, while the effect of pressure and stress sensor can usually be neglected. In this case, the microstructural changes are governed by volume diffusion of substitutional and interstitial elements.

When exposing weld joint for a long time to thermal exposure at elevated temperatures we usually observe appearance and extension of a diffusion-affected region formed by sequences of phase regions of different phase and chemical compositions. Eventually, a critical microstructural region can appear in the weld joint with properties that are substantially worse than the initial properties of the welded materials and the weld metal (e.g. in the decarburized region [6]). Thus even a best-quality weld can under certain circumstances trigger a breakdown even after several years of reliable operation [7].

The laboratory experiments with long-term thermal exposure of structurally unstable weld joint are extremely time demanding, and that is a fundamental drawback for this approach.

The geometry of actual welds made by current techniques is usually not strictly defined and is not suitable for laboratory study. An actual weld joint always includes two partial weld interfaces, which are usually separated by the material of consumable electrode so that the changes, which occur in the whole weld, can be separated into changes on partial weld

interfaces. Simplifying the problem by separating the weld joint into two laboratory diffusion couples makes the study of microstructural stability simpler and yields the same results as examining an actual weld. To have a reproducible experiment, the laboratory diffusion couples were prepared using special techniques [5], so a minimum heat-affected zone and a fusion zone (i.e. fused mixed region on weld interface) only several micrometers thick was achieved. Such couples have a step change in chemical composition and in properties on weld interfaces.

Today, theoretical models are available [8–10] (which are also used in the present paper) that enable conducting a real-time simulations of long-term thermal exposure of heterogeneous diffusion couples. The aim of this paper is to present the results of such simulations.

2. Subject of study

The following steels were introduced in our study (see Table 1): 13CrMoV 2-5-3 low-alloy heat-resistant steel, 12CrMo 10-10 steel (SK3STC Chromocord electrode),

TABLE

Chemical composition (in wt%) of the steels. Impurities were excluded from both equilibrium and diffusion simulations. Metal elements given in bold were always included. Other metal elements were involved in equilibrium calculations but excluded from diffusion simulations in some cases.

Steel	Abbreviation (National mark)	C	N	Cr	Mo	V	Common alloying	Impurities	Other metal component
X10CrMo 9-1 (heat-resistant steel)	**P91**	**0.10**	**0.045**	**8.50**	**0.88**	**0.23**	Si: 0.43 Ni: 0.10 Mn: 0.40	P: 0.015 S: 0.006	Nb: 0.018
13CrMOV 2-5-3 (low-alloy steel)	**LA** (CSN 15128)	**0.13**	–	**0.58**	**0.47**	**0.25**	Si: 0.31 Ni: 0.07 Mn: 0.60	P: 012 S: 0.022	–
12CrMo 10-10 (consumable)	**C** (SK3STC)	**0.12**	–	**2.73**	**0.96**	**0.01**	Si: 0.07 Ni: 0.02 Mn: 0.80	P: 0.008 S: 0.011	Nb: 0.013
X17CrNi 19-9 (high-alloy steel)	**HA** (CSN 17 242)	**0.17**	–	**18.93**	**0.02**	–	Si: 0.44 Ni: 8.75 Mn: 1.13	P: 0.015 S: 0.006	Ti: 0.01
6CrMoV 8-3-2 (low-alloy steel)	**T25**	**0.06**	**0.024**	**1.91**	**0.31**	**0.22**	Si: 0.34 Mn: 0.42	P: 0.0012 S: 0.0011	Nb: 0.058 W: 0.01 B: 0.003
C45 (carbon steel)	**St** (CSN 12 050)	**0.35**	–	**0.05**	–	–	Si: 0.33 Ni: 0.04 Mn: 0.69	–	Al: 0.49

X10CrMo 9-1 chromium heat-resistant steel, X17CrNi 19-9 high-alloy austenitic steel, 6CrMoV 8-3-2 low-alloy steel with nitrogen, and common carbon steel (St). In earlier experimental works [11, 12] some aveld joints of the above materials were examined at temperatures from 575 to 700°C during long-term exposure (as much as 10 000 h)[1]. These experimental studies were aimed primarily at the analysis of carbon concentration profiles after long-term thermal exposures. It resulted from experimental fact that the structure of diffusion-affected zone is given by redistribution of carbon, which may form carbide and carbonitride phases formerly suspended inside diffusion matrix (which is usually BCC). The identification of carbide and carbonitride phases, in particular close to the weld interface, is very difficult and there is a great lack of experimental results given in [11] for example.

3. Phase diagram calculations

To calculate the phase diagrams of the materials under examination the CALPHAD method [8, 10] was used. For all the phase equilibrium calculations presented in this paper the STEEL database was used in a version that had also been used in [17].

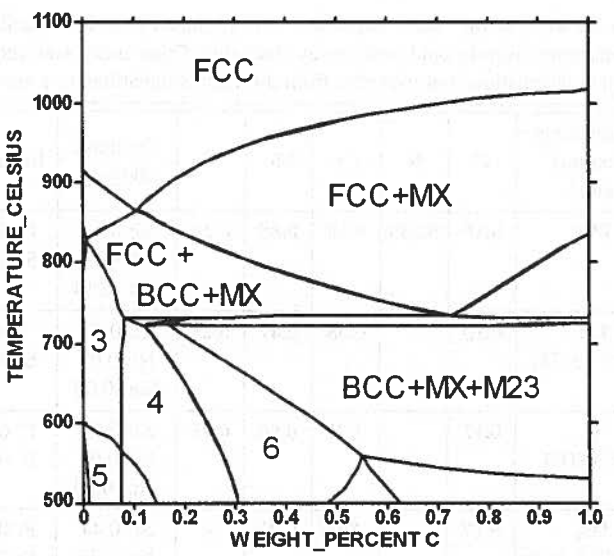

Fig. 1. Phase diagram of 13CrMoV 2-5-3 (LA, ČSN 15128) steel (Fe-C-m%Mn-m%Si-m%Cr-m%Ni-m%Mo-m%V isopleth where m% given in Table 1 and carbon is varying value). 3- means: BCC + MX, 4- means: BCC + MX + M_7C_3, 5- means: BCC + MX + M_7C_3 + M_6C, 6- means: BCC + MX + M_7C_3 + $M_{23}C_6$.
See 0.13wt%C coordinate for predicted equilibrated phase structures of the studied steel at different temperatures

[1] The following designations are used in phase diagram cross-sections (**Figs 1 to 4**)) as well as in **Table 2**: BCC for the ferritic diffusion matrix (BCC-A2 structure), FCC for austentic matrix (FCC-A1 structure), M23 for the $M_{23}C_6$ carbide rich in chromium, M7 for type M_7C_3 carbide rich in chromium, M6 for the M_6C carbide rich in molybdenum, M2 for the M_2C carbide also rich in molybdenum, M3 for cementite, and MX for carbonitrides of vanadium.

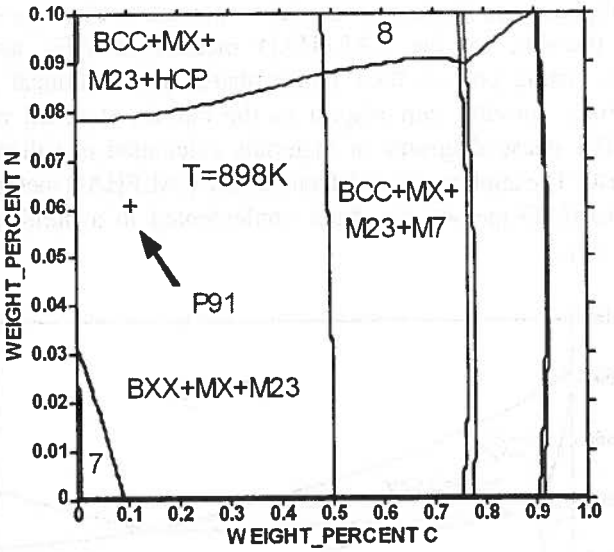

Fig. 2. Isothermal phase diagram cross-section of X10CrMo 9-1 (P91) steel (Fe-C-m%Mn-m%Si-m%Cr-m%Ni-m%Mo-m%V-m%N-m%Nb isopleth, where m% given in Table 1. 7- means: BCC + MX + M_6C + $M_{23}C_6$, 8- means: BCC + MX + M_7C_3 + $M_{23}C_6$ + HCP

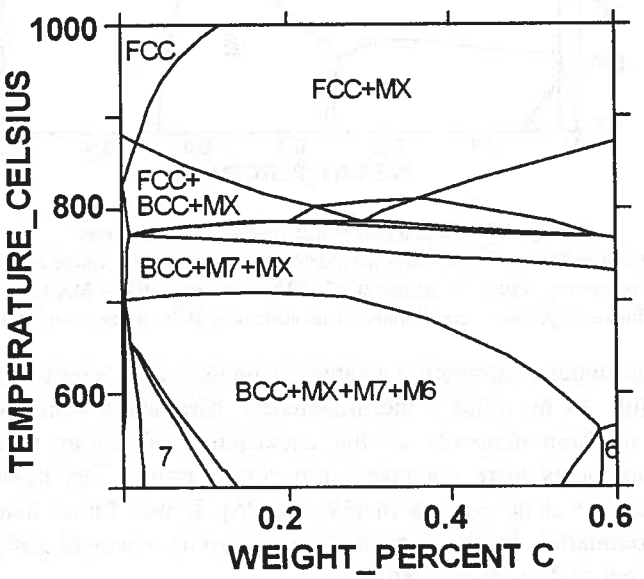

Fig. 3. Phase diagram of 12CrMo 10-10 (C, SK3STC) steel (Fe-C-m%Mn-m%Si-m%Cr-m%Ni-m%Mo-m%V-m%Nb isopleth, where m% given in Table 1 and carbon is varying value). 7- means: BCC + MX + M_7C_3 + $M_{23}C_6$ + M_6C.
See 0.12wt%C coordinate for predicted equilibrated phase structures of the studied steel at different temperatures

The solution of phase equilibrium for a given composition of the system (Table 1), its temperature and pressure by the CALPHAD method includes also the chemical composition of coexisting phases, their molar phase ratio, chemical potentials of the components and their activity with respect to the chosen standard reference state of elements (SER). The phase diagrams of materials calculated can then be presented as isopleths (Figs 1 to 4). The application and details of the CALPHAD method can be found in [18–20]. The CALPHAD method has been implemented in a number of computation programs [14, 21–24].

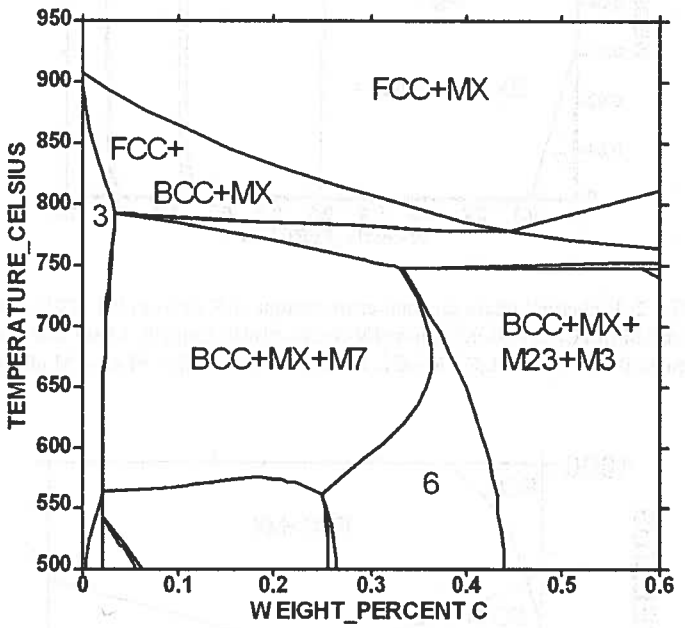

Fig. 4. Phase diagram of 12CrMo 10-10 (T25) steel
(Fe-C-m%Mn-m%Si-m%Cr-m%Ni-m%Mo-m%V-m%Nb-m%N isopleth, where m% given in Table 1 and carbon is varying value). 3- means: BCC + MX, 6- means: BCC + MX + $M_{23}C_6$ + M_7C_3.
See 0.06wt%C coordinate for predicted equilibrated phase structures of the studied steel at different temperatures

The materials under examination (Table 1) include also small amounts of phosphorus and sulphur. As no reliable thermodynamic parameters were available to describe the effect of these elements on the coexistence of phases in the materials in question, these elements were not taken into consideration. The modelling of phases was performed in the same way as in [17, 18, 25]. It was found that the position of phase region boundaries in the isopleths of materials changed only a little if we neglected the effect of Mn, Si and Nb.

An important result of solving phase equilibria is also the carbon activity in the materials examined. In diffusion weld joints of steel the initial value of carbon resp. nitrogen activity is of fundamental importance since a difference in activities at exposure temperature is closely related to the structural stability of weld joint. The temperature

dependence of carbon activities for the steels examined (without phosphorus and sulphur) is shown in Fig. 5.

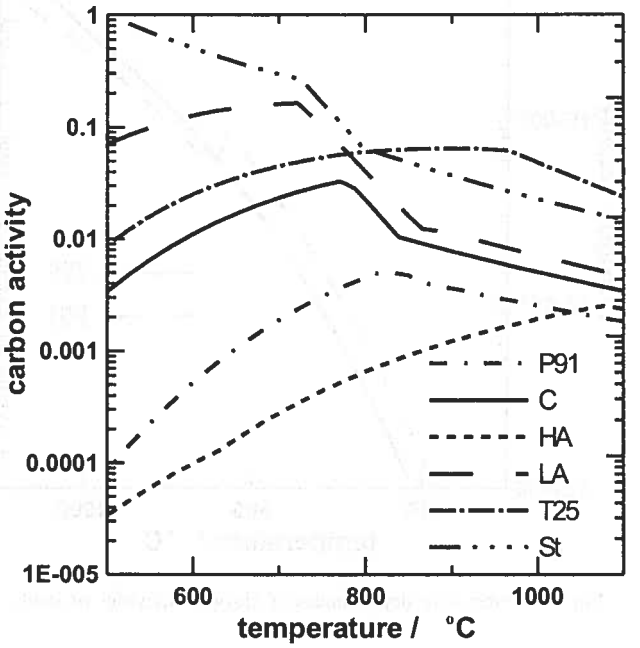

Fig. 5. Temperature dependences of carbon activities of steels

4. Diffusion couple simulations

In the case of heterogeneous welds, at elevated temperatures, thermodynamic phase equilibrium can be assumed to exist also on a local microscale. This assumption allows using the CALPHAD method in the calculation of local chemical potentials of components. Non-zero local gradient of the chemical potential of component is the driving force of diffusion [26].

The presented work used DICTRA software [8], which contains subroutines for the CALPHAD method to calculate the mobilities of individual elements and also contains algorithms for numerical solution of diffusion equations. Each weldment was simulated as a 1-D diffusion couple consisting of two systems with initial phase composition corresponding to the state of two separate systems (steels), each in thermodynamic equilibrium. Fe-Cr-Mo-V-Nb-C-N 7-element base was used with the content of components corresponding to Table 1. The STEEL database [29] was used for the CALPHAD method. The same database of kinetic parameters as mentioned in [17] was used.

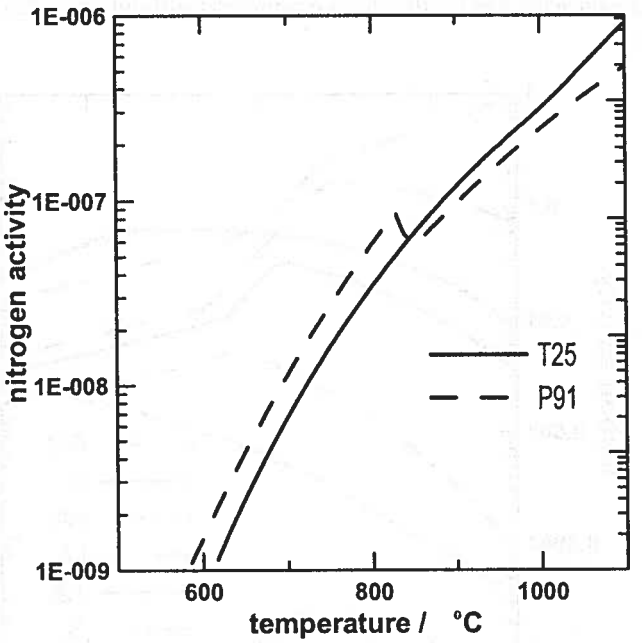

Fig. 6. Temperature dependences of nitrogen activities of steels

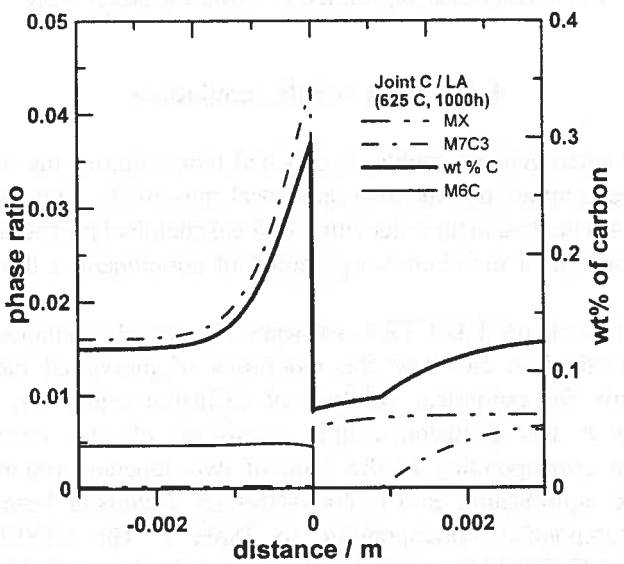

Fig. 7. Simulated phase and carbon profiles C|LA (SK3STC|CSN 15128) (12CrMo 10-10|13CrMOV 2-5-3) welded joint after 1000hrs at 625°C (up-hill carbon diffusion, MX hardening)

The phase composition of diffusion couples of steels is formed predominantly by a solid solution of BCC-A2 (or FCC-A1) structure, various carbides and, possibly, a type MX carbonitride. Diffusion in these materials is only assumed in solid solution (diffusion matrix) while in the carbide phases it is negligible (diffusion-none phase). At the same time, it was taken into consideration that the dispersed carbide phases affected the local equilibrium composition of matrix and reduced the diffusion rate via the labyrinth factor [30]. Examples of the simulation results for steel combinations with BCC-A2 matrix are given on Figs 7 and 8.

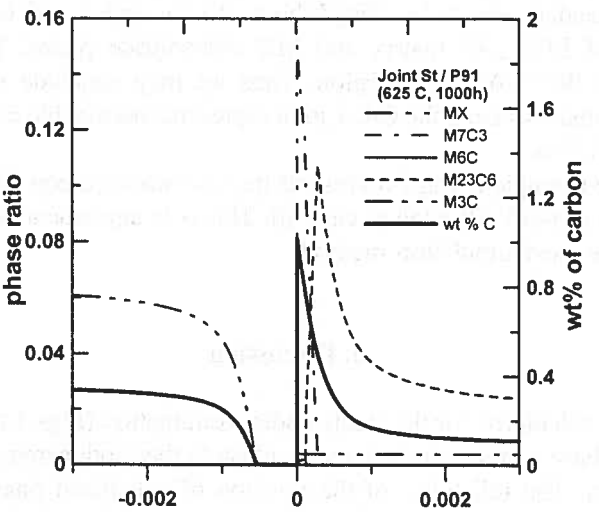

Fig. 8. Simulated phase and carbon profiles St|P91 (CSN 12050|P91) (CSN 12050|X10CrMo 9-1) welded joint after 1000hrs at 625°C (carbon depleted critical zone)

5. Results of simulations

Long-term high temperature exposure of weldments was simulated under conditions analogous to the operating conditions of heat-resistant steels in industry. The results can for example be seen on profiles showing the dependence of phase content or element chemical composition on distance at a chosen time. (see Figs 7 and 8) The phase profiles clearly indicate the coexisting phases in observed diffusion couple and thus local structure may be predicted. This structure significantly influences the local mechanical properties. The sequence of phase regions in the weld joint corresponds to the diffusion path in phase diagram, through which the local bulk composition of the diffusion couple leads [31].

Figs 7 and 8 show also the diffusion profiles of carbon. Just as for carbon, diffusion profiles can be given for other elements too. Similar to phase profile, diffusion profile of an element can exhibit various minima and maxima. The profiles of chemical potential or component activity are only decreasing or increasing functions with the point of inflexion close to the initial weld interface.

Regarding the carbon thermodynamic stability, the most stable weld is the joint of two steels with the same carbon activity (see crossing points on Fig 5). In such a case no driving force for diffusion exists. The practical application of the weld simulation may be demonstrated on two examples, which are given on Figs 7 and 8. They show the carbon and phase profiles after long annealing at the same temperature. Each example reveals a high carbon peak and a carbon-depleted zone. This zone is often the weakest region of the weld joint. However, there are differences. Example on Fig 8 shows carbon-depleted zone close to weld interface. This region consists of BCC-A2 matrix only (ferrite), i.e. no other phases are coexisting. It presents great risk of failure after long heat treatment.

On the other hand, the example in Fig 7 shows also the region with lower carbon but this region consists of BCC_A2 matrix and MX carbonitride phase. The carbonitride is strengthening the BCC_A2+MX region. Thus we may conclude that St/P91 joint is a highly risky combination and the C/LA joint represents reasonable combination at given temperature conditions.

Moreover, the example in Fig 7 represents the case when carbon diffuses into a carbon enriched material (up-hill diffusion of carbon). This is in agreement with thermodynamic background of the used simulation method.

6. Discussion

The isopleths calculated for the steels under examination (Figs 1 to 4) can be used to determine their phase compositions if a state close to thermodynamic equilibrium can be assumed for them. The reliability of the position of calculated phase field boundaries increases with increasing temperature. The precision of these calculations is closely connected with the precision and consistency [8, 14, 15] of the thermodynamic parameters stored in the thermodynamic database.

The phase diagrams contain also phase fields with a MX phase. As nitrogen is present in the nitrogen-alloyed X10CrMo 9-1 steel (see Table 1) it partly replaces carbon in the MX phase, giving thus rise to an MX carbonitride, where X represents C or N. This carbonitride is usually modelled using thermodynamic parameters for the FCC_A1 phase. The calculated chemical composition of MX in thermodynamic equilibrium in this case corresponds to the carbide or nitrocarbide rich in vanadium, which has been found in heat-resistant steels. The chosen thermodynamic description allows non-stoichiometric composition (vacancies in the interstitial lattice) of carbonitride MX. From the calculations performed in the present work it follows that the composition is practically stoichiometric at temperatures lower than 500°C.

According to experiments, this carbide/nitrocarbide is present in the matrix of heat-resistant steels usually in sub-micron sizes, which makes its identification and analysis of its chemical composition by current electron microscopy techniques difficult. In heat-resistant steels vanadium probably forms various carbides [2–4, 6, 32]. In the present work they have been replaced with a single non-stoichiometric carbide/nitrocarbide MX. It should be noted, however, that it is exactly this group of fine carbides and

nitrocarbides that greatly contributes to precipitation strengthening in heat-resistant steels [33].

Thermodynamic stability heterogeneous weld can be inferred from the difference between the calculated carbon activities in the joined materials. The lower the difference in activities at given temperature, the less drastic diffusion processes can be expected after joining the steels. As a first approximation, the results presented in Fig. 5 can be used. In the weld joints of steels carbon will be the fastest diffusing component in the system. The rate of nitrogen diffusion can be comparable, but this does not hold for the steels under examination, where nitrogen is bound primarily by MX phase. In the case of long-term exposure there may be also a diffusion flow of substitutional metallic atoms in a region close to the initial weld interface but the diffusion distance of these atoms is about two-four orders lower than the diffusion distance of carbon.

The selection of materials for a weld joint using only Fig. 5 is however not suitable for assessing the long-term stability of the joint at elevated temperatures. In this case it is more appropriate to simulate long-term thermal exposure of weldments (see Figs 7 and 8). From the results of these simulations it is possible to put together sequences of phase regions and to estimate mechanical stability of the joint. The reliability of the simulations depends on both data accuracy and completeness of the thermodynamic and kinetic databases.

The microstructure and, indirectly, also places that are critical from the viewpoint of mechanical properties can be determined, as they are most dependent on carbon concentration profile. The study of the relations between microstructure and mechanical properties [7, 11, 12, 33] attracts general attention and it can be expected that in the future the prediction of service life of weld joints will be shifted to a new, higher level.

7. Conclusion

The above text presents the calculations of phase diagrams and carbon activities, and the simulation of weldments with long-term exposure to elevated temperatures. Activity calculations yield a rough initial approximation for the design of weld joints.

The use of DICTRA software enables a more qualified choice of electrode also for steels other than those examined above, designed for the manufacture of components operating at elevated temperatures. In particular, the simulations of long-term thermal exposure of weldments can be used with advantage when experimental methods cannot be applied due to lack of time.

On the basis of the results obtained by simulating the effect of temperature on the microstructure of weld joints it is possible to better specify the service life and reliability of weld joints that form part of high-temperature technologies. In this way data can also be obtained for determining the extent of necessary reconstruction of a technology.

Acknowledgements

The support of the Grant Agency of the Czech Republic (No: 106/03/0636) is gratefully acknowledged for funding. The calculations were performed with use of the ThermoCalc and DICTRA programs.

REFERENCES

[1] J.D. R o b s o n, H.K.D.H. B h a d e s h i a, *CALPHAD* **20**, 447-460 (1996).
[2] J.D. R o b s o n, H.K.D.H. B h a d e s h i a, Materials Science and Technology **13**, 931-639 (1997).
[3] J.D. R o b s o n, H.K.D.H. B h a d e s h i a, Materials Science and Technology **13**, 640-644 (1997).
[4] K. S t r á n s k ý, et.al., Hutnické listy **10**, 712-719 (1983).
[5] B. M i l l i o n, et.al., Z. Metallkd. **86**, 706-712 (1995).
[6] V. P i l o u s, K. S t r á n s k ý, Strukturní stálost návarů a svarových spojů v energetickém strojírenství (in Czech), Praha, Academia, 1989.
[7] R. F o r e t, et.al., Proc. Int. Conf. on 'Integrity of high-temperature welds', 135-141; 1998, Suffolk, UK, The Institute of Mechnical Engineers, The Ipswich Book Company.
[8] J.O. A n d e r s s o n, et.al., *CALPHAD* **26**, 273-312 (2002).
[9] A. B o r g e n s t a m, et.al., J. of Phase Equilibria **21**, 269-280 (2000).
[10] N. S a u n d e r s, A.P. M i o d o v n i k, 'CALPHAD (Calculation of Phase Diagram) – A Comprehensive Guide', Pergamon Materials Series **1**, Elsevier Science, Amsterodam, 1998.
[11] R. F o r e t, et.al., Sci. and Technol. Weld. Joining **6**, 405-411 (2001).
[12] B. M i l l i o n, et.al., Metallic Materials **37**, 317-323 (1999).
[13] A.T. D i n s d a l e, *CALPHAD* **15**, 317-425 (1991).
[14] B. S u n d m a n, B. J a n s s o n, J-O.A n d e r s s o n, *CALPHAD* **9**, 153-199 (1985).
[15] B. S u n d m a n, Scandinavian Journal of Metallurgy **20**, 79-85 (1991).
[16] MT DATA, National Physical Laboratory, Teddington, Middlesex, UK, 1989.
[17] J. S o p o u š e k, V. J a n, R. F o r e t, Science and Technology of Welding and Joining **9**, March (2004).
[18] B. S u n d m a n, J. Å g r e n, J. Phys. Chem. Solids **42**, 297-301 (1981).
[19] M. H i l l e r t, Phase equilibria, Phase Diagrams and Phase Transformations – Their Thermodynamic Basis, Cambridge University Press, 1998.
[20] I. A n s a r a, B. S u n d m a n, *CALPHAD* **24**, 181-182 (2000).
[21] C.W. B a l e, et.al., *CALPHAD* **26**, 189-228 (2002).
[22] R.H. D a v i e s, et.al., *CALPHAD* **26**, 229-271 (2002).
[23] J. S o p o u š e k, et.al., *CALPHAD* **17**, 229-235 (1993).
[24] S.L. C h e n, et.al., *CALPHAD* **26**, 175-188 (2002).
[25] B.J. L e e, D.N. L e e, J. of Phase Equilibria **13**, 349-363 (1992).
[26] J.S. K i r k a l d y, D.J. Y o u n g, Diffusion in the Condensed State, The Inst. of Metals, London, 1987.
[27] J.O. A n d e r s o n, J. Å g r e n: J. Appl. Phys. **72**, 1350-1355 (1992).
[28] P. S h e w m o n, Diffusion in Solids, The Minerals, Metals & Materials Society, Warrendale, Pennsylvania, 1989.
[29] A. K r o u p a, et.al., Journal of Phase Equilibria **22**, 312-323 (2001).
[30] R.L. M c C u l l o u g h, Compos. Sci. Technol. **22**, 3-21 (1985).
[31] T. H e l l a n d e r, J. Å g r e n, Acta Mater. **47**, 3291-3300 (1999).
[32] V. P i l o u s, K. S t r á n s k ý, Structural Stability of Deposits and Welded Jonts in Power Engineering, Cambridge Internaional Science Publishing, 1998.
[33] F. B r u n, et.al., Materials Science and Technology **15**, 547-554 (1999).

Received: 15 June 2004.

A R C H I V E S O F M E T A L L U R G Y A N D M A T E R I A L S
Volume 49 2004 Issue 3

J. JANOVEC *, M. JENKO*, V. HOMOLOVÁ**

MICROSTRUCTURE EVOLUTION ON CASTING IN SPECIAL HIGH-ALLOY STEELS

EWOLUCJA MIKROSTRUKTURY W TRAKCIE ODLEWANIA WYSOKOSTOPOWYCH STALI SPECJALNYCH

Practical aspects of thermodynamic calculations were demonstrated on the Ch12MF4, Ch3F12, and CF3M alloys cast under quasi-equilibrium conditions. Good agreement was achieved between experimental findings and thermodynamic predictions performed by THERMOCALC, using the non-commercial database STEEL16. The approach was found to be appropriate for solving practical tasks related to casting (solidification).

Praktyczny aspekt obliczeń termodynamicznych został zademonstrowany na przykładzie stopów Ch12MF4, Ch3F12 i CF3M, odlanych w warunkach quasi-równowagowych. Uzyskano dobrą zgodność między wynikami doświadczalnymi i uzyskanymi na drodze obliczeń termodynamicznych, wykonanych przy użyciu pakietu THERMOCALC z wykorzystaniem niekomercyjnej bazy danych STEEL 16. Ten sposób postępowania okazał się odpowiedni dla rozwiązywania praktycznych zagadnień związanych z krzepnięciem odlanej stali.

1. Introduction

In last decades, the computer modelling (simulation) of microstructure evolution has become an important tool for the characterisation of material [1–4]. Compared with experimental work, the computer modelling is cheaper and saves lot of time. It can be used successfully to predict (simulate) a material's long-term behaviour [5, 6]. The spectrum of scientific activities related to the modelling is exceedingly wide. For instance, F a u l k - n e r et al. [7–9] proposed a model for intergranular precipitation based on the concept of collector plate, C e n i g a et al. [10, 11] applied a model to describe the internal stresses in an isotropic particle-matrix system, X u et al. [12–14] introduces specific kinetic models

* INSTITUTE OF METALS AND TECHNOLOGY, LEPI POT 11, 1000 LJUBLJANA, SLOVENIA
** INSTITUTE OF MATERIALS RESEARCH, SLOVAK ACADEMY OF SCIENCES, WATSONOVA 47, 043 53 KOŠICE, SLOVAKIA

for thermally induced and stress-forced non-equilibrium segregation based on the earlier theory of vacancy-impurity complexes, S o u r m a i l and B h a d e s h i a [15] developed a model for simultaneous precipitation reactions, taking into account interactions between phases, etc. Thermodynamic calculations (predictions) performed by commercially available programs, e.g. THERMOCALC [16], MTDATA [17], DICTRA [18], represent the most extended type of modelling that normally uses commercial thermodynamic databases, e. g. SSUB, SSOL, NSOL, TCFE, OIKA [19]. However, users of commercial programs sometimes need special databases that reflect their particular interests. The STEEL16 database assessed by K r o u p a et al. [20] for the Fe-Cr-Mo-V-C system, is such a database. It contains thermodynamic parameters refined from the experimental results related to the Cr-Mo-V low alloy steels aged for long times at temperatures below 1000 K [21]. The basic thermodynamic data were taken from Q u i [22] and L e e [23].

In parallel with the "scientific" calculations, a form of practically oriented modelling has been developed [24–26]. Basic principles of this modelling are based on achieving credible thermodynamic data, characterising the phase evolution by routine thermodynamic tools, and incorporation of the calculated parameters into the schemes or diagrams that are applicable in practice. Computer programs, e. g. JMATPRO, developed by S a u n d e r s et al. [24], seem to be the most effective tools for the practically oriented modelling. Solidification and evolution of microstructure during casting (topics discussed in this study) are processes that are difficult to describe with experimental techniques, because of the difficulty in determining thermo-physical properties of the liquid phase and the coexisting solid phases. However, the lack of experimental data can be compensated for by thermodynamic calculations. These calculations were found to be a credible tool for providing information on how temperature affects the fraction of transformed solid, the enthalpy release and the chemical composition of the phases.

2. Materials

The investigated Ch12MF4 (marked according to the Russian standard GOST), Ch3F12 (GOST) and CF3M (ASTM) alloys were cast under quasi-equilibrium conditions corresponding to the cooling rate of about 0.17 $K.s^{-1}$. The chemical compositions of the alloys are given Table 1. The as-cast microstructure of the hypoeutectic tool alloy Ch12MF4 is illustrated in Fig. 1. It consists of transformed proeutectic austenite (marked with the solid arrow) and products of the eutectic reaction (dashed arrow). The white areas correspond to eutectic carbides; the grey areas represent the transformed austenite consisting of ferrite, MC, and M_7C_3 [27], [29], [30] (Table 2). As is clear from Fig. 2, the as-cast microstructure of the hypereutectic tool alloy Ch3F12 consists of prior carbides (solid arrow) and products of the eutectic reaction (dashed arrow). The white areas represent proeutectic or eutectic carbides; the grey areas are referred to the transformed austenite containing ferrite, MC, and M_7C_3 [28], [30] (Table 2). The as-cast microstructure of the austenitic stainless steel CF3M is documented in Fig. 3. It is formed with the prior

austenite (solid arrow) and areas of transformed δ-ferrite (dashed arrow) consisting of σ-phase, $M_{23}C_6$ and ferritic matrix [31], [32] (Table 2).

TABLE 1

Chemical compositions of the investigated alloys. Mass contents of the elements are given in %. Contents of trace elements are not included.

Alloy	C	Si	Mn	Ni	Cr	Mo	V	Fe
Ch12MF4	2.37	–	–	–	12.06	1.20	4.00	bal.
Ch3F12	3.00	–	–	–	3.00	–	12.00	bal.
CF3M	0.06	1.68	0.67	9.00	20.80	2.46	–	bal.

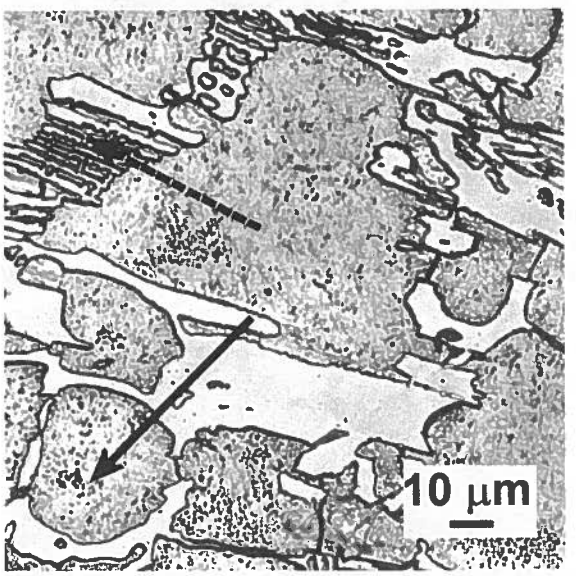

Fig. 1. As-cast microstructure of hypoeutectic tool alloy Ch12MF4. Transformed proeutectic austenite is marked with the solid arrow, products of eutectic reaction with the dashed arrow. Light microscopy, two-step etching in 3% nital (3 ml HNO_3 + 97 ml C_2H_5OH) and Murakami etchant (10 g NaOH + 10 g $K_3[Fe(CN)_6]$ + 100 ml H_2O)

TABLE 2

Phases identified in the final as-cast microstructures of alloys Ch12MF4, Ch3F12 and CF3M. More information about the characterisation of the phases is given in the assigned references. Meanings of the abbreviations used: XRD, X-ray diffraction; DSC, differential scanning calorimetry; LM, light microscopy; TEM, transmission electron microscopy; SAD, selected area electron diffraction.

Alloy	Phases identified	Methods used	References
Ch12MF4	ferrite + M_7C_3 + MC	XRD, DSC, LM	[27], [29], [30]
Ch3F12	ferrite + M_7C_3 + MC	XRD, DSC, LM	[28], [30]
CF3M	ferrite + austenite + σ-phase + $M_{23}C_6$	TEM, SAD, LM	[31], [32]

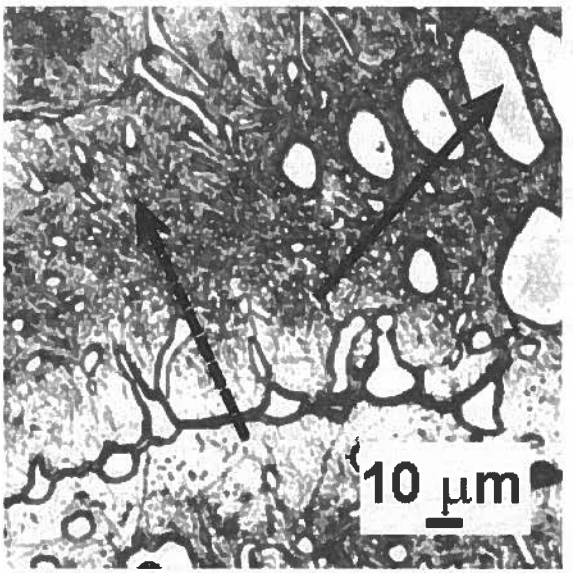

Fig . 2. As-cast microstructure of hypereutectic tool alloy Ch3F12. Prior MC is marked with the solid arrow, products of eutectic reaction with the dashed arrow. Light microscopy, two-step etching in 3% nital (3 ml HNO_3 + 97 ml C_2H_5OH) and Murakami etchant (10 g NaOH + 10 g $K_3[Fe(CN)_6]$ + 100 ml H_2O)

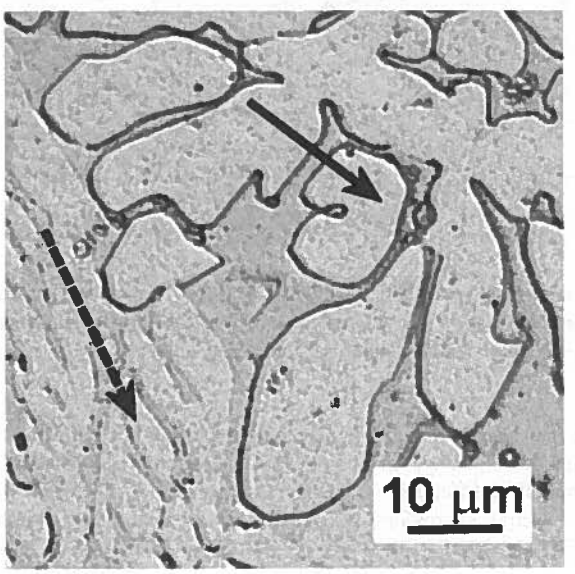

Fig. 3. As-cast microstructure of austenitic stainless steel CF3M. Prior austenite is marked with the solid arrow, areas of transformed δ-ferrite with the dashed arrow. Light microscopy, etched in glyceregia (10 ml HNO_3 + 35 ml HCl + 30 ml glycerol)

3. Aims of the study

A thermodynamic characterisation of the phase evolution in the Ch12MF4, Ch3F12, and CF3M alloys during casting (solidification) is the main goal of this study. The particular aims are as follows:

A. Calculations of phase equilibria in the temperature range 600–1800 K using the THEMOCALC program [16, 19] and the non-commercial database STEEL16 [20]. The phases considered in the calculations are given in Table 3.

B. Calculations of the volume fractions of equilibrium phases to better characterise the solidification processes and the formation of as-cast microstructures. The calculations were made under the same conditions as specified above under point A.

C. Passing judgements on the reliability of the calculated data and suitability of the STEEL16 database for solving practical tasks related to casting (solidification).

TABLE 3

Phases considered in the thermodynamic calculations.

Group of phases	Phase
Basic phases	liquid, austenite, ferrite
Carbides	M_3C, M_7C_3, $M_{23}C_6$, M_6C, M_2C, MC
Intermetallic phases	Laves, σ-phase, χ-phase

4. Results

The predicted phase equilibria are given in Table 4. Diagrams showing the temperature-dependent changes in the calculated volume fractions of equilibrium phases are illustrated in Figs. 4–9. The high temperatures changes (between 1400 and 1700 K) are documented in Figs. 4, 6 and 8 for the Ch12MF4, Ch3F12 and CF3M alloys. Figs. 5 (Ch12MF4) and 7 (Ch3F12) refer to the temperatures of the austenite-ferrite transition. The calculated volume fractions of the $M_{23}C_6$ and σ-phases are illustrated in Fig. 9 for the CF3M steel.

5. Discussion

The sequence of the predicted phase equilibria (Table 4) and the changes in the volume fractions of equilibrium phases (Fig. 4) indicate that the primary solidification of the hypoeutectic Ch12MF4 alloy is austenite what is in agreement with the experiment (Fig. 1). Both carbides identified (M_7C_3 and MC, Table 2) were also predicted to coexist in equilibrium with liquid (Table 4, Fig. 4). This is evidence for the M_7C_3 participation in the eutectic reaction, together with MC and austenite. The white-colour areas observable in Fig. 1 are then agglomerates of both carbides. Even if MC was predicted to crystallize at a slightly higher temperature than M7C3, the latter carbide exhibits a larger volume fraction

(Fig. 4). Considering the above predictions, comparable portions of the carbides in the agglomerates can be expected after the quasi-equilibrium solidification of the alloy. An increase of the predicted volume fractions of the carbides with decreasing temperature (compare Figs. 4 and 5) indicates that the agglomerates should grow during cooling. Austenite was predicted to leave equilibrium at 1078 K. In agreement with the prediction, it was not identified in the final as-cast microstructure of the alloy (Table 2, Fig. 5).

TABLE 4

Phase equilibria predicted for alloys Ch12MF4, Ch3F12 and CF3M in the temperature range 600–1800 K

Phase equilibrium	Temperature range of occurence [K]		
	Ch12MF4	Ch3F12	CF3M
ferrite + austenite + σ-phase + $M_{23}C_6$			600–1052
ferrite + austenite + $M_{23}C_6$			1053–1304
ferrite + austenite			1305–1599
ferrite + M_7C_3 + MC	600–1077	600–1046	
ferrite + austenite + M_7C_3 + MC	1078–1084	1047–1058	
ferrite + austenite + MC		1059–1075	
austenite + M_7C_3 + MC	1085–1475		
austenite + MC		1076–1563	
austenite + M_7C_3 + MC + liquid	1476–1484		
austenite + MC + liquid	1485–1491	1564–1581	
MC + liquid		1582–1643	
austenite + ferrite + liquid			1600–1611
austenite + liquid	1492–1613		
ferrite + liquid			1612–1679
liquid	from 1614	from 1644	from 1680

For the hypereutectic Ch3F12 alloy, formation of the prior MC is characteristic. The micrograph showing fragments of the MC dendrites (Fig. 2, solid arrow) were unambiguously confirmed by thermodynamic calculations (Table 4, Fig. 6). The calculated volume fraction of MC, about 25%, is in good agreement with the experimental assessment. In the transition austenite/ferrite temperature range, M_7C_3 was predicted to enter equilibrium (Table 4, Fig. 7). This indicates the low temperature character of M_7C_3 in the Ch3F12 alloy, whereas this carbide in the Ch12MF4 alloy is the high temperature phase. The lower temperature of the appearance of M_7C_3 in equilibrium predicted for the Ch3F12 alloy is a consequence of the lower bulk Cr/V ratio. In the final as-cast microstructure of the alloy, ferrite, M_7C_3, and MC were identified (Table 2). This is in agreement with the thermodynamic predictions, because austenite should leave equilibrium at 1047 K (Table 4, Fig. 7).

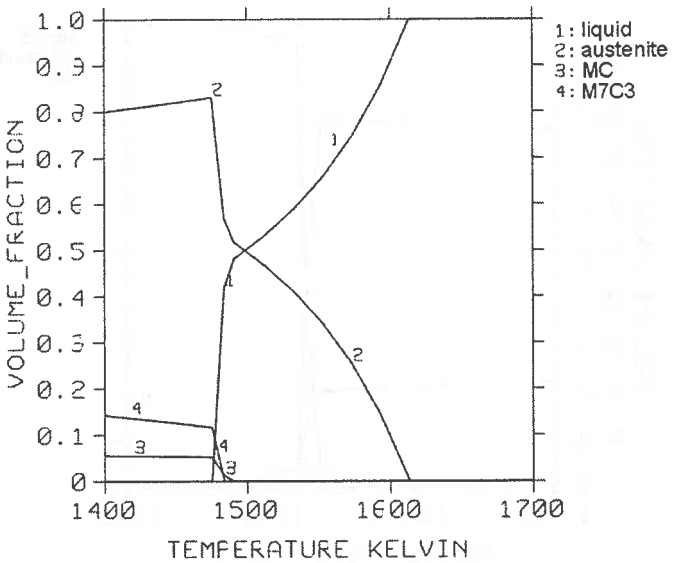

Fig. 4. Calculated volume fractions of liquid, austenite, MC, and M_7C_3 as a function of temperature. Plotted for alloy Ch12MF4 in the emperature range 1400–1700 K

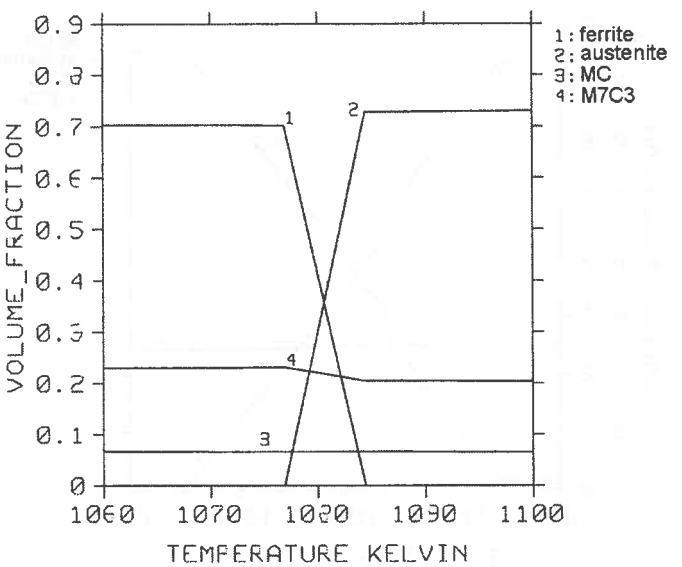

Fig. 5. Calculated volume fractions of ferrite, austenite, MC, and M_7C_3 as a function of temperature. Plotted for alloy Ch12MF4 in the temperature range 1060–1100 K

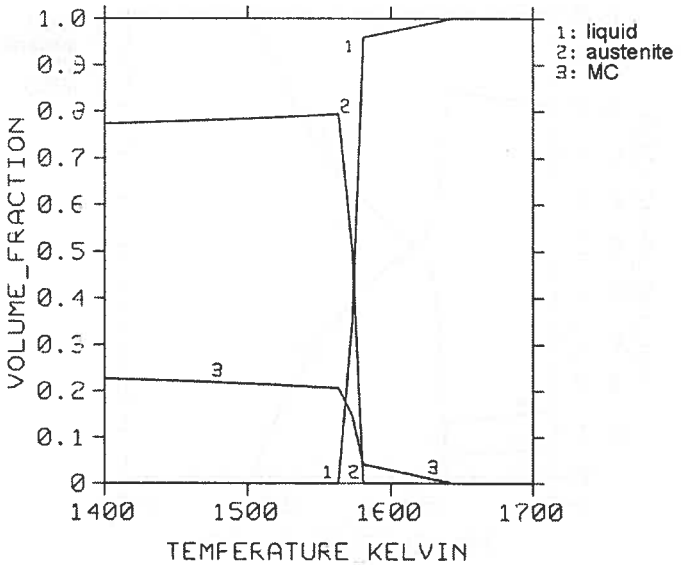

Fig. 6. Calculated volume fractions of liquid, austenite, and MC as a function of temperature. Plotted for alloy Ch3F12 in the temperature range 1400–1700 K

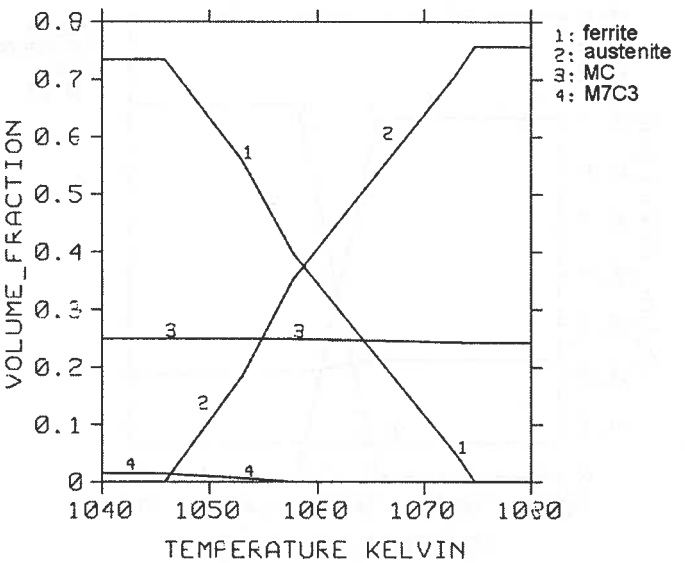

Fig. 7. Calculated volume fractions of ferrite, austenite, MC, and M_7C_3 as a function of temperature. Plotted for tool alloy Ch3F12 in the temperature range 1040–1080 K

In comparison to the first two alloys, solidification of the CF3M steel is specific, because carbides were not predicted to coexist with liquid (Fig. 8). Fragments of the austenitic dendrites marked with the solid arrow in Fig. 3 indicate the primary solidification of the steel as austenite.

However, δ-ferrite was predicted to coexist with liquid across a wide temperature range (79 K), with a maximum calculated volume fraction of 95% (Table 4, Fig. 8). Austenite was predicted to coexist with liquid in a narrow temperature range (11 K), but the calculated volume fraction of the phase increases strongly with decreasing temperature at the expense of δ-ferrite. The above facts suggest the following course of the solidification:

A. Both δ-ferrite (to a larger extent) and austenite (only slightly) crystallise from liquid in the first step of the solidification.

B. Cooling in the quasi-equilibrium regime stabilises austenite and supports the growth of austenitic dendrites at the expense of ferritic dendrites. This process is accompanied by fragmentation of dendrites. Finally, the growing austenitic fragments remain saved, but the δ-ferrite areas lose their dendrite morphology.

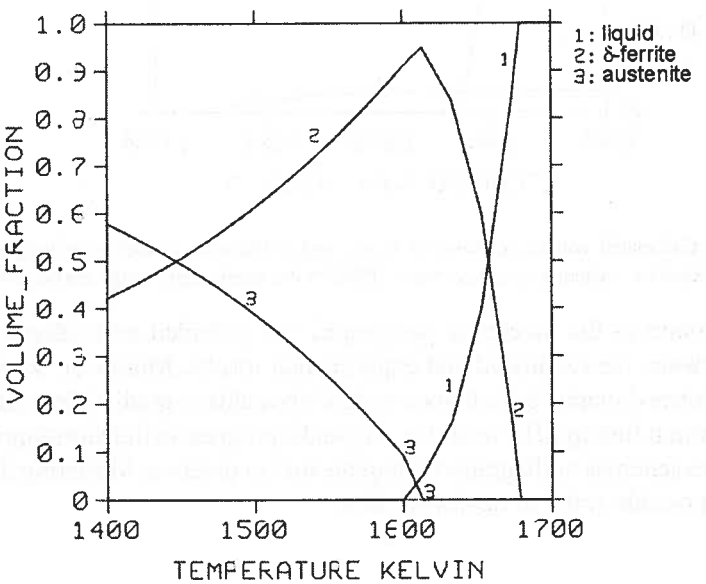

Fig. 8. Calculated volume fractions of liquid, δ-ferrite, and austenite as a function of temperature. Plotted for austenitic stainless steel CF3M in the temperature range 1400–1700 K

$M_{23}C_6$ was predicted to precipitate at temperatures below 1304 K (Table 4, Fig. 9). It was shown experimentally that particles of this chromium-rich carbide precipitate along ferrite/austenite interfaces, where chromium (from ferrite) and carbon (from austenite) are available in sufficient amounts [31, 33]. The $M_{23}C_6$ is a truly minor phase, because it comprises only about 2% of the steel's overall volume. The σ-phase should appear at temperature below 1052 K as a product of the δ-ferrite spinodal decomposition [31, 34] (Table 4, Fig. 9). In the final as-cast microstructure, it was found inside of the ferritic areas as a part of so-called "basket structure" (Fig. 3, darker places in areas marked with the dashed arrow). All the predicted phases were identified experimentally in the final as-cast microstructure of the steel (compare data in Tables 2 and 4).

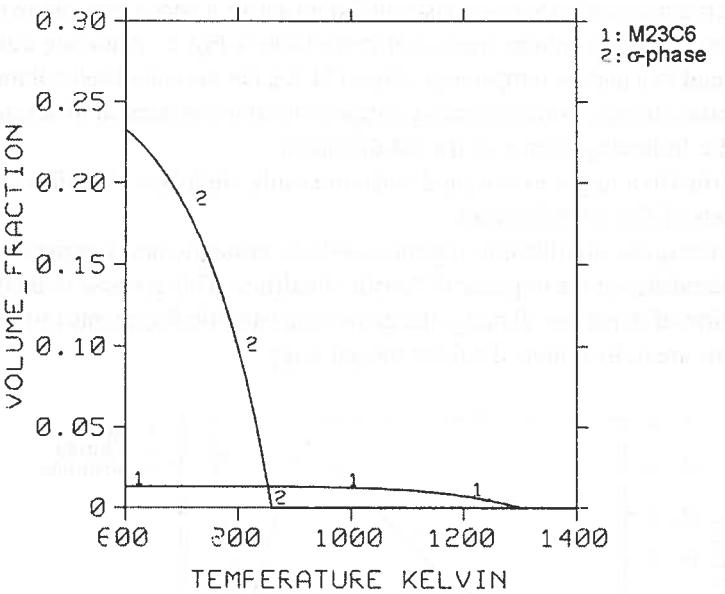

Fig. 9. Calculated volume fractions of $M_{23}C_6$ and σ-phase as a function of temperature. Plotted for austenitic stainless steel CF3M in the temperature range 600–1400 K

The discussion in the preceding paragraphs has provided an evidence for the good agreement between the calculated and experimental results. Moreover, some information achieved by thermodynamic calculations makes it possible to predict more than can be seen in the experimental finding. The next step is to make progress in transforming the calculated parameters into schemes or diagrams that applicable in practice. Mastering the JMATPRO program is a possible route to achieving this.

6. Conclusions

In this study, thermodynamic calculations were used to characterise the solidification process and/or microstructure evolution during casting. The thermodynamic calculations were performed for the Ch12MF4, Ch3F12, and CF3M alloys, cast under quasi-equilibrium conditions. For all the alloys, good agreement between the thermodynamic predictions and the experimental findings was found. The STEEL16 database working in the program THERMOCALC was found to be appropriate tool for a characterisation of the casting (solidification) processes in the investigated alloys.

Acknowledgement

The authors wish to thank Dr. Aleš Kroupa of the Institute of Physics of Materials of the Academy of Sciences of the Czech Republic in Brno for providing the non-commercial database STEEL16. The presented experimental

results were achieved in the framework of projects coordinated by Prof. Dr. Peter Grgač of the Faculty of Materials Science of the Slovak University of Technology in Trnava and Dr. Borivoj Šušataršič of the Institute of Metals and Technology in Ljubljana.

REFERENCES

[1] A.D. Pelton, C.W. Bale, Calphad **1** (1977), 253.
[2] L. Kaufman, H. Nesor, Calphad **2** (1978), 81.
[3] A.G. Turnbull, Calphad **7** (1983), 137.
[4] B. Sundman, B. Jansson, J.-O. Andersson, Calphad **9** (1985), 153.
[5] N. Fujita, H.K.D.H. Bhadeshia, Mater. Sci. Technol. **15** (1999), 627.
[6] N. Saunders, Z. Guo, X. Li, A.P. Miodownik, J.-P. Schillé, JOM **55** (2003), December, p. 60.
[7] R.A. Carolan, R.G. Faulkner, Acta Metall. **36** (1988), 257.
[8] H. Jiang, R.G. Faulkner, Acta Mater. **44** (1996), 1857.
[9] Y.F. Yin, R.G. Faulkner, Mater. Sci. Engn. **A344** (2003), 92.
[10] L. Ceniga, F. Kováč, Mater. Sci. Engn. **B86** (2001), 178.
[11] L. Ceniga, J. Mater. Sci. **38** (2003), 3709.
[12] T.D. Xu, S. Song, Acta Metall. **37** (1989), 2499.
[13] T.D. Xu, Philos. Mag. **83** (2003), 889.
[14] T.D. Xu, B.Y. Chen, Progress Mater. Sci. **49** (2004), 109.
[15] T. Sourmail, H.K.D.H. Bhadeshia, Calphad **27** (2003), 169.
[16] B. Sundman, THERMO-CALC, version L, Royal Inst.Tech., Stockholm 1997.
[17] R.H. Davies, A.T. Dinsdale, T.G. Chart, T.I. Barry, M.H. Rand, High Temperature Sci. **26** (1990), 251.
[18] A. Bjärbo, M. Hättestrand, Metall. Mater. Trans. **31A** (2000), 1.
[19] http://www.thermocalc.se
[20] A. Kroupa, J. Havránková, M. Coufalvá, M. Svoboda, J. Vřešťál, J. Phase Equilibria **22** (2001), 312.
[21] A. Výrostková, A. Kroupa, J. Janovec, M. Svoboda, Acta Mater. **46** (1998), 31.
[22] C. Qiu, ISIJ International **32** (1992), 1117.
[23] B.C. Lee, Calphad **16** (1992), 121.
[24] N. Saunders, A.P. Miodownik, CALPHAD-calculation of phase diagrams, ed. R.W. Cahn, Elsevier, Oxford 1998.
[25] N. Saunders, Materials Science Forum **217-222** (1996), 667.
[26] R.A. Harding, N. Saunders, Trans. American Found. Soc. **105** (1997), 451.
[27] M. Behúlova, R. Moravčík, M. Kusý, L. Čaplovič, P. Grgač, L. Stančeк, Mater. Sci. Engn. **A304-306** (2001), 540.
[28] M. Kusý, PhD thesis, Slovak University of Technology, Trnava 2001.
[29] R. Moravčík, PhD thesis, Slovak University of Technology, Trnava 2003.
[30] V. Homolová, J. Janovec, M. Kusý, R. Moravčík, E. Illeková, P. Grgač, Canadian Metall. Quart. **42** (2003), 89.
[31] J. Janovec, B. Šuštaršič, J. Medved, M. Jenko, Mater. Technol. **37** (2003), 307.
[32] J. Janovec, M. Bogyó, J. Blach, P. Záhumenský, A. Výrostková, Canadian Metall. Quart. **40** (2001), 97.
[33] J. Janovec, M. Svoboda, J. Blach, Mater. Sci. Engn. **A249** (1998), 184.
[34] J. Janovec, Nature of alloy steel intergranular embrittlement, VEDA, Bratislava 1999.

Received: 15 June 2004.

A R C H I V E S O F M E T A L L U R G Y A N D M A T E R I A L S
Volume 49 2004 Issue 3

A. KOSTOV *, D. ŽIVKOVIĆ**, D. ŽIVKOVIĆ**

THERMODYNAMICS AND CHARACTERIZATION OF ALLOYS IN Ga-Ge-Sb SYSTEM

TERMODYNAMIKA I CHARAKTERYSTYKA STOPÓW W UKŁADZIE Ga-Ge-Sb

The Ga-Ge-Sb system belongs to the group of Ga-based alloys of interest in semiconductors industry. Thermodynamic analysis of this ternary system and alloys characterization is given in this paper. Thermodynamic properties for analyzed system were obtained by O e l s e n's calorimetry as experimental method and analytically using K o h l e r and H i l l e r t predicting method at the temperature of 1273K. Obtained results were compared with literature data and mutual agreement was noticed. Characterization of alloys was done using SEM-EDX and DTA method.
Keywords: thermodynamics, alloys, semiconductors, Ga-Ge-Sb system

Układ Ga-Ge-Sb należy do grupy stopów na bazie galu, które są interesujące dla przemysłu półprzewodników. Analiza termodynamiczna tego układu trójskładnikowego i charakterytyka stopów jest przedmiotem obecnej pracy. Własności termodynamiczne analizowanego układu zostały uzyskane przy pomocy metody kalorymetrycznej O e l s e n a. Zostały one opisane analitycznie dla temperatury 1273K przy użyciu metody K o h l e r a i H i l l e r t a. Otrzymane wyniki porównano z danymi literaturowymi, uzyskując dobrą zgodność. Charakterystyka struktury stopów została zrealizowana przy pomocy metod SEM-EDX oraz DTA.

1. Introduction

Invention of the first electronic device represented a revolution event, which caused a completely new wave in the use and application of rare metals for production of components in electronic devices and instruments [1]. Generally, rare metals, such as gallium and germanium, possess special characteristics necessary and needed in the further progress in electronics [2, 3]. These metals are used [4–8] in electro-techniques, radio-techniques and electronics, in electronic and optic devices and instruments as functional materials for diodes, transistors, conductors, correctors, in integrated circuits, optical

* COPPER INSTITUTE BOR, ZELENI BULEVAR 35, 19210 BOR, SERBIA AND MONTENEGRO
** UNIVERSITY OF BELGRADE, TECHNICAL FACULTY BOR, VJ 12, 19210 BOR, SERBIA AND MONTENEGRO

cables, as well as in atomic and astrophysical investigations, atomic reactors, in laser technology, as sensors of neuron grids, in semiconductors industry, etc.

In consideration of their large use and application in almost all important branches and fields of techniques, it is very important to know complete thermodynamic determination and description of gallium and germanium based systems.

The Ga-Ge-Sb system belongs to the group of Ga-based alloys of interest in semiconductors industry. For its binary constitutive systems, there are many thermodynamic data [10–13], while there are just a few articles dealing with its thermodynamic behavior [14–17] for the whole ternary system. In the work of K a t a y a m a and coworkers [14], measurements of gallium activity by EMF method with zirconia as solid electrolyte are presented in the temperature range from 1058–1236K, while K o s t o v and coworkers [15–20] gave comparative thermodynamic analysis of alloys done experimentally by O e l s e n calorimetry and analytically using different calculation methods (C h o u, H a j r a, *R*-function).

Thermodynamic analysis of Ga-Ge-Sb system and alloys characterization are given in this paper. Thermodynamic properties for analyzed system were obtained using O e l s e n's calorimetry as experimental method and analytically using K o h l e r and H i l l e r t predicting method at the temperature of 1273K. Characterization of alloys was done using SEM-EDX and DTA method.

2. Experimental

All experimental investigations by O e l s e n calorimetry were carried out with pure germanium, gallium and antimony of p.a. grade. Descriptions of this experimental technique were reported in Refs. [16, 17].

SEM-EDX analysis was carried out by electronic microscope (PHILIPS XL-300) with energetic dispersion spectrometer EDX.

DTA experiments were performed by derivatograph (MOM, Hungary) in an air atmosphere and at constant heating rate of 10°C/min.

3. Results and discussion

3.1. Thermodynamic analysis

There are several traditional models to extrapolate the ternary thermodynamic properties based on three constitutive binary systems, which are classified according to H i l l e r t [9] into two categories: symmetrical and asymmetrical. In this paper one symmetrical – K o h l e r [21], and one asymmetrical model – H i l l e r t [9], were used for thermodynamic analysis of Ga-Ge-Sb ternary system. These models are given as follows:

– K o h l e r model [21]

$$\Delta G^E = (x_1 + x_2)^2 \Delta G^E_{12}\left(\frac{x_1}{x_1 + x_2}; \frac{x_2}{x_1 + x_2}\right) + (x_2 + x_3)^2 \Delta G^E_{23}\left(\frac{x_2}{x_2 + x_3}; \frac{x_3}{x_2 + x_3}\right) + (x_3 + x_1)^2 \Delta G^E_{31}\left(\frac{x_3}{x_1 + x_3}; \frac{x_1}{x_1 + x_3}\right). \quad (1)$$

– H i l l e r t model [9]

$$\Delta G^E = \frac{x_2}{1 - x_1}\Delta G^E_{12}(x_1; 1 - x_1) + \frac{x_3}{1 - x_1}\Delta G^E_{13}(x_1; 1 - x_1) + \frac{x_2 x_3}{v_{23} v_{32}}\Delta G^E_{23}(v_{23}; v_{32}), \quad (2)$$

where is: $v_{ij} = (1 + x_i - x_j)/2$.

In all given equations, ΔG^E and ΔG^E_{ij} correspond to the integral molar excess G i b b s energy for ternary and binary systems, respectively, while x_1, x_2, x_3 correspond to the mole fraction of components in investigated ternary system.

The excess free energies for the three binary systems Ga-Ge, Ge-Sb and Sb-Ga are taken from [10, 11, 12] respectively:

$$\Delta G^E_{Ga-Ge} = X_{Ge}(1 - X_{Ge})(4602.8 X^2_{Ge} - 7790.6 X_{Ge} - 2032.5) \quad (3)$$

$$\Delta G^E_{Ge-Sb} = X_{Sb}(1 - X_{Sb})(-41725.1 X^2_{Sb} + 37434 X_{Sb} - 1246) \quad (4)$$

$$\Delta G^E_{Sb-Ga} = X_{Ga}(1 - X_{Ga})(8835.9 X^2_{Ga} - 15514.8 X_{Ga} - 7588.8). \quad (5)$$

TABLE 1

Integral molar excess G i b b s energies at 1273K according to the K o h l e r model

ΔG^E (J/mol)										
x_{Ga}	$x_{Ge} : x_{Sb}$									
	9/1	8/2	7/3	6/4	5/5	4/6	3/7	2/8	1/9	eut
0	−1613	−2469	−2892	−3108	−3241	−3314	−3253	−2881	−1922	−2448
0.2	−2024	−2690	−3057	−3276	−3431	−3540	−3557	−3371	−2811	−3170
0.4	−2004	−2519	−2865	−3123	−3338	−3523	−3653	−3670	−3483	−3614
0.6	−1534	−1890	−2178	−2433	−2673	−2903	−3113	−3278	−3356	−3328
0.8	−770	−968	−1152	−1331	−1509	−1688	−1865	−2033	−2182	−2103
1	0	0	0	0	0	0	0	0	0	0

TABLE 2

Integral molar excess G i b b s energies at 1273K according to the H i l l e r t model

ΔG^E (J/mol)										
x_{Ga}	$x_{Ge} : x_{Sb}$									
	9/1	8/2	7/3	6/4	5/5	4/6	3/7	2/8	1/9	eut
0	−1613	−2469	−2892	−3108	−3241	−3314	−3253	−2881	−1922	−2448
0.2	−1845	−2480	−2886	−3152	−3327	−3418	−3391	−3173	−2646	−2976
0.4	−1853	−2344	−2727	−3027	−3259	−3423	−3508	−3489	−3327	−3434
0.6	−1475	−1840	−2162	−2446	−2694	−2906	−3079	−3206	−3281	−3249
0.8	−767	−978	−1179	−1369	−1550	−1721	−1882	−2031	−2170	−2095
1	0	0	0	0	0	0	0	0	0	0

TABLE 3

Activity for gallium at 1273K according to the K o h l e r model

a_{Ga}										
x_{Ga}	$x_{Ge} : x_{Sb}$									
	9/1	8/2	7/3	6/4	5/5	4/6	3/7	2/8	1/9	eut
0	0	0	0	0	0	0	0	0	0	0
0.2	0.149	0.142	0.139	0.136	0.135	0.135	0.135	0.137	0.140	0.141
0.4	0.309	0.298	0.290	0.284	0.279	0.275	0.272	0.270	0.269	0.273
0.6	0.498	0.486	0.475	0.464	0.454	0.445	0.436	0.427	0.418	0.427
0.8	0.731	0.720	0.709	0.697	0.686	0.674	0.663	0.651	0.637	0.647
1	1	1	1	1	1	1	1	1	1	1

TABLE 4

Activity for gallium at 1273K according to the H i l l e r t model

a_{Ga}										
x_{Ga}	$x_{Ge} : x_{Sb}$									
	9/1	8/2	7/3	6/4	5/5	4/6	3/7	2/8	1/9	eut
0	0	0	0	0	0	0	0	0	0	0
0.2	0.157	0.152	0.147	0.143	0.141	0.141	0.143	0.145	0.148	0.148
0.4	0.321	0.313	0.302	0.293	0.287	0.284	0.283	0.283	0.280	0.284
0.6	0.509	0.497	0.483	0.469	0.458	0.450	0.444	0.437	0.427	0.435
0.8	0.736	0.725	0.712	0.698	0.686	0.676	0.666	0.655	0.641	0.651
1	1	1	1	1	1	1	1	1	1	1

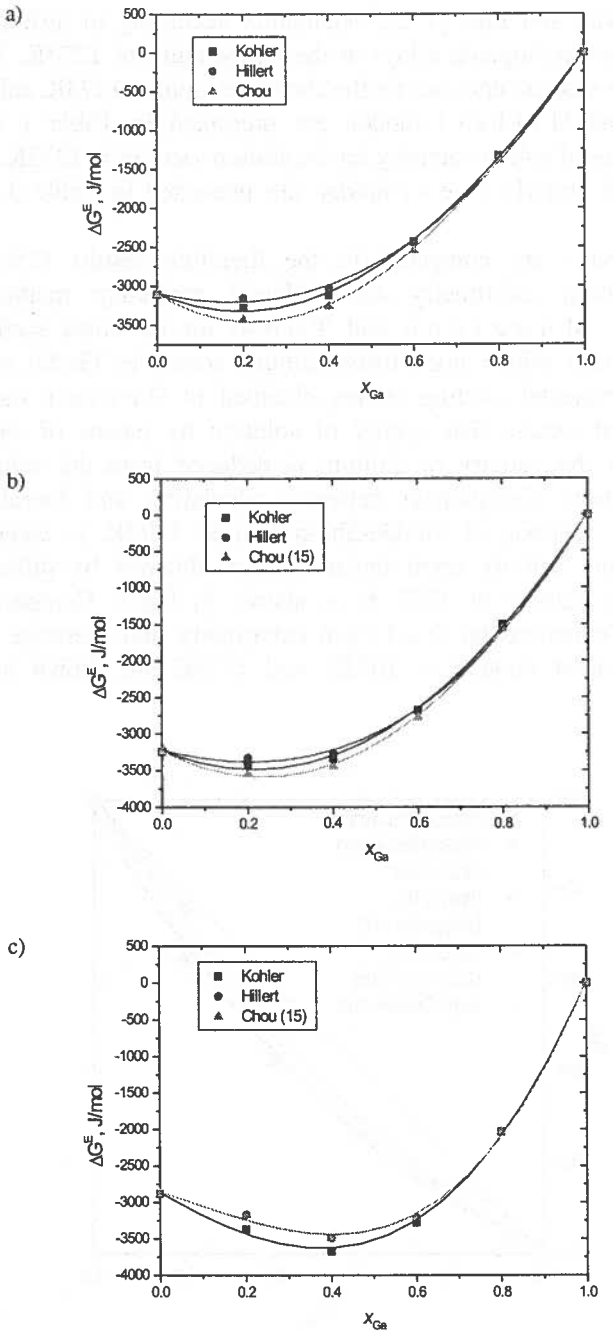

Fig. 1. Comparison between calculated and literature data [15] for ΔG^E of Ga-Ge-Sb alloys in the sections with molar ratio $x_{Ge} : x_{Sb}$ = 6/4 (a); 5/5 (b); 2/8 (c) at 1273K

Based on these data and Eqs. (1–2), calculation according to different predicting methods was done for investigated alloys at the temperature of 1273K. The values of integral molar G i b b s excess energies for the chosen sections at 1273K, calculated by the K o h l e r model and H i l l e r t model, are presented in Table 1 and Table 2, respectively. The values of gallium activity for the chosen sections at 1273K, calculated by the K o h l e r model and H i l l e r t model, are presented in Table 3 and Table 4, respectively.

The obtained results are compared to the literature results [15–20] obtained by experimental Oelsen calorimetry and different predicting methods (C h o u, H a j r a, *R*-function, M u g g i a n u and T o o p) for all cross sections, as well as for the cross section which goes from gallium corner to Ge-Sb eutectics (Ga-$GeSb_{0.855}$). The experimental cooling curves obtained in O e l s e n calorimetry are used in calculation of excess free energy of solution by means of so-called O e - l s e n integral. Next the activity of gallium is deduced from the values of excess free energy of solution. Comparison between calculation and literature data for ΔG^E in some cross sections of Ga-Ge-Sb system at 1273K is shown in Fig 1. Dependence of gallium activity upon molar content obtained by different methods in Ga-$GeSb_{0.855}$ cross section at 1273 K is shown in Fig.2. Comparison between calculation methods, experimental O e l s e n calorimetry and literature data for gallium activity upon molar content at 1073K and 1173K are shown in Fig. 3 and Fig. 4, respectively.

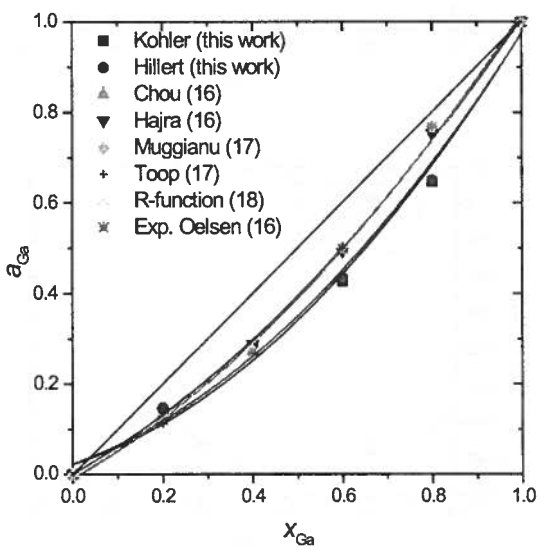

Fig. 2. Comparison between experimentally obtained gallium activity and calculated values in Ga-$GeSb_{0.855}$ cross section of Ga-Ge-Sb ternary system at 1273K

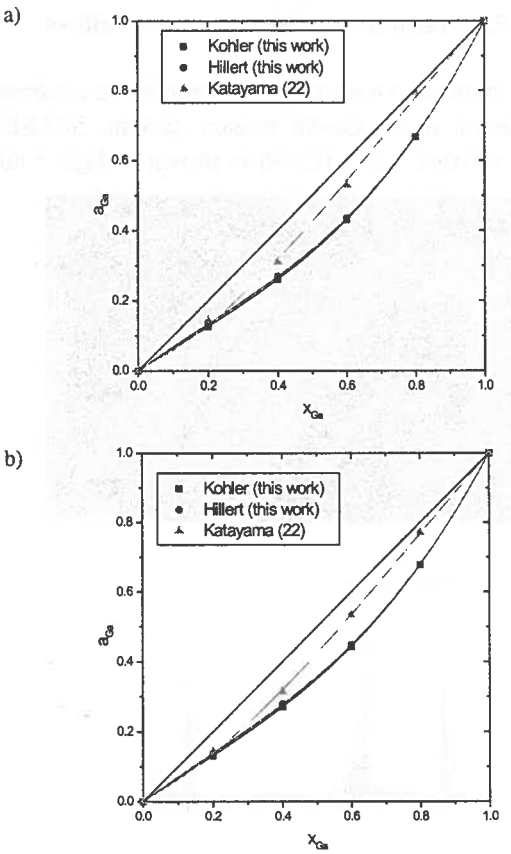

Fig. 3. Comparison between calculated and literature data [22] for gallium activity in Ga-Ge-Sb ternary system in the section with molar ratio $x_{Ge} : x_{Sb}$ = 5/5 at 1073K (a) and 1173K (b)

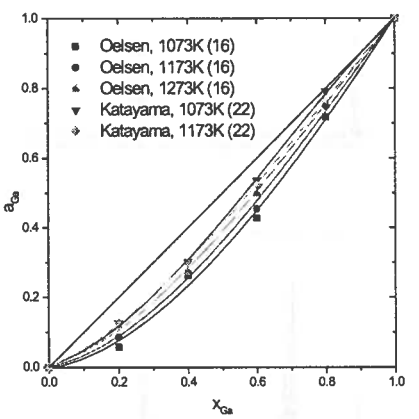

Fig. 4. Comparison between experimental Oelsen calorimetry and Katayama literature data [16] for gallium activity in Ga-Ge-Sb ternary system 1073K and 1173K

3.2. Characterization of obtained alloys

SEM-EDX and DTA methods were carried out in order to confirm alloy compositions of eut (Ga-$GeSb_{0.855}$) section in Ga-Ge-Sb ternary system. SEM-EDX photo of alloy (content: $x_{Ga} = 0.60$, $x_{Ge} = 0.061$, $x_{Sb} = 0.339$) is shown in Figs 5 and 6.

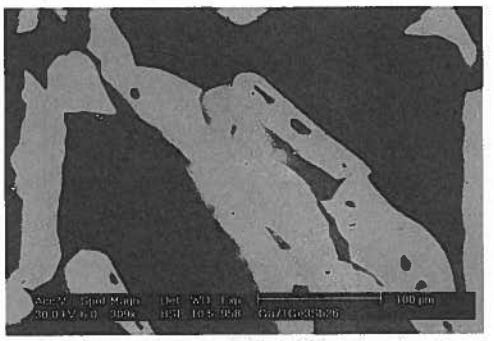

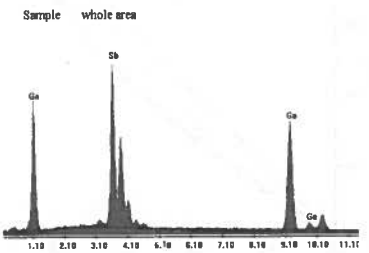

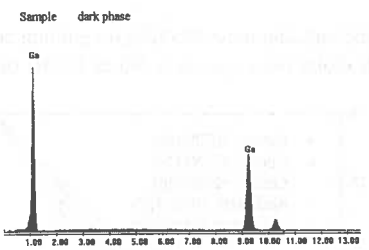

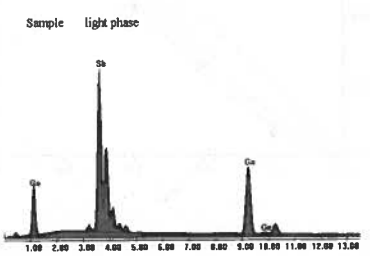

Fig. 5. SEM-EDX analysis of sample $x_{Ga} = 0.60$, $x_{Ge} = 0.061$, $x_{Sb} = 0.339$

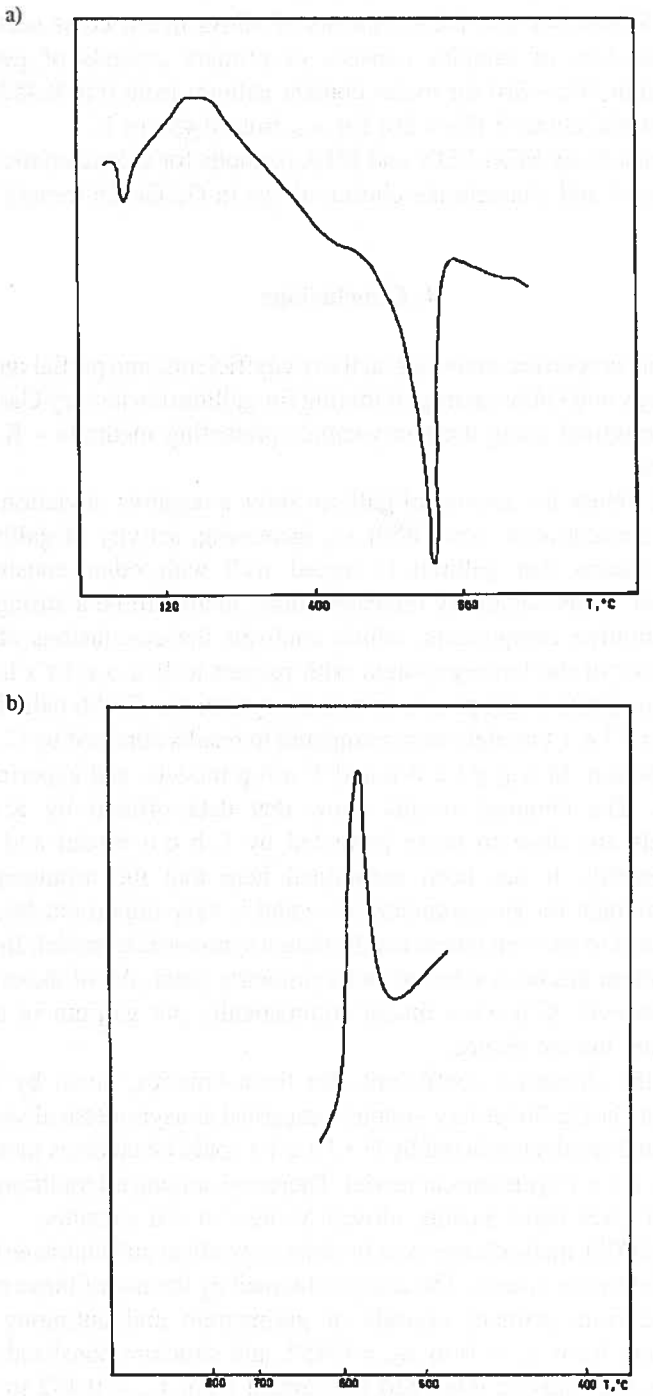

Fig. 6. DTA curves of sample $x_{Ga} = 0.60$, $x_{Ge} = 0.061$, $x_{Sb} = 0.339$ heating (a) and cooling (b)

According to SEM-EDX and DTA analysis of alloys in eut cross section, it can be concluded that structure of samples consists of primary crystals of germanium and antimony and eutectic (Ga+Sb) for molar content gallium from 0 to 0.452, and primary crystals of gallium and eutectic (Ga+Sb) for x_{Ga} from 0.452 to 1.

The obtained results by SEM-EDX and DTA methods for characteristic compositions completely determine and characterize chosen alloys in Ga-Ge-Sb ternary system.

4. Conclusions

Thermodynamic properties: activities, activity coefficients, and partial molar properties (excess Gibbs energy and Gibbs energy of mixing for gallium) in ternary Ga-Ge-Sb system at 1273K, are determined using thermodynamics predicting methods – K o h l e r and H i l l e r t models.

The calculated values for activity of gallium show a negative deviation from Raoults law in the whole concentration area. With x_{Ga} increasing, activity of gallium uniformly increases, which means that gallium is mixed well with other constituents in the investigated section. If the negativity increases more, there will be a stronger interaction between the constitutive components, which confirms the conclusions about the thermodynamic behavior of the ternary system with respect to R a o u l t's law.

Also, the thermodynamic properties in ternary system Ga-Ge-Sb calculated by using K o h l e r and H i l l e r t models were compared to results obtained by C h o u, as well as H a j r a, *R*-function, M u g g i a n u and T o o p models, and experimental O e l s e n calorimetry. The obtained results show that data offered by K o h l e r and H i l l e r t models are close to those predicted by C h o u model and experimental O e l s e n calorimetry. It has been mentioned here that the arrangement of three components to a triangle for an asymmetrical model is very important, because a wrong arrangement will lead to an even worse results than a symmetrical model. In this example, the component gallium has been selected as a symmetric point. All of these are a result of human choice. However, C h o u's model automatically put gallium in a symmetrical position without any human choice.

According to the similarity coefficients for three binaries, given by the C h o u's model, indicate that Ga-Ge-Sb ternary system is regarded as asymmetrical system. Because of that, the calculated results predicted by H i l l e r t could be taken as more correct than those from the K o h l e r symmetrical model. Therefore, among all traditional models, the H i l l e r t model gives better results, closest to the C h o u's results.

SEM-EDX and DTA methods are used in order to confirm and characterize the chosen alloys in Ga-Ge-Sb ternary system. The results obtained by the use of these methods, show structure consisted from primary crystals of germanium and antimony and eutectic (Ga+Sb) for content from $x_{Ga} = 0$ to $x_{Ga} = 0.452$, and structure consisted from primary crystals of gallium and eutectic (Ga+Sb) for content from $x_{Ga} = 0.452$ to $x_{Ga} = 1$.

The results presented in this paper could contribute to a better knowledge of this ternary system.

REFERENCES

[1] M.C. Roberts, Materials and Society **13**, 4, 411-430 (1989).
[2] R.D. Agrawal, V.N.S. Mathur, M.L. Kapoor, High Temperature Materials and Processes **9**, 201-216 (1990).
[3] J. Hafner, W. Jank, J. Holzmannhofer, Journal of Non-Crystalline Solids **150**, 266-270 (1992).
[4] R.E. Green, Annual Review of Materials Science **20**, 197-217 (1990).
[5] L.H. Belz, Adv. Mater. Process. Inc. Met. Prog. **132**, 5, 65-69 (1987).
[6] J.H. Westbrook, Liquid Metal Conductors, Pergamon Press, Oxford London, UK, 1986.
[7] D.M. Jacobson, Critical Materials in the Electrical and Electronics Industry, The Institution of Metallurgists, Available from the Institute of Metals, 1 Carlton House Terrace, London, UK, p. 59, 1984.
[8] J.W. Soh, H.M. Lee, Scripta Metalurgica et Materialia **27**, 7, 783-788 (1992).
[9] M. Hillert, CALPHAD **4**, 1 (1980).
[10] M. Fornaris, Y.M. Muggianu, M. Gambino, J.P. Bros, Z. Naturforsch. **35a**, 1256-1264 (1980).
[11] V.B. Predel, D.W. Stein, Zeitschrift fur Metallkunde **61**, 12, 909-914 (1970).
[12] I. Katayama, J. Nakayama, T. Nakai, Z. Kozuka, Transactions of the Japan Institute of Metals **28**, 2, 129-134 (1987).
[13] R. Hultgren, P.D. Desai, D.T. Hawkins, M. Gleiser, K. Kelley, The Selected Values of the Thermodynamic Properties of Binary Alloys, ASM, Metals Park, OH, 1973.
[14] I. Katayama, Y. Fukuda, Y. Hattori, Ber. Bunsenges. Phys. Chem. **102**, 9, 1235-1239 (1998).
[15] A. Kostov, D. Zivkovic, Z. Zivkovic, Journal of Mining and Metallurgy **4B**, 423-435 (1999).
[16] A. Kostov, D. Zivkovic, Z. Zivkovic, Journal of Thermal Analysis and Calorimetry **60**, 473-487 (2000).
[17] A. Kostov, D. Zivkovic, Z. Zivkovic, Journal of Thermal Analysis and Calorimetry **65**, 955-964 (2001).
[18] A. Kostov, D. Zivkovic, Z. Zivkovic, Journal of Metallurgy **6**, 1 (2000) 19-26. (in Serbian)
[19] A. Kostov, D. Zivkovic, D. Manasijevic, Z. Zivkovic, 34th International October Conference on Mining and Metallurgy, Proceedings, 30 September – 3 October 2002, Bor Lake, Yugoslavia, p. 595-600.
[20] D. Zivkovic, I. Katayama, A. Kostov, Z. Zivkovic, Journal of Thermal Analysis and Calorimetry **71**, 567-582 (2003).
[21] F. Kohler, Monatsh. Chem. 91, 738 (1960).
[22] I. Katayama, Y. Fukuda, Y. Hattori, Ber. Bunsenges. Phys. Chem. **102**, 9, 1235-1239 (1998).

Received: 15 June 2004.

A R C H I V E S O F M E T A L L U R G Y A N D M A T E R I A L S
Volume 49 2004 Issue 3

J. BURŠÍK *

PHASE EQUILIBRIA IN Ni-Al-Cr-Co-W-Re SYSTEM: MODELLING AND EXPERIMENTS

RÓWNOWAGI FAZOWE W UKŁADZIE Ni-Al-Cr-Co-W-Re: MODELOWANIE I EKSPERYMENT

Ordering processes typical for Ni-base superalloys were studied in a multicomponent system Ni-Al-Cr-Co-W-Re by means of computer modelling using Monte Carlo method combined with *ab initio* calculations. Complementary calculations were also run using ThermoCalc software for modelling of thermodynamic equilibria. Together with modelling, experiments were carried out by means of analytical scanning and transmission electron microscopy after a long term annealing at high temperatures typical for application of Ni-based superalloys. The microstructure of equilibrium states was characterized as regards the phase constitution and chemical composition of phases. The comparison of results of applied methods is given.
Keywords: phase diagram, Monte Carlo, ab initio, nickel

Proces porządkowania, typowy dla nadstopów na bazie niklu, był obiektem badań w układzie wieloskładnikowym Ni-Al-Cr-Co-W-Re przy pomocy modelowania komputerowego stosując metodę Monte Carlo w połączeniu z obliczeniami *ab initio*. Równolegle obliczenia prowadzono również za pomocą pakietu ThermoCalc. Doświadczenia przeprowadzono stosując metodę elektronowej mikroskopii skaningowej i transmisyjnej. Na podstawie wyników badań scharakteryzowano zarówno równowagową mikrostrukturę stopów jak również ich skład chemiczny i fazowy. Porównano wyniki badań różnymi metodami.

1. Introduction

Nickel-base superalloys for aeroengine turbine blades are continuously developed and improved by complex alloying and processing [1]. The superalloys typically have a high volume fraction of cubical $L1_2$ ordered γ' precipitates in face centred cubic (fcc) disordered γ matrix. Their exceptional mechanical properties are controlled by specific geometry and by the properties of the two phases and their interaction. Recent advances in the creep

* INSTITUTE OF PHYSICS OF MATERIALS, ACADEMY OF SCIENCES OF THE CZECH REPUBLIC, ŽIŽKOVA 22, 616 62 BRNO, CZECH REPUBLIC

rupture strength of superalloys have been accomplished mainly by the addition of refractory elements. Microstructural stability is of utmost importance during alloy development.

The sophisticated tools for thermodynamic modelling are available for theoretical prediction of phase constitution of multicomponent alloys. Modelling of phase equilibria and kinetics of phase transformations are now standard tools used in the process of new alloys design. Another class of promising methods of predicting phase constitution is based on computer modelling at the atomic level. The methods often use a Monte Carlo (MC) approach [2, 3] which can be combined with other well-established methods such as molecular dynamics, static relaxation or *ab initio* calculation [4–6]. MC simulation is often used in this area especially for modelling the order/disorder phase transitions, which is also the case of the two-phase $\gamma + \gamma'$ structure of superalloys.

MC simulation has above the other mentioned methods the advantage of direct visualisation of atomic structure in different stages of ordering process at various temperatures. To compare results of MC simulations with the results of other computational methods (CVM, thermodynamic modelling) and with experimental observations (atom-probe ion field microscopy and *X*-ray analytical methods in electron microscopy), the atomic structure generated by MC simulation has to be quantified. Methods based on phenomenological thermodynamics very much depend on reliable thermodynamic data coming not only from binaries and ternaries, but also from higher order systems. These data are in many cases scarce.

The present paper combines modelling on the atomic level and modelling using phenomenological thermodynamics with experimental measurements of multicomponent Ni-base system in the composition and temperature range of application of superalloys.

2. Experimental

Samples of three alloys were studied (see Tab. 1 for nominal compositions) with 70.8 at.% Ni, 0.4 at.% Re and different amounts of other alloying elements, i.e. Al, Co, W and Cr. The specimens were prepared from pure metals (purity from 99.9% to 99.99%) by vacuum melting and casting. Further remelting in an induction furnace under an Ar atmosphere followed by chill casting was done to increase the compositional homogeneity. Samples with the dimensions 4×4 mm were cut with a spark-erosion saw from disc-shaped ingots (diameter 32 mm, thickness 4 mm). At first they were homogenised for 1 hour at 1373K, quenched in water and then annealed to achieve a state close to the thermodynamic equilibrium. The annealing proceeded at one of the following regimes: 650 hours at 1173K, 120 hours at 1273K, 48 hours at 1373K, 16 hours at 1474K or 2 hours at 1573K. During the annealing the samples were sealed in evacuated quartz capsules. The heat treatment was finished by crushing the capsules and water quenching. The samples for scanning electron microscopy (SEM) underwent the standard metallographic surface preparation procedure. The samples for the transmission electron microscopy (TEM) were prepared from sandwiches cut with a spark-erosion saw, ground and finally twin-jet electropolished (electrolyte: 95% of acetic acid and 5% of perchloric acid, voltage 95V). Ion-beam milling

was used in several cases instead of electropolishing to avoid selective etching of one of the constituent phases.

The microstructure and alloying element redistribution caused by the long-term heat treatment were studied by means of a Philips SEM 505 scanning electron microscope equipped with EDAX analyser and a Philips CM12 STEM analytical transmission electron microscope with UTW EDAX Phoenix analyser. The nominal chemical composition of as-cast experimental alloys was measured by means of energy dispersive *X*-ray microanalysis (EDS) in SEM and verified once again after the long-term annealing. Phases present after the heat treatment were identified by a selected area diffraction (SAD) in TEM and their local chemical composition was measured by means of EDS in STEM mode using a 10 nm probe size and thin sample approximation. The method of standardless EDS spectra quantification of multicomponent alloys with k-factor optimisation was used for this purpose [7].

3. Modelling techniques

3.1. Monte Carlo simulation

The crystal was modelled as a block of 32×32×32 face centred cubic (fcc) cells containing 131072 sites. Periodic boundary conditions were used. K a w a s a k i dynamics [8] and an I s i n g model taking into account the pairwise interaction up to the third nearest neighbours were used. Pair interactions were introduced by means of phenomenological L e n n a r d - J o n e s potentials [9, 10] in the form

$$e_{ij}(r) = e_{ij}^{0}\left[\left(\frac{r_{ij}}{r}\right)^{m} - \frac{m}{n}\left(\frac{r_{ij}}{r}\right)^{n}\right], \tag{1}$$

where i, j denote atomic species; $m = 8$ and $n = 4$ in our case.
The exchange of randomly selected nearest neighbours was realised with the probability W expressed by G l a u b e r function [2]:

$$W = \frac{1}{1 + \exp(\Delta E/k_B T)}, \tag{2}$$

where ΔE is energy change due to exchange, T is temperature and k_B is B o l t z m a n n constant. More details are given in the previous paper [11]. The size effect was accounted for by readjusting the average lattice parameter periodically during the simulation to minimize the system energy.

Simulations were conducted at temperatures from 1173K to 1373K for compositions listed in Table 1. The simulations were started from random atom distribution and they were

extended to 10^5–10^6 MC steps (MCS). W a r r e n - C o w l e y short-range order (SRO) parameters [12] were calculated to describe the ordering evolution:

$$\alpha_{AB}^{(k)} = 1 - \frac{p_{AB}^{(k)}}{p_{AB}^{(k)rnd}}, \tag{3}$$

where $p_{AB}^{(k)}$ is the probability of forming an A-B pair with a spacing equal to the radius of the k-th co-ordination sphere, $p_{AB}^{(k)rnd}$ is the probability of forming a similar A-B pair in a random solid solution. An improved method of quantitative analysis [13] was finally applied to the resulting ordered configurations to evaluate volume fraction and chemical composition of phases and site occupation in the ordered phase.

TABLE 1

Composition (at.%) of alloys selected for simulations and experiments

alloy	Ni	Al	Cr	Co	Re	W
N1	70.8	14.2	2.6	10.6	0.4	1.4
N2	70.8	16.7	1.2	10.9	0.4	0.0
N3	70.8	17.6	1.2	8.6	0.4	1.4

Alternatively, *ab initio* calculations of cohesive energies of tetrahedral atomic clusters were used instead of L e n n a r d - J o n e s pair potentials. In general, the local spin density approximation (LSDA) within the density functional theory (DFT) has been proven to be very useful for calculating electronic and ground state properties of solids, molecules and atoms. Recent progress has been made by adding gradient terms of the electron density to the exchange-correlation energy [14, 15].

Preliminary calculations have been carried out to optimise the input parameters of *ab initio* calculations to obtain fast convergence, namely the number of k-points in the reciprocal space and the radii around atoms, where the potential is described in terms of spherical waves. The volume dependence of the energy was then calculated for every possible combination of atoms from the set {Ni, Al, Cr, Co, Re, W} using a computer code Wien2k [16]. The energy–volume curves were fitted by four-parametric M u r n a g h a n's equation of state [17] and used in the Monte Carlo code, again with readjusting the average lattice parameter periodically during the simulation.

3.2. Thermodynamic modelling

CALPHAD approach [18] was used for thermodynamic and phase diagram calculations. This method deals with the composition and temperature dependent G i b b s energies of the constituent phases and minimizes the overall energy to obtain phase equilibria. The G i b b s energies may be expressed using thermodynamic parameters, which result from thermodynamic assessments and are collected in thermodynamic

databases. In this case, a commercial thermodynamic database for Ni-base supperalloys developed recently by the Thermo-Calc group [19] was used with a small modification based on our previous work [20]. ThermoCalc software package [21] based on CALPHAD approach routines was applied.

Ni-based alloys are modelled in a specific way because of the occurrence of ordering processes. Recent descriptions are based on the model developed by A n s a r a et al. [22, 23], who incorporated the process of ordering into the basic Ni-Al system by modelling the ordered and disordered phase by means of sublattice approach, where both the ordered and disordered phases were described as having two sublattices. The disordered structure in this model is characterized by the assumption of the equality of site fractions of the same elements in different sublattices.

4. Results and discussion

An example of characteristic evolution of SRO parameters during ordering is shown in Fig. 1 for alloy N3 and temperature 1273K. It is seen, that in case of many types of atomic pairs SRO parameters change rapidly in the initial period and are streaming either to + 1 (which means that the appearance of particular atomic pair in the later period of ordering is highly improbable) or to a negative value (frequent appearance of the atomic pair).

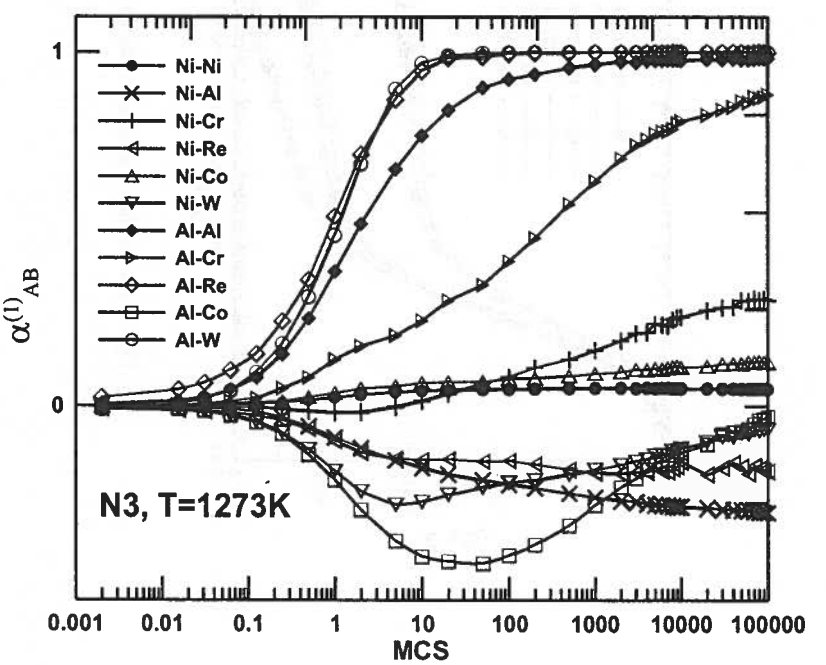

Fig. 1. Evolution of SRO parameters in course of ordering of the alloy N3 at 1273K

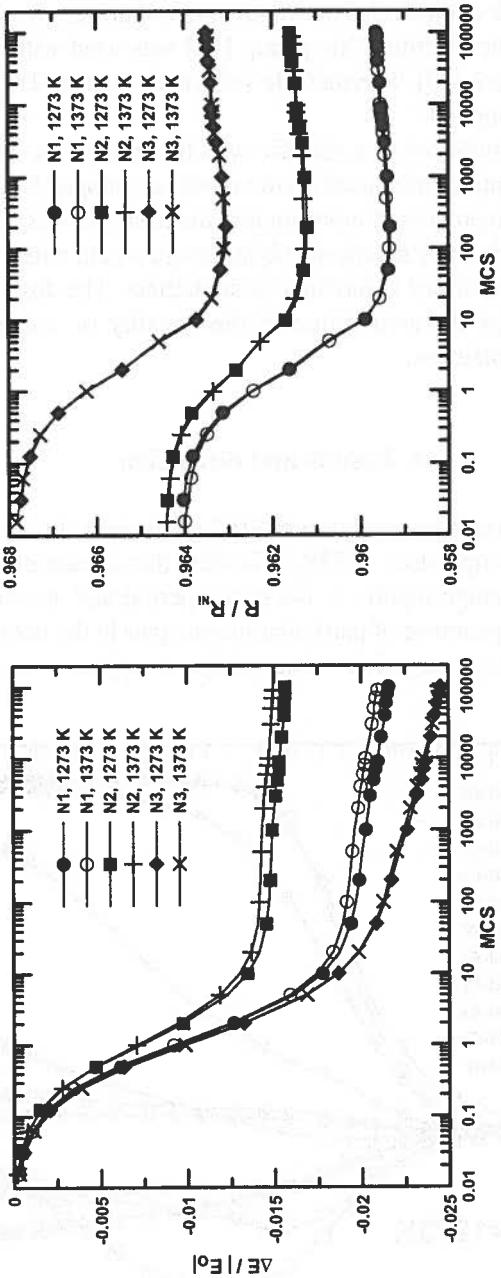

Fig. 2. The evolution of system energy (left) and lattice parameter (right) in course of ordering

By comparison of selected curves it is possible in some cases make conclusion about the substitutional behaviour of alloying elements. E. g., from comparison of the curves $\alpha^{(1)}_{NiNi}$, $\alpha^{(1)}_{NiAl}$, $\alpha^{(1)}_{AlAl}$, $\alpha^{(1)}_{NiRe}$ and $\alpha^{(1)}_{AlRe}$ in Fig. 1 we can conclude that Re and Al behave in a similar way and hence Re resides preferentially in Al sublattice of basic Ni_3Al $L1_2$ structure.

The evolution of energy of the system is shown for three compositions and two temperatures in the Fig. 2. Again, it is seen, that the most dramatic changes occur at the very beginning of the ordering (during the first 10 MCS). This is the effect of atoms rearrangement and forming the ordered domains. The slow energy decrease in the later stages is due to domain coarsening. It eventually stops only after forming a single ordered domain in the whole modelled block.

The evolution of the mean lattice parameter is demonstrated in the Fig. 2 as well. The lattice parameter R was relaxed periodically in course of simulation by finding the minimum of E(R). The rapid initial increase is followed by a small increase during domain coarsening. The total relative change of about 0.5% is not dramatic by itself, nevertheless it seems to be important to take the lattice parameter changes into account, as the pair energies could be substantially influenced even by small changes of atom distances.

To estimate the importance of the relaxation of *local* atomic positions and to quantify its impact on the system's total energy, equilibrium atomic positions were computed in the case of sample N3 annealed at 1273K using a molecular dynamics taking into account forces from the three coordination spheres. The results are in Fig. 3. After reaching 9×10^4 MCS all the atomic positions were locally relaxed in nearly 10^3 molecular dynamic steps (MDS) of time interval 2.5 fs. It was found, that the change of both E and R due to the local relaxation is small compared to the change due to the ordering, though not negligible. We consider running the Monte Carlo on a rigid lattice with changing only the mean lattice parameter as a satisfactory compromise. Incorporating local shifts into ordering simulation would dramatically slow down the program execution, as it would make impossible to use pre-calculated internal tables of pair energies.

The experimental results obtained on thin foils by means of analytical transmission electron microscopy are summarized in the Table 2. The majority of samples were two-phase, consisting of ordered domains of γ' embedded in disordered matrix γ. The morphology, volume fraction and size of phase regions in two-phase samples were quite diverse, as demonstrated on selected SEM and TEM micrographs in Fig. 4 and 5. Alloys annealed at 1173K and 1273K have fine $\gamma+\gamma'$ structure with domain size below 1 μm (Fig. 4a, 5a), as well as alloy N1 annealed at 1373K (Fig. 5b). Structure of N3 annealed at 1373K contains both fine and larger (2-5 μm) domains (Fig. 4b). Structure of N2 annealed at 1373K and N3 annealed at 1473K consists of coarse phase objects with characteristic dimension from 5 to 10 μm (Fig. 4c, 5c). Remaining alloys, i.e. those annealed at higher temperatures, were single-phase γ, namely N1 and N2 annealed at 1473 K and all three alloys annealed at 1573K.

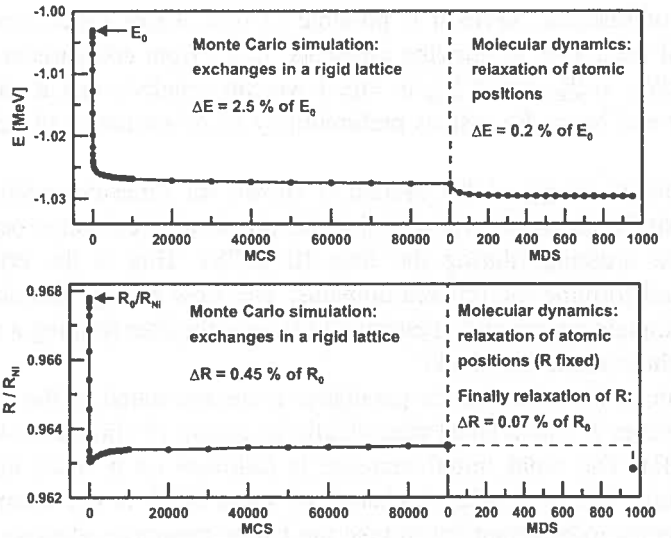

Fig. 3. The effect of local lattice relaxations on system energy (upper part) and on relative lattice parameter (bottom) in sample N3 annealed at 1273K

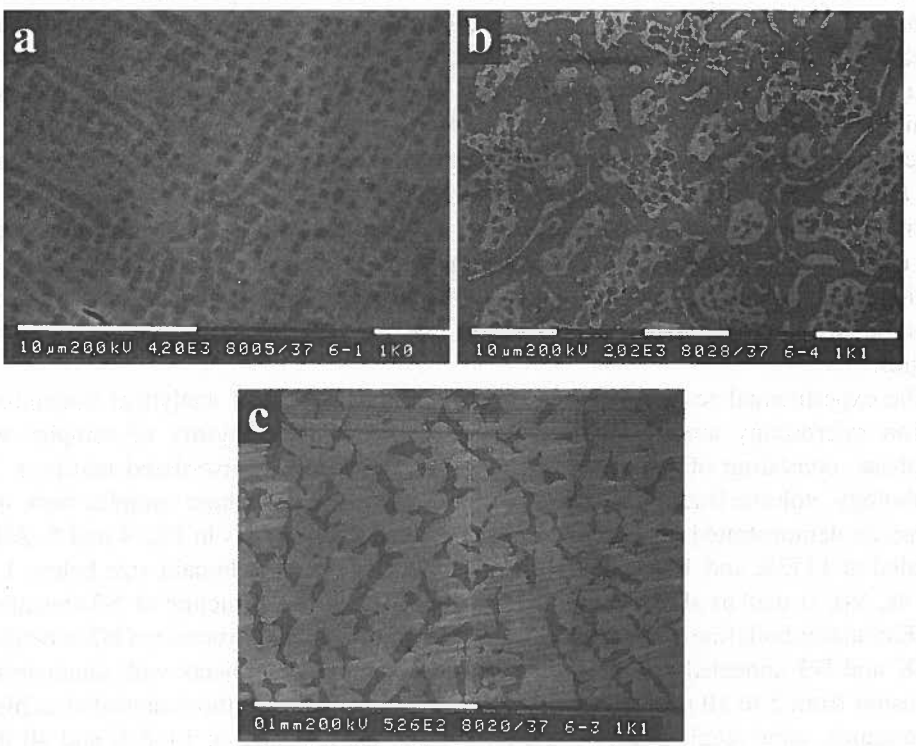

Fig. 4. SEM micrographs of characteristic types of microstructure: alloy N1 annealed at 1273K (a), alloy N3 annealed at 1373K (b) and alloy N2 annealed at 1373K (c)

TABLE 2

Composition (at.%) and volume fraction of constituting phases as found by EDS analysis in STEM

alloy	T[K]	phase	Al	W	Cr	Co	Ni	Re	f_v
N1	1173	γ'	18.3	1.7	1.5	6.9	71.3	0.3	0.54
		γ	10.3	1.0	3.5	15.6	69.1	0.5	0.46
N2		γ'	20.1	0.0	0.9	7.5	71.1	0.4	0.57
		γ	12.9	0.0	1.5	15.9	69.2	0.5	0.43
N3		γ'	18.1	1.7	0.9	7.4	71.5	0.4	0.89
		γ	10.3	1.8	2.2	16.5	68.1	1.2	0.11
N1	1273	γ'	16.3	1.4	1.4	7.7	73.0	0.2	0.56
		γ	9.9	1.1	3.2	13.7	71.7	0.5	0.44
N2		γ'	18.9	0.0	1.1	7.7	72.2	0.2	0.50
		γ	13.5	0.0	1.6	13.4	71.3	0.2	0.50
N3		γ'	18.1	1.8	0.9	7.5	71.4	0.4	0.87
		γ	11.5	1.7	2.1	14.6	69.0	1.1	0.13
N1	1373	γ'	12.3	1.1	1.4	8.2	76.8	0.2	0.05
		γ	11.1	1.0	2.6	12.1	72.7	0.4	0.95
N2		γ'	20.1	0.0	0.8	7.4	71.4	0.3	0.28
		γ	15.0	0.0	1.4	11.9	71.4	0.4	0.72
N3		γ'	15.9	1.2	0.8	7.5	74.4	0.2	0.92
		γ	11.1	1.0	1.8	12.7	72.7	0.6	0.08
N1	1473	γ	15.8	1.4	2.7	11.1	68.7	0.4	1.00
N2		γ	18.4	0.0	1.4	10.6	69.1	0.5	1.00
N3		γ'	19.0	1.3	0.9	7.4	71.4	0.1	0.69
		γ	14.3	1.1	1.7	11.2	71.2	0.5	0.31
N1	1573	γ	14.3	1.4	2.7	11.1	70.2	0.4	1.00
N2		γ	18.2	0.0	1.8	10.6	69.0	0.4	1.00
N3		γ	18.3	1.7	1.5	6.9	71.3	0.3	1.00

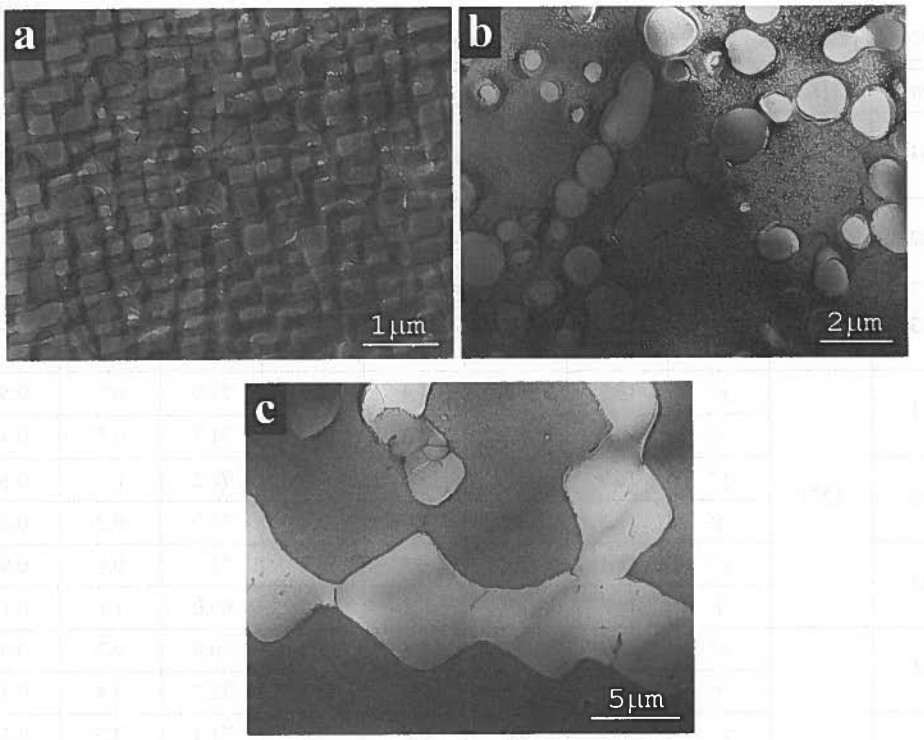

Fig. 5. TEM micrographs of characteristic types of microstructure: alloy N1 annealed at 1173K (a), alloy N1 annealed at 1373K (b) and alloy N2 annealed at 1373K (c)

The results of thermodynamic modelling with ThermoCalc are summarized in Table 3 and Figure 6. The values in Tab. 3 agree well with the experimental measurements (Tab. 2) except the alloy N1 annealed at 1373K, where a two-phase structure was observed, but the thermodynamic modelling predicts only one phase. Even in this case the results are close, as the volume fraction of γ found experimentally is 95%. The comparison of experimental results with the predictions obtained by Thermocalc is shown also in a series of isothermal sections of equilibrium phase diagrams in Figure 6. Alloys N1 and N3 are represented by symbols that are distinguished according to number of phases. The composition of alloy N2 doesn't lie in the section shown in Fig. 6, that is why it is not present. The vertical section of phase diagram at the last plot in Fig. 6 contains the similar information together with line of liquidus. It is seen that the N1 alloy annealed at 1373K is situated close to the border between one-phase and two-phase region.

TABLE 3

Composition (at.%) and volume fraction of constituting phases as calculated by ThermoCalc

alloy	T[K]	phase	Al	W	Cr	Co	Ni	Re	f_v
N1	1173	γ'	19.7	1.0	2.1	6.4	70.8	0.1	0.40
		γ	10.6	1.7	2.9	13.4	70.8	0.6	0.60
N2		γ'	21.1	0.0	1.1	7.1	70.5	0.2	0.50
		γ	12.3	0.0	1.3	14.7	71.1	0.6	0.50
N3		γ'	20.2	1.2	1.1	6.6	70.8	0.2	0.72
		γ	10.7	2.0	1.5	14.0	70.9	0.9	0.28
N1	1273	γ'	20.0	1.0	1.9	6.5	70.4	0.1	0.23
		γ	12.5	1.5	2.8	11.8	70.9	0.5	0.77
N2		γ'	21.5	0.0	1.0	7.2	70.2	0.2	0.36
		γ	14.0	0.0	1.3	13.0	71.1	0.5	0.64
N3		γ'	20.4	1.2	1.1	6.6	70.5	0.2	0.64
		γ	12.6	1.8	1.5	12.1	71.3	0.7	0.36
N1	1373	γ	14.2	1.4	2.6	10.6	70.8	0.4	1.00
N2		γ'	21.9	0.0	0.9	7.1	69.9	0.2	0.15
		γ	15.8	0.0	1.3	11.6	71.0	0.4	0.85
N3		γ'	20.6	1.3	1.0	6.6	70.3	0.2	0.50
		γ	14.5	1.6	1.4	10.6	71.3	0.6	0.50
N1	1473	γ	14.2	1.4	2.6	10.6	70.8	0.4	1.00
N2		γ	16.7	0.0	1.2	10.9	70.8	0.4	1.00
N3		γ'	21.0	1.3	0.9	6.6	70.0	0.2	0.26
		γ	16.4	1.4	1.3	9.3	71.1	0.5	0.74
N1	1573	γ	14.2	1.4	2.6	10.6	70.8	0.4	1.00
N2		γ	16.7	0.0	1.2	10.9	70.8	0.4	1.00
N3		γ	17.6	1.4	1.2	8.6	70.8	0.4	1.00

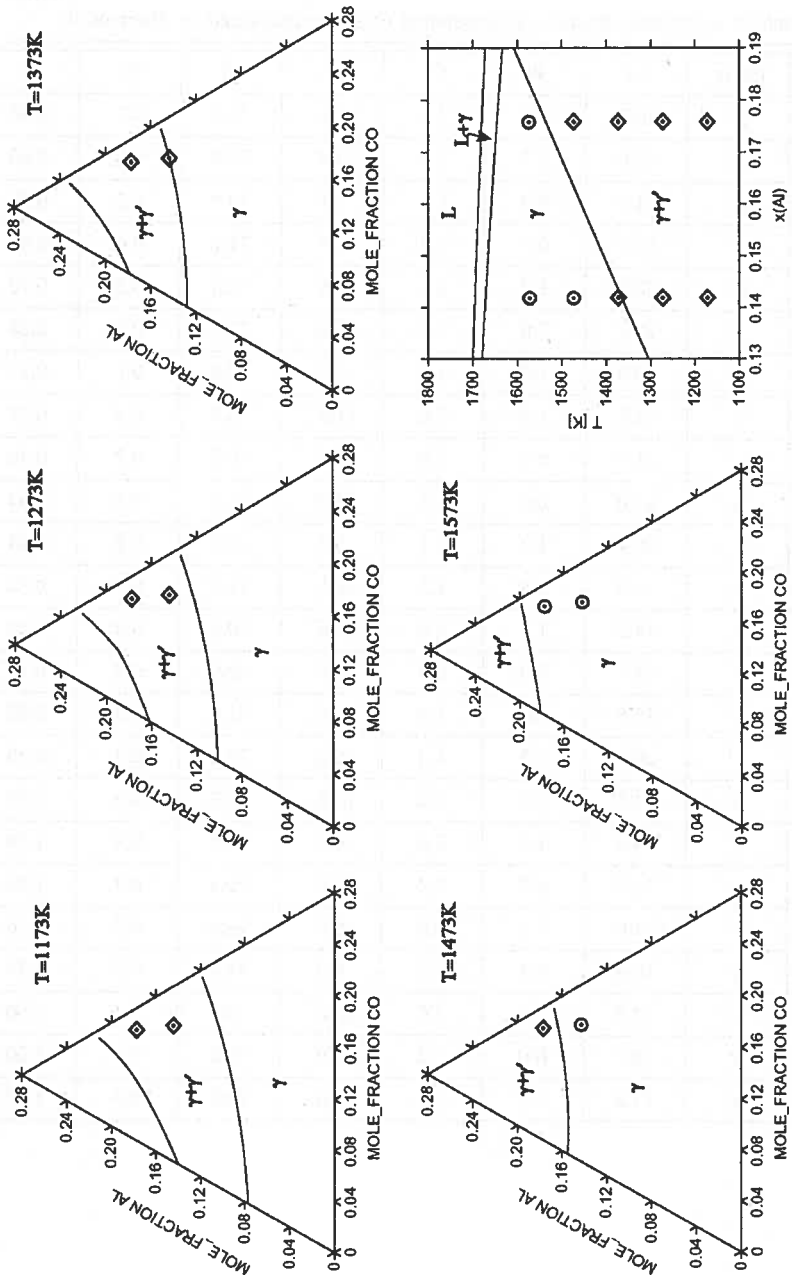

Fig. 6. Isothermal sections of equilibrium phase diagrams of the system Ni-Al-Cr-Re-Co-W with 70.8 Ni, 1.4 W and 0.4 Re (at.%). Experimental alloys N1 and N3 are marked by either ◊ (if two-phase structure was found experimentally) or ⊙(one-phase structure). Last of the series is the vertical section of the equilibrium phase diagram along the composition line connecting alloys N1 and N3

The comparison of the results of Monte Carlo simulations with those obtained by ThermoCalc is shown in Figure 7 for alloy N2 annealed at 1273K and for alloy N3 annealed at 1373K. It is seen, that the results agree at least qualitatively, i.e. by the preference of atomic species for either γ or γ'. However, the quantitative comparison reveals differences. While the results of thermodynamic modelling agree quite well with experimental data, Monte Carlo simulations generally exaggerate the composition differences between the two phases. Namely, the content of Cr, Co Al and W is lower in γ' and higher in γ compared to other two methods. It indicates, that the quality of potentials used in Monte Carlo simulations still might be worked on to reach the better agreement with reality. Other point is the limitation of model used for atomistic simulation. Calculation of broader dataset of cohesion energies for larger clusters (octahedrons) would probably further improve the applicability of atomistic simulations in this case.

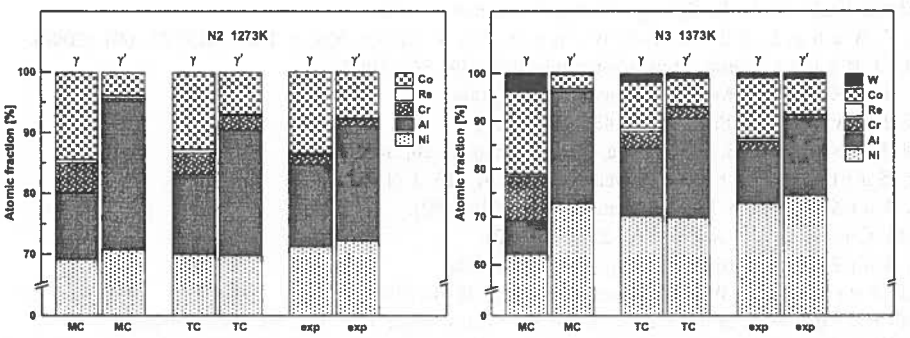

Fig. 7. Comparison of the results of atomistic simulations (MC) with predictions from Thermo-Calc (TC) and with the measured data (exp) for the alloy N2 annealed at 1273K (left) and alloy N3 annealed at 1373K (right)

5. Summary

Development of two-phase structure formed by disordered solid solution with face centred cubic lattice and its ordered $L1_2$ modification was studied by several methods on a multicomponent system Ni-Al-Cr-Co-W-Re. The alloy compositions and studied temperatures were close to the application range of advanced Ni-based superalloys. Computer modelling using Monte Carlo method combined optionally with *ab initio* calculations was used to study the kinetics of the ordering transformation and the correlation between short range order parameters in course of the process. Complementary calculations were also run using ThermoCalc software for modelling of thermodynamic equilibria. Together with modelling, experiments were carried out by means of analytical scanning and transmission electron microscopy after a long term annealing at high temperatures typical for application of Ni-based superalloys. The microstructure of equilibrium states was characterized as regards the phase constitution and chemical composition of phases. The comparison of results of applied methods was given.

Acknowledgment

The financial support was provided by the Grant Agency of the Czech Republic (Project No. 202/01/0383). The author is also indebted to Dr. A. Kroupa for the help with running calculations in ThermoCalc and to Prof. M. Šob for valuable discussions concerning *ab initio* calculations.

REFERENCES

[1] High-Temperature Ordered Intermetallic Alloys, ed. I. Baker et al., MRS, Pittsburgh, Pennsylvania (1993).
[2] K. B i n d e r, D.W. H e e r m a n n, Monte Carlo Simulation in Statistical Physics, Springer-Verlag, Heidelberg (1997).
[3] W. S c h w e i k a, Disordered Alloys – Diffuse Scattering and Monte Carlo Simulations, Springer-Verlag, Heidelberg (1998).
[4] K. O h n o, K. E s f a r j a n i, Y. K a w a z o e, Computational Materials Science: From Ab Initio to Monte Carlo Methods, Springer-Verlag, Heidelberg (1999).
[5] J.-T. W a n g, L. Z h o u, D.-S. W a n g, Y. K a w a z o e, Mater. Trans. JIM **41**, 601 (2000).
[6] H.-O. H e u e r, Comp. Phys. Communications **59**, 387 (1990).
[7] J. B u r š í k, Acta Metall. Slovaca **10**, 461 (2004).
[8] K. K a w a s a k i, Phys. Rev. **145**, 224 (1966).
[9] M. E n o m o t o, H. H a r a d a, Metall. Trans. A **20**, 649 (1989).
[10] Y. S a i t o, H. H a r a d a, Mater. Sci. Eng. A **223**, 1 (1997).
[11] J. B u r š í k, Comp. Phys. Commun. **147**, 162 (2002).
[12] J.M. C o w l e y, J. Appl. Phys. **21**, 24 (1950).
[13] J. B u r š í k, J. Alloys and Comp. **378**, 66 (2004).
[14] J.P. P e r d e w, Y. W a n g, Phys.Rev. B**45**, 13244 (1992).
[15] J.P. P e r d e w, S. B u r k e, M. E r n z e r h o f, Phys. Rev. Let. **77**, 3865 (1996).
[16] P. B l a h a, K. S c h w a r z, G.K.H. M a d s e n, D. K v a s n i c k a, J. L u i t z, Wien2k, An Augmented Plane Wave + Local Orbitals Program for Calculating Crystal Properties. K. Schwarz, TU Wien, Austria (2001).
[17] F.D. M u r n a g h a n, Proc. Natl Acad. Sci. USA **30**, 244 (1944).
[18] N. S a u n d e r s, A.P. M i o d o w n i k, CALPHAD (calculation of phase diagrams) – A Comprehensive Guide, Elsevier Science, Amsterdam (1998).
[19] N. D u p i n, B. S u n d m a n, Scan. J. Metall. **30**, 184 (2001).
[20] J. B u r š í k, P. B r o ž, R. P i c h a, Intermetallics **11**, 483 (2003).
[21] ThermoCalc User's Guide, Div. of Comput. Thermodynamics, Dept. of Mater. Science and Engineering, Royal Inst. of Technology, Stockholm (1997).
[22] I. A n s a r a, B. S u n d m a n, P. W i l l e m i n, Acta Metall. **36**, 977 (1988).
[23] I. A n s a r a, N. D u p i n, H.L. L u k a s, B. S u n d m a n, J. Alloys and Comp. **247**, 20 (1997).

Received: 15 June 2004.

A R C H I V E S O F M E T A L L U R G Y A N D M A T E R I A L S
Volume 49 2004 Issue 3

G.P. VASSILEV *

PHASE FORMATION IN THE SYSTEM Ti-Sn-Si

TWORZENIE SIĘ FAZ W UKŁADZIE Ti-Sn-Si

The phases formed in the system Ti-Sn-Si have been studied by optical and scanning electron microscopy. Two kinds of experiments have been used for the preparation of the alloys: arc-melting in argon atmosphere, and direct chemical interaction between titanium and silicon oxide.

A non-stoichiometric ternary compound corresponding approximately to the formula Ti3SnSi has been observed. Data about the mutual solubility of tin and silicon in the ternary extensions of their binary compounds with Ti have been obtained: Ti_5Sn_3 and Ti_2Sn dissolve up to around 9 at.% Si; Ti_5Si_4 and Ti_5Si_3 dissolve up to 6 at.% Sn and 2 at.% Sn, respectively. The silicon does not dissolve into the tin-rich liquid solution, practically. Data about the homogeneity ranges of the solid solution phases have been acquired as well.

An isothermal section of the Ti-Sn-Si phase diagram, at 600°C, based on the present work has been constructed.

Stosując mikroskop optyczny oraz skanindowy mikroskop elektronowy przeprowadzono badania tworzących się faz w układzie Ti-Sn-Si. Stopy do badań przygotowano dwoma metodami: poprzez topienie łukiem elektrycznym w atmosferze argonu oraz z bezpośredniej reakcji chemicznej pomiędzy tytanem i tlenkiem krzemu. Zaobserwowano istnienie niestechiometrycznego związku trójskładnikowego o formule zbliżonej do Ti_3SnSi. Uzyskano dane odnośnie wzajemnej rozpuszczalności cyny i krzemu w dwuskładnikowych fazach z tytanem, wynoszące: do ok. 9% at. Si w przypadku Ti_5Sn_3 i Ti_2Sn; do 6% at. Sn w przypadku Ti_5Si_4 oraz 2% at. Sn dla Ti_5Si_3. Stwierdzono praktyczny brak rozpuszczalności krzemu w bogatych w cynę ciekłych roztworach. Zebrano dane odnośnie zakresów rozpuszczalności występujących roztworów stałych. W oparciu o uzyskane wyniki badań skonstruowano przekrój izotermiczny układu Ti-Sn-Si dla 600°C.

1. Introduction

New lead-free solders are currently under development due to legal or technological reasons. The tin is and will probably stey as one of the most important constituents of the

* UNIVERSITY OF SOFIA, FACULTY OF CHEMISTRY, J. BOURCHIER AVENUE 1, 1164 SOFIA, BULGARIA

solders, while titanium additions to these materials might be prospective for improving their wetting and mechanical properties, for example. From the other side, Si chips are largely used in the electronic devises and solar cells. That is why the interactions of Si with these metals are both of fundamental and practical interest. Moreover, the silicon could be useful as alloying addition for developing of creep resistance in some titanium alloys [1].

Thus, the purpose of the present work is to study the phase relations in the Ti-Sn-Si system.

The Ti-corner of the Ti-Si-Sn system has been studied by B u l a n o v a et al. [2, 3]. As a result an isoplethic section at 90 at.% Ti was constructed and the reaction scheme at crystallization has been suggested.

Description of the binary phases relevant to the Ti-Sn-Si system is presented in Table 1 [4–11]. It is interesting to note the existence of two isotypic (Mn_5Si_3 type) binary compounds (Ti_5Sn_3 and Ti_5Si_3).

TABLE 1

Description of the binary solid phases relevant to the ternary Ti-Sn-Si system [4–11]

Phase	Approx. concentr. interval, at%	Pearson symbol	Space group	Strukturb. designation	Prototype
(α-Ti)	≈ 100 at.% Ti	hP2	$P6_3/mmc$	A3	Mg
(β-Ti)[a]	0–17 at.% Sn	cI2	$Im\bar{3}m$	A2	W
(α-Sn)	≈ 100 at.% Sn	cF8	$Fd\bar{3}m$	A4	C-diamond
(β-Sn)[a,b]	≈ 100 at.% Sn	tI4	$I4_1/amd$	A5	(β-Sn)
Ti_3Sn	23–25 at.% Sn	hP8	$P4_12_12$	$D0_{19}$	Ni_3Sn
Ti_2Sn	32–36 at.% Sn	hP6	$P6_3/mmc$	$B8_2$	$InNi_2$
Ti_5Sn_3	37.5 at.% Sn	hP16	$P6_3/mcm$	$D8_8$	Mn_5Si_3
αTi_6Sn_5	45.5 at.% Sn	oI44	$Immm$	...	Nb_6Sn_5
βTi_6Sn_5[a]	45.5 at.% Sn	...	...	...	hexagonal
Ti_2Sn_3	60.0 at.% Sn	oC40 or oS40	$Cmca$	...	V_2GaSn_2
(Si)	≈ 100 at.% Si	cF8	$Fd\bar{3}m$	A4	C-diamond
Ti_3Si	25.0 at.% Si	tP32	$P4_2/n$	...	PTi_3
Ti_5Si_3	60.5–64.5 at.% Ti	hP16	$P6_3/mcm$	$D8_8$	Mn_5Si_3
Ti_5Si_4	55.6 at.% Ti	tP36	$P4_12_12$	...	Si_4Zr_5
TiSi	50.0 at.% Si	oP8	$Pmm2$ or $Pmma$	...	SiTi
$TiSi_2$	66.7 at.% Si	oF24	$Fddd$	C54	$TiSi_2$

[a] – high temperature forms; [b] – stable at temperatures higher than 13°C

This work is also part of a series of studies on the phase diagrams of titanium with some low melting elements (Sn, Zn, Bi) [12–15] where the laboratory syntheses of Ti containing alloys are done using quartz (SiO_2) tubes. In this connection, the knowledge of eventual reactions between titanium and SiO_2 is of interest, in order to prevent such alloys from contamination during the syntheses. The thermodynamic possibility for such interactions is due to the large negative standard Gibbs energies of formation of titanium oxides [16, 17]. Thus, the pure titanium may act, as reducing agent, on the silicon dioxide, leading to changes of the specimens compositions. In the quartz tubes this reaction, usually, is slow due to kinetic reasons, but when SiO_2 is introduced in the bulk of an alloy the pertinent

chemical interactions would be easier to occur. The latter idea has been verified in this investigation and quartz pieces were used as source of Si.

2. Experimental

Pure (5N) bulk titanium (obtained by chemical vapor transport deposition), 4N Si lamellae and tin pellets (p.a.) have been used for the alloys syntheses. Pieces of titanium have been cut and boiled in alcohol + acetone mixture, just before being closed under vacuum ($10^{-5} - 10^{-6}$ Tore) in quartz tubes, containing weighted amounts of these elements. The chemical compositions of the successful specimens are represented in Table 2. The tubes have been gradually heated up to 1000°C during three days and gradually cooled to room temperature. After such a thermal treating, in many cases the titanium pieces stuck to quartz walls, making difficult to separate them even after breaking the tubes. Sometimes the tubes broke themselves during the cooling cycle. We observed that the reaction between the titanium and the tin, at relatively low temperatures (e.g. at about 500°C) is sluggish while the reaction at 600°C is much faster. This is in agreement with the hypothesis [18] that oxide barrier layers form on the titanium surfaces and dissolve at temperatures higher than around 500°C.

TABLE 2

Nominal chemical compositions of the initial mixtures. Specimens nos. 1–3 have been annealed at 600°C. Specimens 4–6 have been arc-melted and studied as cast. X_{Ti}, X_{Sn}, X_{Si} – mole fraction of the respective element, No – consecutive numbe of the specimens. The mass of specimens nos. 1–3 is approx. 2 g each. The mass of specimens nos. 4–6 is around 6 g each.

No.	X_{Ti}	X_{Sn}	X_{Si}
1	0.131	0.869	–
2	0.300	0.700	–
3	0.060	0.930	$\approx 0.01^{*}$
4	0.561	0.352	0.087
5	0.329	0.347	0.324
6	0.503	0.304	0.193

* – Assessed by the difference between the original mass of the sample and the mass after braking the tube (i.e. with the piece of quartz).

The ampoule No. 3 has been broken after the first heating-cooling cycle. Small quartz pieces, stuck to the alloy have been left, the specimen was grinded in agate mortar and re-sealed under vacuum.

Three alloys (nos. 4–6, Table 2) have been arc-melted under high vacuum argon atmosphere. The buttons have been turned over and re-melted. Thereafter these alloys have been studied as cast.

The chemical composition of the phases contained in the alloys synthesized by both methods were found by optical microscopy and electron microprobe analyses using wave disperse system (WDS) method.

3. Results and discussion

A silicon diffusion flux is generated, in such experimental conditions, from the SiO_2 piece to the bulk of the adjacent alloy. Theoretically, it might be controlled by a few factors as: the rate of the chemical reaction between the titanium and the SiO_2; the silicon and titanium diffusion mobilities into the alloy; the formation and growth kinetics of various phases. Considering the results in such cases, it is reasonable to apply the local equilibrium principle (largely used for diffusion couple studies of phase diagram [19]) as well as the conception of local nominal composition (or contact line path) developed by R ö n k ä et all. [20].

Concerning the oxygen flux (also generated by the reaction between the titanium and SiO_2) one can reasonably admit (taking into account the Ti-O phase diagram) that the oxygen ions (being in feeble quantity and much smaller atomic radius than these ones of the titanium and the silicon) form interstitial solid solutions with the solid phases as e.g. (α-Ti,O) and (β-Ti,O) [4].

TABLE 3

Summarized experimental data for the specimens annealed at 600°C, obtained by electron microprobe analyses, X_{IJ} – mole fraction of the pertinent element

No.	Phases	Note
1	(a) Liquid phase; (b) Ti_2Sn_3; (c) Ti_5Sn_3; (d) Ti_3Sn	(a) Around 0.01 at.% Ti; (b) $X_{Ti} = 0.398$, $X_{Sn} = 0.602$; (c) $X_{Ti} = 0.630$, $X_{Sn} = 0.370$; (d) $X_{Ti} = 0.765$, $X_{Sn} = 0.235$; Si has not been found in the specimen
2	(a) Liquid phase; (b) Ti_2Sn_3	(a) Around 0.01 at.% Ti; (b) $X_{Ti} = 0.404$, $X_{Sn} = 0.596$ Si has not been found in the specimen
3	(a) Liquid phase; (b) Ti_5Sn_3; (c) Ti_3Sn; (d) (α-Ti); (e) Ti_5Si_3; (f) SiO_2	(a) Around 0.01 at.% Ti; (b) $X_{Ti} = 0.575$, $X_{Sn} = 0.340$, $X_{Si} = 0.085$; (c) $X_{Ti} = 0.782$, $X_{Sn} = 0.218$; (d) $X_{Ti} = 0.947$, $X_{Sn} = 0.053$; (e) $X_{Ti} = 0.632$, $X_{Sn} = 0.368$; (f) $X_O = 0.662$, $X_{Sn} = 0.338$; Specimen annealed with SiO_2 into the ampoule.

The results obtained with the specimens annealed at 600°C are shown in Table 3. Silicon was not found in specimens nos. 1 and 2 (without quartz pieces into the alloys), while in specimen No. 3 an intermediate layer of Ti_5Si_3 has grown between the piece of SiO_2 and (α-Ti,Sn). Regions of Ti_3Sn are disposed (Fig. 1) between the titanium-tin solid solutions

(α-Ti,Sn) and the liquid phase, while the crystal (Ti_5Sn_3 with 8.5 at.% Si) is surrounded by molten Sn. Thus, the schematic representation of the sequence of phases between the two end members (SiO_2, respectively (Si)) and liquid tin (Liq (Sn)), as found experimentally, would be:

$$(Si)/Ti_5Si_3/(\alpha\text{-Ti}) / Ti_3Sn / Ti_5Sn_3/Liq\ (Sn). \quad (1)$$

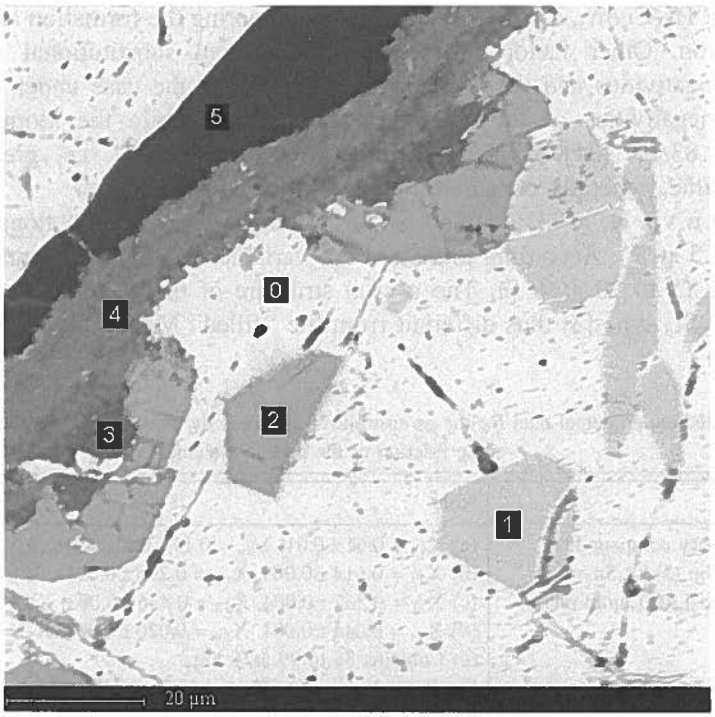

Fig. 1. Micrograph of specimen No3, annealed consecutively at 1000°C and at 600°C. The photo has been taken in secondary electrons. Phase fields: 0 – Sn-rich liquid phase; 1 – Ti_5Sn_3-crystal; 2 – Ti_3Sn; 3 – (αTi)-; 4 – Ti_5Si_3; 5 – SiO_2

The absence of some phases from the diffusion zone often happens and might be due to kinetic reasons [18], or simply to the instrumental technical restrictions.

We would like to notice that the tin content of the liquid phase for the alloys annealed at 600°C (Table 3) is much greater (around 99 at.% Sn) than it should be according to the equilibrium phase diagram [4, 5] (around 85.5 at.% Sn at 600°C). In the liquid phase of the alloys studied "as cast" the tin content is greater as well (more than 88 at.% Sn, Table 4) than the expected according to the phase diagram.

In sample No 2, two equilibrium phases – Ti_2Sn_3 and tin-rich liquid have been observed only. The phases' amounts estimated using the lever rule and accepting no Ti solubility in the liquid phase, are in agreement with the measurements done by quantitative metallographic analysis (i.e. around 75% Ti_2Sn_3 and 25% Liq). The titanium content of the liquid phase was

rather feeble and could not be measured exactly, although the system has reached equilibrium. This is another evidence that the liquidus line in this region might be steep.

In ternary systems where two isotypic binary compounds (in this case Ti_5Sn_3 and Ti_5Si_3, Table 1) exist one should consider two possibilities: formation of a continuous solution region, and on the other side - the hypothesis for the existence of a ternary compound between them. In the case considered in this work, the binary compounds may take up the third element to form the so-called "filled" Mn_5Si_3 hexagonal structure (e.g. Hf_5CuSn_3, Mo_5Si_3C) [10, 11] thus favoring the formation of a continuous solution region. Other factors influencing the mutual substitutional solubility are the electro negativities and the atomic radii (r) ratio. In the case under consideration, the electro negativities of the Si and Sn are equal, while the atomic radii ratio is $r_{Si}/r_{Sn} \approx 83.7\%$ [21]. Thus, a difference of around 16%, i.e. greater than the admissible value, generally considered being around 15%, is found.

B u l a n o v a et. al [3] claimed finding a ternary compound "along the titanium content of 62.5 at.%". According to them it has variable Sn and Si contents: 17.5 to 22.5 at.% Sn, and 15 to 20 at.% Si. The crystal structure of the Ti-Sn-Si ternary phase is tetragonal W_5Si_3-type [3] thus different from the "filled" Mn_5Si_3 hexagonal structure.

TABLE 4

Summarized experimental data for the as cast alloys, obtained by electron microprobe analyses. X_{IJ} – mole fraction of the pertinent element

No.	Phases	Note
4	(a) Ternary compound; (b) Ti_2Sn; (c) Ti_6Sn_5; (d) Ti_5Si_3; (e) Liquid phase	(a) $X_{Ti} = 0.61 \pm 0.01$, $X_{Sn} = 0.17 \pm 0.01$, $X_{Si} = 0.22 \pm 0.01$; (b) $X_{Ti} = 0.614 \pm 0.004$, $X_{Sn} = 0.296 \pm 0.003$, $X_{Si} = 0.089 \pm 0.001$; (c) $X_{Ti} = 0.562 \pm 0.004$, $X_{Sn} = 0.436 \pm 0.003$, $X_{Si} = 0.334 \pm 0.001$; (d) $X_{Ti} = 0.646 \pm 0.001$, $X_{Sn} = 0.020 \pm 0.001$, $X_{Si} = 0.334 \pm 0.001$; (e) Contains 88 to 99 at.% Sn; Small amounts of (α-Ti) and (Si) are observed as well. Primary phase is Ti_5Si_3.
5	(a) Ti_5Sn_4; (b) Ti_5Si_3; (c) (Si); (d) Liquid phase	(a) $X_{Ti} = 0.54 \pm 0.02$, $X_{Sn} = 0.05 \pm 0.02$, $X_{Si} = 0.41 \pm 0.01$; (b) $X_{Ti} = 0.645 \pm 0.001$, $X_{Sn} = 0.009 \pm 0.002$, $X_{Si} = 0.346 \pm 0.001$; Inclusions of unidentified tiny particles and (α-Ti) are observed.
6	(a) Ti_5Sn_4; (b) Ti_5Si_3; (c) TiSi; (d) Ti_5Si_3; (e) Ti_3Sn (f) Liquid phase	(a) $X_{Ti} = 0.577 \pm 0.001$, $X_{Sn} = 0.004 \pm 0.001$, $X_{Si} = 0.419 \pm 0.002$; (b) $X_{Ti} = 0.645 \pm 0.001$, $X_{Sn} = 0.009 \pm 0.002$, $X_{Si} = 0.346 \pm 0.001$; (c) $X_{Ti} = 0.523$, $X_{Sn} = 0.0$, $X_{Si} = 0.477$; (d) $X_{Ti} = 0.606 \pm 0.001$, $X_{Sn} = 0.391 \pm 0.001$, $X_{Si} = 0.003 \pm 0.001$; (e) $X_{Ti} = 0.780 \pm 0.001$, $X_{Sn} = 0.215 \pm 0.002$, $X_{Si} = 0.005 \pm 0.002$; Primary phase is Ti_5Si_3.

In the work we have found a ternary phase slightly displaced from the above cited titanium content (Table 4). According to us its approximate formula is Ti_3SnSi. The experimental data indicate that the contents of the components may vary as follows: 60 to 63 at.% Ti, 17 to 23 at.% Sn, 15 to 23 at.% Si. It is interesting to report that, recently, we have found another ternary compound with analogous formula (Ti_3SnBi) in the Ti-Sn-Bi system [12, 13].

In Fig. 2 the micrograph of a section of specimen No 4 is represented. The dark-black areas belong to Ti_5Si_3 (primary crystallizing phase), the black – to the hypothetic ternary compound (with approximate formula as found by the authors $Ti_{6.1}Si_{2.2}Sn_{1.7}$), the dark-gray – to Ti_2Sn, the gray areas – to Ti_6Sn_5 and the white – to the tin-rich iquid.

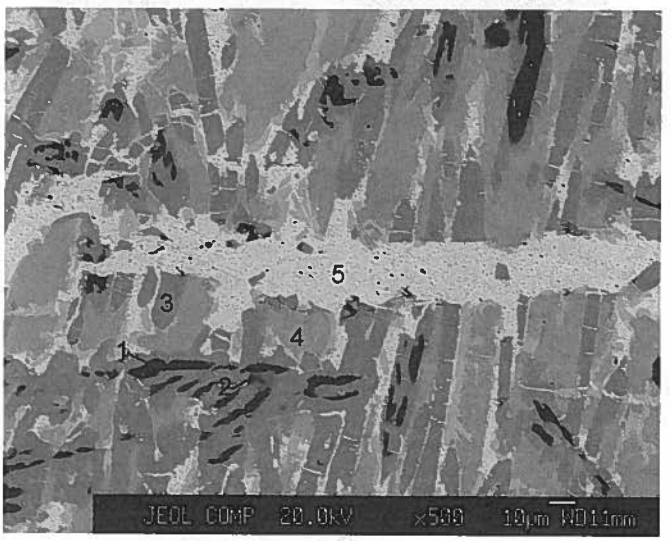

Fig. 2. Micrograph of specimen No 4, "as cast". The photo has been taken in secondary electrons. The dark-black areas (1) belong to Ti_5Si_3, the black (2) – to a ternary phase ((~Ti_3SnSi), the dark-gray (3) – Ti_2Sn, the gray areas (4) – to Ti_6Sn_5 and the white (5) – to the tin-rich liquid phase

Fig. 3. Micrograph of specimen No 5, "as cast". The photo has been taken in secondary electrons. The black crystals are of Ti_5Si_3 and Ti_5Si_4. The light matrix is tin rich. The composition of the tiny crystals could not be measured

In Figs. 3 and 4 micrographs of specimen No. 5 and 6 are shown. In each of the "as cast" alloys Ti_5Si_3 was found to be the primary crystallized phase,

usually in close contact with Ti_5Si_4. The congruent melting Ti_3Sn and Ti_6Sn_5 binary Ti-Sn phases appear regularly as well.

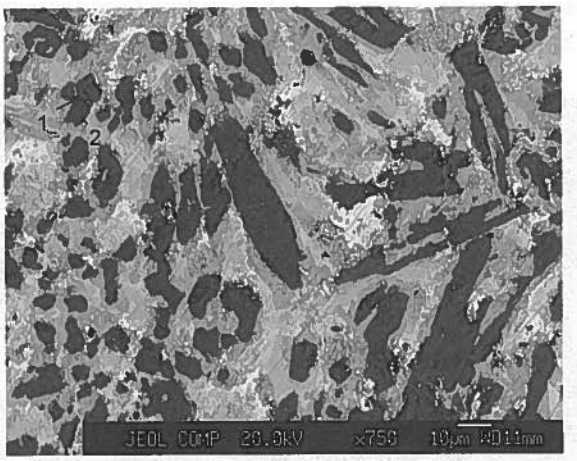

Fig. 4. Micrograph of specimen No 6, "as cast". The photo has been taken in secondary electrons. The black areas (1) are of Ti_5Si_3 and the neighboring dark areas (2) are of Ti_5Si_4. The light areas are tin-rich. The areas with intermediate nuances belong to TiSi, Ti_6Sn_5 and Ti_3Sn phases

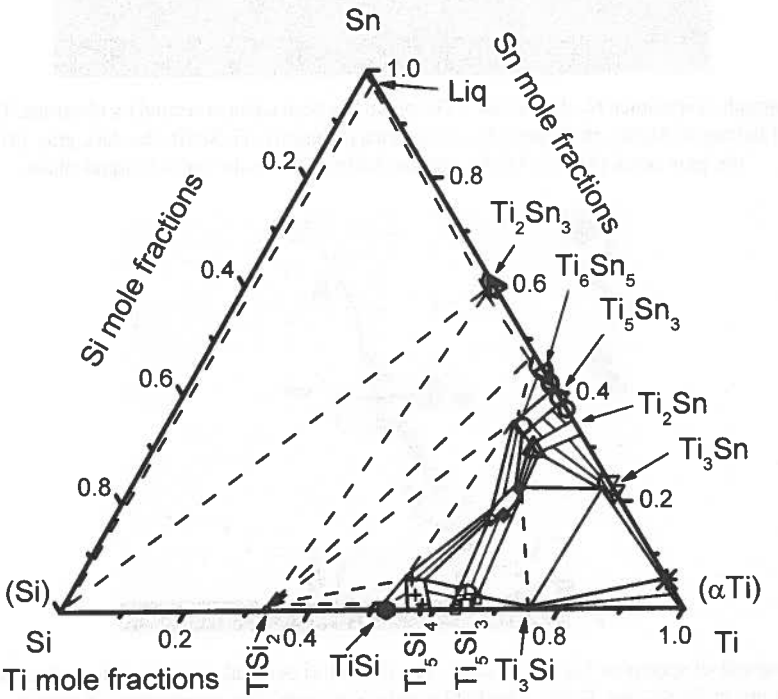

Fig. 5. Isothermal section of the Ti-Sn-Si phase diagram at 600°C. Experimental data about the phase boundaries: ternary compound (~Ti_3SnSi) – this work – ◊ and Bulanova et al. [3] – ◆; Ti_5Si_3 – □; Ti_5Si_4 – +; TiSi – ●; (α-Ti) – ✳; Ti_3Sn – ▽; Ti_2Sn – △; Ti_5Sn_3 – O; Ti_6Sn_5 – ◁; Ti_2Sn_3 – ▷. The thick solid lines show the phase boundaries, while the thin solid lines symbolize the tie-lines in the two-phase areas. The dash lines indicate the phase boundaries that are the most recommendable for further studies

4. Conclusion

The results show that a non-stoichiometric ternary compound corresponding approximately to the formula Ti_3SnSi exists in the Ti-Sn-Si system. Information concerning the mutual solubility of tin and silicon in the ternary extensions of their binary compounds with titanium have been acquired. Data about the homogeneity ranges of the solid phases have been obtained as well.

An isothermal section of the Ti-Sn-Si phase diagram, at 600°C, based on the present work has been constructed.

Acknowledgments

This work is related with the European Concerted Action COST531.

REFERENCES

[1] C.R.F. Azevedo, H.M. Flower **26** (3), 353 (2002).
[2] M. Bulanova, A. Soroka, P. Zheltov, V. Vereshchaka, K. Meleshevich, Z. Metallkd. **90** (7), 505 (1999).
[3] M. Bulanova, L. Tretyachenko, K. Meleshevich, V. Saltykov, V. Vereshchaka, O. Galadzhyl, L. Kulak, S. Firstov, JALCOM **350**, 164 (2003).
[4] T. Massalski, CD ROM: Binary Alloy Phase Diagrams, ASM International, OH, USA, 1996.
[5] C. Kuper, W. Peng, A. Pisch, F. Goesmann, R. Schmid-Fetzer, Z. Metallkd. **89** (12), 855 (1998).
[6] H. King, Bull. Alloy Phase Diagr. **2**, 401 (1981).
[7] P. Rogl, Titanium : Physico-chemical Properties of its compounds and Alloys, IAEA, Vienna,1983.
[8] P. Villars, L. Calvert, Pearson's Handbook of Crystallographic Data for Intermetallic Phases, ASM, Metals Park, Ohio, 1985.
[9] B. Künnen, W. Jeitschko, G. Kotzyba, B. Mosel, Z. Naturforsch. **55b**, 425 (2000).
[10] W. Jeitschko, Metallurgical Transactions **1** (11), 3159 (1970).
[11] J. Kaiser, M. Haase, W. Jeitschko, Z. Anorg. Allg. Chem. **627**, 2369 (2001).
[12] G.P. Vassilev, JALCOM **365** (1-2), 164 (2004).
[13] G.P. Vassilev, K. Ishida, JALCOM 376 (1-2), 125 (2004).
[14] G.P. Vassilev, X.J. Liu, K. Ishida, JALCOM **375** (1-2), 162 (2004).
[15] G.P. Vassilev, Cryst. Reas. Techn. **39** (9), 763 (2004).
[16] R. Swalin, Thermodynamics of Solids, John Wiley &Sons, N.Y.-London, 1961.
[17] I. Barin, Thermochemical Data of Pure Substances, VCH Verlags, Weinheim, 1993.
[18] Materials Properties Handbook: Titanium Alloys, ASM International, 1994.
[19] A. Kodentsov, G. Bastin, F.J.J. van Loo, JALCOM **320**, 207 (2001).
[20] K. Rönkä, F. van Loo, J. Kivilahti, Scripta Materialia **37**, 1575 (1997).
[21] Chemicool periodic table, http://www-tech.mit.edu/Chemicool/index.html.

Received: 15 June 2004.

A R C H I V E S O F M E T A L L U R G Y A N D M A T E R I A L S
Volume 49 2004 Issue 3

C. GUMIŃSKI *, H.U. BORGSTEDT**

REGULARITIES AND PECULIARITIES OF THE LITHIUM BINARY PHASE DIAGRAMS

PRAWIDŁOWOŚCI I OSOBLIWOŚCI DIAGRAMÓW FAZOWYCH BINARNYCH STOPÓW LITU

This presentation is an actualized extract from the monograph devoted to the critical evaluations of solubility data of elements in liquid alkali metals. Preparation of these assessments required the permanent confrontation of the solubility results with the respective phase diagrams. The binary phase diagrams of lithium in up-dated forms are sketched integrally showing changes within periods and groups of the periodic table of elements. Peculiarities of selected diagrams are shortly commented.
Keywords: lithium binary phase diagrams, solubility of elements in liquid lithium.

Niniejsza prezentacja stanowi zaktualizowany wyciąg z monografii poświęconej krytycznej ocenie danych rozpuszczalności pierwiastków w ciekłych metalach alkalicznych. Rzeczowa ocena rezultatów eksperymentalnych rozpuszczalności wymagała bowiem ciągłej konfrontacji z odpowiednimi diagramami fazowymi. Przedstawiono komplet diagramów w zaktualizowanej formie dla binarnych stopów litu, który ukazuje ewolucję zmian w okresach i grupach układu okresowego pierwiastków. Skomentowano osobliwości wybranych diagramów.

1. Introduction

Due to its special properties, lithium (Li) seems to play significant role in the future technology of energy production and conversion (fusion reactors, space technology, high energy batteries), extractive metallurgy as well as an additive in the light constructional materials. Thus the knowledge of the Li binary phase diagrams is in a permanent demand and should be supplemented.

Because many regularities of these diagrams may be easily seen in Figs. 1–3, we will rather concentrate on peculiarities. This presentation is based on numerous papers which were abstracted in [1]. The remaining diagrams and those needing corrections and

* DEPARTMENT OF CHEMISTRY, UNIVERSITY OF WARSAW, 02-093 WARSZAWA, PASTEURA 1, POLAND
** ALBERT-SCHWEITZER STR. 33, 76139 KARLSRUHE, GERMANY

supplements are quoted from the solubility monograph [2]. Some informations contained in recent reports are also included. The dashed lines in the figures reflect situations where either investigations furnished uncertain results or boundary lines were predicted according to the well-known rules of phase diagram construction.

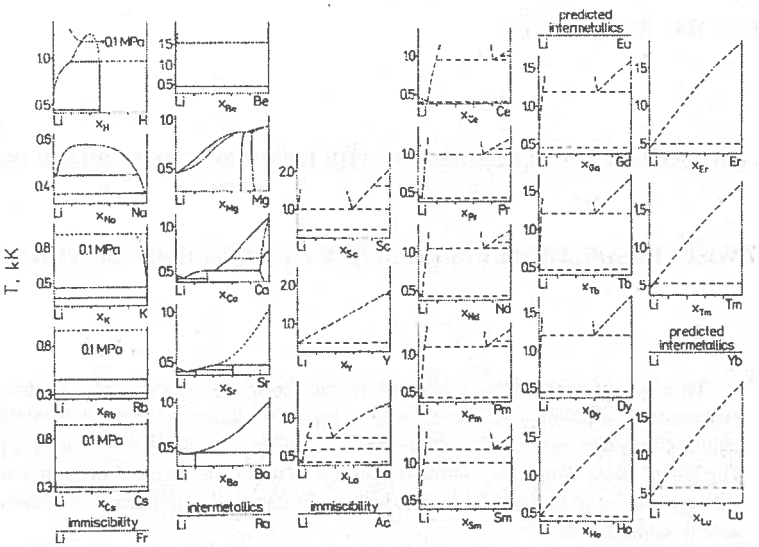

Fig. 1. Binary phase diagrams of Li with alkali, alkaline earth and lanthanide metals

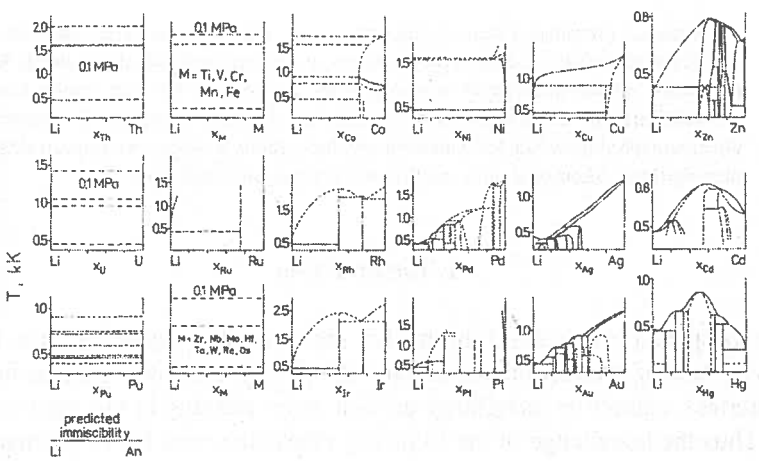

Fig. 2. Binary phase diagrams of Li with actinide and transition metals

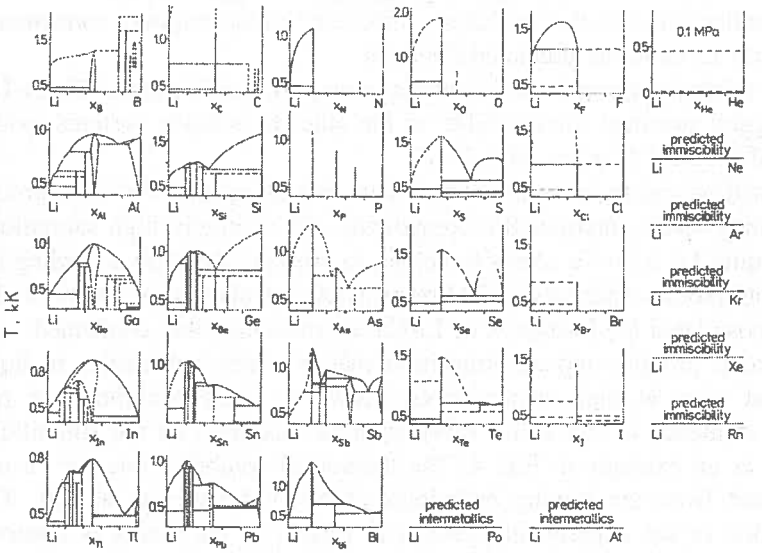

Fig. 3. Binary phase diagrams of Li with p electron elements

2. Comments

According to the recent suggestion of the IUPAC, hydrogen does not belong to any group of the first period [3]. In fact the Li-H phase diagram reminds more those of the Li-halogen systems than of the Li-alkali metals; see Figs. 1 and 3 for comparison. A tendency to immiscibility of the heavier alkali metals with Li increases from Na to Cs. However, the binary combinations with metals of the next group demonstrate a reverse tendency. Moreover, Ca, Sr and Ba form relatively stable intermetallics with Li. Authors of this paper confirm the reservations of Pelton and Bale to the Wang's identification of Sr-rich compounds at high temperatures; it seems that traces of H or N could stabilize such phases [4].

Alloys of lanthanides (Ln) with Li were superficially investigated by G a n i e v et al. [5]. Usually, 1:1 alloy compositions were examined by thermal analysis with the high heating/cooling rates of 20–80 K/min; the rest of the diagram details were predicted. The typical allotropic transformations of Ln were not observed; those in Fig. 1 are added here. The resulting diagrams display a relatively good or almost ideal miscibility of Ln with Li. It is in a contrast with qualitative reports of P a v l y u k et al. [6] pointing on immiscibility in the Li-Ce and Li-Gd systems at 470 K. In case of the Li-Y system, the determined solubility of Y in liquid Li is not higher than 01 at.% at 1223 K [7] what is in complete disagreement with the diagram proposed by [5]. Since all Ln (with exception of divalent Eu and Yb) possess quite similar features, our fundamental reservation to the Li-Y phase diagram extends over the remaining Li-Ln diagrams. Alloying properties of Eu and Yb are

generally similar to the alkali earth metals therefore similar shapes of corresponding phase diagrams with Li could be predicted for them.

The low solubilities measured and the diagrams published for the Li-Th, Li-U and Li-Pu systems suggest practical immiscibility in the other Li-actinide systems (with probable exception of divalent No); see Fig. 2.

The transition metals may be devided into two categories. The first group contains metals forming stable intermetallic compounds and relatively high saturation concentrations in liquid Li. Also Cu seems to belong to this class because according to the most recent potentiometric experiments and first principle calculations of Van de Valle et al. [8], the earlier postulated [2] formation of Li-Cu intermetallics was confirmed.

The second group comprises transition metals which solubilities in liquid Li are very limited even at high temperatures. However, such equilibria are not simple. Significant influence of impurities (even in trace amounts) on the solubilities may be easily seen as an example in Fig. 4. The theoretical solubility line for Fe in liquid Li was predicted from the mixing enthalpies of M i e d e m a et al. [9]. The highest overestimation of the experimental results in respect to the theory is observed for the oldest works and the best agreement for the data obtained with the use of specially purified metals. A controlled addition of C, H, N and O to the Li-Fe system was carefully investigated and it was evidently found that N has the most crucial influence on the Fe solubility [2]. A detailed analysis of many other systems [2] showed that the non-metallic elements may influence the solubility equilibria by the formation of binary oxides, nitrides, carbides, hydrides and various ternary compounds (for example: Ce_2N_2O, Li_2CeN_2, Th_2N_2O, Li_5TiN_3, Li_7TaN_4, Li_3MoN_3, Li_7MnN_4, Li_3FeN_2). These compounds are generally better soluble for several orders of magnitude than the pure transition metals in liquid Li and this explains the discrepancies of the solubility results shown exemplarily in Fig. 4.

The majority phase diagrams of Li with p electron elements show distinct similarities within the groups. The most stable intermetallic formula for the alloys of Al group is 1:1 but for the groups of Si, N, O and F the most stable compound composition corresponds to the most typical valency of these elements: ~4, 3, 2 and 1, respectively.

There are, however, special cases that demand short comments. It was found in the Li-B system, elaborated recently on a basis of many divergent papers [10], that B unusually melts at ~573 K upon addition of Li and forms a metastable colloidal solution in which B_{12} icosahedrons are solvated by 4 Li atoms. Further heating of the melt leads to an irreversible formation of $LiB_{08-1.0}$. The stable B-rich compounds are formed effectively only at high temperatures.

Li is reversibly able to enter between graphite layers resulting in the formation of a series of intercalate compounds: LiC_6, LiC_{12}, LiC_{18}, LiC_{24}. However over ~723 K the intercalates are irretrievably decomposed with a subsequent Li_2C_2 formation. Therefore a division of the Li-C diagram for independent parts of the intercalate and the carbide regions seems to be rational [11].

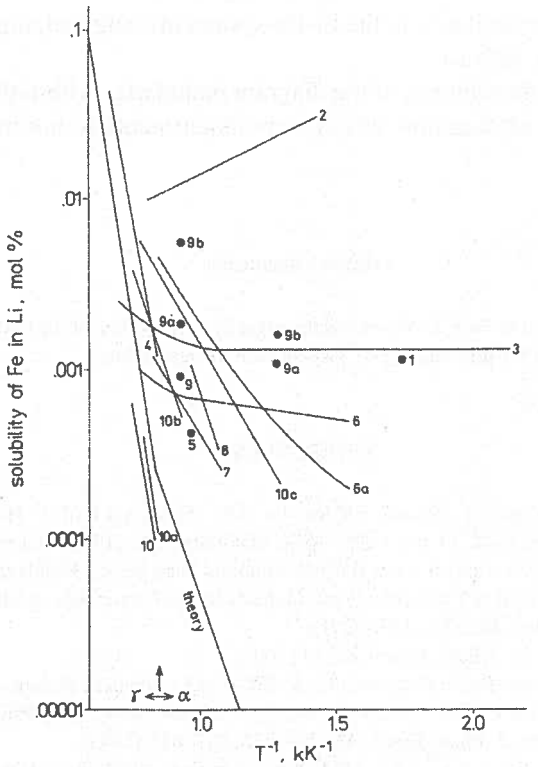

Fig. 4. Dependence of solubility data of Fe in liquid Li on reciprocal temperature. The points and lines represent mean experimental values obtained in the following papers: 1 – W.D. Wilkinson, F.L. Yaggee, U.S. Atom. Ener. Comm. Rep. ANL-4990 (1950); 2 – D.S. Jesseman et al., U.S. Atom. Ener. Comm. Rep. NEPA-1465 (1950); 3 – J.J. Sand, U.S. Air Force Rep. OMCC-HEF-166 (1958); 4 – Yu.F. Bychkov et al., Atom. Energiya, **7**, 531 (1959); B. Minushkin, H. Steinmetz, U.S. Naval Res. Rep. NDA-2118-1 (1960); 6 – N.M. Beskorovainyi, E.I. Yakovlev, Metall. Metalloved. Chist. Met., **2**, 189 (1960); 7 – H.W. Leavenworth, U.S. Atom. Ener. Comm. Rep. PWAC-356 (1961); 8 – B. Minushkin, U.S. Naval Res. Rep. NDA-2141-1 (1961); 9, 9a, 9b – G.A. Plekhanov et al., Atom. Energiya, **45**, 143 (1978); 10, 10a, 10b, 10c – N.M. Beskorovainyi et al., Metall. Metalloved. Chist. Met., **14**, 135 (1980). Specified concentrations of N in Li: 2 – <0.01, 3 – 0.03, 5 – 0.005, 7 – 0.0045, 8 – 0.005, 9 – ~0.005, 9a – 0.25, 9b – 0.50, 10 – <0.0005, 10a – 0.025, 10b – 0.055, 10c – 0.244 at.% N.

The experimental liquidus line in the Li-rich part of the Li-Sb system determined by Fedorov [12] looks very improbable when one compares it to the analogous parts of the Li-N and Li-Bi systems. The very recent calculations of this diagram by Kaufman [13] confirm our reservation.

Due to the ionic character of compounds formed by Li with the elements of group of O and F, distinct tendencies to immiscibility in these systems are observed. Untypically in comparison to the heavier alkali metals, no formation of Li polysulfides, polytellurides and polyiodides is observed.

It is expected that, by similarity to the Li-He system investigated, the other noble gases are also hardly miscible with Li.

Taking into account the changes of the diagram boundaries within the groups one may project probable shapes of diagrams which were experimentally not investigated (Li-Fr, Li-Ra, Li-Po, Li-At).

Acknowledgements

The authors are greatly indebted to Prof. Z. Moser and the organizing commitee of the CALPHAD XXXIII (May 30 – June 4, Kraków, Poland) for a possibility of presentation of this report.

REFERENCES

[1] Binary Alloy Phase Diagrams, Second Edition by T.B. Massalski, H. Okamoto, P.R. Subramanian and L. Kacprzak, ASM, Materials Park, (1990) and references therein.
[2] H.U. Borgstedt, C. Guminski, IUPAC Solubility Data Series, Metals in Liquid Alkali Metals (Be-Os) **63**, (Co-Bi) **64**, Oxford University Press, Oxford (1996); Non-metals in Liquid Alkali Metals **75**, J. Phys. Chem. Refer. Data **30**, 835-1159 (2001).
[3] H. Kaesz, P. Atkins, Chem. Intern. **25**, 14 (2003).
[4] C. Guminski, J. Phase Equil. Diffusion **25**, 5 (2004) and references therein.
[5] I.N. Ganiev, Kh.M. Nazarov, M.D. Badalov, Metally, no 4, 163 (1996) and no 6, 109 (1998); abstracted by H. Okamoto, J. Phase Equil., **18**, 486–488, 673–675 (1997).
[6] V.V. Pavlyuk, V.K. Pecharskii, O.I. Bodak, Dop. Akad. Nauk Ukrain. RSR, Ser. B **2**, 50 (1989); Metally 2, 211 (1993).
[7] I.N. Lyublinskii, Prana Center, Moscow; private communication (2004).
[8] A. Van de Valle, Z. Moser, W. Gąsior, communicated on CALPHAD XXXIII Conference, May 30 – June 4, 2004, Kraków, Poland.
[9] A.K. Niessen, F.R. de Boer, R. Boom, P.F. de Chatel, W.C.M. Mattens, A.R. Miedema, CALPHAD **7**, 51 (1981).
[10] C. Guminski, J. Phase Equil. **24**, 572 (2003).
[11] C. Guminski, Polska Metallurgia 1998-2002, Komitet Metalurgii PAN, Kraków, 107-112 (2002).
[12] P.I. Fedorov, Zh. Neorg. Khim., **40**, 844 (1995); abstracted by H. Okamoto, J. Phase Equil., **17**, 271 (1997).
[13] L. Kaufman, communicated on CALPHAD XXXIII Conference, May 30 – June 4, 2004, Kraków, Poland.

Received: 15 June 2004.

A R C H I V E S O F M E T A L L U R G Y A N D M A T E R I A L S
Volume 49 2004 Issue 3

A. VAN DE WALLE *, Z. MOSER**, W. GĄSIOR**

FIRST-PRINCIPLES CALCULATION OF THE Cu-Li PHASE DIAGRAM

WYZNACZENIE WYKRESU RÓWNOWAGI UKŁADU Cu-Li METODĄ OBLICZEŃ AB INITIO

We present first-principles calculations of the solid-state portion of the Cu-Li phase diagram based on the cluster expansion formalism coupled with the use of (i) bond length-dependent transferable force constants and lattice dynamics calculations to model of vibrational disorder and (ii) lattice gas Monte Carlo simulations to model configurational disorder. These calculations help settle the existence of additional phases in the Cu-Li phase diagram that have been postulated, but not yet clearly established. Our calculations predict the presence of at least one additional phase and the associated predicted phase transitions are consistent with our electrochemical measurements, which exhibit clear plateaus in the electromotive force-composition curve.

Prezentujemy obliczenia *ab initio* wykresu równowagi fazy stałej układu Cu-Li. Obliczenia opierają się na formalizmie Cluster Expansion (CE) realizowanym przy : (i) zastosowaniu stałych siłowych zależnych od długości wiązania oraz obliczeń dynamiki sieci do modelowania wibracyjnego stanu nieuporządkowania : (ii) zastosowaniu symulacji Monte Carlo gazu sieciowego do modelowania stanu nieuporządkowania konfiguracyjnego. Obliczenia te umożliwiły wykazanie dodatkowych faz w układzie równowagi układu Cu-Li, które były wcześniej postulowane, lecz nie potwierdzone. Nasze obliczenia przewidują obecność co najmniej jednej dodatkowej fazy, a postulowane przejścia fazowe są zgodne z naszymi badaniami elektrochemicznymi, które wykazały wyraźne załamania w zależnościach sił elektromotorycznych względem stężenia.

1. Introduction

In 1976, S m i t h and M o s e r [1] published the thermodynamic assessments of binary lithium alloys using information from the literature, followed by experimental investigations by galvanic cells initiated at the Institute of Metallurgy and Materials

* MATERIALS SCIENCE AND ENGINEERING DEPARTMENT, NORTHWESTERN UNIVERSITY EVANSTON, IL. USA
** INSTITUTE OF METALLURGY AND MATERIALS SCIENCE, POLISH ACADEMY OF SCIENCE, 30-059 KRAKÓW, REYMONTA STREET 25, POLAND

Sciences in Kraków in 1981 in cooperation with the University of Saarland in Germany. The following binary systems were studied: Li-Sn [2], Al-Li [3], Li-Zn [4], Li-In [5], Li-Zn [6],Li-Tl [7], Li-Bi [8], Li-Sn [9],Li-Mg [10] and Li-Pb [11]. These studies were extended later to ternary Al-Li-Mg alloys including calorimetric measurements in cooperation with the Max Planck Institute in Stuttgart [12] and to phase diagram calculations of Al-Li-Mg [13] and on Al-Li-Cu [14] systems. In 1998 [14] during the *Thermodynamics of Alloys Conference*, thermodynamic studies of solid Cu-Li alloys from electromotive force (emf) measurements were presented that suggested the existence of intermetallic phases.

Previous phase diagram assessments of P e l t o n [15] and of S a u n d e r s [16] do not indicate the existence of intermetallic phases. In 1996, B o r g s t e d t and G u m i ń s k i [17] performed a critical evaluation of previous phase diagram assessments. They indicated that the only experimental thermodynamic data of enthalpies of mixing [18] of liquid alloys based on Cu exhibiting slight exothermic effect (-1.1 kJ/mol) suggests negative deviations from ideal behavior. In addition, taking into account results of K r a u s et al. [19] and O l d et al. [20] who suggested the formation of Cu_4Li phase, probably formed at the temperature 473–873 K, B o r g s t e d t and G u m i ń s k i [17] introduced this phase into a schematic phase diagram of the Cu-Li system based on P e l t o n's [15] assessment. It should be noted that estimates of enthalpy of mixing by M i e d e m a et al. [21] yield a much more exothermic effect for the Cu-Li system amounting to −39 kJ/mol.

In this article, we employ first-principles calculations in conjunction with electrochemical measurements to investigate the presence of intermetallic phases in the Cu-Li system. Our findings suggest that the only stable ordered compound above room temperature is the B32 phase at 50 at % Li, which undergoes a second order phase transition into a bcc solid solution around 900 K – 1200 K. Our results also indicate that the previously suggested Cu_4Li phase is probably a Cu-rich bcc solid solution.

2. Methodology

2.1 Computational

All thermodynamics calculations were performed with the Alloy Theoretic Automated Toolkit (ATAT) [22–24] using, as an input, first-principles total energy calculations obtained with the Vienna Ab initio Simulation Package (VASP) [25–26] within the Local Density Approximation (LDA). The energetics of the bcc and fcc phases of the alloy were modeled using the cluster expansion formalism [27–32], in which the configurational dependence of the alloy's energy is represented as a polynomial function of spin-like occupation variables taking the value +1 or −1, depending on the chemical species residing on a given lattice site. The coefficients of this polynomial, called the Effective Custer Interactions (ECI), are determined by a least-squares fit to the energies calculated from first-principles.

An automated algorithm, described in [23], was used to select of the optimal number of terms in the cluster expansion as well as to select the structural energies to be included in the fit.

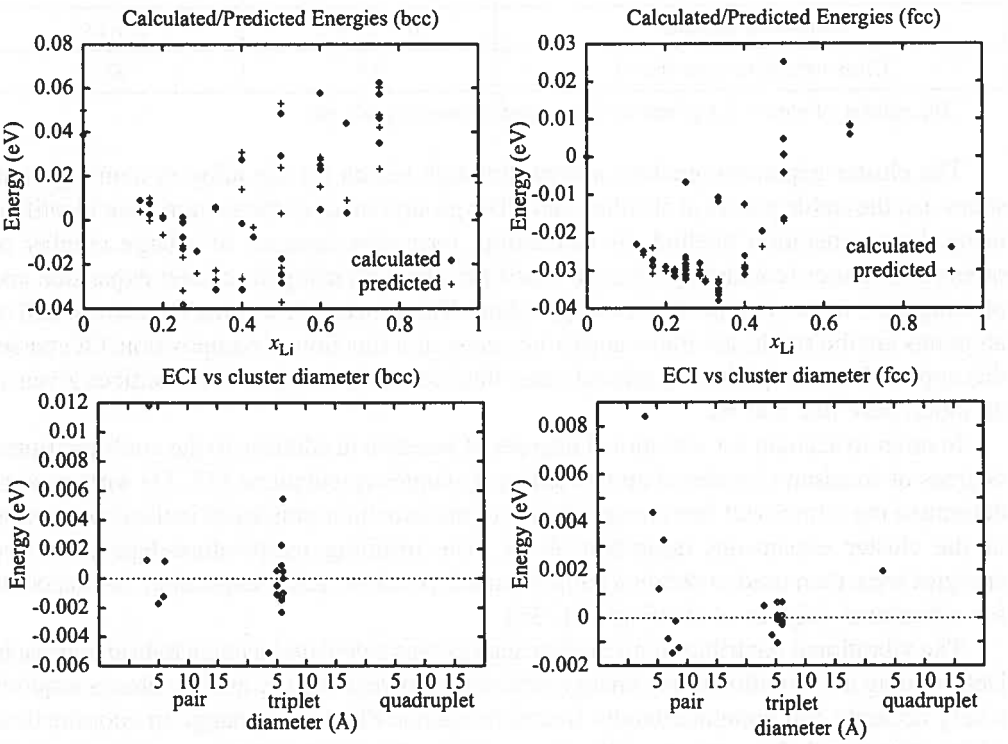

Fig. 1. Database of first-principles energies (top) used to determine the ECI (botom)

Figure 1 depicts the database of structural energies, plotted as a function of composition, (top) that were used to obtain the ECI (bottom). The characteristics of the resulting cluster expansions used are summarized in Table. While the accuracy of the fit, as measured by the crossvalidation score [23], is quite good for the fcc lattice, the cluster expansion for the bcc lattice appears somewhat less accurate. However, inspection of the residuals of the least-squares fit reveals that most of the prediction error is concentrated in the region 50 at% $< x_{Li} <$ 95 at%, in the unstable portion of the miscibility gap of the bcc phase. The prediction error in the concentration range where the bcc phase is stable is only about 15 meV. These "statistical" errors dominate the numerical precision of the first-principles calculations used as an input, which is of the order of a few meV. This accuracy was obtained by using the "high" precision setting of the VASP code and a k-point mesh consisting of no less than 2000 points in the reciprocal cell of the fcc or bcc primitive unit cell.

TABLE

Characteristics of the cluster expansion used

Lattice	fcc	bcc
Number of structures	41	35
Number of clusters*	8 + 12 + 1	5 + 13
Cross-validation score (meV)	3.9	33

* The number of cluster is reported as the number of pairs, triplets, etc.

The cluster expansion enables a very thorough search for the alloy system's ground states, i.e. the stable phases at absolute zero. The ground states of the system were identified using the enumeration method, by calculating formation energies of a large number of ordered structures (containing up to 10 atoms per unit cell) using the cluster expansion and plotting them in the (composition, energy) plane. The structures touching the convex hull of all points are the stable structures at absolute zero, as a function of composition. Of course, this approach can only identify ground states that are superstructures of the lattices given as an input, here bcc and fcc.

In order to account for vibrational degrees of freedom in addition to the configurational degrees of freedom considered above, lattice dynamics calculations [33, 34] were used to determine the vibrational free energy of each of the structures employed in the construction of the cluster expansions described above. The resulting temperature-dependent free energies were then used to obtain a temperature-dependent cluster expansion that accounts for vibrational degrees of freedom [34, 35].

The vibrational contribution to the free energy was calculated using a hybrid approach. Determining the vibrational free energy difference between the bcc and fcc phases requires a very accurate and computationally intensive method due to the change in coordination, while vibrational free energy differences within the same lattice can be accurately calculated using a simplified method. In light of this observation, the vibrational free energy of pure Li and pure Cu in both the bcc and fcc crystal structures were obtained by constructing a 4^{th} nearest neighbor volume-dependent Born-von Kármán spring model [33, 34]. To this effect, the reaction forces induced by small imposed displacements (0.2 Å) were calculated from first-principles and were used to determine the values of all the spring constant tensors via a least-squares fit. The same analysis was carried out after applying isotropic strains of 1, 2, and 3% in order to determine the volume dependence of the spring constants, thus permitting the use of the quasi-harmonic approximation [34], which provides free energies that properly account for thermal expansion.

The determination of vibrational free energy differences within the same lattice relies a simplified model based on Length-Dependent Transferable Force Constant (LDTFC) [34, 36]. The basic idea is to rely on the observation that bond length is a good predictor of bond stiffness (for a given lattice and a given type of chemical bond). The bond length-bond stiffness relationship can be determined by calculating, from first-principles, the stretching and bending force constants in a few ordered compounds as a function of volume (see Figure 2). Once this relationship is known, the force constants needed for the calculation of

the vibrational free energy of a given structure can be predicted solely from the knowledge of its relaxed geometry (which provides the bond lengths).

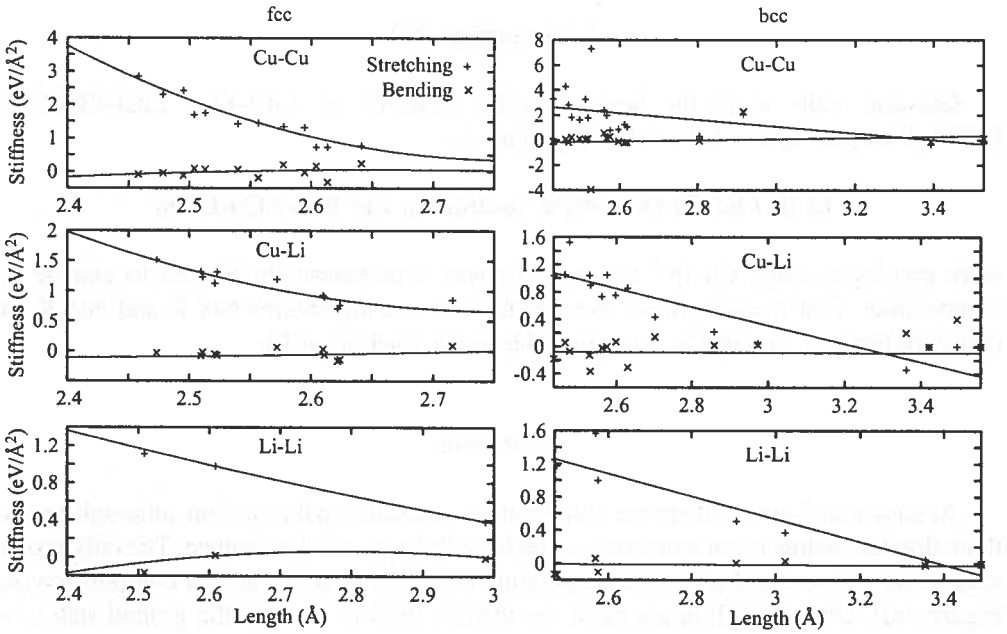

Fig. 2. Determination of the Lenght-Dependent Force Constants

Finite temperature thermodynamic properties accounting for both configurational and vibrational degrees of freedom were obtained using lattice gas Monte Carlo simulations [37, 38] within a grand canonical ensemble, where the alloy's energetics are described by the temperature-dependent cluster expansion constructed above. Free energies were calculated via thermodynamic integration using either internal energy or composition (appropriately scaled by a function of temperature) as the integrand and a low temperature expansion of the free energy was used as the initial conditions for the integration procedure [24]. The temperature-composition phase boundaries associated with first-order transition were located using the standard common tangent construction while the location of the second-order transitions were determined by tracking a peak in the heat capacity.

Since modeling the liquid phase from first-principles is difficult, we simply used the experimentally determined free energy available in the COST light metal database [16]. To ensure that the reference states used in the database and in our calculations are compatible, the free energy of the liquid $G_L(x)$ at a composition of x at % Li was corrected as follows:

$$G_L(x) = G_{L,ex}(x) - (1 - x)\, G_{Cu,fcc,ex} - x\, G_{Li,bcc,ex} + (1 - x)\, G_{Cu,fcc,fp} + x\, G_{Li,bcc,fp},$$

where the experimental and the first-principles values are denoted by the subscripts "ex" and "fp", respectively.

2.2 Experimental

Galvanic cells using the liquid eutectic mixtures of: LiCl-KCl, LiCl-KCl-CsCl, LiCl-LiF or pure LiCl of the following scheme:

Li (l) / liquid electrolyte containing Li+ ions / Cu-Li (s)

were employed using Cu foil to which Li was coulometrically titrated to change the composition. Emf measurements were performed at temperatures 648 K and 885 K and concentrations of Li slightly exceeding 0.6 molar fraction of Li.

3. Results

As shown in Figure 3, there are numerous ground states in this system, although most of them disorder below room temperature and have little practical relevance. The only ground state remaining stable above room temperature is the B32 structure at 50% composition (see Figure 4a)). Due to the limitations of the method used to identify the ground states, we cannot rule out the existence of ordered phases based on other lattices than bcc and fcc.

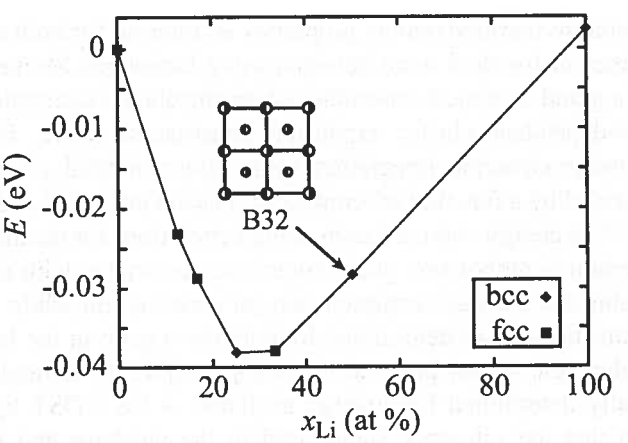

Fig. 3. Ground states of the Cu-Li system

The B32 structure may appear an unlikely candidate to be so stable since it barely breaks the convex hull. However, as temperature increases, the relative stability of B32 substantially increase, for two reasons:

1. The bcc phases have a larger vibrational entropy than comparable fcc phases, so that B32 becomes favored over fcc-based competing phases as temperature increases.
2. The interatomic interactions in this system allow the B32 phase to accommodate a substantial number of point defects without loosing its long range order. This disorder increases the entropy of the B32 phase and promotes its stability at elevated temperature.

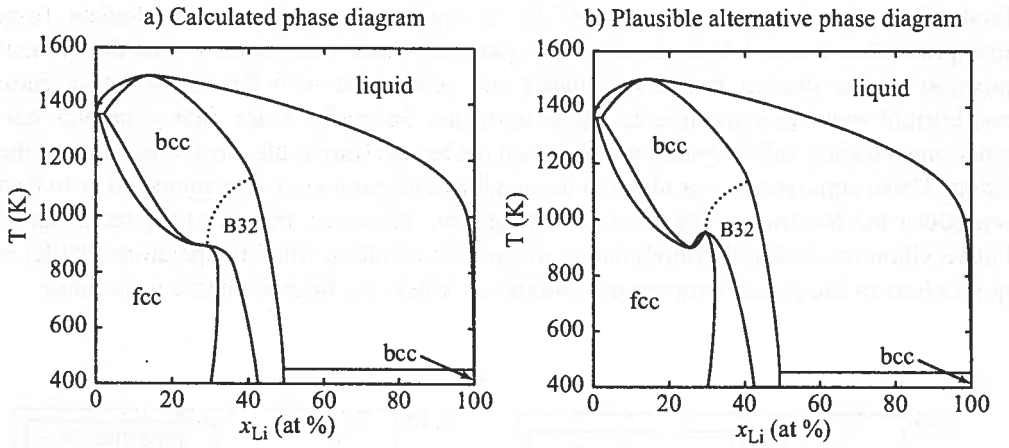

Fig. 4. Cu-Li phase diagram

Given the unexpected topology of the calculated phase diagram, a few remarks are in order. Although the presence of a Cu-rich bcc solid solution is surprising, given the assessments of P e l t o n [15] and of S a u n d e r s [16], this phase is consistent with the suggestion of K r a u s et al. [19] and O l d et al. [20] that a solid phase with about 20 at.% Li may be present. Interestingly, the shape of the fcc phase boundary is qualitatively similar to the one proposed by P e l t o n, thus indicating that our findings do corroborate some aspects of his assessment.

Another interesting feature is that the 1st order transition between the fcc and bcc phases becomes extremely narrow at the point where it intersect the 2nd order transition between the B32 phase of the Li-rich bcc solid solution. Although, the presence of the B32 phase may be unexpected given the earlier work on the Cu-Li system, such a phase is present in the related Al-Li system [39–41].

The calculated shapes of the liquidus and the solidus exhibit a congruent point at about 18 at % Li, which conflicts with all previous assessments. Such a discrepancy could easily arise due to errors in our calculated free energy of the bcc phase that are within the estimated precision of the method, as quoted in Table 1. Another possibility is that the free energy of mixing of both the liquid and the solid phases are slightly underestimated in the COST database. As a result, the liquidus and the solidus as predicted by the COST database match the known experimental phase boundaries, but when the liquid thermodynamic data from the COST database is combined with first-principles solid-state thermodynamic data, the

bias becomes visible. In any event, this small problem could be easily corrected in a full thermodynamic assessment relying on both first-principle data and experimentally observed solidus-liquidus boundaries.

Verifying whether our thermodynamic model is able to reproduce our emf measurements provides a very sensitive benchmark of the accuracy of the methods employed. As seen in Figure 5a), the calculations compare favorably with the experimental results. To facilitate the comparison, two adjustable parameters were introduced into the calculations. First, since the chemical potential of Li in liquid Li is difficult to calculate from first-principles, it was left as an adjustable parameter and determined so that the vertical position of the plateau in the calculated emf associated with the fcc-bcc two-phase equilibrium matches experimental measurements. Secondly, since first-principles calculations typically suffer systematic biases on the temperature scale, the temperature of the Monte Carlo simulations was also left as an adjustable parameter determined so as to best reproduce the location of the fcc to bcc transition. However, thanks to the inclusion of lattice vibrations in the thermodynamic model, the resulting fitted temperature (950K) is quite close to the actual temperature (885K) at which the measurements were made.

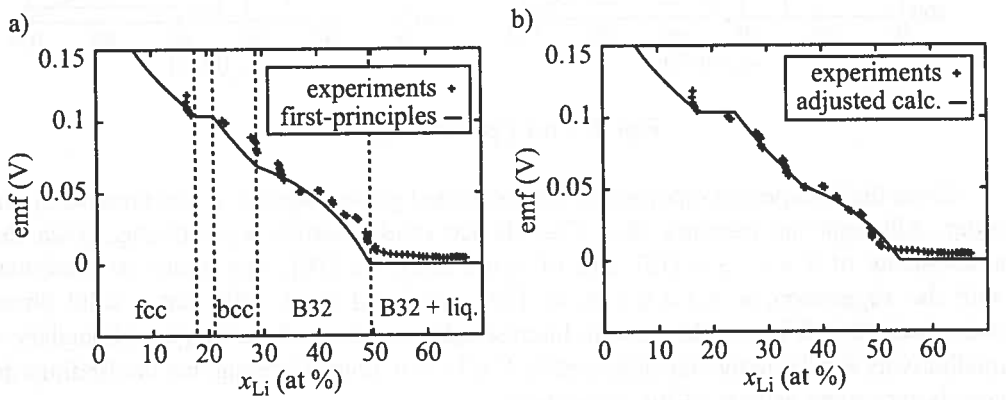

Fig. 5. Calculated and measured emf curves

A full thermodynamic assessment of the Cu-Li system would likely include both experimental and first-principles data. To illustrate how well such an optimized thermodynamic model including only one fcc phase, one bcc phase and a B32 phase would reproduce the emf curve, we slightly adjusted the width of the 1st order transition and the location of the 2nd order transition. These semi-empirically "adjusted" results, shown in Figure 5b) suggest that no other phases are needed to describe the shape of the emf curve at 885K. However, given the accuracy of our calculations, we cannot rule out that the bcc phase may be actually slightly less stable than we have found. This might cause the fcc and the bcc free energy curves to cross 3 times at around 885K, resulting in 3 plateaus in the emf curve, which is also compatible with the experimental measurements. The phase diagram corresponding to this alternative scenario is schematically depicted in Figure 4b).

4. Conclusions

Our first-principles calculations and electrochemical measurements suggest that the only stable ordered compound above room temperature is a B32 phase at 50 at % Li, which undergoes a second order phase transition into a bcc solid solution around 900K–1200K, thus indicating that the previously suggested Cu_4Li phase is probably a Cu-rich bcc solid solution (although we cannot entirely rule out the presence of ordered phase that are not superstructures of bcc or fcc). Our results would certainly benefit from further experimental corroboration. For instance, it should be possible to obtain the high-temperature bcc phase or the B32 phase by cooling a liquid solution containing more than 70 at.% Li. The composition of the resulting solid precipitates would be such that the bcc coordination would probably be maintained even after quenching, thus enabling room-temperature X-ray diffraction analysis. The present study illustrates how first-principles calculations can be very helpful in order to clarify the topology of a phase diagram and guide further experimental investigations.

Acknowledgements

This work is supported by the U.S. National Science Foundation under programs DMR-0080766 and DMR-0076097 and by the U.S. Department of Energy under contract no. DE-F502-96ER 45571. This work was supported also by the Polish Ministry of Scientific Research and Information Technology under project no. 7 T08B 04812.

The authors are grateful fo Professor D. de Fontaine for many helpful constructive comments and discussions and to Professor P. Turchi for providing us with some of his preliminary results which guided the early stages of this project.

REFERENCES

[1] J.F. Smith, Z. Moser, J. Nucl. Mater. **59**, 158 (1976).
[2] Z. Moser, W. Gąsior, F. Sommer, G. Schwitzgebel, B. Predel, Met. Trans. B **17**, 791 (1986).
[3] Z. Moser, F. Sommer, B. Predel, Z. Metallkde. **79**, 705 (1988).
[4] Z. Moser, F. Sommer, J.J. Lee, B. Predel, Thermochim. Acta **142**, 117 (1989).
[5] W. Gąsior, G. Schwitzgebel, Archs. of Metallurgy **37**, 25 (1992).
[6] W. Gąsior, Z. Moser. J. Chem. Phys. **90**, 387 (1993).
[7] W. Gąsior, G. Schwitzgebel, H. Ruppersberg, Archs. of Metallurgy **39**, 25 (1994).
[8] W. Gąsior, Z. Moser, W. Zakulski, J. Non-Crystalline Solids **205-207**, 379 (1996).
[9] W. Gąsior, Z. Moser, W. Zakulski, Archs. of Metallurgy **39**, 356 (1994).
[10] W. Gąsior, Z. Moser, W. Zakulski, G. Schwitzgebel, Mater. Met. Trans. A **27**, 2419 (1996).
[11] W. Gąsior, Z. Moser, J. Nucl. Mater. **249**, 77-83 (2001).
[12] Z. Moser, R. Agarwal, F. Sommer, B. Predel, Z. Metallkde. **82**, 317 (1991).
[13] Z. Moser, W. Gąsior, F. Sommer, W. Zakulski, H.J. Seifert, H.L. Lukas, CALPHAD XXIV, Kyoto, Japan, 21-26 May 1995. Program and Abstracts, p. 29.
[14] W. Gąsior, Z. Moser, B. Onderka, F. Sommer, B. Kim, Proceedings of 10th International IUPAC Conference on High Temperature Materials Chemistry, 10-14 April 2000, Jülich,Germany.

[15] A.D. Pelton, Bull. Alloy Phase Diagrams **7**, 142 (1986).
[16] N. Saunders, COST 537 Thermochemical database for light metal alloys **2**, Ed. I. Ansara, A.T. Dinsdale, M.H. Rand, European Communities, p. 168, 1998.
[17] H. Borgsttedt, C. Guminski, Metals in Liquid Alkali Metals, Solubility Data Series **64**, Oxford University Press, Oxford, p. 59, 1996.
[18] M.V. Mikhailovskaya, V.S. Sudavtsova, Ukr. Khim. Zh. **55**, 1106 (1989).
[19] A.R. Krauss, M.H. Mendelson, D.M. Gruen, R.W. Coon, D.M. Goebel, Y. Hiroaka, W.K. Leung, J. Bohdanowsky, J. US Dep. Ener. Rep. CONF-86-0807-3, 1986.
[20] C.F. Old, P. Trawena, Met. Sci, **15**, 281 (1981).
[21] A.R. Miedema, F.R. de Boer, R. Boom, CALPHAD **1**, 314 (1977).
[22] A. van de Walle, M. Asta, G. Ceder, CALPHAD Journal **26**, 539 (2002).
[23] A. van de Walle, G. Ceder, Journal of Phase Equilibria **23**, 348 (2002).
[24] A. van de Walle, M. Asta, Modelling Simul. Mater. Sci. Eng. **10**, 521 (2002).
[25] G. Kresse, J. Furthmüller, Phys. Rev. B **54**, 11169 (1996).
[26] G. Kresse, J. Furthmüller, Comp. Mat. Sci. **6**, 15 (1996).
[27] J.M. Sanchez, F. Ducastelle. D. Gratias, Physica **128A** 334 (1984).
[28] F. Ducastelle, Order and Phase Stability in Alloys. Elsevier Science, New York, (1991).
[29] D. de Fontaine, Solid State Phys. **47**, 33 (1994).
[30] A. Zunger. First principles statistical mechanics of semiconductor alloys and intermetallic compounds. In P. E. Turchi and A. Gonis, editors, NATO ASI on Statics and Dynamics of Alloy Phase Transformation, **319**, 361, Plenum Press, New York (1994).
[31] M. Asta, V. Ozolins, C. Woodward, Journal of the Minerals Metals & Materials Society **53**, 16 (2001).
[32] G. Ceder, A. van der Ven, C. Marianetti, D. Morgan, Modelling Simul. Mater. Sci. Eng. **8**, 311 (2000).
[33] A.A. Maradudin, E.W. Montroll, G.H. Weiss, Theory of Lattice Dynamics in the Harmonic Approximation, Second Edition, Academic Press, New York (1971).
[34] A. van de Walle, G. Ceder, Rev. Mod. Phys. **74**, 11 (2002).
[35] G. Ceder, Comput. Mater. Sci. **1**, 144 (1993).
[36] E. Wu, G. Ceder, A. van de Walle, Phys. Rev. B **67**, 134103 (2003).
[37] K. Binder, D.W. Heermann, Monte Carlo Simulation in Statistical Physics. Springer-Verlag, New York (1988).
[38] M.E.J. Newman, G.T. Barkema, Monte Carlo Methods in Statistical Physics, Clarendon Press, Oxford (1999).
[39] M.L. Saboungi, C.C. Hsu, Calphad **1**, 237 (1977).
[40] A.J. McAlister, Bull. Alloy Phase Diagrams **3**, 177-1982.
[41] M.H.F. Sluiter, Y. Watanabe, D. de Fontaine, Y. Kawazoe, Phys. Rev. B **53**, 6137 (1996), and references therein.

Received: 15 June 2004.

A R C H I V E S O F M E T A L L U R G Y A N D M A T E R I A L S
Volume 49 2004 Issue 3

K. RZYMAN *, Z. MOSER**, J-C. GACHON***

CALORIMETRIC STUDIES OF THE ENTHALPIES OF FORMATION OF Al_3Ti, $AlTi$, $AlTi_3$ and Al_2Ti COMPOUNDS

BADANIA KALORYMETRYCZNE ENTALPII TWORZENIA ZWIĄZKÓW Al_3Ti, $AlTi$, $AlTi_3$ i Al_2Ti

Two calorimetric methods: solution and direct reaction technique were used for determination of the enthalpy of formation of titanium aluminides – candidates for high temperature application. The special construction of solution calorimeter enables to determine enthalpy of formation at various temperatures what was realised for Al_3Ti compound. The differences between results obtained by solution method and direct reaction technique grows up with the decrease of aluminium content in the phases – this tendency was explained by mechanism of formation of phases from powders – in particular by the sequence of phases formation. Comparison with results of Calphad estimations of formation enthalpy and theoretical *ab initio* calculations are also included.

Dwie metody kalorymetryczne: rozpuszczania i bezpośredniej reakcji użyto dla określenia entalpii tworzenia aluminidków tytanu – będących kandydatami do wysokotemperaturowych zastosowań. Specjalna konstrukcja kalorymetru typu rozpuszczania umożliwiła wyznaczyć entalpię tworzenia w różnych temperaturach, zostało to wykorzystane w przypadku związku Al_3Ti. Różnice pomiędzy wynikami otrzymanymi metodą rozpuszczania a bezpośredniej syntezy wzrastały wraz ze zmniejszającym się udziałem aluminium w fazie – ta tendencja została wytłumaczona mechanizmem tworzenia się faz z proszków – w szczególności kolejnością tworzenia się faz.. W pracy włączono oszacowania metodą Calpgad oraz wyniki obliczeń teoretycznych typu *ab initio*.

* SILESIAN UNIVERSITY OF TECHNOLOGY, FACULTY OF MATERIALS SCIENCES AND METALLURGY, 40-019 KATOWICE, KRASIŃSKIEGO STREET 8, POLAND and INSTITUTE OF METALLURGY AND MATERIALS SCIENCES, POLISH ACADEMY OF SCIENCES, 30-059 KRAKÓW, REYMONTA STREET 25, POLAND

** INSTITUTE OF METALLURGY AND MATERIALS SCIENCE, POLISH ACADEMY OF SCIENCES, 30-059 KRAKÓW, REYMONTA STREET 25, POLAND

*** LABORATOIRE DU CHEMIE MINERAL, UMR 7555, GROUPE THERMODYNAMIQUE METALLURGIQUE, UNIVERSITE HENRY POINCARE, NANCY 1, BP 239, 54500 VANDOEUVRE-LES-NANCY, FRANCE

1. Introduction

The phases belonging to Al-Ti system and alloys based on these phases are the object of the intensive fundamental studies and studies directed for their application. Recently, more than half of papers referring to the intermetallic phases relates to the phases of Al-Ti system [1].

Such a considerable interest in these phases is a result of their merits, which are important from application viewpoint. The property which attracts the attention is their high strength to density ratio [2] what makes it possible reduction by ca. half the weight of constructional materials like exhaust valves, turbine wheels, comparing with classical superalloys. It is also worth to note their outstanding corrosion resistance [2]. A good mechanical properties, obtained for two phase AlTi/$AlTi_3$ alloys [3] or by introduction of alloy additions for example niobium [4] makes interest in these materials understandable by the automotive, aircraft industry and space investigations agency.

In this situation the precise determination of phase equilibria of Ti-Al system is of very importance, but up till now there are significant discrepancies between of authors regarding phase equilibrium mentioned above [5], [6], [7], [8], [9], [10]. There is although a concordant opinion that one of main reasons of dimness of determination of phase equilibrium of Al-Ti system is inconsiderable (in some temperature extent) difference between values of Gibbs free energy of liquid phase and other phases being in equilibrium with each other. In this situation impurities of phases may play an important role in difficulties in precise determination of phase equilibria.

One of the guiding principles of this work was to deliver the data serving for the accurate determination of phase equilibria. Apart from formation enthalpy of $AlTi_3$, AlTi, $AlTi_3$ studied previously (results are gathered in [11]), data for Al_2Ti investigated recently are presented in this paper.

The measurements were performed by calorimetric solution method, the results obtained by calorimetric direct reaction technique were also presented.

Results obtained experimentally were compared with data obtained by calculations performed with use of Calphad estimation method, Miedema model and *ab initio* calculation method at 0K.

2. Calorimetric techniques used in this work

2.1. Solution calorimetry

The enthalpy of formation ($\Delta_f H$) of the considered phase, determined by this method, is obtained from the difference of heat effects accompanying the dissolution in the aluminium bath of the studied phase and its components. In the case of the two-component phase the following equation is applied:

$$\Delta_f H = x_A \Delta H_A^{ef,0} + x_B \Delta H_B^{ef,0} - \Delta H^{ef.0}{}_{X_A X_B} \ldots\ldots\ldots \quad (1)$$

where: $\Delta_f H$ – formation enthalpy of the alloy, x_A, x_B - concentrations (mole fractions) of the alloy components, $\Delta H_A^{ef.0}, \Delta H_B^{ef.0}, \Delta H^{ef.0}{}_{x_A x_B}$ – heat effects accompanying the dissolution of the components and the alloy in the bath.

Schematic diagram of solution method is presented in the figure 1.

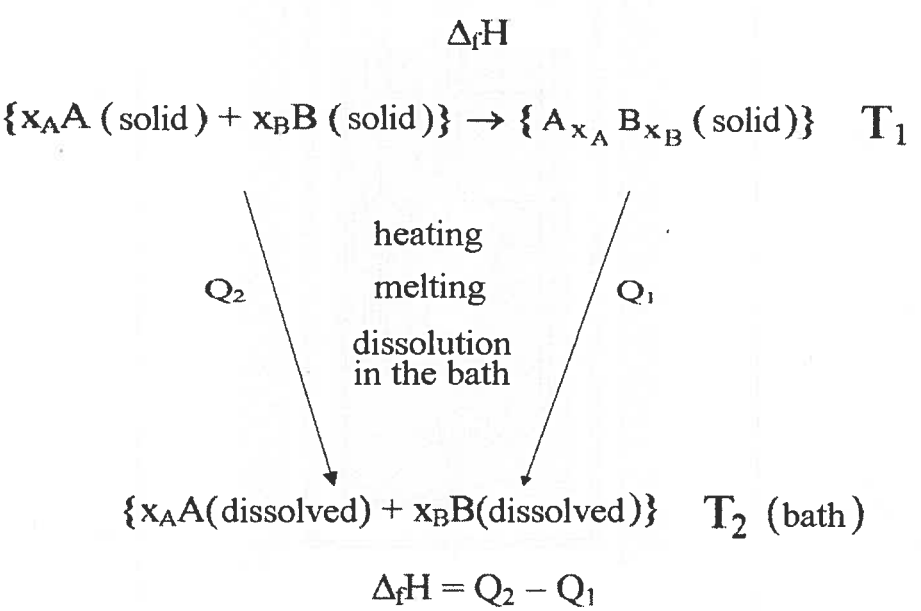

Fig. 1. Schematic diagram of calorimetric solution method

Value $\Delta H_A^{ef.0}$ and $\Delta H_B^{ef.0}$ consists of the following terms: 1/ enthalpy of heating up of the solid component from room temperature to the temperature of the calorimeter ($H_{room}^{calor.}$), 2/ heat of melting of the component (H_{melt}), 3/ limiting partial heat of solution of titanium in liquid aluminium for zero concentration of titanium (H^0_{Ti}) – this value were determined in our own measurements and is equal – 128.3 kJ/gramatom at 1356K; (respective value for aluminium equals zero) 4/ $\Delta H_{melting}$ – if melting of component takes place at temperatures higher than temperature of the bath, one should add the value of enthalpy of melting of this component. Thermochemical data were taken from [12].

Details of the applied high-temperature calorimeter constructed at the Institute of Metallurgy and Materials Science, PAS and experimental procedure are described in [13] , [14].

A previously described prototype calorimeter [15] was reconstructed at the Institute of Metallurgy and Materials Science [13].

The main modification is an installation of intermediate rotary multiple container enabling simultaneous annealing of several samples at any temperature from ambient up to

1300K before dropping the samples into the liquid bath. The phase Al_3Ti was studied both: at room temperature and at 1031K.

The calorimeter block of solution calorimeter is shown in Fig. 2.

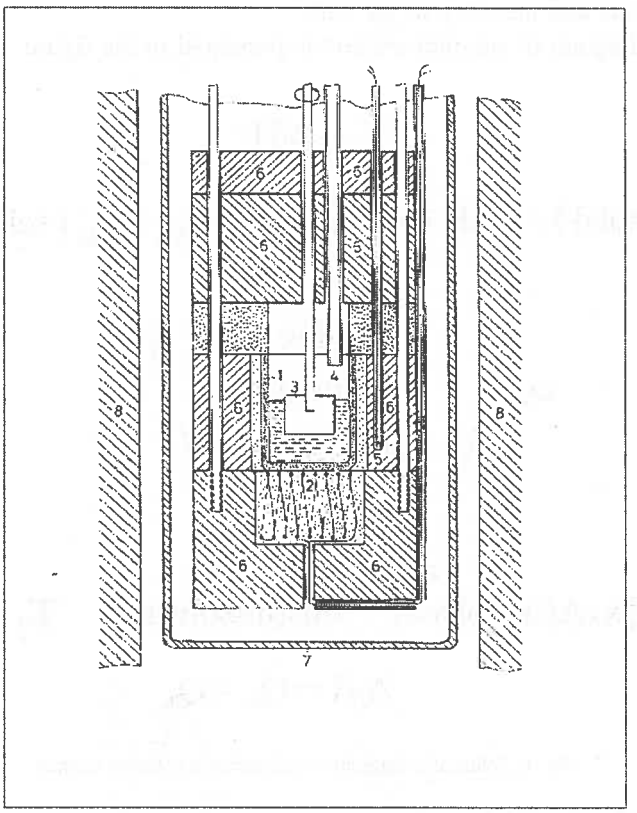

Fig. 2. Calorimeter block (solution method)

In the central part is placed crucible (1) made of sintered alumina holding about 55 grams of Al to which there are added during measurements samples of intermetallic compounds amounting from 0.3 to 0.5 grams. Due to small weight of added samples of compounds in comparison to the Al bath, extrapolation of the heat effects of separate single measurements to the limiting concentration in the bath of the investigated material requires only the averaging. Very important is also negligible change of filling of crucible during experimental series. The measurement of the heat effect is done by means of thermopile (2) composed of about 50 thermocouples AlNi-CrNi situated directly below the bottom of the bath crucible. In the figure we can also see effective ceramic stirrer (3), lower part of device facilitating delivery of the samples crucible with the bath (4), thermocouple (5), blocks of calorimeter (6). All elements of block are immersed in a heat-resistant tube (7), which in turn is installed inside calorimetric furnace (8).

The front view of the calorimeter is shown in Fig. 3.

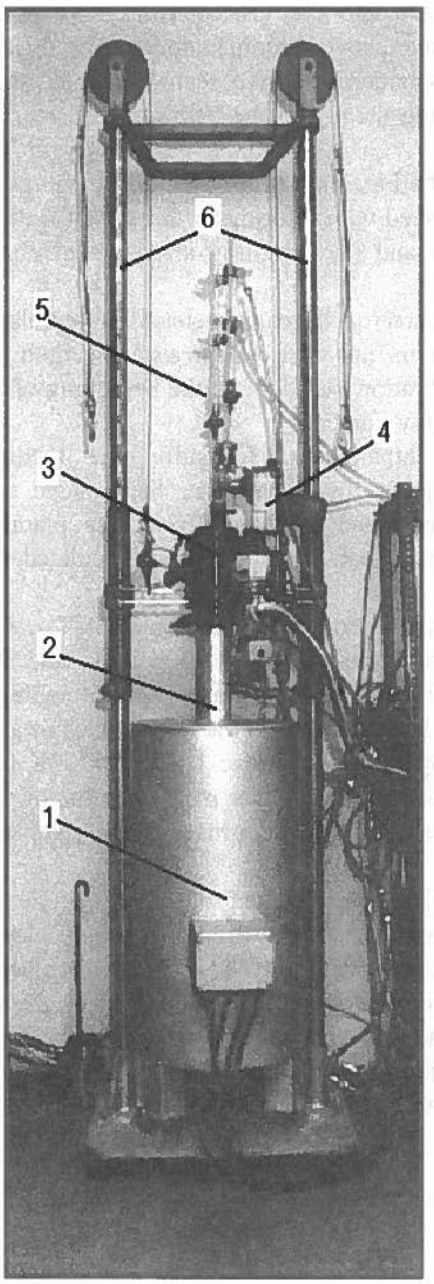

Fig. 3. The front view of solution calorimeter

At the bottom part is situated the vertical furnace (1) heated by three independent heating elements. It enables from one side to maintain the constant zone of temperature at the length of 15 centimetres, and from the other to get the temperature gradient amounting 12 K/cm along the vertical axis of the furnace. The latter enables to heat the sample in the container to any temperature between room temperature and 1200 K before dropping it into the bath. This rotary container with five seating enabled the simultaneous heating of 5 samples before dropping them into the bath and considerably decreased the time of measurements.

The other details of the Fig. 3 are as follows: (2) – heat resistant holder containing the calorimetric block connected with calorimeter head (3), (4) driving gear of the stirrer, (5) – glass interconnections and (6) – pulling arrangement enabling to operate with the calorimeter block.

Before each experimental run, the calorimeter was threefold evacuated and flushed with high purity argon. Numerous runs were done in a steady argon atmosphere with continuous stirring of the bath. Calibration was done at the beginning of a run by adding several Al samples of known enthalpy content.

The calculation of enthalpies of formation was facilitated by coupling of the calorimeter with a computer. In this manner the voltage signal from the thermopile was amplified and transformed to digital form, the planimetration was done automatically, and the enthalpies of formation were calculated directly from the recorded enthalpy effects.

Samples of investigated intermetallic compounds $AlTi_3$, AlTi, Al_3Ti and Al_2Ti were obtained from the proper amounts of 99,99 wt.%Ti and 99.99 wt.%Al by fivefold arc-melting under an Ar atmosphere. After every arc-melting the samples were turned (180°). Then, they were homogenised in the quarz tubes in a separate furnace under the same atmosphere at temperatures of range 1223K ÷1273K for 72 h. Then the samples Al_3Ti, AlTi, $AlTi_3$ and Al_2Ti devoted for measurements of formation enthalpy at room temperature were cooled slowly with the furnace. These samples were delivered into a bath at room temperature.

Another part of Al_3Ti samples devoted for the measurements of formation enthalpy at 1031K, after homogenising annealing at 1123K, were annealed at 1031K for 24 hours and then rapidly quenched in water with ice. The last stage of annealing was performed also at 1031K for 12 hours inside intermediate container inside the calorimeter directly before dropping samples into the bath. The alloys were tested by X-ray analysis to confirm the existence of a desired intermetallic phase.

The equilibrium phase diagram of Al-Ti system [16] is presented in Fig. 4.

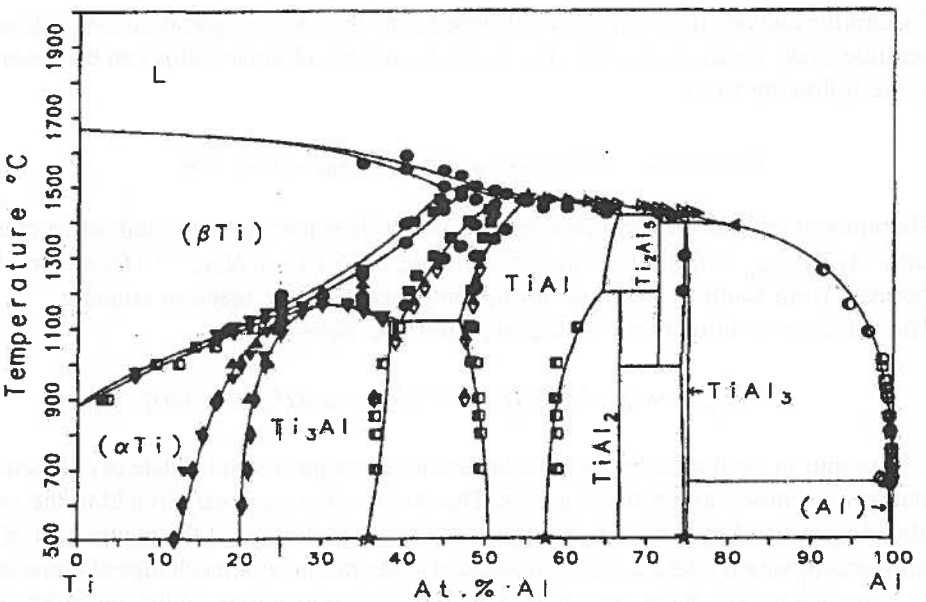

Fig. 4. Phase diagram of the Al – Ti system [16]

2.2. Direct reaction method

In this method, the basis of determination of formation enthalpy is the measurement of the heat effect accompanying the direct reaction of powder components at elevated temperature in the calorimeter accordingly to the scheme in Fig. 5.

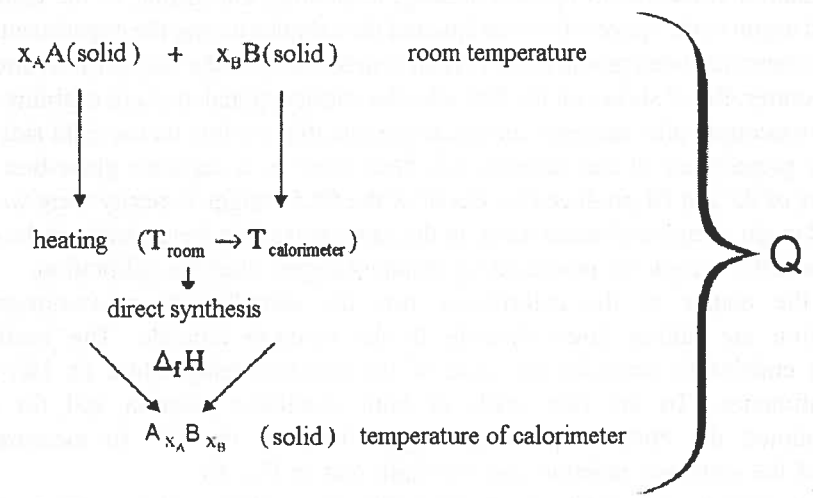

Fig. 5. Schematic diagram of calorimetric direct reaction method

Calibration and reaction samples are dropped from the room temperature to the elevated temperature of the reaction crucible. The desired synthesis of binary alloy can be presented using the following form:

$$A_{X_A(\text{room temp.})} + B_{X_B(\text{room temp.})} \rightarrow A_{X_A}B_{X_B(\text{calor. temp.})} + Q. \quad (2)$$

The amount of heat measured calorimetrically (Q) is the algebraic sum of formation enthalpy $\Delta_f H_{A_{X_A}B_{X_B}}$ and the heating effects $\Delta H_{\text{room}}^{\text{calor.}}$ (A), $\Delta H_{\text{room}}^{\text{calor.}}$ (B) of the alloy components from room temperature to the temperature of the reaction crucible.

The enthalpy of formation is calculated from the equation:

$$\Delta_f H_{A_{X_A}B_{X_B}} = Q - [x_A \Delta H_{\text{room}}^{\text{calor.}}(A) + x_B \Delta H_{\text{room}}^{\text{calor.}}(B)]. \quad (3)$$

In the solution method and in the direct reaction technique, the solid state of components and phase was chosen as a reference state. Due to this, it is necessary to add to the value calculated from Eq. 3, a portion proportional to the concentration of the component of the enthalpy accompanying the change of the state of aggregation or other change of conversion of the component. The latter remark is valid for the conversions taking place between ambient temperature and the temperature of the reaction crucible of the calorimeter.

Calorimetric investigations with the use of this method were performed (K.R.) at the University of Nancy as a part of our long-term co-operation. Calorimeter used at the University of Nancy was described in [17] and its general view is shown in Fig. 6.

Samples used for calibration and for measurements of enthalpies of formation were placed alternately in supporter pocket (1), which has been hermetically closed in the glove-box and installed at the top of the calorimeter. In Fig. 6, in the central part is shown the calorimeter furnace (2) heated by graphite bars. At the bottom of the furnace is placed a distribution board (3) to operate heating, evaluating and filling of the calorimeter by purified argon in the space where are situated the samples during the experiment. A furnace of calorimeter has been produced by French firm Setaram. In the vertical axis, directly below the supporter, Fig. 7 shows on the left side, the constructional element enabling hanging of the thermocouple pile, reaction and reference crucible (visible on the right side of Fig. 7).

The preparation of the samples has been done in a separate glove-box where the powders of Al and Ni produced by Cerac of the 99.5 weight % purity were weighted and pressed to get samples of about 0.5 g. In the same glove-box were weighted the α-alumina samples (99.7 weight %, produced by Haldenwanger) used for calibration.

In the course of the calorimeter run, the samples for measurement and for calibration are falling down directly to the reaction crucible. The heating of the furnace enables to maintain the zone of the constant temperature ($\pm$ 1K) amounting 10 centimetres. To the side walls of both crucibles: reaction and for calibration are mounted the NiCr-NiAl thermocouples forming the pile to measure the heat effect of the synthesis reaction (see the right part of Fig. 6).

During the experimental run the heat effect is visible on the monitor screen of the computer due to coupling with the thermocouples file. Integration of the resulting heat

effect and the calculation of the enthalpy of formation is facilitated by the computer program as reported in [17].

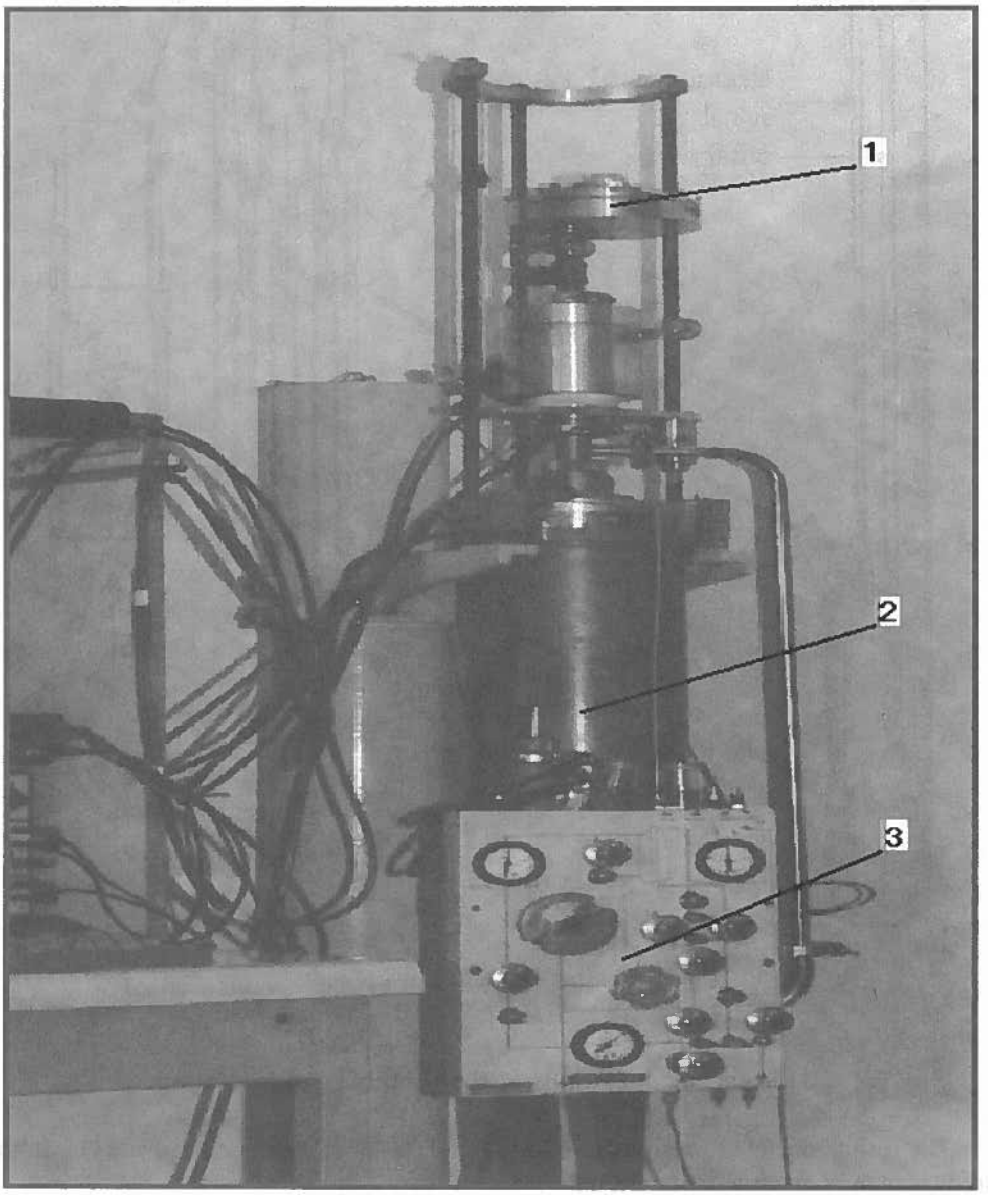

Fig. 6. The front view of direct reaction calorimeter

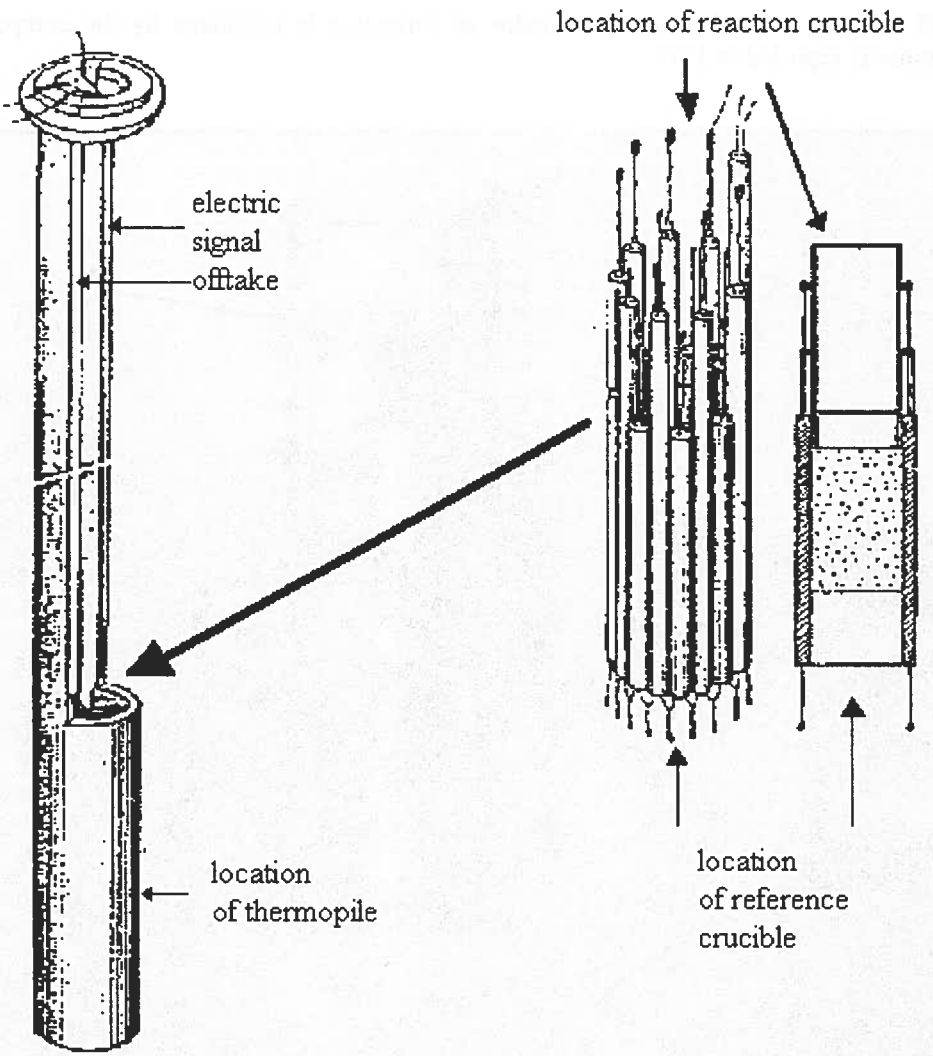

Fig. 7. Schematic presentation of calorimetric block in direct reaction method

3. Experimental results of the enthalpies of formation

The results obtained previously for Al_3Ti, AlTi, $AlTi_3$ were gathered in [11]. In this study, for the first time there are reported results for Al_2Ti.

Apart our own experimental results of the enthalpies of formation obtained by solution and direct reaction methods, the values of formation enthalpy determined experimentally and theoretically by other authors are also included.

3.1. Data for Al_3Ti

TABLE 3.1.1

Results obtained by calorimetric solution method for Al_3Ti intermetallic compound; samples were delivered into the bath at room temperature = 303K; temperature of the bath = 1335K [11]

The tempetature of intermediate container [K]	Temperature of Al bath [K]	Meas. no.	Heat effects accompanying the dissolution of Al_3Ti intermetallic compound in liquid aluminium [kJ/mole of atoms]
303	1335	1	47.8
		2	50.1
		3	48.4
		4	48.4
		5	48.5
			Average value: 48.7 ± 1.0
Formation enthalpy = −37.8 ± 2.3			

TABLE 3.1.2

Results obtained by calorimetric solution method for Al_3Ti intermetallic compound; samples were delivered into the bath at temperature = 1031K; temperature of the bath = 1335K [11]

The tempetature of intermediate container [K]	Temperature of Al bath [K]	Meas. no.	Heat effects accompanying the dissolution of Al_3Ti intermetallic compound in liquid aluminium [kJ/mole of atoms]
1031	1335	1	27.9
		2	27.5
		3	28.4
		4	26.4
		5	27.8
			Average value: 27.8 ± 0.8
Formation enthalpy = −37.3 ± 2.3 kJ/mole of atoms			

TABLE 3.1.3

The values of formation enthalpy of Al_3Ti determined experimentally and theoretically by other authors

Method	Formation enthalpy of Al_3Ti [kJ/mole of atoms]	Temperature [K]	References
Experimental methods			
Calorimetric method of direct synthesis	−37	1073	[18] cit. [19]
As above	−37	298	[20]
As above	−39.6	298	[21]
As above	−35.7	298	[22]
EMF measurements	−36	960	[23]
Optimization of experimental data	−36.6	298	[24] cit. [25], [26]
As above	−36	298	[27], [28]
Theoretical estimations			
Miedema's method	−39		[29]
CALPHAD estimation	−39.0	298	[5]
Theoretical calculations of *ab initio* type	−41.5	0	[30]
	−41.5	0	[31]
	−39.6	0	[32]

3.2. Recent new data for Al_2Ti

TABLE 3.2.1

Results obtained by calorimetric solution method for Al_2Ti intermetallic compound; samples were delivered into the bath at temperature = 306K; temperature of the bath = 1337K

The tempetature of intermediate container [K]	Temperature of Al bath [K]	Meas. no.	Heat effects accompanying the dissolution of Al_2Ti intermetallic compound in liquid aluminium [kJ/mole of atoms]
306	1337	1	39.8
		2	41.6
		3	38.8
		4	39.0
		5	36.9
			Average value: 39.2 ± 1.9
Formation enthalpy = −38.6 ± 2.6 [kJ/mole of atoms]			

TABLE 3.2.2

The values of formation enthalpy of Al_2Ti determined experimentally and theoretically by other authors

Method	Formation enthalpy of Al_2Ti [kJ/mole of atoms]	Temperature [K]	References
Experimental methods			
Calorimetric method of direct synthesis	−38.4	298	[26]
Theoretical estimations			
CALPHAD estimation	−36	298	[33]
As above	−42	298	[5]

3.3. Data for AlTi

TABLE 3.3.1

Results obtained by calorimetric solution method for AlTi intermetallic compound; samples were delivered into the bath at temperature = 299K; temperature of the bath = 1360K [34]

The tempetature of intermediate container [K]	Temperature of Al bath [K]	Meas. no.	Heat effects accompanying the dissolution of AlTi intermetallic compound in liquid aluminium [kJ/mole of atoms]
299	1360	1	−23.6
		2	−24.1
		3	−21.7
		4	−22.4
			Average value: −23.0 ± 1.1
Formation enthalpy = −41.9 ± 3.1 kJ/mole of aroms			

TABLE 3.3.2

Formation enthalpy of AlTi determined by the method of direct synthesis; room temperature = 300K; temperature of rection crucible = 1306K [11]

Measurement no.	Formation enthalpy of AlTi [kJ/mol of atoms]
1	−37.3
2	−36.9
3	−37.9
4	−36.0
5	−37.6
Average value	−37.1 ± 1.0

TABLE 3.3.3

The values of formation enthalpy of AlTi determined experimentally and theoretically by other authors

Method	Enthalpy of formation of AlTi [kJ/mole of atoms]	Temperature [K]	References
Experimental methods			
Calorimetric method of direct reaction	−38	298	[24] cit. [25] and [26]
EMF measurements	−36	960	[23]
Optimization of experimental data	−36	298	[27], [28]
Theoretical estimations			
Miedema's method	−61		[29]
CALPHAD estimation	−38.4	298	[5]
Theoretical	−42.4	0	[31]
	−39.6	0	[32]

3.4. Data for $AlTi_3$

TABLE 3.4.1

Results obtained by calorimetric solution method for $AlTi_3$ intermetallic compound; samples were delivered into the bath at temperature = 300K; temperature of the bath = 1356K [34]

The tempetature of intermediate container [K]	Temperature of Al bath [K]	Meas. no.		Heat effects accompanying the dissolution of $AlTi_3$ intermetallic compound in liquid aluminium [kJ/mole of atoms]
300	1356	Series 1	1	−17.7
			2	−19.1
			3	−21.6
		Series 2	1	−21.6
			2	−18.2
			3	−21.6
				Average value: −19.7 ± 1.9
Formation enthalpy = 29.9 ± 3.3 kJ/mole of aroms				

TABLE 3.4.2
Formation enthalpy of $AlTi_3$ determined by the method of direct synthesis; room temperature = 299K; temperature of rection crucible = 1306K [11]

Measurement no.	Formation enthalpy of AlT_i [kJ/mol of atoms]
1	−18.3
2	−21.1
3	−21.6
Average value	−20.3 ± 1.9

TABLE 3.4.3
The values of formation enthalpy of $AlTi_3$ determined experimentally and theoretically by other authors

Method	Formation enthalpy of $AlTi_3$ [kJ/mole of atoms]	Temperature [K]	References
Experimental methods			
Calorimetric method of direct synthesis	−25	198	[25]
EMF measurements	−24	960	[23]
Theoretical estimations			
Miedema's method	−39		[29]
CALPHAD estimation	−28.6	298	[5]
Theoretical calculations of *ab initio* type	−27.0	0	[35]
	−28.9	0	[31]
	−27.0	0	[32]

4. Discussion and final remarks

Analysing results obtained by solution method and by direct reaction method obtained both in CNRS centre in Nancy [11] and by K u b a s c h e w s k i [25], [26] the considerable difference between results obtained by two calorimetric methods for compounds AlTi and $AlTi_3$ focus the attention. Simultaneously, very similar results obtained for Al_3Ti obtained by both methods were noted. Also similar values of formation enthalpy of Al_3Ti obtained by solution method for room temperature ($\Delta_f H = -37.8 \pm 2.3$ kJ/mole of atoms) and 1031K ($\Delta_f H = -37.3 \pm 2.3$ kJ/mole of atoms).

To recognise the sources of differences between results obtained by both methods in the case of AlTi and $AlTi_3$ and their accordance in the case of Al_3Ti, it is worth to recall results of studies concerning the recognition of the mechanism of formation of phases in the Al-Ti system.

The results of numerous works where powders were used as the initial material [36], [37], [18], [38], [39], [40], [41], [42] indicate, that irrespectively on the proportions of the amount of introduced powders of aluminium and titanium, first obtained product is phase Al_3Ti. An important factor is melting of aluminium, which coats the particles of titanium. This reaction dominates up to exhausting of metallic aluminium. If quantitative proportion of titanium to aluminium is higher than 1:3 (at.%), the particles of titanium which did not react , start to react with Al_3Ti phase, forming the layer of AlTi and Al_2Ti directly around metallic titanium. It is worth to notice, that after melting and reacting of aluminium to mainly Al_3Ti, the further reactions take place between solid substances much slower. This reflects the change of temperature during reaction between initial powder materials in a ratio 3:1 of Ti:Al [36], [37]. In the first moments of process temperature considerably increases although majority of titanium remains non-reacted. The further reactions occur quicker at temperatures higher than 1165K. At this temperature titanium allotropic form (β), of high diffusitivity appears, contrary to the (α) titanium existing at lower temperatures. Much slower reaction between solid substances causes distinct decrease of temperature.

Only in works O r r and others [36], [37] where reactions were initiated and developed by electric field (field activated combustion synthesis /FACS/, among the products studied by *X*-ray diffraction and scanning electron microscopy the presence of $AlTi_3$ was stated exclusively. In other works structural analysis indicate also existence of phases like AlTi, Al_2Ti, Al_3Ti. Ti(Al) among the products.

In the context of remarks above work [18] it is worth to mention, where reaction was registered by real time *X*-ray analysis (2048 diffractograms per minute) ,the products were also analysed by back scattered electrons (BSE),and chemical analysis by *X*-ray micro-analyser was done.

It is interesting to analyse the results of enthalpy of formation, comparing data obtained by solution and direct reaction calorimetry. In the case of solution method, problems connected to mechanism of formation of desired phase are focused on the stage of formation of the compound of demanded composition. It takes place before application the sample to the calorimetric measurements, that is before dropping the sample into metallic bath. Description of the procedure of formation of alloys was given in a chapter presenting applied experimental method. *X*-ray analysis confirmed that only one desired phase was obtained. Considering compound AlTi, in the case direct synthesis we noted that similar values were obtained by the author (K.R.) in the Centre in Nancy (-37.1 ± 1.0 kJ/mol of atoms) [11] and by K u b a s c h e w s k i (37.7 ± 2.1 kJ/mol of atoms) [25]. For other compounds the difference is bigger what was discussed in detail in [11]. The basic problem which needs to be emphasised is the distinct difference between results obtained in solution and direct reaction methods in the case of AlTi and Al_3Ti and good agreement of results obtained for Al_3Ti. We noted a great rate of formation of Al_3Ti first in the presence of liquid Al; comparing with the rate of formation of other phase of this system, where reaction occur between solid substances. Basing on the work of [43] one can conclude that at the first stage of mechanical milling process, particles form long strips being in tight contact. Apart from it the oxides are teared off from the particles.

Two kinds of the powder materials were studied in our work: 1) one directly after direct synthesis in calorimeter (Fig. 8 – left side 2) after direct synthesis in calorimeter + 2 hours of mechanical alloying + one more synthesis in calorimeter (Fig. 8 – right side). In the latter figure $AlTi_3$ phase is dominating.

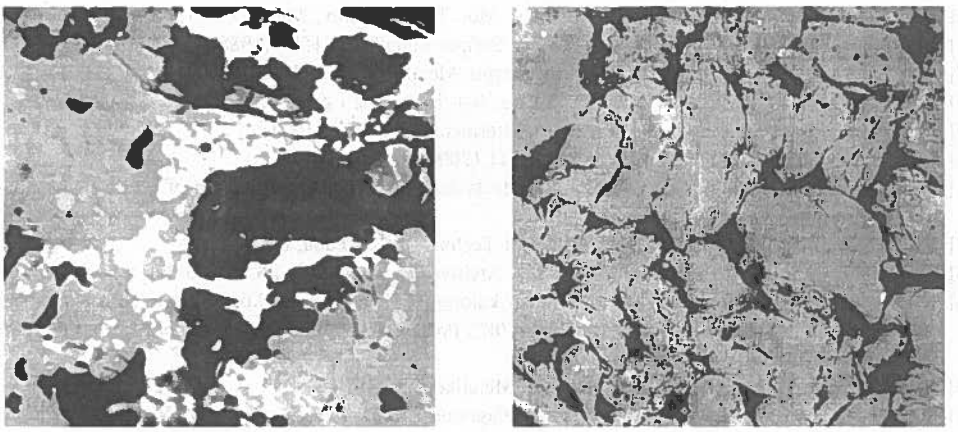

Fig. 8. The BSE microstructures of the phases achieved by direct synthesis performed in calorimeter: left side the – synthesis non-preceded by the mechanical alloying process, right side – synthesis preceded by the mechanical alloying process

Obtained result indicates an interesting technological path: in initial stage of application mechanical alloying, then spontaneous synthesis or synthesis with assistance of external source of heat.

Presented studies refer to the compounds from system Al-Ti and are a part of a wide program of investigations of intermetallic phases. In frames of these studies, compounds from Al-Ni system were investigated by calorimetric solution method and direct reaction method and published as a review paper [44]. Results obtained by solution method showed very slight dependence of temperature of formation enthalpy. Small difference between results obtained for AlNI and Al_3Ni_2 were explained by the similarity of their structures. High negative values of formation enthalpy of mentioned compounds is connected with a stability of these phases up to high temperatures.

Very interesting temperature dependence of formation enthalpy of compound AlFe, which was also studied, was explained by magnetic properties of iron and anti-site defects in the compound. All obtained results were gathered in [11].

In our Cracow laboratory activity measurements in the aluminium titanium solid alloys by EMF measurements are also performed [45].

REFERENCES

[1] J. Bystrzycki, H. Garbacz, W. Przetakiewicz, K.J. Kurzydłowski, Inżynieria Materialowa **1**, 8 (2001).

[2] K. F a l l e r, F.H (Sam) F r o e s, JOM **53**, 4, 27, 2001.
[3] M. E c k e r t, L. B e n c z e, D. K a t h, H. N i c k e l, K. H i l p e r t, Ber. Bunenes. Phys. Chem. **100**, 4, 418-424 (1996).
[4] D. B a n e r j e e, Ti_3Al and its Alloys, chapter in book: Intermetallic Compounds **2**, Practice. Edited by J.H. Westbrook i R.L. Fleischer, John Wiley and Sons Ltd, 91-131, (1994).
[5] U.R. K a t t n e r, J.C. L i n, Y.A. C h a n g, Met. Trans. A **23A**, 2081-2090 (1992).
[6] J.P. G r o s, B. S u n d m a n, I. A n s a r a, Scripta Metall. **22**, 1587 (1988).
[7] A. H e l l w i g, G. I n d e n, M. P a l m, Scripta Metall. **27**, 143 (1992).
[8] C.D. A n d e r s o n, W.H. H o f m e i s t e r, R.J. B a y u z i c k, Met. Trans. A **24A**, 61 (1993).
[9] R. K a i n u m a, M. P a l m, G. I n d e n, Intermetallics **2**, 321 (1994).
[10] H. O k a m o t o, J. Phase Equilibria **21**, 3, 311 (2000).
[11] K. R z y m a n, Habilitation work: Energy effects accompanying the formation of intermetallic phases, 1-110, Kraków, (2002).
[12] SGTE Substance Data Base, Royal Institute of Technology, Sweden, (1994).
[13] K. R z y m a n, Z. M o s e r, B. K i e c k a, Archives of Metallurgy **38**, 4, 393-396 (1993).
[14] K. R z y m a n, Z. M o s e r, Rozwój badań kalorymetrycznych związków i faz międzymetalicznych, XII Konferencja Sprawozdawcza „Metalurgia 98", Polska Akademia Nauk, Komitet Metalurgii, Krynica 1998, 626÷631.
[15] F. S o m m e r, J.J. L e e, B. P r e d e l, Z. Metallkde **71**, 818 (1980).
[16] T.B. M a s s a l s k i, Binary Alloy Phase Diagrams, ed..2, ASM International Materials Information Society, (1990).
[17] J.C. G a c h o n, M. N o t i n, J. H e r t z, Journees de Calorimetrie et Analyse Thermique de l'Assocation Francaise de Calorimetrie et Analyse Chemique, Marseille, HT. **2**, 1-11 (1979).
[18] Jean-Francois J a v e l, Thesis, Universyté Henri Poincaré, Nancy, (France), (1997).
[19] Chrifi-Alaoui N a s s i k F.A., Thesis , Université Henri Poincaré, Nancy, (France), (1997).
[20] W.W. L i a n g, Calphad **7**, 13 (1983).
[21] O.J. K l e p p a, J. Phase Equilibria **15**, 240 (1994).
[22] Smithels Metals Reference Book, ed. By E.A. Brandes i G. B. Brook (Butterworth, Oxford, 1992).
[23] V.V. S a m o k h v a l, P.A. P o l e s h c h u k, A.A. V e c h e r, Russ. J. Phys. Chem. **45**, 1174 (1971).
[24] R. H u l t g r e n, P.D. D e s a i, D.T. H a w k i n s, M. G l e s e r, K.K. K e l l e y, Selected Values of Thermodynamic Properties of Binary Alloys, ASM,Metals Park, Ohio, (1973).
[25] O. K u b a s c h e w s k i, W.A. D e n c h, Acta Metall. **3**, 339-346 (1955).
[26] O. K u b a s c h e w s k i, G. H e y m e r, Trans. Faraday Soc. **56**, 473-478 (1960).
[27] I. B a r i n, O. K n a c k e, O. K u b a s c h e w s k i, Thermochemical Properties of Inorganic Substances, Supplement (Springer Verlag, Berlin, Heilderberg, New York, and Verlag Stahleisen, Dsseldorf, 1977.
[28] O. K u b a s c h e w s k i, C.B. A l c o c k, Metallurgical Thermochemistry (Pergamon Press, Oxford, New York, Toronto, Sidney, Paris, Frankfurt, 1979.
[29] F.R. de B o e r, R. B o o m, W.C.M. M a t t e n s, A.R. M i e d e m a, A.K. N i e s s e n, Cohesion in Metals, Transition Metal Alloys, ed.North-Holland, 1988.
[30] C.L. F u, J. Mater. Res. **5**, 971 (1990).
[31] M. A s t a, D. de F o n t a i n e, M. van S c h i l f g a a r d e, M. S l u i t e r, M. M e t h f e s s e l, Phys. Rev. B **46**, 5055 (1992).
[32] R.E. W a t s o n, M. W e i n e r t, Phys. Rev. B **58**, 10, 5981-5988 (1998).
[33] F. Z h a n g, S.L. C h e n, Y.A. C h a n g, U.R. K a t t n e r, Intermetallics **5**, 471 (1997).
[34] K. R z y m a n, Z. M o s e r, J.-C. G a c h o n, Inżynieria Materiałowa **5**, (124) 2001.
[35] T. H o n g, J. W a t s o n - Y u n g, X.Q. G u o, A.J. F r e e m a n, T. O g u c h, J.H. X u, Phys. Rev. B **43**, 1940 (1991).
[36] R. O r r ú, G. C a o, Z.A. M u n i r, Metall and Mater. Trans. A **30A**, 1101-1108 (1999).
[37] R. O r r ú, G. C a o, Z.A. M u n i r, Chemical Engineering Science **54**, 3349-3355 (1999).
[38] H.C. Y i, A. P e t r i c, J.J. M o o r e, J. Mater. Sci. **27**, 6797-6806 (1992).

[39] W.Y. Y a n g, Baker, Scripta Metall. Mater. **34**, 803 (1996).
[40] M. H o - Y i, Y. H o n g - Y u, M. S h u - X i a, Y. S h e n g, Int..J. SHS, **1**, 6797-6806 (1992).
[41] M. D a h m s, T.J. J e w e t t, C. M i c h a e l n, Z. Metallkde **88**, 125-130 (1997).
[42] M. S u j a t a, S. B h a r g a v a, S. S a n g a l, J. Mater. Sci. Lett. **16**, 1175-1178 (1997).
[43] Olivier H e l d, Thesis, Université Henri Poincaré Nancy (France), (1998).
[44] K. R z y m a n, Z. M o s e r, Progress in Materials Science **49**, 581-606 (2004).
[45] W. G ą s i o r, Z. M o s e r, Archives of Metallurgy **48**, 344-353 (2002).

Received: 15 June 2004.

A R C H I V E S O F M E T A L L U R G Y A N D M A T E R I A L S
Volume 49 2004 Issue 3

M. KUCHARSKI *, P. FIMA*

THE SURFACE TENSION AND DENSITY OF Cu-Pb-Fe ALLOYS

NAPIĘCIE POWIERZCHNIOWE I GĘSTOŚĆ STOPÓW Cu-Pb-Fe

The surface tension and density for twelve Cu-Pb-Fe alloys were determined by sessile drop method. The X-ray radiographic technique was used to obtain images of Cu-Pb-Fe drops, and computer programs were employed to calculate densities and surface tensions of investigated alloys. Investigated alloys were selected to cover the composition of reduced alloys from slag obtained during direct-to-blister flash smelting process. The surface tension was found to increase with temperature. It suggests that lead atoms were replaced by iron and copper atoms in the surface phase of the Cu-Pb-Fe alloys.

Praca zawiera wyniki pomiarów napięcia powierzchniowego i gęstości dla dwunastu stopów Cu-Pb-Fe wykonanych za pomocą metody leżącej kropli. Obrazy kropel badanych stopów otrzymywano za pomocą techniki rentgenowskiej, przy czym ich napięcie powierzchniowe i gęstość obliczano za pomocą odpowiednich programów komputerowych. Skład badanych stopów pokrywał się ze składami stopów Cu-Pb-Fe otrzymywanymi w procesie odmiedziowywania żużli z procesu jednostadialnego otrzymywania miedzi. Dla wszystkich badanych stopów napięcie powierzchniowe rośnie ze wzrostem temperatury. Sugeruje to, że atomy ołowiu są zamieniane przez atomy miedzi i żelaza w warstwie powierzchniowej badanych stopów.

1. Introduction

The idea of one-step process for copper production was for the first time implemented in Poland in 1977 by Outokumpu. In this process approximately 1/3 of the copper contained in smelting concentrates reports to the slag, and therefore slag cleaning process in electrical furnace is used to bring the copper loss down to an acceptable level of 0.5 wt. %. In consequence Cu-Pb-Fe alloys are obtained. However, the copper recovery from these slags proved to be quite difficult when copper concentration drops below 2 wt%. There are two possibilities in such case, prolonging the process in order to decrease the copper content in

* FACULTY OF NON-FERROUS METALS. DEPARTMENT OF METALLURGY OF NON-FERROUS METALS. AGH – UNIVERSITY OF SCIENCE AND TECHNOLOGY, 30-059 KRAKÓW, MICKIEWICZA 30. POLAND

slag or accepting higher copper losses. Both solutions increase production cost and therefore should be avoided.
Presented paper is a part of the project aimed to determine the surface properties of Cu-Pb-Fe- flush smelting slag system. It was found that these properties play important role in the copper recovery from the slag.

2. The surface tension and densities measurements for Cu-Pb-Fe alloys

Cu-Pb-Fe alloys show miscibility gap, and therefore it is very difficult to obtain homogeneous mixture. On the other hand, lead has high vapour pressure above 1000 °C and to overcome these problems, Cu-Pb-Fe alloys were melted in sealed ampoules at 1200 °C. The samples were kept in this temperature for two hours and then quenched in water. Next the ampoules were broken down, and the samples removed. The samples were pressed into conically shaped hole in steel matrix and then placed in the alumina crucible. The crucible was then placed inside the graphite container with screwed lid. In this way, the lead vaporization was limited and mass losses of the samples in all cases after experiments were lower than 1%. The sessile drop profile method combined with X-ray radiography was used for these measurements. The apparatus employed for these determinations is shown in Fig.1.

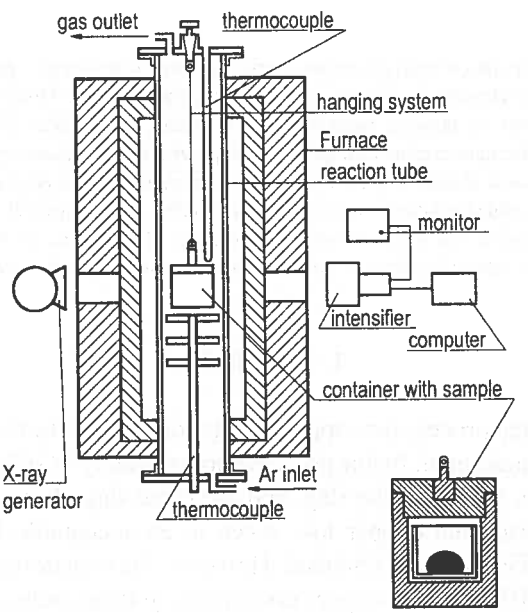

Fig. 1. Schematic diagram of the experimental apparatus.

The graphite container with the sample was suspended from alumina tube fixed to the bottom of conically shaped stopper with watch chain. A perfect alignment of the container was secured by this suspension, which also could be turned around.
Purified argon was allowed to pass throughout the system for a few hours to flush out the reaction tube. Next the furnace was switched on with temperature setting of 300 °C and kept in this temperature for 12 hours. Then the temperature of the furnace was increased to 1300 °C , and after thermal equilibration a picture of the alloy drop was recorded as can be seen in Fig.2.

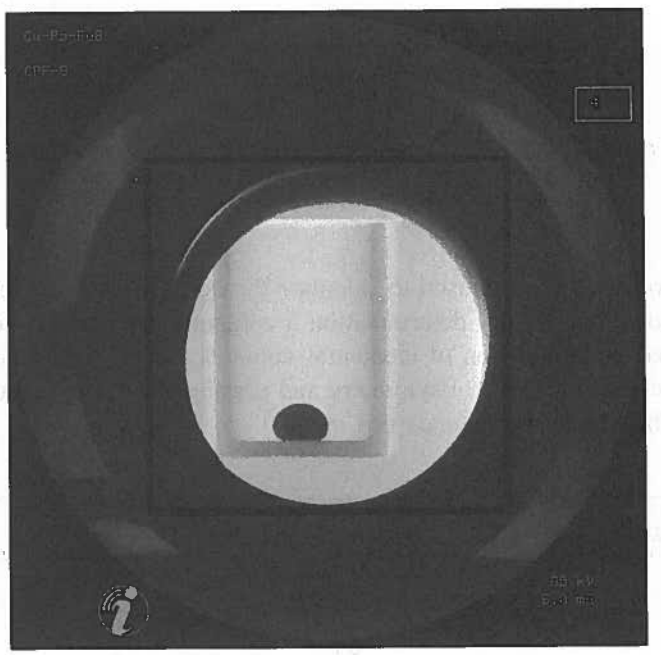

Rys. 2. X-ray image of Cu-Pb-Fe alloy of composition $x_{Pb} = 0.0708$; $\frac{x_{Fe}}{x_{Fe} + x_{Cu}} = 0.0361$ at 1300 °C

At the same temperature six pictures were taken for investigated alloy and after each picture the container with the sample was turned by angle of 60°. Every picture was taken after switching off the furnace for 20 seconds. Such power brake was too short to decrease the temperature of the sample but long enough to eliminate the interference of eddy current on the drop shape. Then the temperature of the furnace was decreased to 1200 °C and after thermal equilibration the measurements were performed in the same manner as at 1300 °C. The last measurements were carried out at 1100 °C and then the furnace was switched off. After cooling down the furnace, the container with the sample was removed and the sample weighted. It was found that in each case mass loss was lower than 1%.

Using a computer program, the profile coordinates of the points on meridian section of the drop image were determined as can be seen in Fig.3.

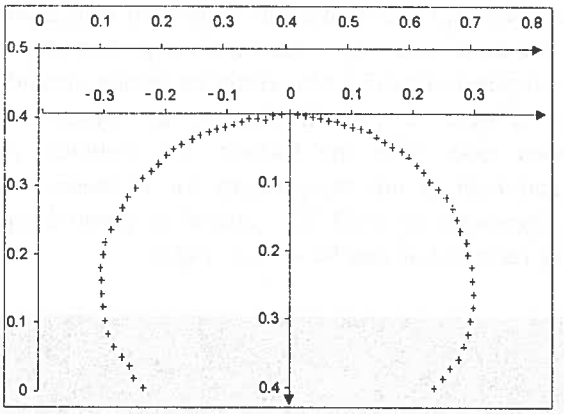

Fig. 3. Coordinates of the sessile drop of Cu-Pb-Fe alloy. Composition of the drop is $x_{Pb} = 0.0708$, $\frac{x_{Fe}}{x_{Fe} + x_{Cu}} = 0.0361$ and temperature 1300 °C

These profile coordinates were used to calculate the densities and surface tension of the investigated alloys. For density determination a computer program was developed. This program is based on summation of elemental volumes, which are located between two plains perpendicular to the axis of symmetry and passing through neighbouring points on drop surface. The Figure 4 illustrates this method.

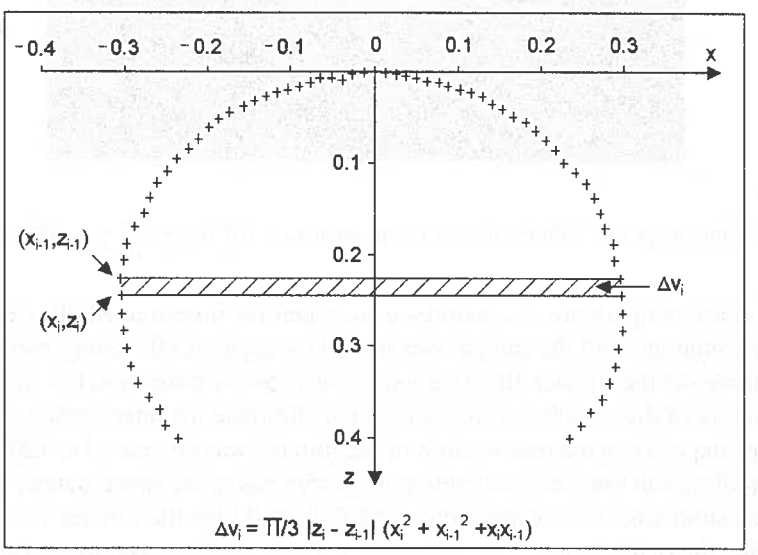

Fig. 4. The method of computation of volume of sessile drop

Density was computed with the relation:

$$\rho = \frac{m}{\sum_i \Delta V_i}, \tag{2}$$

where: m – mass of investigated alloy,

$\sum_i \Delta V_i$ – volume of the drop.

Surface tension of the investigated alloys is related to shape of the drop by L a p l a c e equation

$$\gamma\left(\frac{1}{R_1} + \frac{1}{R_2}\right) = \Delta P_0 + \Delta\rho \times g \times z, \tag{4}$$

where: γ – is the surface tension, R_1, R_2 – are two principle radii of curvature, ΔP_0 – is the pressure difference at the origin, $\Delta\rho$ – is the difference in the densities of alloys and surrounding gas, g – is the gravitational acceleration, z – is the vertical distance of the datum point from apex.

Surface tension was determined with computer program based on the method proposed by R o t e n b e r g et al [1]. This method minimizes sum of squares of normal distances between calculated Laplacian curve and experimental points. In consequence the computed value depends on location of origin (x_0, z_0), radius of curvature at the origin (R_0) and shape parameter $\left(\frac{\Delta\rho \times g \times R_0^2}{\gamma}\right)$.

3. Density and surface tension of Cu-Pb-Fe alloys

Composition of the investigated alloys was selected to cover composition range of the alloys obtained in copper recovery process from flush smelting slags. Measured densities of Cu-Pb-Fe alloys are listed in Table 1, and the relation between density and temperature for some alloys is presented in Fig. 5.

As predicted, densities of Cu-Pb-Fe alloys decrease with the temperature increase and replacement of copper by iron while lead content remains constant. Results of measured surface tension for Cu-Pb-Fe alloys are listed in Table 2, and Fig. 6 illustrates temperature dependence for some alloys.

As can be seen the surface tension of Cu-Pb-Fe alloys increases with temperature increase, which is not common case. In the most cases, the surface tension decreases with temperature increase. This phenomena could be explained with Gibbs equation:

$$d\gamma_{CuPbFe} = -\Gamma_{Cu} d\mu_{Cu} - \Gamma_{Fe} d\mu_{Fe} - \Gamma_{Pb} d\mu_{Pb}. \tag{5}$$

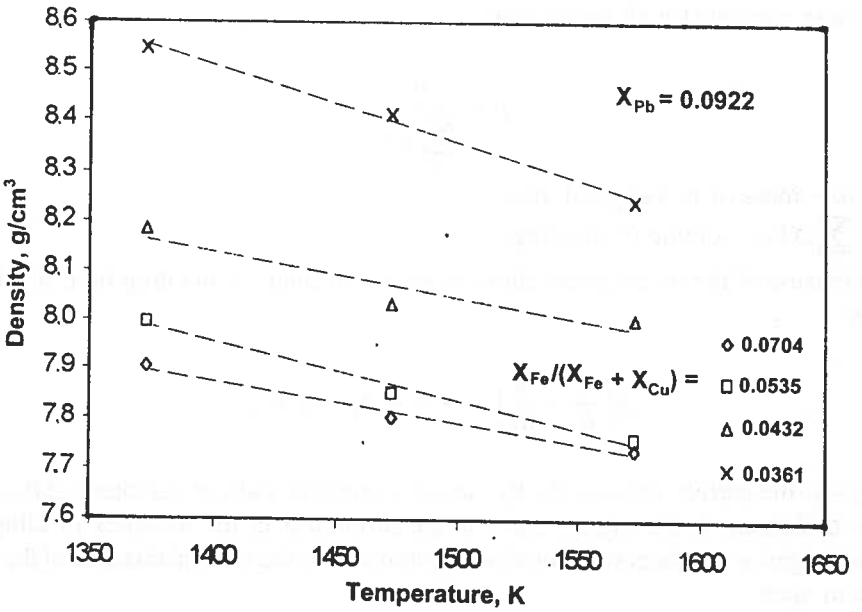

Fig. 5. Densities of Cu-Pb-Fe alloys as a function of temperature

TABLE 1

The results of density measurements for Cu-Pb-Fe alloys

X_{Pb}	$\frac{x_{Fe}}{x_{Fe}+x_{Cu}}$	ρ_{1373K}, $g \times cm^{-3}$	ρ_{1373K}, $g \times cm^{-3}$	ρ_{1373K}, $g \times cm^{-3}$
0.0510	0.0704	8.254	8.152	8.086
	0.0535	8.072	7.952	7.878
	0.0432	7.916	7.884	7.795
	0.0361	7.905	7.808	7.754
0.0708	0.0704	7.826	7.700	7.643
	0.0535	7.807	7.686	7.607
	0.0432	7.942	7.892	7.806
	0.0361	8.079	8.038	7.974
0.0922	0.0704	7.905	7.804	7.739
	0.0535	7.995	7.853	7.761
	0.0432	8.181	8.034	8.003
	0.0361	8.546	8.414	8.240

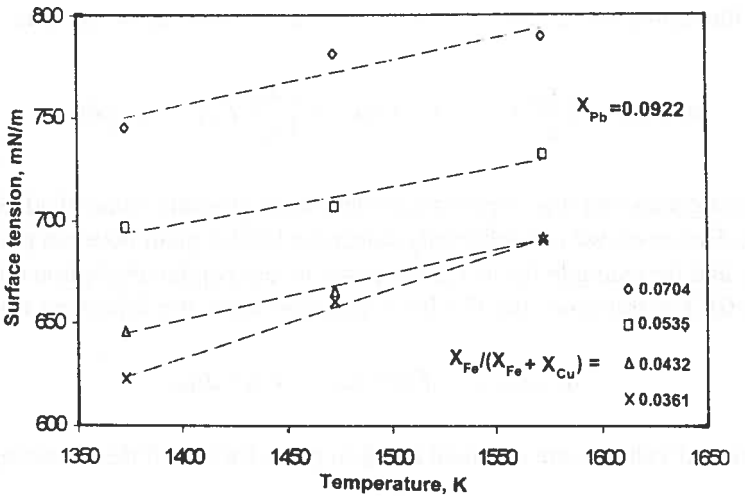

Fig. 6. Temperature dependence of the surface tension for some Cu-Pb-Fe alloys

TABLE 2

The surface tension of Cu-Pb-Fe as a function of composition and temperature

X_{Pb}	$\frac{x_{Fe}}{x_{Fe}+x_{Cu}}$	$\gamma_{1373}, \frac{mN}{m}$	$\gamma_{1474}, \frac{mN}{m}$	$\gamma_{1573}, \frac{mN}{m}$
0.0510	0.0704	909	944	980
	0.0535	808	824	853
	0.0432	752	780	820
	0.0361	700	719	759
0.0708	0.0704	856	906	956
	0.0535	774	815	837
	0.0432	733	772	799
	0.0361	720	736	767
0.0922	0.0704	745	781	789
	0.0535	697	707	732
	0.0432	646	665	692
	0.0361	623	660	690

Utilizing the G i b b s - D u h e m equation one can obtain:

$$x_{Cu}d\mu_{Cu} + x_{Fe}d\mu_{Cu} + x_{Pb}d\mu_{Pb} = 0. \qquad (6)$$

Combining the equations (5) and (6) the following relation can be written:

$$d\gamma_{CuPbFe} = \left(\frac{x_{Pb}}{x_{Cu}}\Gamma_{Cu} - \Gamma_{Fe}\right) d\mu_{Fe} + \left(\frac{x_{Pb}}{x_{Cu}}\Gamma_{Cu} - \Gamma_{Pb}\right) d\mu_{Pb}. \tag{7}$$

This relation suggests that it is impossible to determine absolute value of adsorption of the components. However, we can arbitrarily select the border plain between the surface and bulk phases, and for example for its certain position, the copper absorption could be equal zero ($\Gamma_{Cu} = 0$). For this case, the G i b b s equation takes the following form:

$$d\gamma_{CuPbFe} = -\Gamma_{Fe}^{(Cu)}\, d\mu_{Fe} - \Gamma_{Pb}^{(Cu)}\, d\mu_{Pb}. \tag{8}$$

The experimental values were obtained along to paths for which the following conditions are valid:

$$\frac{x_{Fe}}{x_{Cu} + x_{Fe}} = \frac{1}{1 + \dfrac{x_{Cu}}{x_{Fe}}} = const \tag{9}$$

$$x_{Pb} = const \tag{10}$$

Taking everything into account one can write two independent equations:

$$-\left(\frac{\partial\gamma_{CuPbFe}}{\partial\mu_{Fe}}\right)_{x_{Cu}x_{Fe}} = \Gamma_{Fe}^{(Cu)} + \Gamma_{Pb}^{(Cu)}\left(\frac{\partial\mu_{Pb}}{\partial\mu_{Fe}}\right)_{x_{Cu}x_{Fe}} \tag{11}$$

$$-\left(\frac{\partial\gamma_{CuPbFe}}{\partial\mu_{Pb}}\right)_{x_{Pb}} = \Gamma_{Fe}^{(Cu)}\left(\frac{\partial\mu_{Pb}}{\partial\mu_{Pb}}\right)_{x_{Pb}} + \Gamma_{Pb}^{(Cu)}. \tag{12}$$

Solving these two non-linear equations the adsorption values ($\Gamma_{Fe}^{(Cu)}$, $\Gamma_{Pb}^{(Cu)}$) can be determined.

According to G i b b s equation, the composition of the surface phase is enriched by components which lower the surface energy of the alloy. In our case the surface phase is enriched in lead in expense of iron and copper. Under our assumption ($\Gamma_{Cu} = 0$), temperature increase causes iron concentration increase in surface phase in expense of lead. Because of large difference between surface tensions of iron and lead, the surface tension of the solution increases despite the fact that for pure metals (Fe, Pb) the surface tension decreases with temperature.

4. Conclusions

- The surface tension and densities of Cu-Pb-Fe alloys were determined with sessile drop method as a function of temperature and composition.
- Density of investigated alloys decrease with increasing temperature and iron content in investigated alloys.
- Surface tension increases with increasing temperature for all investigated alloys and this phenomenon could be explained by replacement of lead by copper and iron atoms in the surface layer.

Acknowledgments

The paper is a part of the project no 7 T08B 056 21 financed by the State Committee for Scientific Research in Poland.

REFERENCES

[1] Y. Rotenberg, L. Boruvka, A.W. Neumann, Determination of Surface Tension and Contact Angle from the Shapes of Axisymmetric Fluid Interfaces, Journal of Colloid and Interface Science, 93, 1, May (1983).

Received: 10 June 2004.

A R C H I V E S O F M E T A L L U R G Y A N D M A T E R I A L S
Volume 49 2004 Issue 3

W. GĄSIOR *, Z. MOSER*, A. DĘBSKI*

SURDAT – DATABASE OF THE PHYSICAL PROPERTIES OF LIQUID LEAD-FREE SOLDERS

SURDAT – BAZA DANYCH WŁAŚCIWOŚCI FIZYCZNYCH CIEKŁYCH SPOIW BEZOŁOWIOWYCH

The SURDAT database was constructed using the experimental data of the surface tension, density and the molar volume. Most results presented here were obtained at the Institute of Metallurgy and Materials Science, Polish Academy of Sciences in Kraków during the last 7 years. The measurements of the surface tension and density were performed by the maximum bubble pressure and the dilatometric methods, while the molar volumes were calculated. SURDAT database comprises data for 7 pure metals, 9 binary, 5 ternary, 2 quaternary and 1 quinary Pb-free systems, enabling presentation in the numerical and the graphical form, such as temperature dependences and the isotherms at fixed temperatures. Moreover, SURDAT is linked with computer software BUTLER for modeling the surface tension of liquid alloys from the optimized thermodynamic parameters of the liquid phase and surface tensions of pure components. A comparison of the experimental results of the surface tension data with those from calculated from the optimized thermodynamic parameters of different authors is also possible.

Opracowana została baza właściwości fizycznych SURDAT zawierająca dane napięcia powierzchniowego, gęstości i objętości molowej. Większość danych eksperymentalnych została zmierzone w ostatnich 7-u latach w Instytucie Metalurgii i Inżynierii Materiałowej PAN w Krakowie. Pomiary napięcia powierzchniowego zostały wykonane metodą maksymalnego ciśnienia w pęcherzykach gazowych a pomiary gęstości metodą dylatometryczną. Objętość molowa była obliczana z wykorzystaniem danych gęstości. Baza SURDAT zawiera dane dla 7 czystych metali, 9 układów dwuskładnikowych, 5 trójskładnikowych, 2 czteroskładnikowych oraz jednego układu pięcioskładnikowego i umożliwia prezentację danych w postaci numerycznej oraz graficznej formie zależności temperaturowych oraz izotermicznych. Ponadto, baza SURDAT współpracuje z programem BUTLER służącym do modelowania napięcia powierzchniowego wykorzystując zoptymalizowane parametry termodynamiczne fazy ciekłej oraz napięcie powierzchniowe i gęstość czystych metali oraz daje możliwość porównania ich ze wskazanymi danymi eksperymentalnymi oraz obliczonymi z wykorzystaniem parametrów termodynamicznych różnych autorów.

* INSTITUTE OF METALLURGY AND MATERIALS SCIENCE, POLISH ACADEMY OF SCIENCES, 30-059 KRAKÓW, 25 REYMONTA STREET, POLAND

1. Introduction

In the last decade the binary and the multicomponent Sn alloys, with alloying elements such as Ag, In, Bi, Sb Cu and Zn, have been investigated all over the world to find a substitute for toxic eutectic Pb-Sn (73.9 at.%Sn) solders. These studies were stimulated by the Memorandum of EU to eliminate lead in all products starting from 2007, including micro- soldering in electronics. Studies, however, were mainly concerned on :

- calculation of phase equilibria of the binary and multicomponent systems characteristic of the low temperature eutectics,
- experimental studies of the equilibria in the solid and liquid phases,
- the microcalorimetry measurements of heat content and the temperatures of phase transformations,
- structural investigations of alloys and the interface solder/substrates,
- activity measurements of components,
- (rarely) the meniscographic measurements of the interfacial tension, contact angle, wetting force and wetting time.

The investigations of physical properties of liquid solders, such as the surface tension, viscosity, density or molar volume in the broad temperature and concentration ranges, were in fact not undertaken, and the surface tension or viscosity were mainly calculated from thermodynamic models basing on the properties of liquid alloys and the data of pure components.

The measurements of the surface tension and the density have been carried at the Institute of Metallurgy and Materials Science, PAS in Kraków since 1970, primarily for molten salts (and their pure molten components), and in 1997 the same systematic experiments for pure metals and alloys were undertaken due to the interest in Pb-free soldering materials. As the first, however, the Pb-Sn liquid alloys [1] were investigated, commonly used for comparison with further investigations on Pb-free solders when applying the same method and the same apparatus.

For the last 7 years there have been studied the binary and the multicomponent liquid alloys listed in Table [2–12] and the measurements of the density and the surface tension were performed because the lack of such data in literature.

For binary alloys the investigations were conducted in the entire range of concentrations, whereas for the ternary, quaternary and quinary systems for the alloys based on binary eutectic $(Sn\text{-}Ag)_{eut} + X$ (X = Bi, Cu, Sb, In, Zn) and ternary near-eutectic Sn-Ag-Cu alloys with Bi and Sb additions, all in the extensive range of temperatures.

Apart from the experimental investigations the computer software has been created for modeling the surface tension using B u t l e r ' s method [13] with constant β and L parameters, applying excess G i b b s energies of the components of investigated alloys and their surface tension data. The thermodynamic parameters describing excess Gibbs energies of liquid alloys were taken from the literature, or were obtained in the frame of co-operation with professor Ishida's group from Tohoku University in Japan. In the latter centre, optimized thermodynamic parameters were obtained from phase equilibria studies

and they were used for phase diagram calculations as well as for simulation of solidification when comparing equilibrium solidification with Scheil's model.

TABLE

The investigated liquid metals and alloys

METALS	Ref.	BINARY ALLOYS	Ref.	MULTICOMPONENT ALLOYS	Ref.
Pb	1	Pb – Sn	1	$(Sn\text{-}Ag)_{eut}$ + Zn	*
Sn	2	Ag – Sn	2	$(Sn\text{-}Ag)_{eut}$ + In	6
In	3	Ag – In	3	$(Sn\text{-}Ag)_{eut}$ + Bi	4
Ag	3	Bi – Sn	4	$(Sn\text{-}Ag)_{eut}$ + Cu	8, 9
Bi	4	In – Sn	6	$(Sn\text{-}Ag)_{eut}$ + Sb	10
Sb	5	Ag – Bi	7	$(Sn\text{-}Ag)_{eut}$ + Cu + Sb	11
Cu	*	Sb – Sn	5	$(Sn\text{-}Ag)_{eut}$ + Cu + Bi	12
		Sn – Zn	*	$(Sn\text{-}Ag)_{eut}$ + Cu + Bi + Sb	*
		In – Zn	*		

* not published

In 2001, Institute of Metallurgy and Materials Science, PAS initiated the cooperation with the Institute of Non-Ferrous Metals in Gliwice, Tele- and Radio Research Institute in Warsaw and Technical University in Warsaw for the realization of the project directed on the measurements of the surface tension, density, molar volume and wettability (meniscographic investigations), electrical and mechanical properties of the lead-free solders based on the near-eutectic Sn-Ag-Cu alloys with the bismuth and antimony additions.

Additionally, participating in the COST 531 action since 2003, the surface tension and density data of the Sn-Ag-Cu-Sb [11] liquid alloys were published, and similar studies on Sn-Ag-Cu-In system are planned. It should be added, that for all the investigated liquid alloys, the linear dependence of the surface tension vs. temperature was proved, while for the same dependence B u t l e r ' s modeling shows the curvilinear behaviour, as discussed in [7].

Having gathered the numerous results of investigated lead-free solder alloys listed in Table, in 2003 at the Institute of Metallurgy and Materials Science, PAS there were started the preliminary steps to construct the computer database SURDAT of the physical properties comprising surface tension, density and molar volume in the form of figures and the equations describing the temperature and concentration dependences of those quantities. Next, the computer program for modeling of the surface tension from the B u t l e r's method was added to SURDAT, together with the excess G i b b s energies database (parameters of the R e d l i c h - K i s t e r relations).

The main aim of this paper is to present the possibility of the SURDAT database by describing the active windows on the example of the surface tension of pure tin and surface tension, density and molar volume of the Bi-Sn alloys.

2. Presentation of the SURDAT database

The functioning of the database is shortly presented at the scheme in Fig.1.

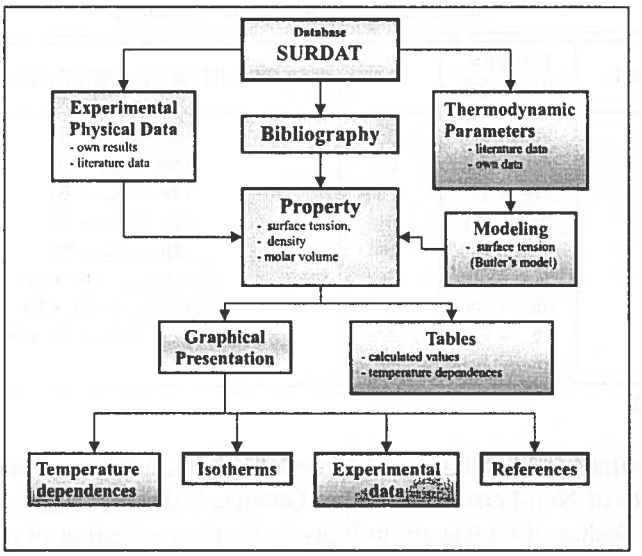

Fig. 1. Scheme of the database functioning

After activation of the SURDAT database, in the first two steps, the choice of the system and the property (surface tension, density, molar volume) should be selected (Fig.2 and Fig.3).

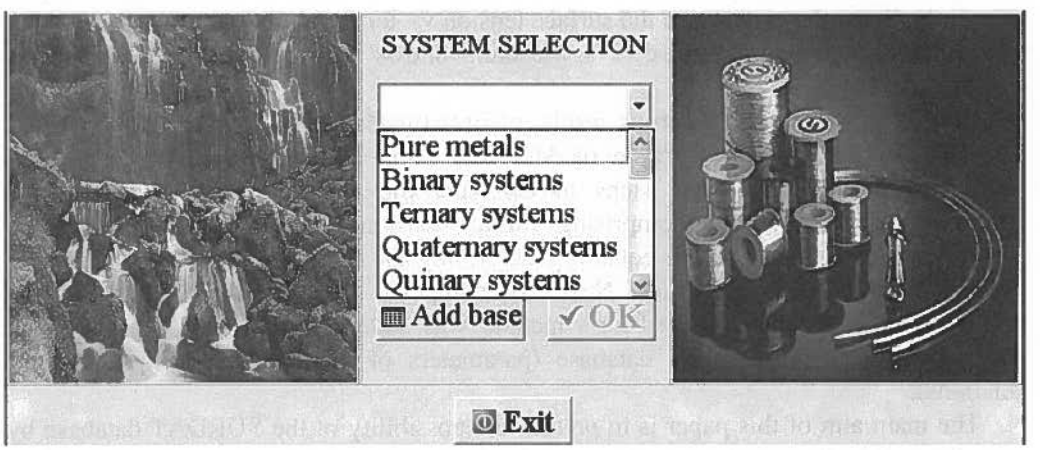

Fig. 2. First window of the database SURDAT-selection kind of the system

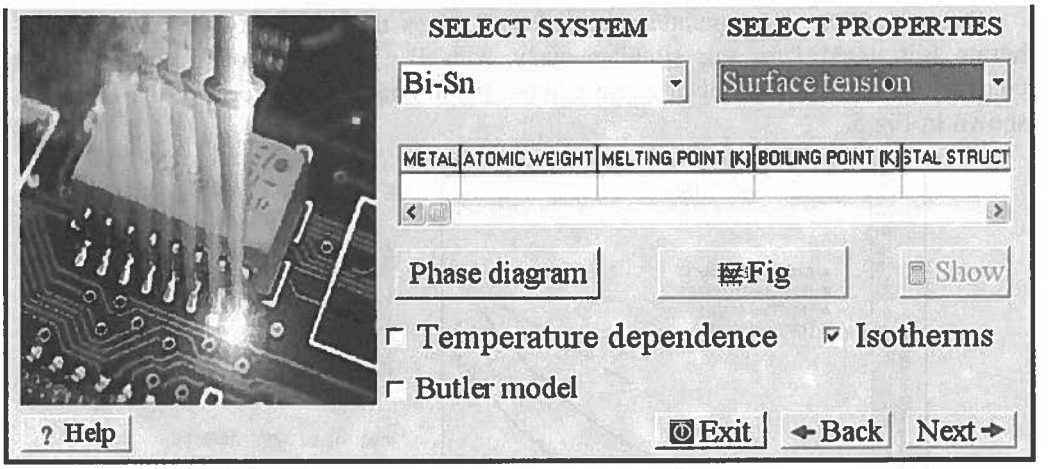

Fig. 3. Selection of the system and the property

When the system is already chosen, there are possible four other options: Fig. Temperature dependence, Isotherms and B u t l e r model. The five's option: Phase diagram is only available for binary systems, and will be extended in the future for higher order systems.

The first option „Fig" enables to observe the physical properties in the graphical form for different combinations of plots from previous publications listed in Table 1. An example, for liquid tin is given in Fig.4.

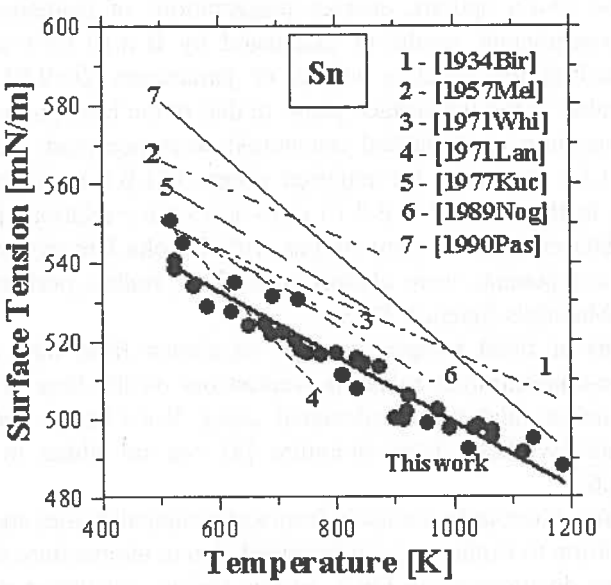

Fig. 4. The temperature dependence of the surface tension for liquid tin from Ref.2

Second option: "Temperature dependence" gives the possibility of not only isotherms (discussed later on, simultaneously with B u t l e r's model), but also the comparison with the data of different authors (additionally in the form of the tables) as shown in Fig.5.

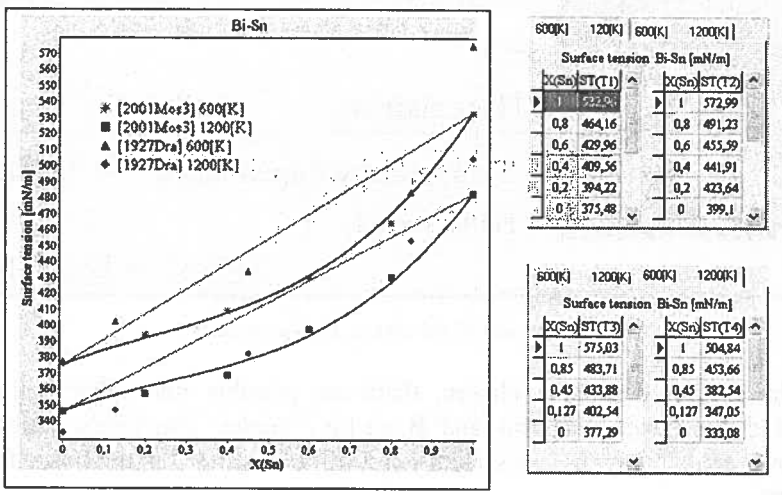

Fig. 5. The comparison of the data of surface tension of different authors [4 – 2001Mos3, 14 – 1927Dra] obtained from the database SURDAT at 600 K and 1200 K

The third and four's options, enables presentations of isotherms both determined directly from experimental results or calculated by B u t l e r's model [13]. In the B u t l e r 's method the constant values of parameters $\beta = 0.83$ (the ratio of the coordination number in the the surface phase to that in the bulk phase) and L = 1.091(for liquid metals assuming close-packed structures) were accepted. To calculate surface tension by B u t l e r's model the required excess G i b b s energies of liquid components, usually in the form of R e d l i c h - K i s t e r relations [15] were accepted from literature data or from the joint studies with Tohoku University, while the surface tension of pure components were always taken from studies performed in Institute of Metallurgy and Materials Science, PAS.

The isotherms at fixed temperature can be shown from data calculated directly from temperature-concentration relations worked out on the base of experimental data of the chosen author, and those calculated using B u t l e r's model. The selected experimental data (symbols) from literature [4] can be added to the plots for the comparison (Fig.6).

The comparison of the surface tension from experimental studies and from B u t l e r's modeling (in addition to isotherms) can be added also to temperature dependencies of the surface tension as documented in Fig.7. In this option, calculated data were drawn as continuous lines, together with symbols referring to results from [4].

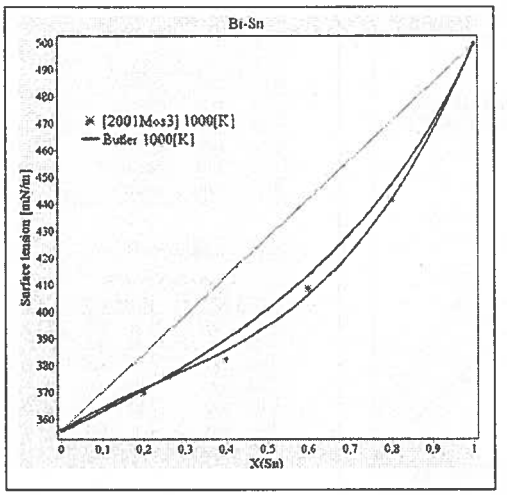

Surface tension Bi-Sn = A+B*T

X	A	B
0	405	-0,0492
0,2	431	-0,0613
0,4	450	-0,0674
0,6	462	-0,0534
0,8	498	-0,0564
1	583	-0,0834

Fig. 6. The comparison of isotherms calculated from B u t l e r's model (upper curve) and from temperature-concentration relation (lower curve) describing the experimental data (asterisk) [4 – 2001Mos3]

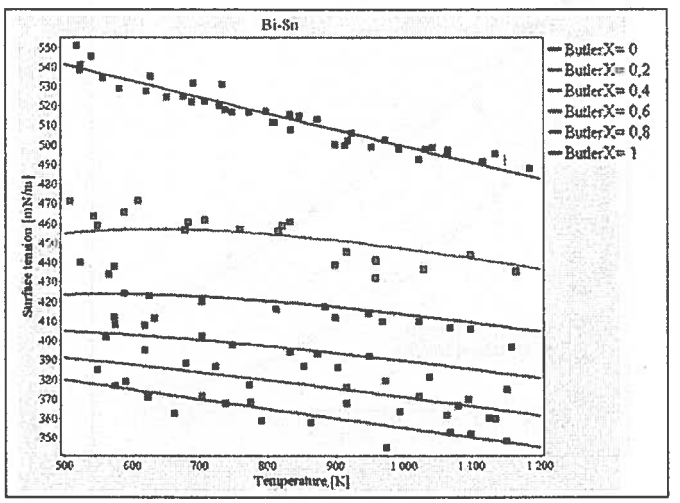

Fig. 7. The temperature dependences of the surface tension calculated from B u t l e r's model compared with the experimental data [4 – 2001Mos3]

The same options of presentation, as for surface tension (except the modeling) are possible for density (Fig.8) and molar volume (Fig. 9). In Figs.8 and 9 continuous lines were obtained from SURDAT database, and are compared with experimental data presented in [4].

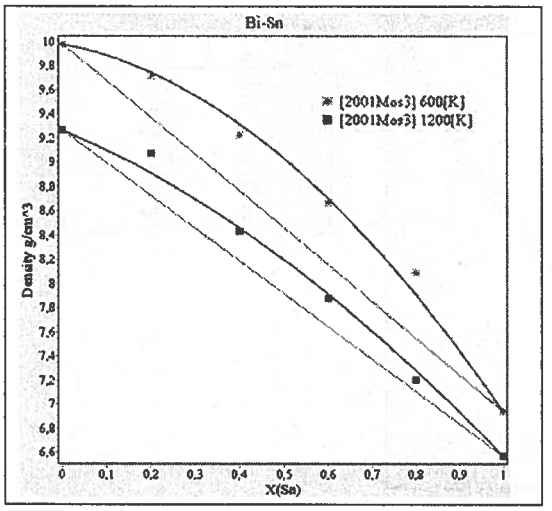

Density Bi-Sn = A+B*T

X	A	B
0	7,312	-0,00062
0,2	10,36	-0,00107
0,4	10,024	-0,00133
0,6	9,453	-0,00131
0,8	8,978	-0,00148
1	10,692	-0,00119

600[K] 1200[K] T3 T4

Density Bi-Sn [g/cm^3]

X(Sn)	d(T1)	X(Sn)	d(T2)
1	9,98	1	9,26
0,8	8,09	0,8	7,2
0,6	8,67	0,6	7,88
0,4	9,23	0,4	8,43
0,2	9,72	0,2	9,08
0	6,94	0	6,57

Fig. 8. Isotherms of the density accessed from SURDAT data base at 600 K and 1200 K compared with experimental data [4 – 2001 Mos3]

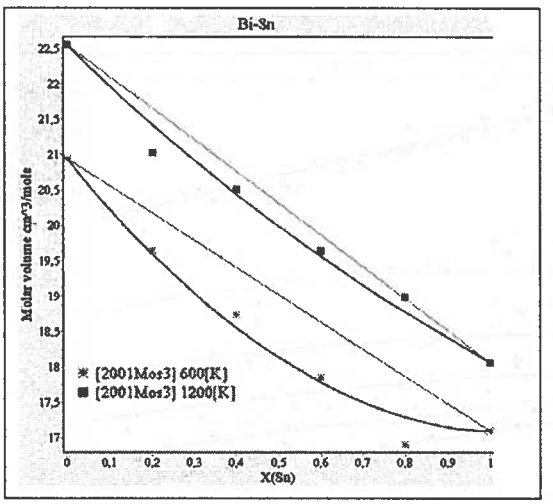

Fig. 9. Isotherms of the molar volume accessed from SURDAT database at 600 K and 1200 K together with the experimental data from [4 – 2001Mos3]

3. Summarising

The database of physical properties of the pure metals and binary, ternary, quaternary and quinary lead-free solders alloys was composed basing in most cases on the experimental data gathered by authors in last 7 years. The software co-operates with the program based on the

B u t l e r's relation for the calculation of the surface tension of liquid alloys. There are different possibilities of the overview the physical properties data. For the pure metals it is possible to have the information of the atomic weight, density and molar volume, structure at room temperature, melting and boiling points and temperature dependences of the surface tension and density. For alloys the database can present the isotherms and the temperature dependences of the surface tension and density and the calculation of the surface tension from the thermodynamic data by the Butler's model. It is also possible to make comparison between experimental and modeled data. It should be noted that in all alloys listed in Table 1, the experimental temperature dependence of the surface tension was linear, while from Butler's model, there were curvilinear. The limitations of this model were discussed in Ref.8 with the suggestion that constant values of β and L are questionable.

The development of the database will be continued in the direction to new binary, ternary and multicomponent systems and to the new physical properties including electrical resistivity, mechanical properties of solders and solders connections and modeling of other physical properties like for instance viscosity.

Acknowledgement

This work was supported by Polish Ministry of Scientific Research and Information Technology.

REFERENCES

[1] W. G ą s i o r, Z. M o s e r, J. P s t r u ś, J. Phase Equilibria **22** 20 (2001).
[2] Z. M o s e r, W. G ą s i o r, J. P s t r u ś, J. Phase Equilibria **22** 254 (2001).
[3] Z. M o s e r, W. G ą s i o r, J. P s t r u ś, W. Z a k u l s k i, I. O h n u m a, X. J. L i u, Y. I n o h a n a, K. I s h i d a J. Electronic Materials **30** 1120 (2001).
[4] Z. M o s e r, W. G ą s i o r, J. P s t r u ś, J. Electronics Materials **30** 1104 (2001).
[5] W. G ą s i o r, Z. M o s e r, J. P s t r u ś, J. Phase Equilibria **23** 504 (2003).
[6] X. J. L i u, Y. I n o h a n a, I. O h n u m a, R. K a i n u m a, K. I s h i d a, Z. M o s e r, W. G ą s i o r, J. P s t r u ś, J. Electronic Materials **31** 1139 (2002).
[7] W. G ą s i o r, Z. M o s e r, J. P s t r u ś, B. K r z y ż a k, K. F i t z n e r, J. Phase Equilibria, **24** 40 (2003).
[8] Z. M o s e r, W. G ą s i o r, J. P s t r u ś, S. K s i ę ż a r e k, J. Electronic Materials **31** 1225 (2002).
[9] W. G ą s i o r, Z. M o s e r, J. P s t r u ś, K. B u k a t, R. K i s i e l, J. S i t e k, J. Phase Equilibria and Diffusion **24** 115 (2004), (Part 1).
[10] Z. M o s e r, W. G ą s i o r, J. P s t r u ś, S. I s h i h a r a, X.J. L i u, I. O h n u m a, R. K a i n u m a, K. I s h i d a, Mater. Trans. **45** 652 (2004).
[11] W. G a s i o r, Z. M o s e r, J. P s t r u ś, Archs of Metallurgy and Materials **49** 155 (2004).
[12] Z. M o s e r, W. G ą s i o r, K. I s h i d a, I. O h n u m a, K. B u k a t, J. P s t r u s, J. S i t e k, R. K i s i e l, CALPHAD XXXIII, Program of Abstract p. 81. May 30- June 4, 2004, Kraków.
[13] J.A.V. B u t l e r, Proc. Roy. Soc. **135A** 348 (1932).
[14] G. D r a t h, F. S a u e r w a l d, Z.Anorg.Chemie. **162** 301 (1927).
[15] O. R e d l i c h, A.T. K i s t e r, Ind. Eng. Chem **40** 345 (1948).

Received: 15 June 2004.

A R C H I V E S O F M E T A L L U R G Y A N D M A T E R I A L S
Volume 49 2004 Issue 3

Z. KALICKA *, E. KAWECKA-CEBULA*, J. WYPARTOWICZ*

THE SOLUBILITY OF SULPHUR IN OXIDE INCLUSIONS IN Si AND Mn DEOXIDISED STEEL

ROZPUSZCZALNOŚĆ SIARKI WE WTRĄCENIACH TLENKOWYCH W STALI ODTLENIANEJ Si I Mn

The solubility of MnS in liquid oxide melts: $MnO-SiO_2$, $MnO-SiO_2-Al_2O_3$, $MnO-SiO_2-FeO$ and $MnO-SiO_2-TiO_2$ have been calculated from the values of MnO activity and sulphide capacity of these melts. The MnO activity in $MnO-SiO_2$ melt was based on the experimental data of Rao and Gaskell. The Ban-ya regular solution model was checked on the base of experimental data and it appeared inadequate to the $MnO-SiO_2$ liquid solution. The sulphide capacity of oxide solutions was calculated from the model of Nzotta, Sichen and Seetharaman, with exception of $MnO-SiO_2-TiO_2$ melt, for which model parameters are incomplete. It appeared that replacement of SiO_2 with Al_2O_3 and FeO decreases MnS solubility, while introduction of TiO_2 increases this solubility. The highest solubility, up to 80 mass % was obtained in binary $MnO-SiO_2$ solutions.
Keywords: steel deoxidisation, oxide liquid solution, sulphide capacity, MnS solubility.

Obliczono rozpuszczalność MnS w ciekłym roztworze tlenków: $MnO-SiO_2$, $MnO-SiO_2-Al_2O_3$, $MnO-SiO_2-FeO$ and $MnO-SiO_2-TiO_2$ na podstawie wartości aktywności MnO w tych roztworach i ich pojemności siarczkowej. Aktywności MnO w ciekłym roztworze $MnO-SiO_2$ zostały wyznaczone z danych doświadczalnych Rao i Gaskella. Na podstawie dostępnych danych doświadczalnych zweryfikowano również stosowalność modelu roztworu regularnego Ban-ya. Model ten okazał się nieodpowiedni dla opisu roztworu $MnO-SiO_2$. Pojemność siarczkowa roztworów tlenkowych została obliczona na podstawie modelu Nzotta, Sichen, Seetharaman, za wyjątkiem roztworu $MnO-SiO_2-TiO_2$, dla którego niekompletne są parametry modelu. Stwierdzono, że zastąpienie SiO_2 przez Al_2O_3 i FeO obniża rozpuszczalność MnS, podczas gdy wprowadzenie TiO_2 podnosi rozpuszczalność MnS. Najwyższe wartości rozpuszczalności, do 80% masowych, występują w przypadku roztworu dwuskładnikowego $MnO-SiO_2$.

1. Introduction

Deoxidisation of steel prior to its casting is the necessary operation, which reduces the oxygen content by a factor up to 100. During deoxidisation two kinds of oxide inclusions in

* FACULTY OF METALLURGY AND MATERIALS SCIENCE, AGH-UNIVERSITY OF SCIENCE AND TECHNOLOGY, 30-059 KRAKÓW, AL. MICKIEWICZA 30, POLAND

steel are formed, which are termed primary and secondary. Primary inclusions precipitate during pouring the steel to the ladle, where Al acts as a main deoxidiser. The main component of primary inclusions is Al_2O_3, CaO and SiO_2 are also present. These inclusions may be partly removed from liquid steel by flotation supported by inert gas flow and reaction with the slag.

Secondary inclusions precipitate during solidification of steel. They result from the reaction of dissolved oxygen with deoxidising agents: Si, Mn and Ti, which are also dissolved. These inclusions remain in steel and are unevenly distributed due to the microsegregation of components. The main components of secondary inclusions are SiO_2, MnO, TiO_2; and MnS. Such "soft" deoxidisation which leads to secondary inclusions, is applied in many cases, where the Al_2O_3 based inclusions are not acceptable and the Al_2O_3 concentration in inclusions has to be reduced below 20 mass %.

The inclusions with considerable amount of MnS play an important role in production of several steel grades. In grain oriented 3 mass % Si transformer steels the MnS inclusions control the grain boundaries and assure proper texture and magnetic properties. During austenite to ferrite transformation the MnS-rich inclusions act as nucleation sites for small ferrite grains, and thus improves the mechanical properties. The thermodynamic characterisation of oxide melts containing MnS is important for analysis of inclusions formation, growth and behaviour during heat treatment.

The aim of the present work is the calculation of MnS solubility in the liquid binary $MnO\text{-}SiO_2$ and ternary: $MnO\text{-}SiO_2\text{-}Al_2O_3$, $MnO\text{-}SiO_2\text{-}TiO_2$, $MnO\text{-}SiO_2\text{-}FeO$ solutions. However, the activity of MnO in these liquid oxide solutions has to be determined first.

2. The solubility of sulphur in liquid oxide melts

Sulphur dissolves in the liquid oxide melts according to the reaction:

$$MnO(l) + 1/2\,\{S_2\} = MnS(l) + 1/2\,\{O_2\} \qquad (1)$$

Reactions with other oxides do not occur, if the amount of MnO is sufficient for reaction (1) to proceed. The equilibrium constant of this reaction:

$$\mathbf{K_{(l)}} = \frac{\mathbf{a_{MnS}} \cdot \mathbf{p}_{O_2}^{1/2}}{\mathbf{a_{MnO}} \cdot \mathbf{p}_{S_2}^{1/2}}. \qquad (2)$$

The value of equilibrium constant was calculated from $\Delta G^0_{(l)}$ used by A b r a h a m et al [1]:

$$\log \mathbf{K_{(l)}} = -\frac{3984}{\mathbf{T}} - \frac{771.9 \log \mathbf{T}}{\mathbf{T}} + 0.6524. \qquad (3)$$

Standard state: solid MnO, solid MnS.

The maximum amount of sulphur which can be absorbed by the oxide melt of given composition at given chemical potentials of oxygen and sulphur in the phase which acts as a sulphur source is termed the sulphide capacity C_S of this slag. This property was defined by W a g n e r [2] for sulphur exchange reaction between the slag and the gas phase,

$$(O^{2-}) + 1/2\,\{S_2\} = (S^{2-}) + 1/2\,\{O_2\} \tag{4}$$

$$\mathbf{C_S} = (\mathbf{mass\ \%\ S^{2-}}) \cdot \left(\frac{\mathbf{p_{O_2}}}{\mathbf{p_{S_2}}}\right)^{1/2} = \frac{\mathbf{K_{(4)}\, a_{O^{2-}}}}{\mathbf{f_{S^{2-}}}}, \tag{5}$$

where: $\mathbf{p_{O_2}}$, $\mathbf{p_{S_2}}$ – the partial pressures of oxygen and sulphur in the gas phase in equilibrium with the slag
$K_{(4)}$ – the equilibrium constant of equation (4)
$\mathbf{a_{O^{2-}}}$ – the chemical activity of the oxygen anions, O^{2-}, in the slag
$\mathbf{f_{S^{2-}}}$ – the H e n r y's chemical activity coefficient of the sulphide anions, S^{2-}, in the slag
Combining (2) and (5) one obtains:

$$(\mathbf{mass\ \%\ S}) = \frac{\mathbf{a_{MnS}} \cdot \mathbf{C_S}}{\mathbf{a_{MnO}} \cdot \mathbf{K_{(1)}}}. \tag{6}$$

From equation (6) the solubility of MnS (in mass. %) in oxide melts may be calculated, provided that the sulphide capacity C_S and the MnO activity are known. For solid standard state the MnS activity at solubility limit (saturated solution) $a_{MnS} = 1$.

3. The sulphide capacity model

The sulphide capacity model of N z o t t a , D u S i c h e n and S e e t h a r a m a n [3,4] was used in the present work. They expressed the sulphide capacity as:

$$C_S = \exp\left(\frac{-\Delta G^0_{(4)}}{RT}\right) \cdot \exp\left(\frac{-\xi}{RT}\right). \tag{7}$$

If the exchange reaction (4) proceeds with pure liquid FeO, the $\Delta G^0_{(4)}$ is:

$$\Delta G^0_{(4)} = 118535 - 58.8157 \cdot T\,[J/mole] \tag{8}$$

The ξ parameter is composed of unary terms and binary as well as ternary interactions:

$$\xi = \sum X_i \cdot \xi_i + \xi_{mix} = X_{MnO} \cdot \xi_{MnO} + X_{Al_2O_3} \cdot \xi_{Al_2O_3} + X_{SiO_2} \cdot \xi_{SiO_2} + \\ + \xi^{MnO-Al_2O_3}_{\text{int}} + \xi^{MnO-SiO_2}_{\text{int}} + \xi^{Al_2O_3-SiO_2}_{\text{int}} + \xi^{MnO-Al_2O_3-SiO_2}_{\text{int}}. \tag{9}$$

The examples of interaction parameters values (in J/mole) are presented:
a) Unary parameters:

$$\xi_{MnO} = -3.6626 \cdot 10^4; \qquad \xi_{SiO_2} = 1.6887 \cdot 10^5; \qquad \xi_{Al_2O_3} = 1.577 \cdot 10^5 \tag{10}$$

$$\xi_{FeO} = 0 \ (\Delta G^0_{(4)} \text{ due to the convention refers to FeO}). \tag{11}$$

b) Binary interaction parameters:

$$\xi_{int}^{MnO-Al_2O_3} = y_{Mn^{2+}} \cdot y_{Al^{3+}} \cdot [4.3398 \cdot 10^5 + 2.4912 \cdot 10^2 \cdot T \cdot (y_{Al^{3+}} - y_{Mn^{2+}})]. \tag{12}$$

c) Ternary interaction parameter:

$$\xi_{int}^{MnO-Al_2O_3-SiO_2} = y_{Mn^{2+}} \cdot y_{Al^{3+}} \cdot y_{Si^{4+}} \cdot$$
$$\cdot [1.5658 \cdot 10^6 - 6.6249 \cdot 10^2 \cdot T - 5.3229 \cdot 10^6 \cdot y_{Al^{3+}}],$$

$y_{Mn^{2+}}$, $y_{Al^{3+}}$ etc. denote cationic mole fraction.
Sulphide capacities calculated from this model agree well with experimental data.
In the present work C_S for various solutions was calculated from the relation:

$$\log C_S = \frac{\Delta G^0_{(4)}}{2.303RT} - \frac{\xi}{2.303RT} = -\frac{6190.7}{T} + 3.07177 - \frac{\xi}{2.303RT}. \tag{13}$$

4. Activity of MnO in $MnO\text{-}SiO_2$ liquid solution

The regular solution model, modified by Ban-ya [5] makes the simplest way to deduce the activities of components in $MnO\text{-}SiO_2$ liquid solution. B a n - y a added the correction term I into D a r k e n ' s simple quadratic formalism of regular solution. The additional term I represents the difference in G i b b s free energy between hypothetical "regular solution state" of solution component and the state in real solution.

$$RT \cdot \ln\gamma_i = \sum_j \alpha_{ij} \cdot X_j^2 + \sum_j \sum_k (\alpha_{ij} + \alpha_{ik} - \alpha_{jk}) \cdot X_j \cdot X_k + I. \tag{14}$$

X_j, X_k are the mole fractions of oxides in the system composed of MnO, SiO_2, $AlO_{1.5}$ etc.

This energy difference should be obtained from the experimental data through the extrapolation of $RT \cdot \ln\gamma_i$ vs. $(1 - X_i)^2$ plot to pure "i" component ($X_i = 1$). For the transition: **MnO(l) → MnO(regular solution)** B a n - y a recommends the relation:

$$\Delta G^0 = -86860 + 51.465 \cdot T \quad \text{J/mole.} \tag{15}$$

This relation was obtained from the data for various binary MnO systems. However, in the case of MnO – SiO_2 solutions the experimental results from various sources lead to serious differences in values of I obtained through the above extrapolation. This is illustrated in Fig. 1, where the values of I were deduced from experimental data of A b r a h a m et al [1], R a o and G a s k e l l [6] and I t o et al [7]. They strongly deviate from the line predicted from B a n - y a formalism.

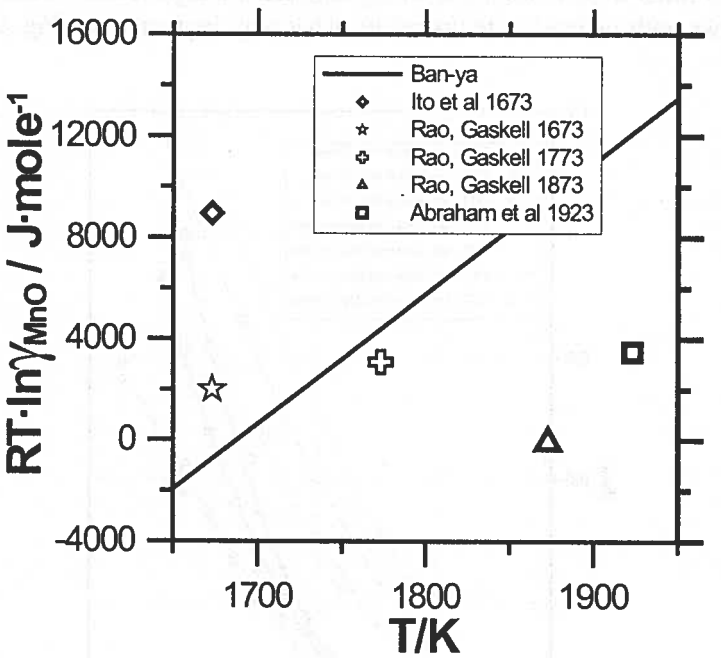

Fig. 1. Verification of B a n - y a model through the comparison with experimental data for MnO-SiO_2 liquid solution. Standard state for MnO activity – pure liquid

Actually, the values of MnO (solid standard state) activity calculated from the experimental data of R a o and G a s k e l l [6] were used in the present work. They were described as the polynomials:
For 1673 K:

$$a_{MnO} = 15.091\ X^3_{MnO} - 10.345\ X^2_{MnO} - 0.6149\ X_{MnO} + 1.1697, \quad R^2 = 0.9978 \qquad (16)$$

For 1773 K:

$$a_{MnO} = 17.197\ X^3_{MnO} - 19.844\ X^2_{MnO} + 7.8066\ X_{MnO} - 0.9376; \quad R^2 = 0.9996 \qquad (17)$$

For 1873 K:

$$a_{MnO} = 17.795\ X^3_{MnO} - 39.144\ X^2_{MnO} - 25.565\ X_{MnO} + 5.3721, \quad R^2 = 0.09936. \qquad (18)$$

In all cases the correlation factor is better than 0.99. These relations are valid only in the range of liquid phase. The data of R a o and G a s k e l l as well as their description by equations (16–18) were presented in Fig. 2, in comparison with the experimental results of I t o et al [7] and the activities calculated from B a n - y a model. The activities described in equations are slightly lower then these determined by I t o et al, and much lower than these deduced from B a n - y a model. Moreover, the B a n - y a model yields in the case of $MnO\text{-}SiO_2$ solution the wrong temperature dependence of activity; the MnO activity grows with increasing temperature, what may be noticed in Fig. 2.

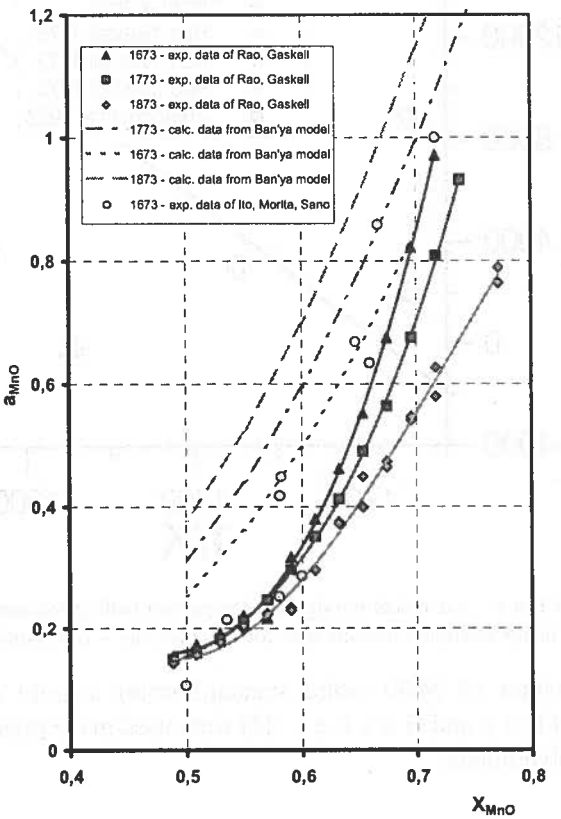

Fig. 2. Activity of MnO in liquid solutions $MnO\text{-}SiO_2$. Heavy lines represent equations (16)-(18). Standard state for MnO activity – pure solid.

5. Sulphur solubility in binary and ternary oxide melts

a) $MnO\text{-}SiO_2$

The solubilities of MnS in binary $MnO\text{-}SiO_2$ melt at the temperature 1673, 1773 and 1873 K calculated from MnO activities given by R a o and G a s k e l l

[6] are presented in Fig. 3. Experimental points of MnS solubility are from publication of H a s e g a w a et al. [8].

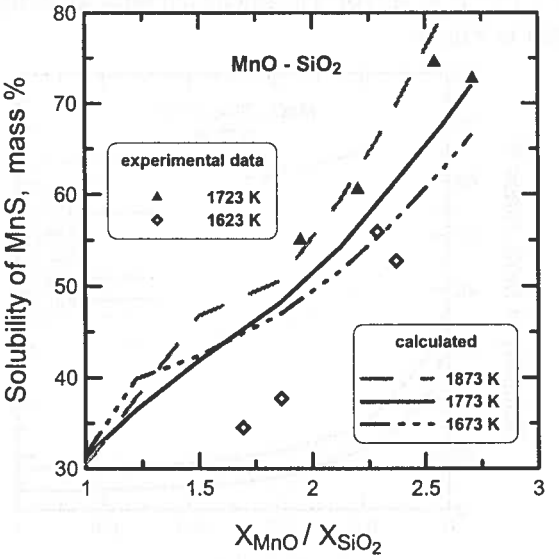

Fig. 3. Solubility of MnS liquid solutions $MnO-SiO_2$

b) $MnO-SiO_2-Al_2O_3$

The MnO activity in $MnO-SiO_2-Al_2O_3$ was calculated for temperature 1823 K from the data of J u n g et al. [9]. The calculated MnS solubility at 1773 K was presented in Fig. 4.

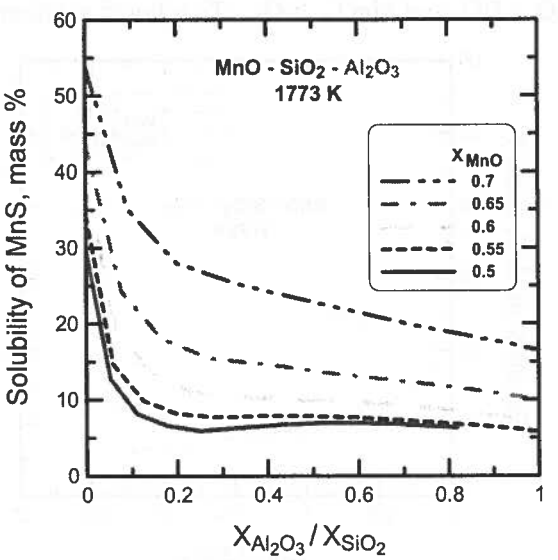

Fig. 4. Solubility of MnS in liquid solution $MnO-SiO_2-Al_2O_3$

c) $MnO-SiO_2-FeO$

The MnO activity in $MnO-SiO_2-FeO$ melt was calculated at 1823 K from experimental data of S o m m e r v i l l e et al [10]. The calculated MnS solubility for the temperature 1773 K was presented in Fig. 5.

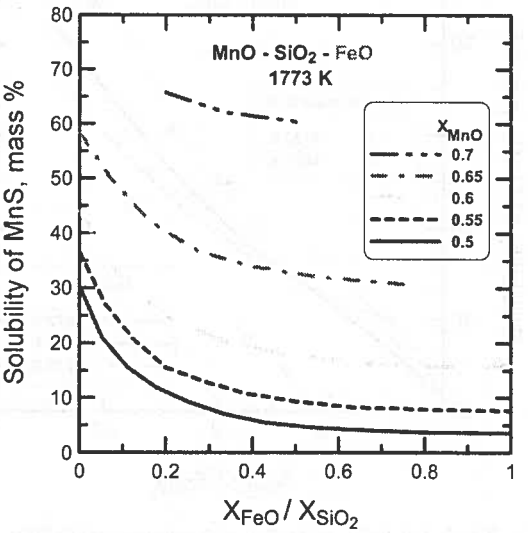

Fig. 5. Solubility of MnS in liquid solutions $MnO-SiO_2-FeO$

d) $MnO-SiO_2-TiO_2$

The MnO activity in $MnO-SiO_2-TiO_2$ melt was deduced from experimental data of I t o et al. [7] for temperature 1673 K. Due to the lack of model parameters sulphide capacities C_S of $MnO - TiO_2$ and $MnO - SiO_2 - TiO_2$ liquid solutions were adopted from

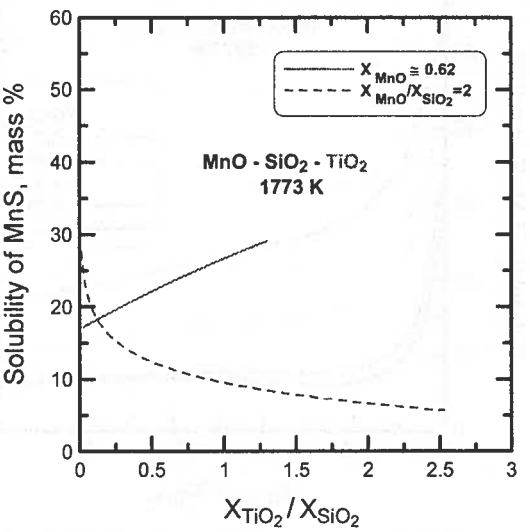

Fig. 6. Solubility of MnS in liquid solutions $MnO-SiO_2-TiO_2$

experimental data of K i m et al.[11] for temperature 1723 K and Ito et al. [7] for temperature 1673 K, respectively. The calculated MnS solubility at 1773 K is demonstrated in Fig. 6.

6. Conclusions:

- The solubility of MnS in oxide melts is roughly proportional to MnO content, as it is directly created in simple exchange reaction.
- This solubility is modified through the composition of oxide solution.
- The highest values of solubility, up to 80 mass % are obtained in binary MnO-SiO_2 melts.
- Substitution of FeO or Al_2O_3 in place of SiO_2 results in decrease of MnS solubility. This effect is stronger in the case of Al_2O_3.
- In the contrary, introduction of TiO_2 in place of SiO_2 seems to increase the MnS solubility.
- Thus the Mn-Si-Ti deoxidiser assures the best conditions for „soft" deoxidisation and production of inclusions rich in MnS.

Financial support by the Polish State Committee for Scientific Research (contract nr 11.11.110.498. – AGH) is gratefully acknowledged.

REFERENCES

[1] K.P. A b r a h a m, M.W. D a v i e s, F.D. R i c h a r d s o n, J. Iron Steel Inst. (London) **196**, 309-312 (1960).
[2] C. W a g n e r, Met. Trans. B. **6B**, 405-409 (1975).
[3] M.M. N z o t t a, Du S i c h e n, S. S e e t h a r a m a n, ISIJ Int. **38**, 1170-1179 (1998).
[4] M.M. N z o t t a, Du S i c h e n, S. S e e t h a r a m a n, Mat. Trans. B **30B**, 909-920 (1999).
[5] S. B a n - y a, ISIJ Int. **33** 2-11. (1993).
[6] B.K. R a o, D.R. G a s k e l l, Met. Trans. B **12B**, 311-317 (1981).
[7] M. I t o, K. M o r i t a, N. S a n o, ISIJ Int. **37**, 839-843 (1997).
[8] A. H a s e g a w a, K. M o r i t a, N. S a n o, T e t s u - t o - H a g a n e **81**, 1109 (1995), cited in: Z. Liu, K. Gu, K. Cai, ISIJ Intern. **42** 950-57 (2002)..
[9] I.H. J u n g, Y.B. K a n g, S.A. D e c t e r o v, A.D. P e l t o n, Met. and Mat. Trans B **35B**, 259÷268 (2004).
[10] J.D. S o m m e r v i l l e, I. I v a n c h e v, H.B. B e l l, Slag Atlas VDEh, Verlag Stahleisen M.B.H. Düsseldorf (1981).
[11] T.G. K i m, W.K. L e e, J.H. P a r k, D.J. M i n ., H.S. S o n g, ISIJ Int. **41**, 1460÷64 (2001).

Received: 15 Juni 2004.

A R C H I V E S O F M E T A L L U R G Y A N D M A T E R I A L S
Volume 49 2004 Issue 3

J. IWANCIW *

THE COEFFICIENTS OF REGULAR SOLUTION MODEL FOR STELMAKING SLAGS

WSPÓŁCZYNNIKI MODELU ROZTWORU REGULARNEGO DLA ŻUŻLI STALOWNICZYCH

The models of steelmaking processes applied to the technology aiding in the real time demand a compromise between precision and pace of calculations. This work reports an attempt to satisfy this compromise by the use of regular model concept to fast evaluation of slag component activity with acceptable accuracy. Regular solution model is the simplest way to describe deviations of any solution from the ideal behavior as it takes into account the interactions between the components of the solution, assuming the mixing entropy equal to the ideal one. Three-stage route of systematic determination of model parameters $H_i^{'}$, $S_i^{'}$ and $Q_{ij} = Q_{ji}$ coefficients is proposed. Enthalpy $H_i^{'}$ and entropy $S_i^{'}$ of melting for selected 8 oxides were optimized by application of the so called "Richard's rule", modified and generalized for all oxides. Lacking coefficients $Q_{ij} = Q_{ji}$ for some oxides (Cr_2O_3 systems, some of TiO_2 systems) has been determined. The activity model of slag components proposed by the author is quick enough to be used as support of steelmaking technologies in the real time.

Keywords: ideal solution, solution model, activity coefficient, oxide system, steelmaking slag, process simulation, technology aiding, real time

Modele procesów stalowniczych stosowane do wspomagania technologii w czasie rzeczywistym wymagają kompromisu pomiędzy dokładnością i szybkością obliczeń. Niniejsza praca przedstawia próbę znalezienia takiego kompromisu poprzez zastosowanie koncepcji modelu roztworu regularnego do szybkiego oszacowania aktywności składników żużla z wystarczającą dokładnością. Model roztworu regularnego stanowi najprostszy sposób opisu odchyleń dowolnego roztworu od jego doskonałego zachowania, jako że uwzględnia wzajemne oddziaływania pomiędzy składnikami roztworu przy założeniu entropii mieszania równej entropii w roztworze doskonałym. Zaproponowano 3-etapowy system wyznaczania parametrów modelu $H_i^{'}$, $S_i^{'}$ oraz $Q_{ij} = Q_{ji}$. Przez zastosowanie tzw. „R e g u ł y R i c h a r d a", zmodyfikowanej dla wszystkich tlenków zoptymalizowano indywidualne wartości entalpii $H_i^{'}$ i entropii $S_i^{'}$ topnienia dla każdego z wybranych 8-miu tlenków. Wyznaczono brakujące współczynniki $Q_{ij} = Q_{ji}$ dla niektórych tlenków (układy zawierające Cr_2O_3, niektóre układy zawierające TiO_2). Proponowany przez autora model aktywności składników żużli jest wystarczająco szybki do zastosowania w narzędziach wspomagania technologii w czasie rzeczywistym.

* FACULTY OF METALLURGY AND MATERIALS ENGINEERING, AGH-UNIVERSITY OF SCIENCE AND TECHNOLOGY, 30-059 KRAKÓW, AL. MICKIEWICZA 30, POLAND

1. Introduction

The motoric force of any reaction, also in metallurgy, is the distance from the equilibrium state. When reaction is at the beginning, the transport factors (diffusion, mixing) and reaction rate constant play the main role of the reaction progress, but when reaction goes near the equilibrium state, the exact knowledge of equilibrium concentrations of all reactants is particularly important [1]. Besides of temperature and activity of reacting components in metal solution, the activities of the oxidation products are important factors for the oxidation/reduction reactions between metal and nonmetallic phase (slag or nonmetallic inclusions).

For simulation of steelmaking processes in the real time [2] more sophisticated, time consuming models are rather useless, so this author looked for simple, but reasonably well fitting models of the oxides solution components' activities better than "ideal solution" model.

The first possibility was the offered by empirical models proposed for fast calculations by K a w e c k a [3,4]. These equations fit very well the experimental data, but unfortunately only in specified concentration ranges and temperatures (with no temperature dependences). The regular solution model was then selected and used below.

2. Regular solution models

The activity of a slag component is usually expressed as the function of its mole fraction multiplied by the chemical activity coefficient:

$$a_i = \gamma_i \cdot X_i . \tag{1}$$

The regular solution model is the simplest way to describe deviations of any solution from the ideal behavior as it takes into account the interactions between the components of the solution, assuming the mixing entropy equal to the ideal one. Therefore, when considering a liquid reference state of the component, its activity coefficient for the regular solution model is related only to the mixing enthalpy, which can be expressed by the following equation:

$$\Delta \bar{G}_i^E = \Delta \bar{H}_i = RT \ln \gamma_i \qquad (\Delta \bar{S}_i^E = 0). \tag{1a}$$

Assumption of the same interaction energy ($Q_{ij} = Q_{ji}$) between two components leeds to only one coefficient for each pair of components. For multi-component system the model equation takes the form [5]:

$$RT \ln \gamma_i = \sum_j Q_{ij} X_j^2 + \sum_j \sum_k (Q_{ij} + Q_{ik} - Q_{jk}) X_j X_k , \tag{2}$$

where: X_j, X_k – *the mole fractions of j,k-cations,*
Q_{ij}, Q_{ik}, Q_{jk} – *the interaction energies between respective pairs of particles (cation i-O-cation j – for the case of slag),*
R – *absolute gas constant,*
T – *temperature (K).*

For binary solution, the equation (2) reduces to the simple D a r k e n ' s square formalism:

$$RT \ln \gamma_i = Q_{ij} X_j^2 = Q_{ji} X_j^2 . \tag{2a}$$

If the melting point of a component is higher then the temperature of slag, the change of reference state have to be included into model equation by addition of the terms of a temperature dependent free enthalpy (enthalpy and entropy) of the component melting:

$$RT \ln \gamma_i = \sum_j Q_{ij} X_j^2 + \sum_j \sum_k (Q_{ij} + Q_{jk} - Q_{jk}) X_j X_k - (\Delta H_i^m - T\Delta S_i^m) , \tag{3}$$

where : ΔH_i^m, ΔS_i^m – *standard melting enthalpy and entropy of i-component, respectively*

This formal manipulation gives us an opportunity to take into account asymmetrical interactions observed in real slag systems [6]. K a w e c k a [3] reported several recent examples of regular solution model variants for modeling of the activities of slag components. Ban-ya [7] proposed artificial (without physico-chemical meaning) so-called "conversion factor", I' (table 1a), instead of the free enthalpy of component melting:

$$RT \ln \gamma_i = \sum_j a_{ij} X_j^2 + \sum_j \sum_k (a_{ij} + a_{ik} - a_{jk}) X_j X_k + I_i' . \tag{3a}$$

Additional asymmetry in the regular model appears, when the slag composition is specified by the cationic fraction instead of the molar one. It is expressed on some reported activity diagrams [6] ($AlO_{1.5}$ instead of Al_2O_3) and it was attempted to bring together the model with ionic structure of slags. For example, L u m s d e n [5] assumed, that oxides dissociate totally into simple metal cations and oxide anions O^{2-} while cations (like Ca^{2+}, Fe^{2+}, Fe^{3+}, $Al3^{3+}$, Si^{4+} and others) are distributed in random in the matrix of the oxide anions, which are common to the all cations occurring in the slag. Thus the concentration has to express the number of cations, i.e., to be set by the cationic fraction, $X_{M_zO_w}$, later called "*regular solution (cationic)*" model, defined as follows:

$$a_{M_zO_w} = (a_{MO_{w/z}})^z , \tag{4}$$

where : z – *the number of metal atoms in one particle of the oxide.*

Another asymmetry is noted after recalculation of the slag composition expressing cationic ratio per one oxygen anion (O^{2-}) in each oxide, $X_{M_zO_w}$, later called ("*regular solution anionic*") model (another variant of Lumsden's "common anion model"), thus:

$$a_{M_zO_w} = (a_{MO_{w/z}})^w, \tag{4a}$$

where : w — *the number of oxygen atoms in one particle of the oxide.*

Jowsa [8] applied cationic model for steelmaking slags using B a n - y a's coefficients (table 1a), as well as enthalpy and entropy of melting data reported by Gaye and Welfringer [9] and he proposed some corrections in the model coefficients database (table 1b).

3. The investigation range and models selection

The analysis presented there considers the selected empirical correlations existing in the literature as well as those resulting from the regular model for the activities of typical components of steel-making slags such as CaO, SiO_2, Al_2O_3, MnO and FeO. As for MgO, Cr_2O_3 and TiO_2 there is no empirical correlations, the authors proposed some correlations based on accessible literature data.

The following models were considered:

1. Ideal solution (only ~1600°C),
2. Multi-regression – K a w e c k a [3] (only ~1600°C),
3. Infinite solution in CaO [10] (only ~1600°C),
4. Regular solution (cationic) – database after B a n - y a [5],
5. Regular solution (cationic) – database after J o w s a [8],
6. Regular solution (cationic) – new database by I w a n c i w,
7. Regular solution (anionic) – new database by I w a n c i w.

The model 1 (ideal solution), 2 (multi-regression) and 3 (infinite solution) were used only for comparison. Other four models (4 to 7) are of the same type (regular solution) and differ only in the database of coefficients used or in the kind of ionic activity (cationic or anionic). The use of the cationic fraction or anionic fraction in these model variants instead of the mole fraction allows us to achieve proper asymmetry without using additional parameters.

The way of estimation and optimization of the coefficients' database applied for the last two models (6 and 7) will be presented below. For this purpose the special software was prepared enabling visualization of model results in binary and ternary systems with possibility of taking into consideration additional other components [10,11]. All these tools use the same new procedure of slag model containing all 7 variants, as will be used in the programs for aiding technology in the real time.

The application of the regular solution model to steel-making slags requires the full set of coefficients H_i, S_i and Q_{ij}. In the sets proposed by B a n - y a [2] and J o w s a [3] there are some gaps (zero values), particularly for the chromium and titanium oxides, as well as B a n - y a ' s "conversion factors" for alumina and titania are not known there (Table 1a and 1b).

TABLE

Databases for regular solution model coefficients

	"Conv.Fact"- 1st term. analogy to H_melt.	"Conv.Fact"- 2nd term. analogy to S_melt.	Calculate analog of T_melt. = =1st/2nd	a) Ban-Ya			Model 4				
	Ban-Ya 1993	Ban-Ya 1993	(model constant)	Parameters Q (alpha) for regular aolution model							
Oxide	J/mole	J/mole/K	K	Al2O3	CaO	Cr2O3	FeO	MgO	MnO	SiO2	TiO2
Al2O3				0	-154810	–	-41000	-71130	-83680	-127610	–
CaO	18 160	23.309	*779*	-154810	0	–	-31380	-100420	-92050	-133890	-167360
Cr2O3				–	–	0	–	–	–	–	–
FeO	*-8 540*	-7.142	*1196*	-41000	-31380	–	0	33470	7110	-41840	-37660
MgO	34 350	16.736	*2052*	-71130	-100420	–	33470	0	61920	-66940	–
MnO	*-32 470*	-26.143	*1242*	-83680	-92050	–	7110	61920	0	-75310	-66940
SiO2	27 030	1.983	*13631*	-127610	-133890	–	-41840	-66940	-75310	0	104600
TiO2				–	-167360	–	-37660	–	-66940	104600	0

	H_melt.	S_melt.	Calculate T_melt. = H_melt. *I* S_melt.	b) Jowsa			Model 5				
	Gaye, Welfringer 1984	Gaye, Welfringer 1984		Parameters Q (alpha) for regular aolution model							
Oxide	J/mole	J/mole/K	K	Al2O3	CaO	Cr2O3	FeO	MgO	MnO	SiO2	TiO2
Al2O3	110 876	47.6976	2325	0	-154810	–	-41000	-71130	-83680	-127610	–
CaO	18 333	28.2420	2844	-154810	0	–	-31380	-100420	-92050	-133890	-167360
Cr2O3				–	–	0	–	–	–	–	–
FeO	8 222	4.1840	1965	-41000	-31380	–	0	33470	2000	-41840	-37660
MgO	77 404	25.0203	3094	-71130	-100420	–	33470	0	61920	-66940	–
MnO	50 208	23.4722	2139	-83680	-92050	–	2000	61920	0	-75310	-59500
SiO2	9 540	4.7698	2000	-127610	-133890	–	-41840	-66940	-75310	0	104600
TiO2				–	-167360	–	-37660	–	-59500	104600	0

	Calculated. H_melt. = 10*Tt*(Ik+Ia) Iwanciw 1999	Calculated S_melt. 10*(Ik+Ia) Iwanciw 1999	T_melt. Kuba-schewski 1979	c) Iwanciw Model 6 & 7 Parameters Q (alpha) for regular aolution model							
Oxide	J/mole	J/mole/K	K	Al203	CaO	Cr2O3	FeO	MgO	MnO	SiO2	TiO2
Al203	*116 208*	50	2324	0	-70000	45000	2000	-20000	-8000	-87000	4000
CaO	*57 763*	20	2888	-70000	0	-63000	-18000	23000	12000	-132000	-135000
Cr2O3	*126 908*	50	2538	45000	-63000	0	6000	-27000	–	61000	–
FeO	*33 023*	20	1651	2000	-18000	6000	0	11000	3000	-42000	-22000
MgO	*61 963*	20	3098	-20000	23000	-27000	11000	0	5000	-78000	-60000
MnO	*42 963*	20	2148	-8000	-12000	–	3000	5000	0	-75000	-55000
SiO2	*80 000*	30	*2666*	-87000	-132000	61000	-42000	-78000	-75000	0	15000
TiO2	*64 295*	30	2143	4000	-135000	–	22000	-60000	-55000	15000	0

Legend:

116208 or 50	–	values calculated from separate model
2666	–	hipothetical "melting temperature" for silica because of monotectic (2 liquids) region
61920	–	recom,mended values by Jowsa, identical values taken by Ban-Ya and Jowsa
13631	–	only model constants, without physico-chemical meaning

The lack of physicochemical meaning of B a n - y a ' s "conversion factors" [5] – not consistent with physicochemical properties of oxide melting is dangerous from theoretical point of view. The values of "analog of melting temperature" (the fourth column of Table 1a) calculated from "conversion factors" indicate in some cases abnormal temperature dependence, for example in the case of FeO the liquid state as reference should be used in temperatures over its real melting point (about 1380°C), but "conversion factors" are used regardless of the temperature of solution. The very high value of "analog of melting temperature" for silica may cause improper model results in the temperatures much higher than 1600°C, particularly in SiO_2 rich corner.

There may be also questionable the use by J o w s a [8] of B a n - y a ' s coefficients Q_{ij} [5] together with H_i and S_i after G a y e and W e l f r i n g e r [9] instead of "conversion factors".

All the mentioned above reasons prompted the authors to make a more systematic determination of the all coefficients needed by the model of regular solution, which will be reviewed below. A new set of the obtained coefficients for the 8 slag constituents according to the task of this work is presented in Table 1c.

4. A systematic way of determination of regular solution model coefficients

Taking into consideration the specific structure of the regular solution model and looking for the best consistency of all parameters:

- the individual constants H and S for each oxide,
- the individual parameter Q for each pair of oxides in spite of the number of oxides in multi-component systems,

a 3-stage route (Fig. 1.) for systematic determination of H_i, S_i and $Q_{ij} = Q_{ji}$ coefficients is proposed below.

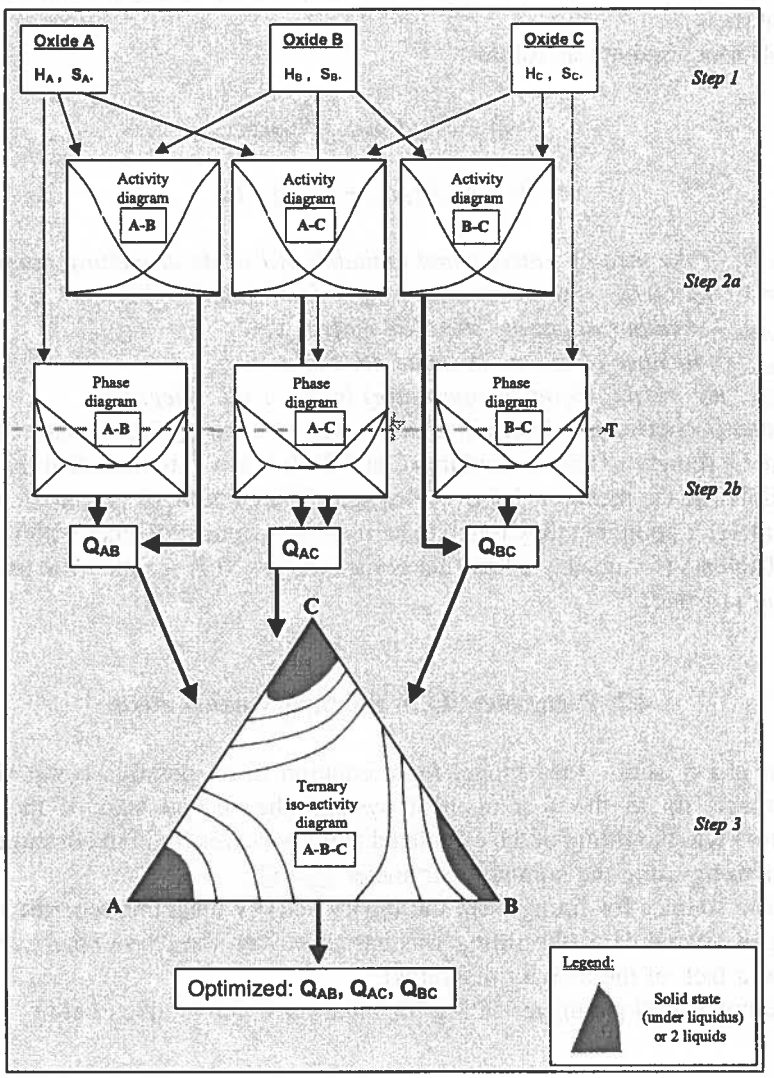

Fig. 1. Scheme of systematic route of coefficients determination for regular solution model of steelmaking slags

4. Standard melting enthalpy and entropy of oxides

At first the individual enthalpy H_i and entropy S_i of melting for the selected 8 oxides was optimized by use of all available data [12–14]. As mentioned earlier, these constants are taken into consideration for each oxide when temperature of solution is lower then the melting point of the considered oxide (solid state reference).

There was adopted so called "Richard's rule" [13], modified by author [15] for oxides, which allows to predict the melting enthalpy from only melting temperature data, which are probably the most available and trustworthy (in comparison with experimental enthalpy and entropy data).

The relations used are as follow:

$$S_i = A \cdot (n_{\text{cation}} + n_{\text{anion}}) \tag{5}$$

$$H_i = A \cdot (n_{\text{cation}} + n_{\text{anion}}) \cdot T_m \tag{5a}$$

where: S_i, H_i – *the melting entropy and enthalpy of i-oxide at melting point,*
$A = 10$ *J/mole/K – constant entropy per 1 ion (modified R i c h a r d ' s rule),*
n_{cation} – *number of cations in oxide molecule,*
n_{anion} – *number of anions in oxide molecule*
T_m – *the melting point (temperature) in K e l v i n degrees.*

The S_i and H_i coefficients determined in this way by author [1] on the base of eq. (5) and eq. (5a) can be found in Table 1c (column 2 and 3). It is worth to note, that the author met problem similar to the mentioned above of S_{SiO2} and H_{SiO2} coefficients consistency with the real silica melting point, but they found to be the best working together with the full set of $Q_{i,SiO2}$ coefficients (fortunately silica rich corner ($X_{SiO2} > 0.7$) is rather not used in recent steelmaking practice).

4.2. Parameters Q in the binary oxide melts

Assuming a possibly good model representation in all possible composition in the binary, ternary, up to the 8-component system, the second step of the coefficient determination was the fitting of the calculated activity curves for both constituents in each binary system by using the common parameter $Q_{ij} = Q_{ji}$.

The basic sources for fitting were the binary activity diagrams reported in literature (6,14), but in several cases the fitting was based only on the phase binary diagrams [6] (because of a lack of the activity diagrams).

The example of Q parameter fitting for binary solution is given below.

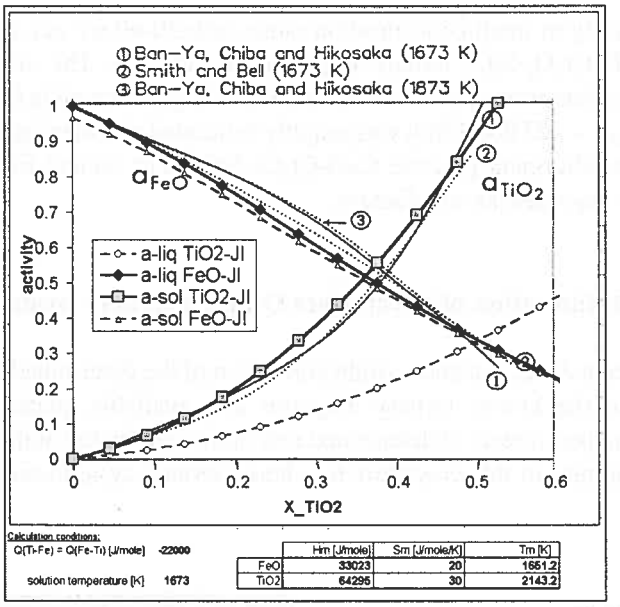

Fig. 2. Example of parameter $Q_{FeO\text{-}TiO2}$ fitting in binary system FeO-TiO2. The solid and liquid state reference is taken into consideration (curves with points of activity calculated by author and numbered curves on the background taken from [6])

It may be seen on the presented example that the choice of reported curves, as the base for model fitting, is difficult and standard statistical approach may not lead to optimal values of model parameters. For this reason, the 'curve shape fitting" method, not very theoretical, but more effective, was adapted to fitting the common properties of various source curves in the all regions, independently of the number and dispersion of the source points.

For the same reason, there was assumed the fitting of the Q parameters in the ternary systems (third step, section 4.3) and again checking the new value of Q in the binary system. If the new model curve was situated still among the source curves, the new value was fixed as model parameter. If not, this procedure was continued until the best fitting both in the binary and ternary systems was achieved. Such a manner we named "optimization of Q parameters".

In some cases, where the data of oxide activities were not available, the phase diagrams (binary or ternary) were used according to the rule, that during near equilibrium melting the activity of component in liquid solution is nearly equal to its activity in solid phase. For example: above 1600 C in the CaO reach region, the solid pure CaO (R a o u l t ' s activity equal to 1) may exist together with the liquid solution with CaO-Al_2O^3 and in this case the activity of CaO in this solution may be assumed to be equal to 1 on the liquidus curve.

The binary system CaO-Cr_2O_3 is the example of the necessity of Q coefficient estimation from phase diagram. This system is rather not used as binary solution in metallurgical slag practice (too high liquidus lines, liquid phase down to about 1060 C some

authors [6] show only in small concentration range near 50-60 wt. pct. of Cr_2O_3), which is also seen on $CaO-Cr_2O_3-SiO_2$ ternary diagram [6] (Fig. 3). The source data are not consistent; this problem was reported and the model fitting discussed in [16]. In this way the parameter $Q_{CaO\text{-}Cr2O3}$ = -63 000 J/mol was roughly estimated and then optimized for ternary system used in metallurgical practice $CaO-Cr_2O_3-SiO_2$ (Fig. 3) and finally the representation curves was regarded as satisfactory.

4.3. Optimization of parameters Q in the ternary oxide melts

In the third step a check out and a slight correction of the determined Q parameters was done according to the known ternary diagrams and available quaternary diagrams or cross-sections. The parameters Q determined and optimized by the author are given in the Table 1c. The examples of this procedure for chosen ternary systems are presented on Fig. 3 and Fig. 4.

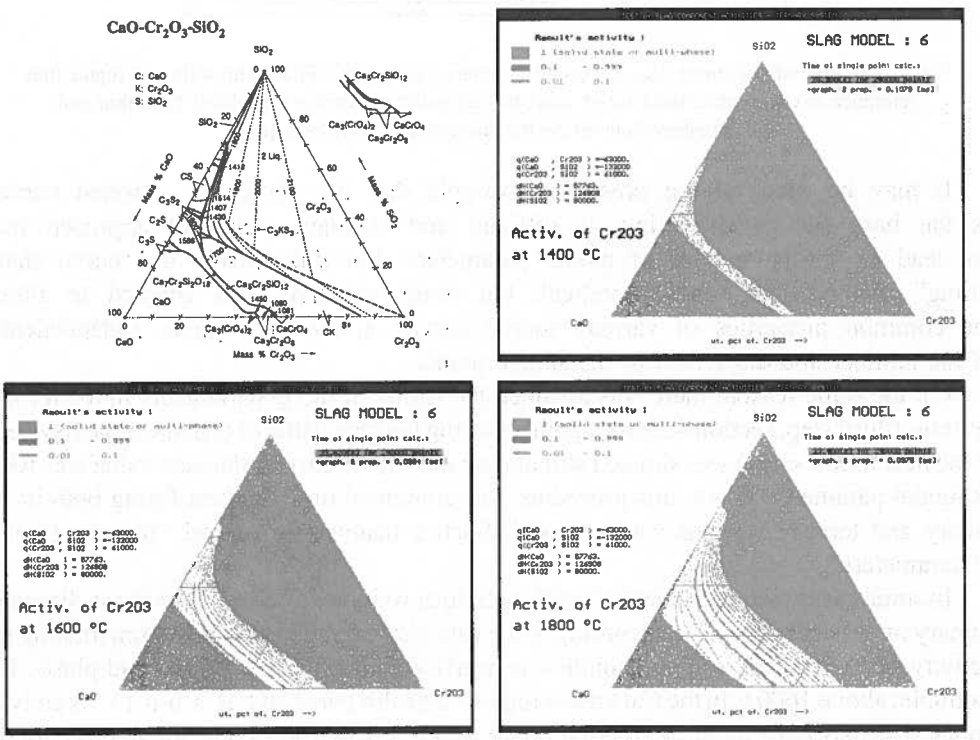

Fig. 3. Comparison of ternary phase diagram taen from [6] for $CaO-Cr_2O_3-SiO_2$ system with iso-activity diagrams obtained from model 6 (regular solution) for various temperatures. The gray zones indicate regions of solid state or 2 liquids in the system

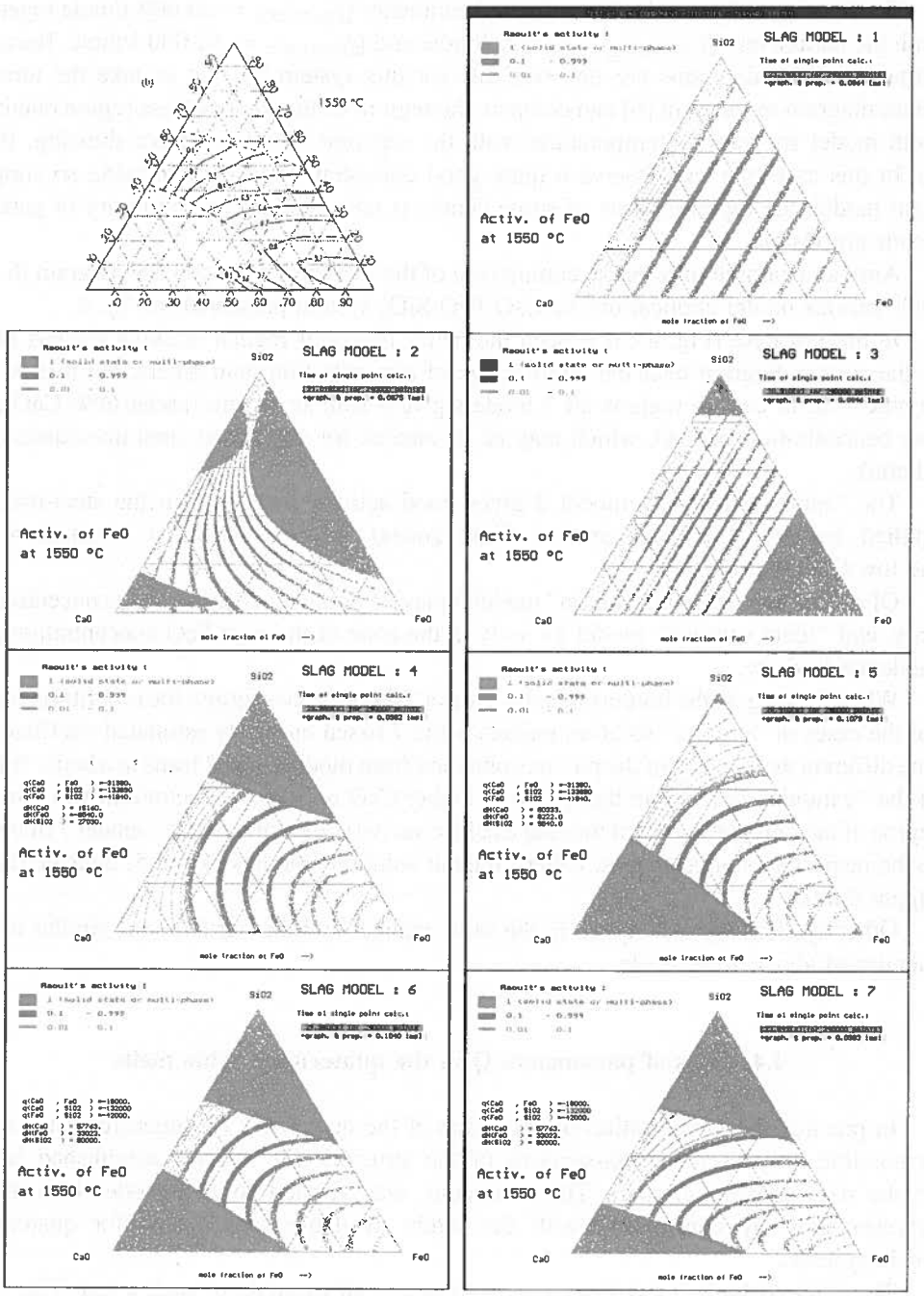

Fig. 4. Diagrams of FeO iso-activities according to various tested models (color or gray lines and zones) in ternary system CaO, FeO and SiO_2 (no other components) in the comparison with data from literature (thin black lines – left upper drawing [6])

To illustrate it let us take the estimated parameter $Q_{CaO\text{-}Cr2O3}$ = -63 000 J/mole together with the parameters $Q_{CaO\text{-}SiO2}$ = -132 000 J/mole and $Q_{Cr2O3\text{-}SiO2}$ = -61 000 J/mole. Because ternary activity diagrams are not available for this system too, let us take the ternary phase diagram reported in [6] and compare the regions of liquid one-phase region obtained from model for various temperatures with the reported liquidus surface drawing. (Fig. 3). In this case one can observe a quite good consistency. Of course, using so simple, rigid model, the representation of some details is not possible, but similarity of general trends are visible.

Another example may be the comparison of the known activity ternary diagram [6,14] with various model applications to CaO-FeO-SiO_2 system presented in Fig. 4.

In the last case (Fig. 4), it is seen the better fitting of regular solution models (4-7) to the source diagram over the entire range of concentration than others, but it is worth to note, that in certain regions all 7 models give a similar picture (about 60% CaO and low concentration of FeO, which may be of interest for slags after steel deoxidation by silicon).

The "multi-regression" model 2 gives good activity map only in the steel-making applied regions (low FeO or low SiO2 zones), but is absolutely inconsistent in the low CaO region.

Of course the "infinite solution" model 3 may be applied in the low FeO concentration only, and "ideal solution" model 1 – only in the zone of the high FeO concentration and moderate basicity.

When looking on the borders of solid state or 2-liquid zones (gray), the best fitting exists for the cases of "regular" solution models 6 and 7 based on newly estimated coefficients. The different asymmetry of the pictures obtained from model 6 and 7 leads to a better fitting of the "cationic" model 6 in the region of higher CaO or SiO_2 concentration, while in the region of the high FeO content the shapes of iso-activity lines of 'anionic" model 7 fit better to the respective source shapes. Other "regular solution" models (4 and 5) indicate rather bigger faults.

Other systems were analyzed in the same manner and the observations similar to the mentioned above were made.

4.4. Tests of parameters Q in the quaternary oxide melts

In practice the visualization on the plane of the quaternary (4-dimension) structures is possible only as the cross-sections of the structure for selected established levels of the 4-component content. This technique was applied to test model iso-activity representation by comparison with the rarely available source data for quaternary oxide systems.

The CaO-Al_2O_3-SiO_2-MgO system is shown as an example of such a test (Fig. 5).

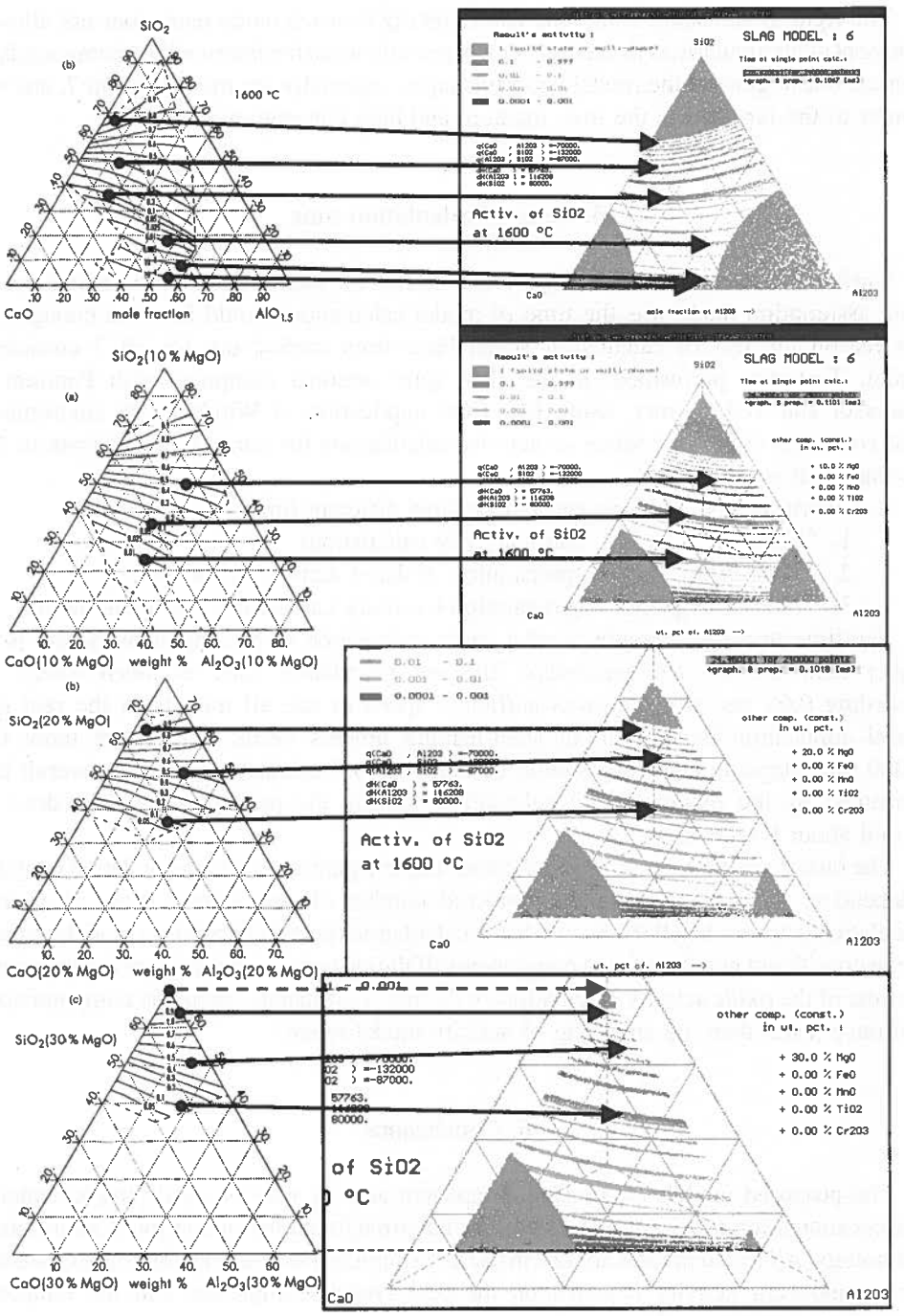

Fig. 5. The best (model 6) fitting of silica activity in the CaO-Al_2O_3-SiO_2-MgO system (0, 10, 20 and 30% Mg0) in comparison with the source iso-activity diagrams [6]

The rigid model shape (only one coefficient Q for each oxide pair) does not allow to represent all particularities in each system, especially when the intermediate compounds are formed, but in general the model activity shapes, especially for models 6 and 7, are very similar to the reported in the low, medium and high concentration regions.

5. Tests of calculation time

During the selection of the slag models useful for applications in the real time, the main assumption made was the time of model calculation should be short enough. For this reason the test of calculation speed have been carried out for all 7 considered model. Test was performed on the IBM type personal computer with Pentium III processor and 1GHz timer, using MS DOS application in Windows 98 environment. Test consisted of several series of activity calculations for various components in 2 to 8 component systems.

It is worth to note, that we can obtain three different times of calculations:

1. "*Time-net*" (only activity calculation)
2. "*Time-brut*" (preparation of data+ activity calculation)
3. "*Time-brut-graph*" (preparation+ activity calculation + graphic output)

The time brut (with graphics) of a single calculation in 8-component system is not higher than 0.1 ms (milliseconds). The net calculation time is much lower, not exceeding 0.05 ms, which proves sufficient speed to use all models in the real time model application (simulation of steel-making process needs usually not more than 20000 time steps, in each step should be done up to 8 calculations, so, the overall time consumed by the oxide activity calculations during the process simulation does not exceed about 8 seconds).

The fastest are the models 1 to 3 based on simple equations with the number of constants independent on temperature and considered number of components (time of a single calculation is lower than 0.01 ms, while the calculation for regular solution models depends on the considered number of slag components. If the system is enlarged over 8 components, the time of the oxide activity calculations will raise. Fortunately, probable computer speed will raise faster then the enlarging of activity model range!

6. Conclusions

The proposed models of the slag component activity may be easily implemented in process simulation programs and used in the real time for aiding or control of steel-making technology. All tested models are fast in use and simplified as possible, thus the exactness of each component activity depends on the real system complexity and the temporary component contents in slag.

The most safe in use over the entire range of composition and in a wider range of temperatures is the model based on solid but rather rigid theoretical bases named Model

6 – regular solution (cationic) with checked set of coefficients Table 1.c), whose implementation was shown earlier. Other tested variants of regular models need extra effort to fit all necessary coefficients.

The most exact in certain ranges of slag composition and one of the fastest, but applied only near the temperature 1600C is Model 2 – derived statistically from experimental data by K a w e c k a [3].

The fastest are the simplest models: Model 1 – ideal solution and Model 3 – infinite solution in CaO, but they may be used only for very fast applications destined to process simulation in the conditions very far from equilibrium state, when the relative error of equilibrium state estimation is small in comparison to the deviation from equilibrium.

Financial supports by the Polish State Committee for Scientific Research (contract AGH nr 11.11.110.401) and by the SMS Demag AG (contract AGH nr 4.4.110.345) are gratefully acknowledged.

REFERENCES

[1] J. I w a n c i w, E. K a w e c k a - C e b u l a, E. C h o m a, K. P y t e l, Międzynar. Konf. Nowoczesne rozwiązania techniczno-technologiczne oraz logistyczne w produkcji wyrobów przemysłu hutniczego, AGH, Kraków, Mat. Konf. 51-58 (2002).
[2] J. I w a n c i w, Polska metalurgia w latach 1998-2002, Krynica 2002, Mat. Konf. KM PAN Kraków **1**, 186-192, (2002).
[3] E. K a w e c k a - C e b u l a, Metallurgy and Foundry Engineering, Kraków **28**, 13-20, (2002).
[4] J. I w a n c i w v, E. K a w e c k a - C e b u l a, Metallurgy and Foundry Engineering, Kraków **28** 21-27 (2002).
[5] J. L u m s d e n, Thermodynamics of molten slags mixtures, Acad. Press, London, (1996).
[6] *Slag Atlas*, 2nd Edition, Verlag Stahleisen, Dusseldorf (1995).
[7] S. B a n - y a, ISIJ Int. **33**, 2÷11, (1993).
[8] J. J o w s a, private com. (2001).
[9] H. G a y e, J. W e l f r i n g e r, Modeling of the thermodynamic properties of complex metallurgical slags, II Int. Symp. on Metall. Slags and Fluxes, 11'84, Reno (Nevada) (1984).
[10] J. I w a n c i w, WMilM AGH report, (1999), (non published).
[11] J. I w a n c i w, report for SMS Demag AG, (2002), (non published).
[12] O. K u b a s c h e w s k i, C.B. A l c o c k, Metallurgical Thermochemistry, 5th Edition, Pergamon Press Ltd, (1979).
[13] Electric Furnace Steelmaking, vol. II, Interscience Publ. (1963).
[14] E.T. T u r k d o g a n, Physicochemical Properties of Molten Slags and Glasses, London, Metals Society, (1983).
[15] J. I w a n c i w, XII Intern. Scientific Conference "Iron and Stelmeking", Podolanky 18-20.9.2002, Sbornik Prednasek, VSB-TU Ostrava (CR), Sekce **II**, 197-200 (2002).
[16] J. I w a n c i w, XII Intern. Scientific Conference "Iron and Stelmeking", Podolanky 18-20.9.2002, Sbornik Prednasek, VSB-TU Ostrava (CR), Sekce **II**, 189-192, (2002).

Received: 15 June 2004.

A R C H I V E S O F M E T A L L U R G Y A N D M A T E R I A L S
Volume 49 2004 Issue 3

G. SIWIEC *, J. BOTOR*

THE INFLUENCE OF ANTIMONY, LEAD AND SULPHUR ON THE SURFACE TENSION OF LIQUID COPPER

WPŁYW ANTYMONU, OŁOWIU I SIARKI NA NAPIĘCIE POWIERZCHNIOWE CIEKŁEJ MIEDZI

In the present paper, the results of the study on the influence of antimony, lead and sulphur on the surface tension of liquid copper are presented. The measurements of the surface tension of liquid Cu-Sb alloys containing maximum $5.12 \cdot 10^{-2}$ mole fraction of Sb, liquid Cu-Pb alloys containing maximum $3.47 \cdot 10^{-2}$ mole fraction of Pb and liquid Cu-S alloys containing maximum $1.59 \cdot 10^{-2}$ mole fraction of S were made. The measurements were carried out by means of the sessile drop method, in the temperature range 1393-1553 K. The results of the experiment show that sulphur has the strongest influence on the decrease in the surface tension of copper. Weaker influence is shown by lead and antimony, consecutively.

W pracy przedstawiono wyniki badań nad wpływem antymonu, ołowiu i siarki na napięcie powierzchniowe ciekłej miedzi. Przeprowadzone badania obejmowały pomiary napięcia powierzchniowego ciekłych stopów miedzi z antymonem o maksymalnej zawartości $5.12 \cdot 10^{-2}$ ułamka molowego Sb, stopów miedzi z ołowiem o maksymalnej zawartości $3.47 \cdot 10^{-2}$ ułamka molowego Pb oraz stopów miedzi z siarką o maksymalnej zawartości $1.59 \cdot 10^{-2}$ ułamka molowego S. Badania prowadzono w zakresie temperatur1393-1553 K. Wykorzystano metodę kropli leżącej. Stwierdzono, że Sb, Pb i S obniżają napięcie powierzchniowe ciekłej miedzi, przy czym największą aktywność powierzchniową wykazuje siarka, w dalszej kolejności ołów i antymon.

1. Introduction

The values of the surface tension of liquid metals are affected by solutes in a distinctively varied manner. Substances which significantly decrease the surface tension of liquids are called surface active solutes. In liquid metals they are mainly non-metals

* FACULTY OF METALLURGY AND MATERIALS SCIENCE, 40-019 KATOWICE, UL. KRASIŃSKIEGO 8, POLAND

(oxygen, sulphur) and metalloids (tellurium, selenium, antimony, arsenic), but also some metals, e.g. lead, bismuth, magnesium, tin and indium [1–4].

Although we can find a large amount of information pertaining to the surface properties of liquid copper, in available literature there are not too many data describing the influence of surface active elements on the value of its surface tension. This is the reason for some difficulties as far as the precise determination of these elements' influence on the surface tension values is concerned. In the present paper, the results of the study on the influence of antimony, lead and sulphur on the surface tension of liquid copper are presented.

2. The method and the results

By means of the sessile drop method described by Siwiec, Botor, Machulec [5], the measurements of the surface tension of liquid Cu-Sb alloys containing $1.08 \cdot 10^{-2}$, $1.64 \cdot 10^{-2}$, $2.57 \cdot 10^{-2}$ and $5.12 \cdot 10^{-2}$ mole fraction of Sb, liquid Cu-Pb alloys containing $0.29 \cdot 10^{-2}$, $0.94 \cdot 10^{-2}$, $1.72 \cdot 10^{-2}$ and $3.47 \cdot 10^{-2}$ mole fraction of Pb as well as liquid Cu-S alloys containing $0.04 \cdot 10^{-2}$, $0.38 \cdot 10^{-2}$, $0.57 \cdot 10^{-2}$ and $1.59 \cdot 10^{-2}$ mole fraction of S were made. The experiment was carried out at 1393, 1433, 1473, 1513 and 1553 K.

The alloys were prepared, using MOOB copper as well as analytically pure antimony, lead and copper sulphide, in the induction furnace PTS 01 TR containing graphite crucibles. The analysis of the antimony and lead contents in copper was carried out by means of the atomic adsorption spectrometer Solar M6 whereas the content of sulphur in copper was determined by means of the Leco CS 444.

The samples, sized approximately 4.5 mm both in diameter and height, were placed in the heating chamber of the high-temperature microscope on the substrates made of Al_2O_3 and produced by the Institute of Refractory Materials. Argon of 99.9999% purity was used as the protective gas during the measurements.

After the experiment had been completed, the samples were weighed. In the case of the Cu-Sb and Cu-S samples no mass changes were noticed while a small decrease in mass was found in the Cu-Pb samples (up to 0.3%). The obtained results can prove the stability of the chemical compositions of the Cu-Sb and Cu-S samples as well as the slight evaporation of lead in the Cu-Pb alloys during the measurements. The state of the substrates after the experiment showed no chemical reaction between the alloys and the substrate surface.

In order to determine the surface tension using the sessile drop method, apart from the shape parameter value [5], it is necessary to know the densities of liquid metals or alloys at given temperatures. The density of liquid copper in the temperature range 1393-1553 K was determined on the basis of the data obtained by N i z i e n k o and F l o k a [6]. For liquid Cu-S alloys, the density of liquid copper was used [7], while the densities of liquid Cu-Sb alloys and Cu-Pb alloys were calculated from the equation [8]:

$$\rho = \sum_{i=1}^{2} \varphi_i \rho_i \tag{1}$$

in which:

$$\varphi_i = \frac{X_i V_i}{\sum_{i=1}^{2} X_i V_i}, \tag{2}$$

where:

ρ – the alloy density,
ρ_i – the density of the component 'i' at given temperature,
φ_i – the volume fraction of the component 'i' at given temperature,
X_i – the mole fraction of the component 'i' in the alloy,
V_i – the molar volume of the component 'i' at given temperature.

The data necessary for determining the density of the liquid phase in the temperature range of the experiment are presented in Table 1.

TABLE 1

The density and the molar volume Vm at the melting point (Tm) of liquid copper, antimony and lead [3, 6]

Metal	$\rho = f(T)$ $g\ cm^{-3}$	V_m $cm^3\ mol^{-1}$	$\frac{1}{V_m}\frac{dV_m}{dT} \cdot 10^6,\ K^{-1}$
Cu	$8.039 - 9.6 \cdot 10^{-4}(T - T_m)$	7.91	100
Sb	$6.45 - 5.8 \cdot 10^{-4}(T - T_m)$	18.63	85
Pb	$10.71 - 13.9 \cdot 10^{-4}(T - T_m)$	19.41	123

In the tables below the following surface tension measurement results are presented:
Table 2 – liquid Cu-Sb alloys,
Table 3 – liquid Cu-Pb alloys,
Table 4 – liquid Cu-S alloys,
where:

Column 1 – the mole fraction X_i of the additive in the alloy,
Column 2 – the temperature T (in K) of the experiment,
Column 3 – the density ρ (in kg m^{-3}) used for determining the surface tension,
Column 4 – mean values of the surface tension γ in N m^{-1},
Column 5 – the standard deviation $S(\gamma)$ in N m^{-1}.

The measured values of the surface tension of the liquid Cu-Sb, Cu-Pb and Cu-S alloys at given temperatures were described by relation (3), known from the literature [6, 9, 10, 11]:

$$\gamma = a - b \ln (1 + cX_i), \tag{3}$$

where:

a – the surface tension of pure copper [5],

b, c – the coefficients calculated by means of the least square method on the basis of all measured surface tension values.

TABLE 2

The results of the surface tension of liquid Cu-Sb alloys measurements

$X_{Sb} \cdot 10^2$	T K	$\rho \cdot 10^{-3}$ $kg\ m^{-3}$	γ $N\ m^{-1}$	$S(\gamma) \cdot 10^2$ $N\ m^{-1}$
1.08	1393	7.95	1.168	1.72
	1433	7.92	1.178	2.08
	1473	7.88	1.184	2.19
	1513	7.84	1.193	1.98
	1553	7.80	1.202	1.95
1.64	1393	7.93	1.087	1.45
	1433	7.90	1.103	1.29
	1473	7.86	1.120	1.60
	1513	7.82	1.127	1.80
	1553	7.78	1.137	1.33
2.57	1393	7.90	0.973	0.64
	1433	7.86	0.982	0.98
	1473	7.82	1.000	0.86
	1513	7.78	1.015	0.88
	1553	7.75	1.027	0.51
5.12	1393	7.80	0.923	1.26
	1433	7.76	0.925	0.90
	1473	7.73	0.944	1.42
	1513	7.69	0.950	1.24
	1553	7.65	0.956	1.17

TABLE 3

The results of the surface tension of liquid Cu-Pb alloys measurements

$X_{Pb} \cdot 10^2$	T K	$\rho \cdot 10^{-3}$ $kg\ m^{-3}$	γ $N\ m^{-1}$	$S(\gamma) \cdot 10^2$ $N\ m^{-1}$
0.29	1393	8.02	1.033	2.07
	1433	7.98	1.065	1.31
	1473	7.94	1.073	0.77
	1513	7.90	1.101	1.02
	1553	7.87	1.117	1.34
0.94	1393	8.05	0.978	0.96
	1433	8.01	1.007	1.05
	1473	7.97	1.024	0.99
	1513	7.93	1.035	1.09
	1553	7.90	1.050	1.49
1.72	1393	8.10	0.860	1.22
	1433	8.06	0.883	1.69
	1473	8.02	0.901	1.33
	1513	7.98	0.929	1.63
	1553	7.94	0.950	1.69
3.47	1393	8.16	0.704	1.03
	1433	8.12	0.730	1.20
	1473	8.08	0.753	1.36
	1513	8.04	0.768	1.24
	1553	8.00	0.785	1.20

TABLE 4

The results of the surface tension of liquid Cu-S alloys measurements

$X_S \cdot 10^2$	T K	$\rho \cdot 10^{-3}$ $kg\ m^{-3}$	γ $N\ m^{-1}$	$S(\gamma) \cdot 10^2$ $N\ m^{-1}$
0.04	1393	8.00	1.054	1.37
	1433	7.97	1.069	1.05
	1473	7.93	1.085	1.46
	1513	7.89	1.097	0.98
	1553	7.85	1.127	1.60
0.38	1393	8.00	0.755	1.19
	1433	7.97	0.779	1.16
	1473	7.93	0.794	0.96
	1513	7.89	0.816	1.38
	1553	7.85	0.839	0.72
0.57	1393	8.00	0.703	0.83
	1433	7.97	0.722	0.92
	1473	7.93	0.748	1.48
	1513	7.89	0.756	1.78
	1553	7.85	0.779	1.37
1.59	1393	8.00	0.516	0.58
	1433	7.97	0.553	0.93
	1473	7.93	0.574	1.09
	1513	7.89	0.611	1.74
	1553	7.85	0.637	1.41

Table 5 presents the values of the surface tension of liquid copper [5], the b and c coefficients from (3) and the correlation coefficient r.

TABLE 5

The parameters of equation (3) for the Cu-Sb, Cu-Pb and Cu-S systems

Alloy	*T* K	*a* N m^{-1}	*b* N m^{-1}	*c*	*r*
Cu-Sb	1393	1.331	0.1840	178.4	0.9843
	1433	1.318	0.2028	127.5	0.9842
	1473	1.304	0.2028	103.7	0.9788
	1513	1.289	0.2339	69.43	0.9791
	1553	1.275	0.2789	45.41	0.9776
Cu-Pb	1393	1.331	0.1589	1179	0.9855
	1433	1.318	0.1630	888.4	0.9873
	1473	1.304	0.1571	779.6	0.9802
	1513	1.289	0.1975	326.2	0.9867
	1553	1.275	0.1998	261.7	0.9891
Cu-S	1393	1.331	0.1542	10889	0.9991
	1433	1.318	0.1535	8894.6	0.9990
	1473	1.304	0.1437	8894.6	0.9989
	1513	1.289	0.1347	8894.6	0.9987
	1553	1.275	0.1439	5154.3	0.9993

3. Discussion

As a result of the experiment pertaining to Cu-Sb alloys it has been noticed that the rise of the Sb content is accompanied by the reduction of the surface tension. The largest decrease in the surface tension of liquid copper caused by Sb was observed at 1393 K. The surface tension values change from 1.331 N m^{-1} for pure copper [5], through 1.168 N m^{-1} for the alloy containing $1.08 \cdot 10^{-2}$ mole fraction of Sb, to 0.923 N m^{-1} for the alloy containing $5.12 \cdot 10^{-2}$ mole fraction of Sb. At 1553 K, the surface tension values decrease as follows: from 1.275 N m^{-1} (pure Cu) [5], through 1.202 N m^{-1} ($X_{Sb} = 1.08 \cdot 10^{-2}$), to 0.956 N m^{-1} ($X_{Sb} = 5.12 \cdot 10^{-2}$). The obtained results show that antimony is a surface active solute, i.e. it concentrates on the surface of the liquid phase, as mentioned in [4]. The temperature rise causes weaker influence of antimony on the decrease of the surface tension of liquid copper. For example, for the alloy containing $1.64 \cdot 10^{-2}$ mole fraction of Sb, the surface tension at 1393 K equals 1.087 N m^{-1} while at 1553 K it increases to 1.137 N m^{-1}. In the case of the alloy containing $2.57 \cdot 10^{-2}$ mole fraction of Sb, the surface tension value increases from 0.973 N m^{-1} at 1393 K to 1.027 N m^{-1} at 1553 K. The obtained results are confirmed by the data found in [2, 4, 12, 13] where the authors notice that if surface active solutes are present

in the alloys, the values of the temperature coefficients $\frac{d\gamma}{dT}$ can be of positive values, contrary to the values characteristic for liquid pure metals. A similar tendency is observed in the alloys containing $X_{Sb} = 1.08 \cdot 10^{-2}$ and $X_{Sb} = 5.12 \cdot 10^{-2}$, for which the temperature coefficients $\frac{d\gamma}{dT}$ equal $0.242 \cdot 10^{-3}$ N m^{-1} K^{-1} and $0.222 \cdot 10^{-3}$ N m^{-1} K^{-1}, respectively. The described increase in the surface tension is probably the effect of the desorption of antimony from the surface layer of liquid alloys (caused by the temperature rise). In Figure 1 the surface tension isotherms of the studied alloys in 1393 and 1553 K are shown. The points represent the mean values of the surface tension and the curves represent the solution of equation (3). Unfortunately, it is impossible to compare the obtained data with any other relevant values as there are no available literature data pertaining to the surface tension of dilute Cu-Sb alloys.

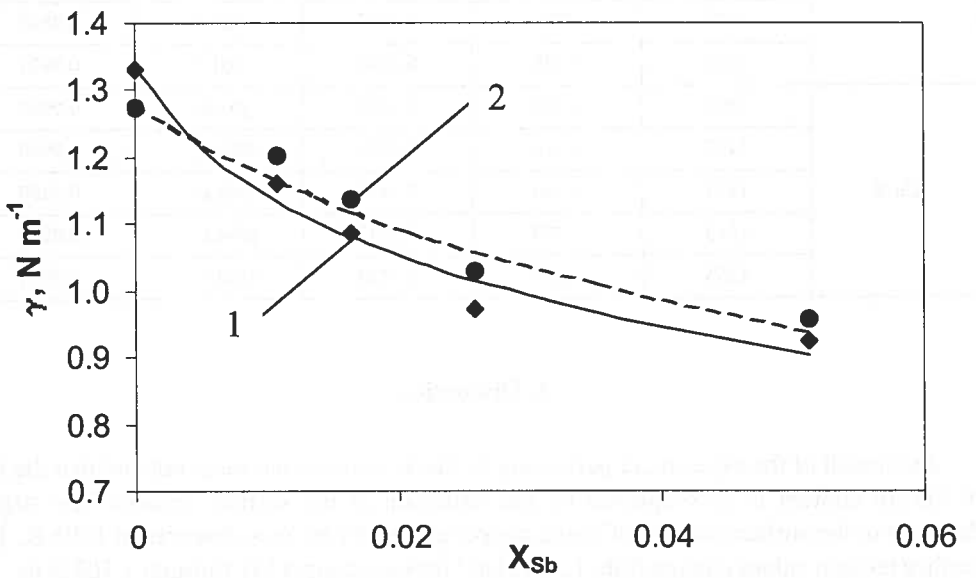

Fig. 1. The surface tension of liquid Cu-Sb alloys at 1393 and 1553 K (1–1393 K, 2–1553 K)

The analysis of the measured surface tension values of the Cu-Pb alloys shows the strong influence of lead on this parameter. For example, at 1393 K the surface tension decreases from the value corresponding to pure copper [5] to 1.033 N m^{-1} for the alloy containing $3.29 \cdot 10^{-2}$ mole fraction of Pb, and to 0.704 N m^{-1} for the alloy containing $3.47 \cdot 10^{-2}$ mole fraction of Pb. At 1553 K the value of this parameter equals 1.117 N m^{-1} for the alloy containing $X_{Pb} = 0.29 \cdot 10^{-2}$, and it decreases to 0.785 N m^{-1} for the alloy with $X_{Pb} = 3.47 \cdot 10^{-2}$. It can also be noticed that, similarly to Cu-Sb alloys, the temperature rise is accompanied by the increase in the surface tension, which is typical of surface active substances. Additionally, this increase can be caused by a small change in the chemical composition of the samples during the measurements.

In Fig.2 the comparison between the values obtained for Cu-Pb alloys and the data provided by M e t z g e r [14] and C z i u r s i n , R i u m s z i n [15] is presented. Basing on Fig.2, it can be seen that the courses of the surface tension isotherms of the studied Cu-Pb alloys are similar to the ones obtained by M e t z g e r [14]. The best agreement occurs in the case of the alloy containing $0.29 \cdot 10^{-2}$ mole fraction of Pb, and it's easily noticed if we compare the value 1.033 N m^{-1} obtained at 1393 K with 1.025 N m^{-1} at 1373 K [14], the value 1.065 N m^{-1} with 1.042 N m^{-1} [14], both obtained at 1433 K, and the value 1.073 N m^{-1} with 1.056 N m^{-1} [14], both obtained at 1473 K. However, the results presented in this paper differ from the ones obtained by C z i u r s i n , R i u m s z i n [15]. It can be suggested that the differences were caused by the difficulties encountered during the measurements of the surface tension of liquid metals at high temperatures [5].

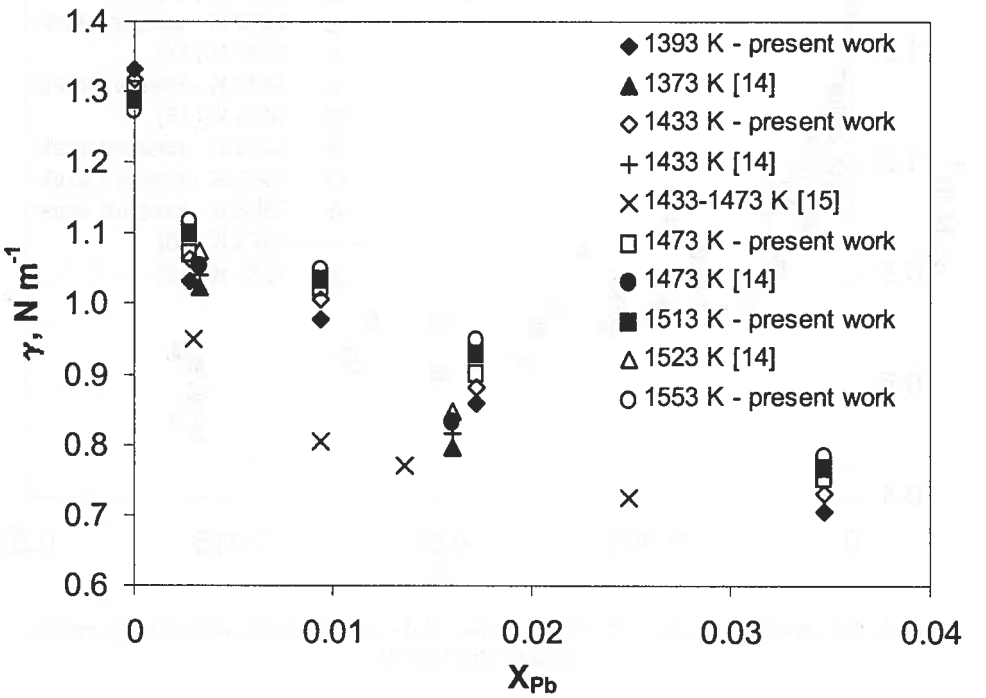

Fig. 2. The comparison between the obtained values of the surface tension of Cu-Pb alloys and the literature data [14, 15]

The measured values of the surface tension of liquid Cu-S alloys show that sulphur is a surface active solute in liquid copper. Such a small amount of this element as $0.04 \cdot 10^{-2}$ causes a significant decrease in the surface tension. For the alloy containing $0.57 \cdot 10^{-2}$ mole fraction of S, the value of the surface tension is twice as small as the value for pure copper [5]. After the analysis of the experiment results it can be seen that, at 1393 K and with $X_S = 0.38 \cdot 10^{-2}$ (S concentration), the surface tension value equals only 0.755 N m^{-1}. It decreases to 0.703 N m^{-1} for the alloy with $X_S = 0.57 \cdot 10^{-2}$, and to 0.516 N m^{-1} for the alloy

containing $1.59 \cdot 10^{-2}$ mole fraction of S. At 1553 K, for the same alloys, the values are 0.839 N m^{-1}, 0.779 N m^{-1} and 0.637 N m^{-1}, respectively. The above-mentioned examples show that the temperature rise, similarly to the previously discussed liquid metal-surface active solute systems, has a weakening effect on the negative influence of the addition on the surface tension value. Figure 3 presents the comparison between the present study results and the measurement results obtained by W i g b e r , P a w l e k and R o p e - n a c k [16], B a e s and K e l l o g [17] as well as M o n m a and S u t o [18]. In all cases the courses of the surface tension of Cu-S alloys isotherms have a similar shape.

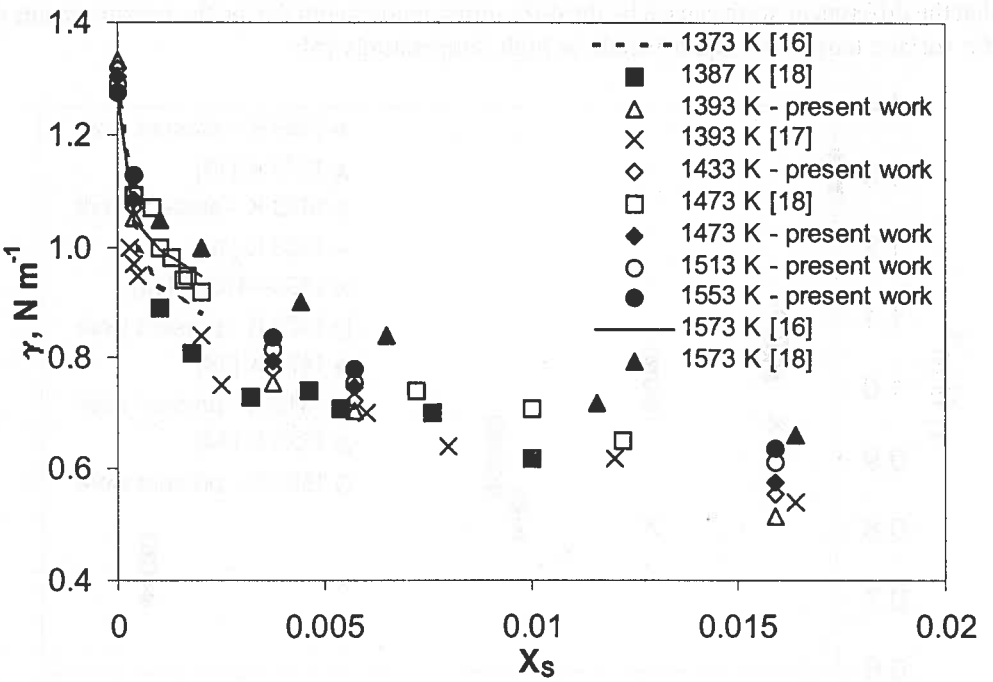

Fig. 3. The comparison between the obtained values of the surface tension of Cu-S alloys and the literature data [16-18]

4. Summary

The measurements of the surface tension of liquid Cu-Sb alloys containing maximum $5.12 \cdot 10^{-2}$ mole fraction of Sb, liquid Cu-Pb alloys containing maximum $3.47 \cdot 10^{-2}$ mole fraction of Pb and liquid Cu-S alloys containing maximum $1.59 \cdot 10^{-2}$ mole fraction of *S* were made. The experiment was conducted in order to examine the influence of temperature and the alloy additive on the surface tension value. The measurements were carried out by means of the sessile drop method, in the temperature range 1393-1553 K.

Summing up, the results of the present study on surface tension show that sulphur, antimony and lead have, in liquid copper, the properties characteristic for surface active

substances. It was noticed that even small amounts (below 0.02 mole fraction) of Sb, Pb and S significantly reduce the surface tension. The results of the experiment show that sulphur has the strongest influence on the decrease in the surface tension of copper [5] (causes the sharpest reduction).Lead and antimony, consecutively, show weaker influence. The changes of this parameter under the influence of the above-mentioned additions were described by equation (3). The observed effect of the surface tension fall is caused by the adsorption of the surface active additions at the surface of the liquid phase [2, 4, 12, 13].

In all studied systems, the surface activity of Sb, Pb and S decreases within the temperature rise, which is probably the result of the desorption (caused by temperature) of these elements from the interfacial surface [2, 4, 12, 13]. Additionally, for Cu-Pb alloys, the decrease in the surface activity is caused by lead evaporation from the alloys.

Acknowledgments

The studies were carried out under Research Project 7 T08B 00718 financed by the Committee of Scientific Research (Poland).

REFERENCES

[1] J. B o t o r, Podstawy Metalurgicznej Inżynierii Procesowej, Wyd. Politechniki Śląskiej, Gliwice, 1999.
[2] F.D. R i c h a r d s o n, Physical Chemistry of Melts in Metallurgy, Academic Press, Londyn, 1974.
[3] E.T. T u r k d o g a n, Physical Chemistry of High Temperature Technology, Academic Press, Londyn, 1980.
[4] P. K o z a k e v i t h, Surface Activity in Liquid Metal Solutions, in the monograph: Surface Phenomena of Metals, Soc. of Chem. Ind., Londyn, 1967.
[5] G. S i w i e c, J. B o t o r, B. M a c h u l e c, Arch. Metall. **48**, (2), 209-221 (2003).
[6] W.I. N i z i e n k o, Ł.I. F l o k a, Povierchnostnoie Natiażienie Żidkich Mietallow i Splavov, Metallurgia, Moskwa, 1981.
[7] K. D i e s, Kupfer und Kupferieger. in the Techn., Springer-Verlag, Berlin, 1967.
[8] J. B o t o r, R. S o s n o w s k i, L. B l a c h a, B. S i k o r a, B. M a c h u l e c, Kinetyka w wysokotemp. ukł. heterogen. ciekły metal-faza gazowa, spr. z proj. badawczego KBN nr 3 3605 91 02, Katowice, 1995.
[9] J.W. N a j d i c z, Kontakt. Iawlienia w Miet. Raspl., Naukowa Dumka, Kijów, 1971.
[10] G.R. B e l t o n, Metall. Trans. B, **7B**, 35-42 (1976).
[11] J.F. E l l i o t t, The Role of Interfaces in Pyrometallurgical Processes, Extraction Metallurgy 85 Symposium, Londyn, 1985.
[12] B.J. K e e n e, Internat. Mater. Rev. **4**, 157-192 (1993).
[13] P. K o z a k e v i t h, Surface Tens. of Liquid Met. and Oxide Melts, in the monograph: Liquids: Struct., Properties Solid Interact., Elsevier Publ. Comp., Amsterdam, 1965.
[14] G. M e t z g e r, Phys. Chem. **1**, 211 (1953), quoted in [6].
[15] W.M. C z i u r s i n, W.M. Riumszin, Cwiet. Miet. **4**, 118-124 (1959).
[16] G. W i g b e r t, F. P a w l e k, A. R o e p e n a c k, Z. Metallkunde **54**, 147 (1963), quoted in [6].
[17] C.F. B a e s, H.H. K e l l o g g, Trans. AIME **197**, 643-648 (1953), quoted in [13].
[18] K. M o n m a, H. S u t o, J. Jap. Inst. Met. **24**, 374-37 (1960).

Received: 20 April 2004.

A R C H I V E S O F M E T A L L U R G Y A N D M A T E R I A L S
Volume 49 2004 Issue 3

J. GRYZIECKI *, A. ŁATKOWSKI*, M. TUMIDAJEWICZ*

CHANGES IN THE STRUCTURE AND STRENGTHENING OF AGED CuNi13Sn5 ALLOY INDUCED BY MICROADDITIONS

ZMIANY STRUKTURY I UMOCNIENIA STARZONEGO STOPU CuNi13Sn5 SPOWODOWANE MIKRODODATKAMI

The decomposition of saturated solid solution of CuNi13Sn5 alloy during ageing is presented. Decomposition of the solution leads to the formation of cellular precipitates of discontinuous transition. Formation of these precipitates is responsible for the fact that the alloy does not acquire appropriately high mechanical properties. Introduction of microadditions in the form of Si or Ti into CuNi13Sn5 alloy changed the precipitation kinetics. Si and Ti microadditions formed phases which decorated the grain boundaries, preventing nucleation and the subsequent migration of cellular precipitates of discontinuous transition. Elimination of cellular precipitates was responsible for the fact that CuNi13Sn5 alloy attained very great strength and plastic properties.

W pracy niniejszej przedstawiono rozpad przesyconego roztworu stałego stopu CuNi13Sn5 podczas starzenia. Rozpad roztworu doprowadza do powstania komórkowych wydzieleń przemiany nieciągłej. Powstanie tych wydzieleń jest przyczyną nie osiągania przez stop odpowiednio dużych własności mechanicznych. Wprowadzenie do stopu CuNi13Sn5 mikrododatków w postaci Si lub Ti zmieniło kinetykę wydzielania. Mikrododatki Si i Ti utworzyły fazy, które udekorowały granice ziaren, uniemożliwiając zarodkowanie a następnie migrację wydzieleń komórkowych przemiany nieciągłej. Eliminacja wydzieleń komórkowych spowodowała, że stop CuNi13Sn5 osiągnął bardzo duże własności wytrzymałościowe jak i plastyczne.

1. Introduction

For many years nickel has been added to zinc bronze mainly in order to improve castability, grain refinement and to increase the hardness of casting materials [1]. It was not known until the years nineteen-sixties and seventies when it was found [1,2] that CuNiSn

* FACULTY OF NON-FERROUS METALS, AGH-UNIVERSITY OF SCIENCE AND TECHNOLOGY, 30-059 KRAKÓW, AL. MICKIEWICZA 30, POLAND

alloys with a large proposition of copper can be precipitation strengthened with good results. Changes in the structure and in the mechanical properties of CuNiSn alloys during precipitation strengthening were the subject of many studies [3-12]. From the conducted investigations it follows that the processes occurring during precipitation strengthening depend on the chemical composition of the alloy, temperature, time of ageing and the method of thermal treatment. An interesting group of CuNiSn alloys on account of the possibility to obtain great strengthening during thermal treatment are the alloys containing less than 15% Ni and less than 10% Sn, the rest being Cu. In these alloys ageing begins with spinodal decomposition [1, 5, 9, 12]. The next stage of decomposition is the formation of a coherent phase γ' – $(Cu, Ni)_3Sn$ with DO_{22} structure. The successive stage of the process of ageing is the formation of cellular precipitates of γ' phase as a result of discontinuous transition with DO_3 structure. It has been found, however, that depending on the applied temperature of ageing, the presented precipitation kinetics of this group of alloys undergoes a change [15]. Investigations carried out so far indicate that the spinodal decomposition and the γ' phase formed as a result of continuous precipitation are processes inducing great strengthening of the alloys. On the other hand, the cellular precipitates occurring as a result of discontinuous transition are responsible for the reduction of hardening [1, 5, 10]. The presence of cellular precipitates reduces also the corrosion resistance of the alloys [16].

The aim of the present study was to induce such a change in the precipitation kinetics during ageing which would eliminate the cellular precipitates of the discontinuous transition. It has been decided to introduce into the examined CuNi13Sn8 alloy some microadditions which, by segregating to the grain boundaries or forming new phases on them, will make them inactive and in this way prevent the formation of cellular precipitates.

2. Investigation method

Investigations were carried out on alloys with the chemical composition given in Table 1. The alloys were prepared in an induction furnace with argon protection. Cast alloys were homogenized at the temperature 850°C and next water quenched. Alloys prepared in this way were cold rolled and then annealed again at the temperature 850°C and water quenched. Ageing of CuNi13Sn5 alloy was conducted in a salt furnace in the temperature range 350°C-450°C for various time periods. Alloys with microadditions were aged at the temperature 400°C. Thermal-mechanical treatment was also applied in the course of which the saturated alloys were subjected to deformation (ε=40%) by rolling and subsequent ageing at the temperature 400°C. The degree of strengthening was determined through the measurements of hardness (HV) and the strength properties obtained from tension tests. Structural investigations were carried out using an optical and an electron microscope. The course of the precipitation processes was also examined by means of a diffraction scanning calorimeter (DSC).

TABLE 1

Chemical composition of the alloys

Alloy Number	Alloy component in wt %					
	Ni	Sn	Si	Ti	Nb	Cu
1	13	5	–	–	–	rest
2	12,7	4,9	0,4	–	–	rest
3	12,9	5,0	–	0,35	–	rest
4	13,1	5,1	–	–	0,45	rest

3. Investigation results

Changes in the strengthening of CuNi13Sn5 alloy during isothermic ageing are shown in Fig. 1. The alloy subjected to ageing shows a monotonic increase of hardness with the increase of the annealing time. With the increase of the ageing temperature there increases the rate of strengthening. The greatest dynamics of strengthening is demonstrated by alloy aged at 400°C. At this temperature the alloy attains the maximal hardness (270 HV). Ageing at temperature higher than or lower than 400°C did not result in strengthening as great as that.

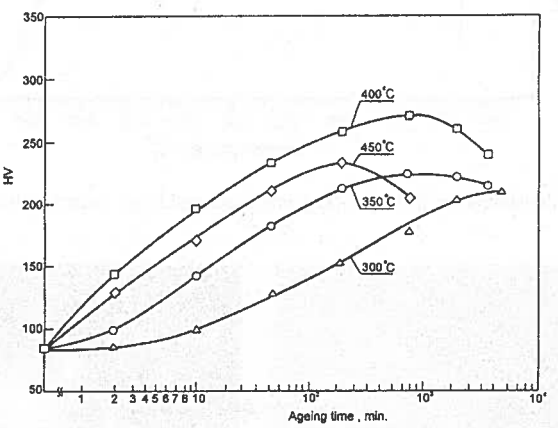

Rys. 1. Hardness of CuNi13Sn5 alloy as depending on the time and the ageing temperature

The performed investigations of the decomposition of a saturated solid solution of CuNi13Sn5 alloy by means of differential scanning calorimeter (DSC) enabled to determine the particular ageing stages. The DSC curve of the decomposition of a saturated solid solution of CuNi13Sn5 alloy is shown in Fig. 2. On the curve there can be distinguished three stages of decomposition (A, B, C). To identify the processes occurring in the particular stages there have been carried out structural investigations which have shown that at the first stage (A) the decomposition of the saturated solid solution of

CuNi13Sn5 alloy begins with spinodal segregation. The structure of the alloy at this stage is shown in Fig. 3. There can be observed the absence of a zone free from precipitates at the grain boundaries and the appearance of additional reflexes on electron diffraction. Longer ageing, during which on the calorimetric curve there occurs the second maximum (stage B), is induced by continuous precipitation of $(Cu, Ni)_3Sn$- γ' phase. These precipitates are very small (about 5 nm) and are uniformly distributed in the grains of the matrix (Fig. 4). Both the spinodal decomposition and the following continuous precipitation of the strengthening γ' phase are accompanied by energy precipitation (A, B). At advanced ageing stages there takes place the third stage of ageing (C), simultaneously with some structural processes. The γ' precipitates of the discontinuous change are growing (10 nm). There takes place also the nucleation at the grain boundaries of the cellular precipitates of the discontinuous transition, followed by migration of their fronts (Fig. 5, 6).

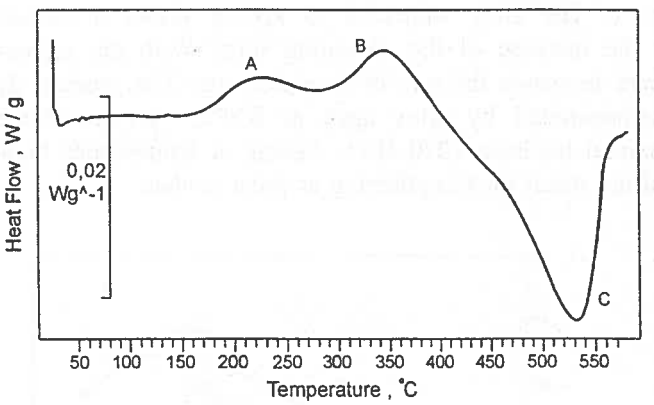

Fig. 2. Calorimetric curve of CuNi13Sn5 alloy saturated and heated at a rate 10°C/ minute

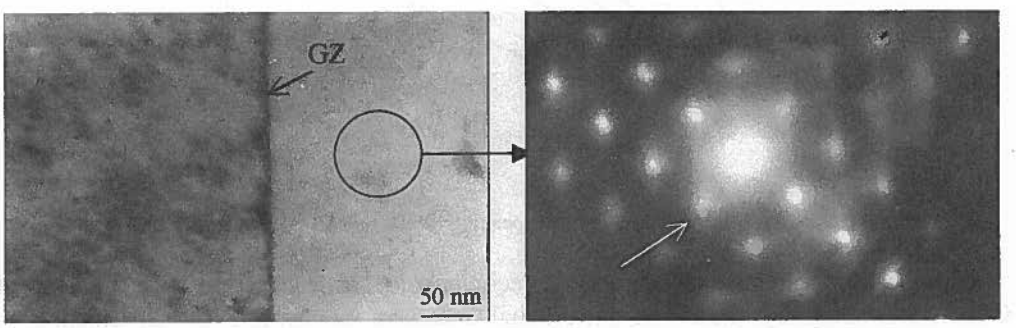

Fig. 3. Microstructure of CuNi13Sn5 alloy heated to 230°C

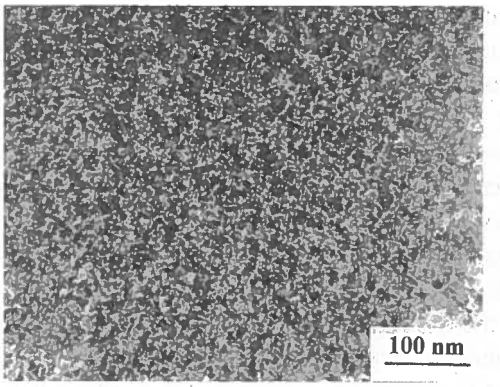

Fig. 4. Microstructure of CuNi13Sn5 alloy heated to 380°C

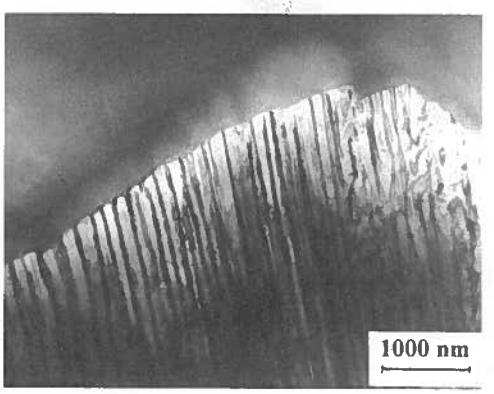

Fig. 5. Microstructure of CuNi13Sn5 alloy heated to 500°C

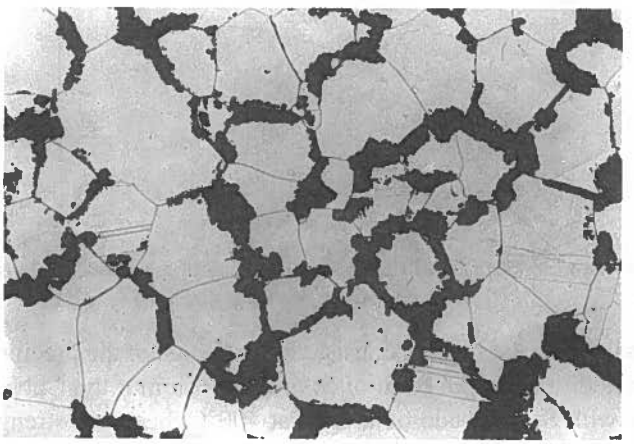

Fig. 6. Microstructure of CuNi13Sn5 alloy heated to 500°C. Magnified 125x

There have been carried out measurements of the microhardness of the grains inside and of the areas at the grain boundaries of CuNi13Sn5 alloy after prolonged ageing. The result of these measurements indicates that the microhardness of the inside of grains which became occupied by the continuous γ' precipitates is 1,5 times higher than the microhardness of the near – the boundary areas, decorated with cellular precipitates (Fig. 7). Changes in the microhardness of the grains inside and in the macrohardness of CuNi13Sn5 alloy, aged at 400°C, as a function of time, are shown in Fig. 8. This dependence indicates that the micro-hardness of the grains inside increases with the time of ageing. This increase of micro-hardness takes place also when at the advanced stage of ageing there occurs a definite decrease of the macrohardness of the alloy. The obtained result is an indication that the cellular precipitates of the discontinuous transition are responsible for the decrease of the strengthening of the alloy after prolonged time of ageing.

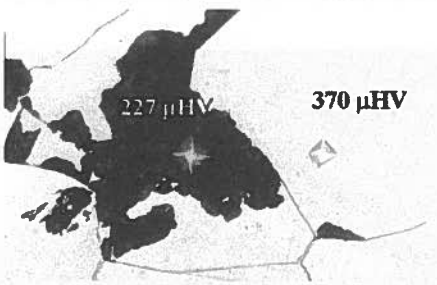

Fig. 7. Microhardness of cellular precipitates and the grains inside in CuNi13Sn5 alloy aged at 400°C for 7×10^2 minutes

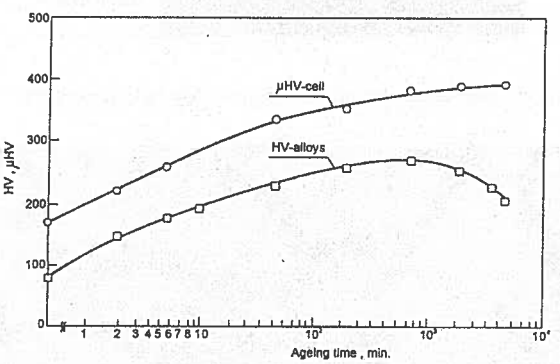

Fig. 8. Change of the macrohardness of CuNi13Sn5 alloy and of the micro-hardness of the inside of its grains during ageing at 400°C

A method has been applied which consisted in a change of the precipitation kinetics by introducing microadditions in the form of Si or Ti or Nb into the CuNi13Sn5 alloy. The CuNi13Sn5 alloy with Si microaddition, aged at 400°C, becomes strengthened at first to a rather small degree. After 10 minutes of ageing the strengthening increases quickly. The strengthening process of the alloy is illustrated by the dependences of the changes in the

mechanical properties as a function of the ageing time, presented in Fig. 9. After $5{,}7 \times 10^3$ minutes of ageing the alloy acquires great strengthening. Then its strength properties attain the following values: R_m = 950 MPa, $R_{0,2}$ = 830 MPa, HV = 310. With these high strength properties the alloy retains good plastic properties evidenced by A_5 = 12%.

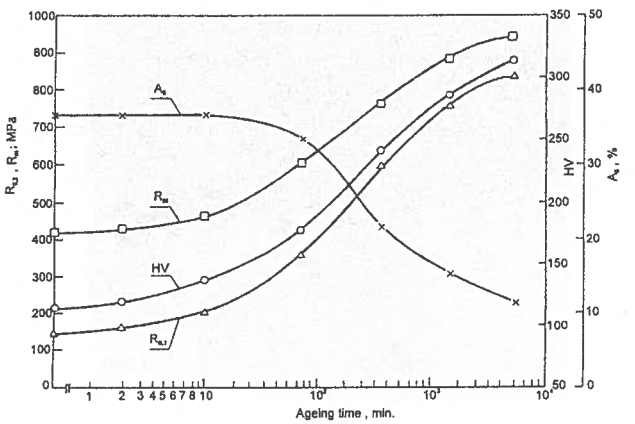

Fig. 9. Change of the mechanical properties of CuNi13Sn5 alloy with Si microaddition, aged at 400°C as a function of time

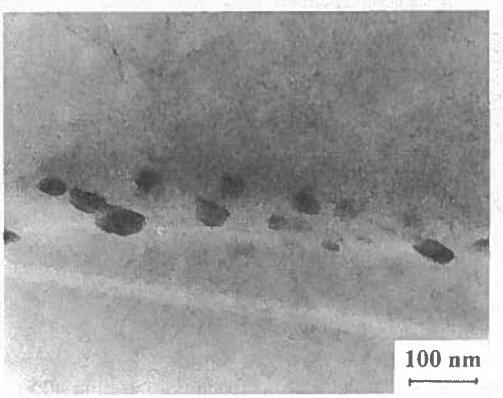

Fig. 10. Microstructure of CuNi13Sn5 alloy with Si microaddition, aged at 400°C for 70 minutes

Structural investigations have shown that in the aged alloy there occur the precipitates of γ' $(Cu, Ni)_3Sn$ phase, formed in the continuous transition. These precipitates have the form of very small, spherical particles inside the grains. After 70 minutes of ageing their size was about 3 nm (Fig. 10). The alloy structure contains also particles of Ni_3Sn phase which are mostly found within the grain boundaries (Fig. 10). The size of these particles is 40÷60 nm. Longer ageing causes the growth of both the hardening γ' phase and Ni_3Si

particles. After $5{,}7 \times 10^3$ minutes of ageing, when the alloy attained very high strength properties, the precipitates of γ' phase reached the size of 6 nm, and those of Ni_3Sn from 50 to100 nm (Fig. 11). The structure of CuNi13Sn5 alloy with a micro-addition of 0,4 wt % Si, aged at 400°C, even for a very long time ($5{,}7 \times 10^3$ min.) did not show the presence of cellular precipitates of discontinuous transition (Fig. 12).

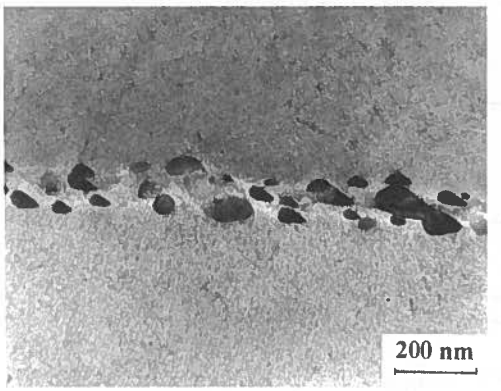

Fig. 11. Microstructure of CuNi13Sn5 alloy with Si microaddition, aged at 400°C for $5{,}7 \times 10^3$ minutes

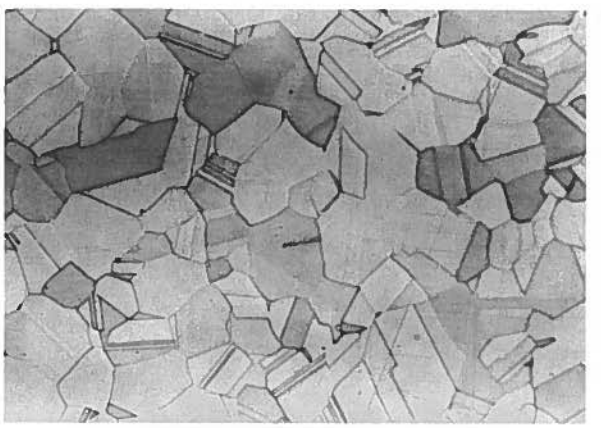

Fig. 12. Structure of CuNi13Sn5 alloy with Si microaddition, aged at 400°C for $5{,}7 \times 10^3$ minutes. Magnified 63×

Plastic deformation ($\varepsilon = 40\%$) of saturated CuNi13Sn5 alloy with Si microaddition caused intensive increase of hardening during ageing. After 7×10^2 minutes the alloy attained maximal strengthening (Fig. 13), the applied thermal-mechanical treatment resulted in attaining very high strength properties $R_m = 1050$ MPa, $R_{0,2} = 900$ MPa, HV = 330. These strength properties were accompanied by $A_5 = 7\%$.

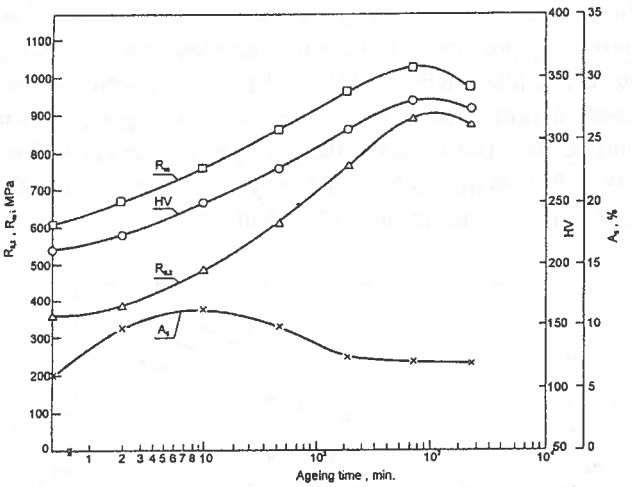

Fig. 13. Change of the mechanical properties of CuNi13Sn5 alloy, saturated and deformed ($\varepsilon = 40\%$) and afterwards aged at 400°C as a function of time

Plastic deformation of a saturated alloy caused high dislocation density and the occurrence of shear bands. The ageing process induced intensive nucleation and afterwards the increase of γ' precipitates of the discontinuous transition in the whole volume of the alloy. The grain boundaries of the deformed alloy are densely decorated with particles of Ni_3Si phase. Figure 14 shows the structure of alloy aged at 400°C for 7×10^2 minutes. There can be observed very small (3 nm) γ' precipitates, Ni_3Si precipitates, measuring from 20 to 30 nm, within the grain boundaries, and shear bands intersecting the grain boundaries. Observations of the structure of CuNi13Sn5 alloy with Si additions have shown that after hermal-mechanical treatment there are no cellular precipitates present in the alloy.

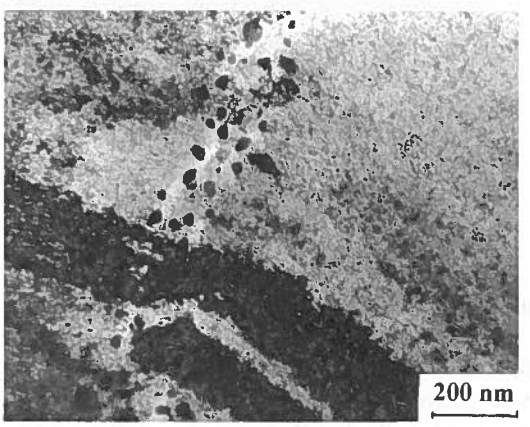

Fig. 14. Microstructure of CuNi13Sn5 alloy with Si microaddition, saturated and deformed ($\varepsilon = 40\%$) and afterwards aged at 400°C for 7×10^2 minutes

The other addition to CuNi13Sn5 alloy whose presence was tested with respect to the possibility to eliminate the precipitates of continuous transition, occurring in the course of ageing, was titanium. The alloy aged at 400°C, after a short period of incubation, showed fast monotonic strengthening. After $5{,}7 \times 10^3$ minutes of ageing it attained very high, maximal strength properties. The values of these properties were as follows: $R_m = 920$ MPa, $R_{0,2} = 810$ MPa, HV = 290. With such high strength properties the alloy retained good deformability which is evidenced by $A_5 = 12\%$ (Fig. 15).

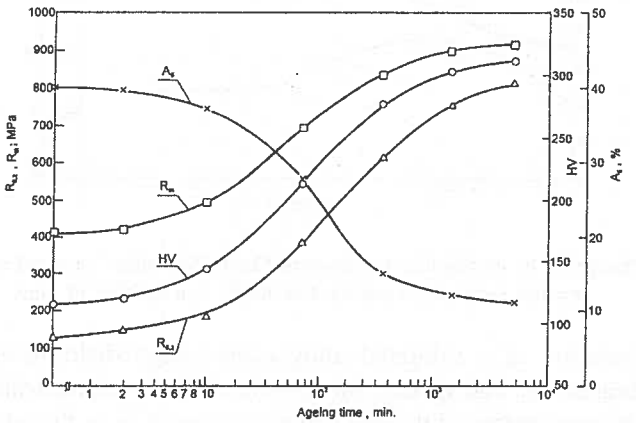

Fig. 15. Change of the mechanical properties of CuNi13Sn5 alloy with Ti microaddition, aged at 400°C as a function of time

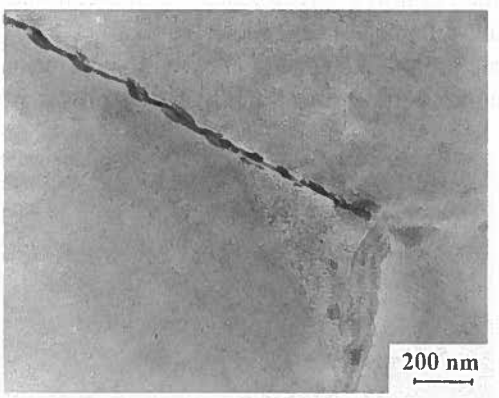

Fig. 16. Microstructure of CuNi13Sn5 alloy with Ti microaddition, aged at 400°C for 70 minutes

In the structure of CuNi13Sn5 alloy with Ti microadditions, aged at the temperature 400°C for 70 minutes, there appear very small (about 2 nm) oval precipitates of γ' discontinuous transition, uniformly distributed in the whole volume of grains (Fig. 16). The grain boundaries became decorated with much larger precipitates. Their size was from 100 to 200 nm. EDS analysis of the chemical composition of these precipitates has shown that

they are built of 18,8÷23,5 at % of Ti and 56,0÷67,2 at % of Ni. The ratio of Ni to Ti content in these precipitates is close to 1÷3. After $5{,}7 \times 10^3$ minutes of ageing, when the alloy attained the maximal strength properties, the precipitates of the strengthening phase increased and reached the size of 10 nm (Fig. 17). In spite of a long time of ageing the alloy structure was free from cellular precipitates of the discontinuous transition.

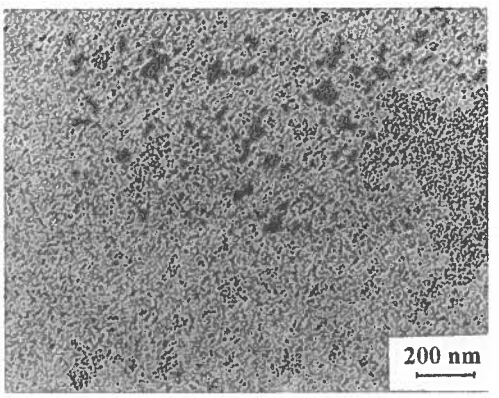

Fig. 17. Microstructure of CuNi13Sn5 alloy with Ti microaddition, aged at 400°C for $5{,}4 \times 10^3$ minutes

The conducted thermal-mechanical treatment, in which CuNi13Sn5 alloy with Ti microaddition after saturation was deformed by 40%, caused the increase of the strength properties and reduction of the plastic properties. The alloy, aged at 400°C, already after 2×10^2 minutes attained the maximal strengthening (Fig. 18). The acquired mechanical properties were as follows: $R_m = 1000$ MPa, $R_{0,2} = 840$ MPa, HV = 320 and $A_5 = 8\%$.

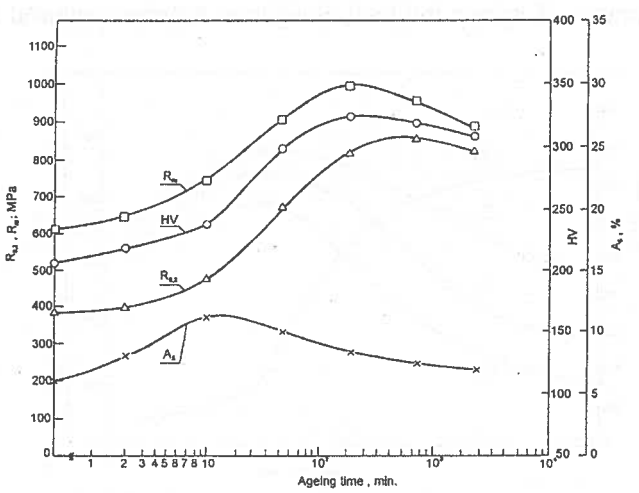

Fig. 18. Change of the mechanical properties of CuNi13Sn5 alloy with Ti microaddition, saturated, deformed (ε = 40%) and afterwards aged at 400°C as a function of time

In the structure of an alloy, saturated and deformed, and next aged at 400°C for 7×10^2 minutes, there occur very small precipitates in the grains of γ' phase (5 nm) and particles of $TiNi_3$ phase at the grain boundaries (Fig. 19). Observations of the structure by means of both an optical and an electron microscope did not reveal the occurrence of precipitates of discontinuous transition.

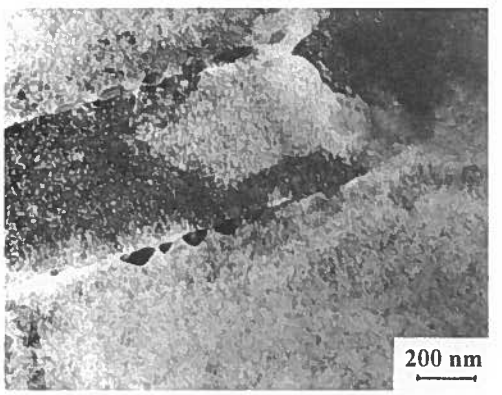

Fig. 19. Microstructure of CuNi13Sn5 alloy with Ti microaddition, saturated, deformed by $\varepsilon = 40\%$, and next aged at 400°C for 7×10^2 minutes

The third microaddition applied to CuNi13Sn5 alloy was Nb. Its influence on the change of the alloy strengthening in the course of ageing at 400°C is shown in Fig. 20. Maximal strengthening of the alloy takes place already after 4×10^2 minutes of ageing. The attained mechanical properties are as follows: $R_m = 780$ MPa, $R_{0,2} = 650$ MPa, HV = 270 and $A_5 = 10\%$. Further ageing causes a decrease of strengthening and reduction of deformability. After $5{,}7 \times 10^3$ minutes of ageing the total elongation becomes reduced to 2%.

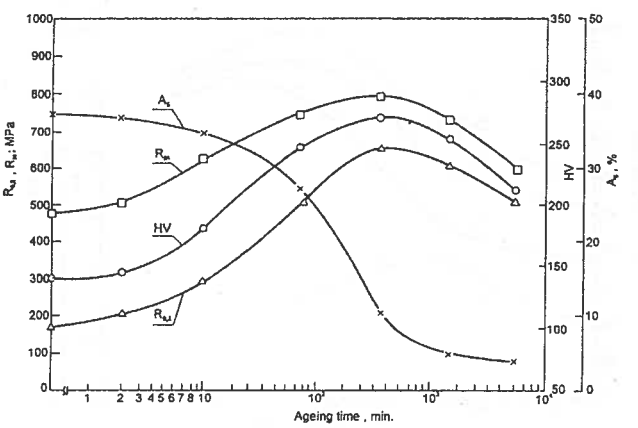

Fig. 20. Change of the mechanical properties of CuNi13Sn5 alloy with Nb microaddition, aged at 400°C as a function of time

In the course of ageing CuNi13Sn5 alloy with Nb microaddition small γ' precipitates (3 nm)are formed in the whole volume of the grains (Fig. 21). There can be observed also large (150÷400 nm) particles of $NbNi_3$ phase, situated chaotically both in the grains and on the grain boundaries (Fig. 22). EDS analysis has shown that their chemical composition is as follows: 16,2÷17,4 at % of Nb and 45,6÷50,2 at % of Ni. After 7×10^2 minutes of ageing the majority of the grain boundaries of the alloy become decorated with γ'precipitates formed in the discontinuous transition (Fig. 23). When the ageing time is prolonged, the cellular precipitates migrate, occupying more and more of the volume of the grains (Fig. 24).

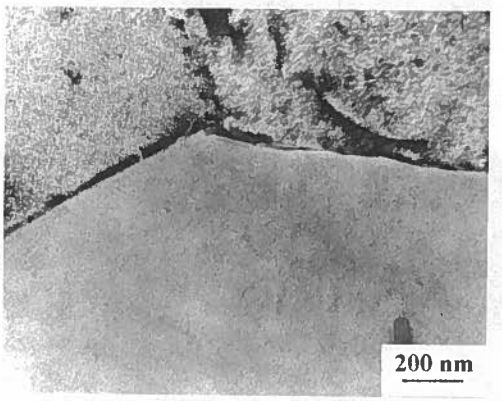

Fig. 21. Microstructure of CuNi13Sn5 alloy with Nb microaddition, aged at 400°C for 30 minutes

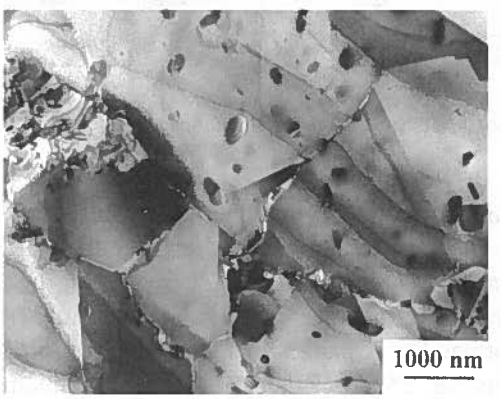

Fig. 22. Microstructure of CuNi13Sn5 alloy with Nb microaddition, aged at 400°C for 100 minutes

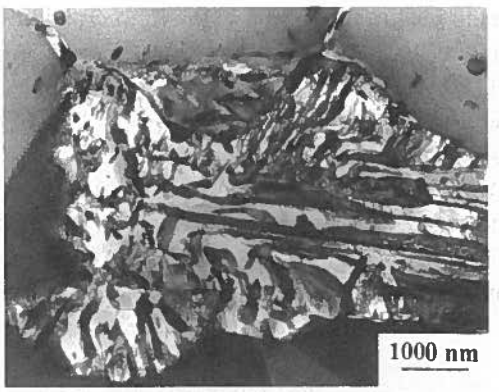

Fig. 23. Microstructure of CuNi13Sn5 alloy with Nb microaddition, aged at 400°C for 7×10^2 minutes

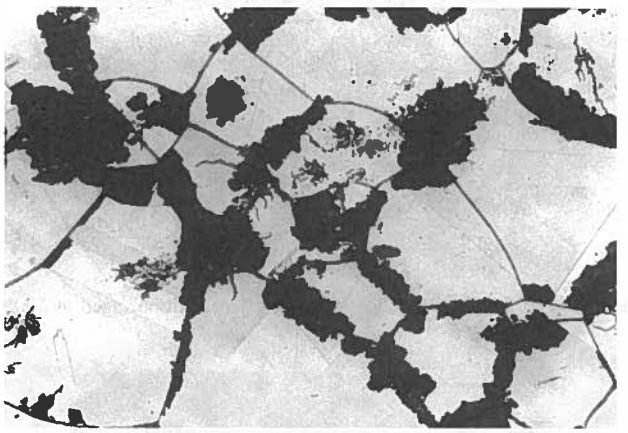

Fig. 24. Microstructure of CuNi13Sn5 alloy with Nb microaddition, aged at 400°C for 7×10^2 minutes. Magnified 125×

The thermal-mechanical treatment, in which after saturation the alloy was deformed by 40%, changed the character of the strengthening curve. The strengthening of the alloy during ageing was very quick. Maximal strengthening of the alloy was observed already after 100 minutes of ageing. Further ageing caused very fast decrease of strengthening and deformability. Changes of the mechanical properties with the time of the ageing are shown in Fig. 25. After thermal-mechanical treatment the alloy acquired the following maximal strength properties: $R_m = 850$ MPa, $R_{0,2} = 750$ MPa, HV = 280, and the elongation $A_5 = 2\%$.

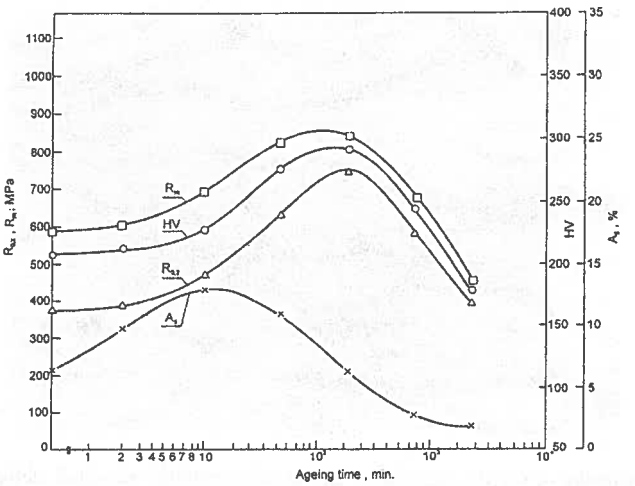

Fig. 25. Change of the mechanical properties of CuNi13Sn5 alloy with Nb microaddition, saturated, deformed by $\varepsilon = 40\%$ and afterwards aged at 400°C as a function of time

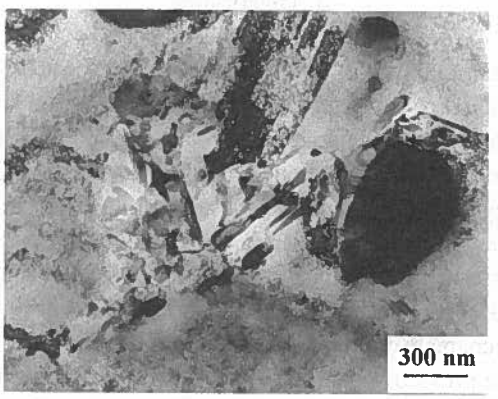

Fig. 26. Microstructure of CuNi13Sn5 alloy with Nb microaddition, saturated, deformed by $\varepsilon = 40\%$ and afterward aged at 400°C for 50 minutes

The structure of CuNi13Sn5 alloy with Nb microaddition, after its thermal-mechanical treatment, is built of small γ' precipitates of continuous transition, $NbNi_3$ precipitates and a great amount of cellular γ' precipitates (Figs 26, 27). The performed structural investigations have indicated that niobium microaddition to CuNi13Sn5 alloy does not prevent the occurrence of discontinuous transition.

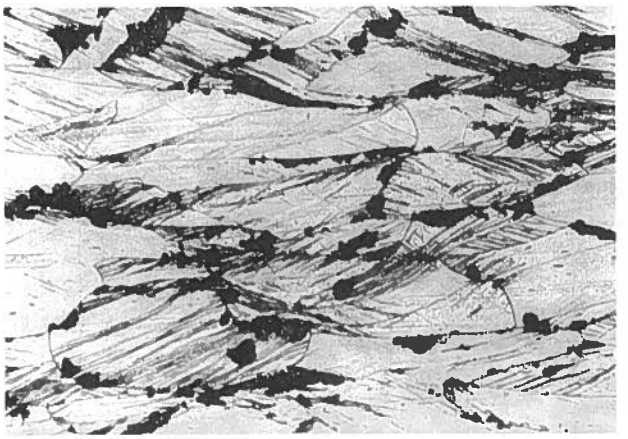

Fig. 27. Microstructure of CuNi13Sn5 alloy with Nb microaddition, saturated, deformed by ε=40% and afterwards aged at 400°C for 50 minutes. Magnified 250×

4. Discussion

Decomposition of saturated solid solution of CuNi13Sn5 alloy begins with spinodal segregation. The occurrence of this transition is evidenced by the spinodal character of the structure, absence of a zone free from precipitates at the grain boundaries and the appearance of additional reflexes on the electron diffraction. After this transition there takes place continuous precipitation of the strengthening phase in the entire volume of the alloy. Both these processes are accompanied by release of energy (A, B). Precipitates of γ' hardening phase are arranged in the direction [001], forming modulations in this direction. This suggests that nucleation of continuous precipitates occurs on modulations of the chemical composition induced by spinodal decomposition. Such mechanism of precipitation is the indication that the kinetics of continuous transition depends on the previous occurrence of spinodal segregation. At advanced stages of ageing there occur simultaneously a few structural processes. The continuous precipitates continue to grow. There begins the nucleation, and next the migration of the fronts of discontinuous transition, which reduces the internal energy of the system. The energetic effect, registered in a calorimeter, represents the resultant of all the processes taking place.

Reduction of the strengthening of CuNi13Sn5 alloy at advanced stages of ageing is the result of the appearance of cellular precipitates of discontinuous transition. This statement has been proved by the measurements of the microhardness of the inside of grains occupied by continuous precipitates and of the near-the boundary areas occupied by cellular precipitates. The microhardness of the grains inside is 1,5 times greater than that of the cellular precipitates and it increases with the time of ageing. This increase takes place also when the macrohardness of the alloy is evidently decreasing.

The performed investigations indicate that in order to maintain high level of the mechanical properties of CuNi13Sn5 alloy as a result of the ageing process the precipitation kinetics must be changed so as to eliminate or reduce to a great extent the occurrence of

cellular precipitates of discontinuous transition. With this aim in view the microadditions in the form of Si, Ti or Nb have been introduced into CuNi13Sn5 alloy.

It is known that the process of discontinuous precipitation occurs only on grain boundaries able to migrate. Migration of the grain boundaries can be made difficult by introducing into the alloy the microadditions which will segregate or form phase precipitates within the boundaries of grains. In CuNi13Sn5 alloy with Si microaddition the boundaries of the grains become blocked by sparingly soluble particles of Ni_3Si phase formed as a result of heterogenisation in the course of homogenisation. Investigations of the effect of Si micro-addition to CuNiSn alloys on the occurrence of discontinuous transition have been also carried out by M. Miki and Y. Ogino [4]. In their opinion both nucleation and the growth of cellular precipitates are inhibited by $Ni_{31}Si_{12}$ phase observed by these authors already in a saturated alloy. It can be assumed that the inactivation of the grain boundaries in the examined alloy was due to the segregation of Si atoms to the grain boundaries. M. Miki and Y. Ogino [11] examined also the effect of an addition of boron (0,05 at %) and phosphorus (0,05 at %) to CuNi42Sn8 alloy on the basis of cellular precipitates. The results obtained by these authors are evidence that both B and P atoms, by segregating to the grain boundaries during ageing at 400°C for $1{,}2 \times 10^6$ s, prevented the occurrence of discontinuous transition. The microaddition of titanium to the examined CuNi13Sn5 alloy also prevented the occurrence of discontinuous transition during ageing. Particles of $TiNi_3$ phase became located in the grain boundaries and made them inactive. Therefore the grain boundaries could not become the sites of nucleation and of the subsequent growth of cellular precipitates.

Both the microaddition of Si as well as of Ti was responsible for the delay of continuous precipitation of γ' phase in the alloy matrix which was manifested in shifting of the strengthening curves towards longer times of ageing.

The most essential effect of changes induced by Si or Ti microaddition is the increase of the mechanical properties of the examined alloy. The aged alloy acquired not only high strength properties but also very good deformability. The applied thermal-mechanical treatment resulted in further increase of the strength properties at a rather small decrease of deformability. The attained mechanical properties of CuNi13Sn5 alloy with Si or Ti micro-addition allow to regard it as belonging to copper alloys of the highest properties.

The third microaddition applied to CuNi13Sn5, which was Nb, did not stop the cellular precipitation in the ageing process. The obtained investigation results indicate that NbNi3 phase was localized in the whole volume of the alloy and it did not block the grain boundaries. The Nb segregation to the grain boundaries did not occur either. Niobium contributed only to the grain refinement of the structure. Intensive occurrence of cellular precipitates caused that CuNi13Sn5 alloy with Nb microaddition attained much lower strength as well as lower plastic properties than the alloy with Si or Ti microaddition.

5. Conclusions

1. The ageing process of CuNi13Sn5 alloy begins with spinodal decomposition followed by continuous precipitation of the γ' strengthening phase. At advanced

stage of ageing there takes place an intensive process of formation and migration of the fronts of discontinuous transition.

2. The newly formed cellular precipitates of discontinuous transition are responsible for the decrease of the alloy strengthening after a longer time of ageing.
3. Microadditions in the form of Si (0,4 wt %) or Ti (0,35 wt %) in CuNi13Sn5 alloy make the grain boundaries inactive, preventing the formation of cellular precipitates of discontinuous transition.
4. CuNi13Sn5 alloy with Si or Ti microaddition, aged at 400°C is characterized by very great strength properties and good deformability. These properties are as follows:
   a. with Si microaddition: $R_m = 950$ MPa, $R_{0,2} = 830$ MPa, HV = 310, $A_5 = 12\%$,
   b. with Ti microaddition: $R_m = 920$ MPa, $R_{0,2} = 810$ MPa, HV = 290, $A_5 = 12\%$.
5. Still higher strength properties are attained by CuNi13Sn5 alloy with Si or Ti microadditions after its thermo-mechanical treatment. These properties are as follows:
   a. with Si microaddition: $R_m = 1050$ MPa, $R_{0,2} = 900$ MPa, HV = 330, $A_5 = 7\%$,
   b. with Ti microaddition: $R_m = 1000$ MPa, $R_{0,2} = 840$ MPa, HV = 320, $A_5 = 8\%$.
6. Nb microaddition (0,45 wt %) to CuNi13Sn5 alloy does not stop the cellular precipitates of discontinuous transition in the course of ageing.
7. The mechanical properties of aged CuNi13Sn5 alloy with Nb microaddition as well as after thermo-mechanical treatment are definitely lower than those of an alloy with Si or Ti microaddition.

Financial support from the Polish Committee for Scientific Research (KBN), grant number 4 T08 B04322 is acknowledged.

REFERENCES

[1] B. Ditchek, L. H. Schwartz, Acta Metallurgica **28** (4), 807 (1980).
[2] W. Leo, Metall. **21**, 908 (1957).
[3] J. C. Zhao, M. R. Notis, Scripta Materialia **39** (11), 1509 (1998).
[4] M. Miki, Y. Ogino, Materials Transactions **31** (11), 969, (1990).
[5] P. H. Hermann, D. G. Morris, Metallurgical and Materials Trans. **25A** (6), 1403 (1994).
[6] P. Kratochvil, J. Menel, J. Pesicka, S. N. Komnik, Acta Metallurgica **32** (9), 1495 (1984).
[7] J. H. Abboud, E. S. Dwarakadasa, Journal of Materials Sci. Letters **2**, 233 (1983).
[8] M. Karolini, Prace Instytutu Odlewnictwa **1**, 61 (1983).
[9] M. P. Quin, L. H. Schwartz, Materials Sci. And Engineering **54**, 121 (1982).
[10] L. H. Schwartz, J. T. Plewes, Acta Metallurgica **22**, 911 (1974).
[11] M. Miki, Y. Ogino, Trans. of the Japan Institute of Metals **25** (9), 611 (1984).
[12] H. Sagane, N. Kuwano, K. Oki, Japan of Metals **56** (9), 998 (1992).
[13] L. Ciura, W. Malee, J. Stobrawa, Rudy i Metale Nieżelazne **39** (9), 242 (1994).
[14] P. Zięba, Zeszyty Naukowe Politechniki Śląskiej, Gliwice, 51 (1996).
[15] M. Tumidajewicz, praca doktorska, AGH, Kraków (2002).
[16] L. Deyong, M. Elboujdaini, R. Tremblay, E. Ghali, Journal of Applied Electrochemistry **20**, 756 (1990).

A R C H I V E S O F M E T A L L U R G Y A N D M A T E R I A L S
Volume 49 2004 Issue 3

M. SUŁOWSKI *

THE STRUCTURE AND MECHANICAL PROPERTIES OF SINTERED Fe-Mn-C PARTS

STRUKTURA I WŁASNOŚCI MECHANICZNE KONSTRUKCYJNYCH SPIEKÓW ŻELAZO-MANGAN-WĘGIEL

Nickel and copper, and in some cases molybdenum, are the alloying elements which have traditionally been used in sintered steels. High performance of PM heavy duty structural parts from iron powders is reached mainly by alloying of nickel. The use of manganese in iron-base PM structural parts has been avoided because of high affinity of this element to oxygen. It makes difficult to sinter steels containing manganese, without oxidation, in industrial atmospheres. However, the powder metallurgy industry follows also possibilities in order to develop nickel-free sintered steels which render as high mechanical properties as diffusion alloyed nickel-containing sintered steels and further fulfil the requirements of health protection. In recent years manganese have been introduced as alloying element in iron based structural parts, on laboratory scale and also for pilot scale production.

In this paper the factors that contribute to the structure and mechanical properties of sintered manganese steels are summarised. The paper shows the influence of processing parameters on the mechanical properties of Ni-free PM steels.

Spiekane stale manganowe są od lat przedmiotem badań laboratoryjnych. Nikiel, miedź i niekiedy molibden są pierwiastkami stopowymi używanymi podczas produkcji spiekanych stali, w celu zapewnienia im wysokich własności wytrzymałościowych oraz znacznej odporności na ścieranie. Bardzo dobrym zamiennikiem dla drogiego, a zarazem szkodliwego dla zdrowia niklu jest mangan, którego obecność w stali powoduje zwiększenie odporności na ścieranie oraz przyczynia się do wzrostu hartowności stali. Jednak zastosowanie elementarnego proszku manganu przy produkcji konstrukcyjnych spieków żelazo-mangan-węgiel jest ograniczone z uwagi na jego wysokie powinowactwo do tlenu. Aby zapobiec łatwemu utlenianiu, mangan najczęściej dodawany jest do mieszanki proszków w postaci żelazostopu, co jednak przyczynia się do pogorszenia zgęszczalności mieszanki. W celu ochrony przed utlenieniem wyprasek zawierających mangan możliwe jest również prowadzenie procesu spiekania w specjalnej zasypce lub w półhermetycznych łódkach.

Zastosowanie odpowiednich warunków wytwarzania spiekanych stali manganowych pozwala obecnie na wykorzystanie tych materiałów do produkcji spiekanych elementów konstrukcyjnych

* FACULTY OF METALLURGY AND MATERIALS SCIENCE, UNIVERSITY OF SCIENCE AND TECHNOLOGY, 30-059 KRAKÓW, AL. MICKIEWICZA 30, POLAND

o wysokich własnościach mechanicznych, przeznaczonych np. na kola zębate, znajdujące zastosowanie w elektronarzędziach.

List of Symbols

A	– tensile elongation at fracture
ATM	– sintering atmosphere
d_0	– green density of compacts
d_1	– as-sintered density
DF	– do not flow
DP	– sintering atmosphere dew point
CR	– cooling rate
HV_{10} app.	– apparent hardness
HV_{10} cross.	– apparent cross-sectional hardness
ISO	– tensile strength test bars
KC	– impact energy
mag.	– magnification
NT	– not tempered
ND	– not defined
rect.	– rectangular test bars
$R_{0.2}$ offset	– 0.2% offset yield strength
SEM	– scanning electron microscopy
ST	– sintering temperature
TRS	– transverse rupture strength
TT	– tempering temperature
UTS	– ultimate tensile strength
τ	– sintering time

1. Objectives of research work and state of the art

Most powder metallurgy (PM) steels differ significantly from their wrought counterparts. Nickel and copper, and in some cases molybdenum, are the alloying elements which have traditionally been used in high-strength sintered structural steels. Manganese has a significant influence on hardenability but its use is restricted because of its strong affinity for oxygen. Consideration of E l l i n g h a m - R i c h a r d s o n diagrams [1] indicates that sintering of manganese steels is not practicable in endogas and, even in pure hydrogen, the dew point requirements for sintering temperatures of 1120 and 1250°C are −60°C and −50°C, respectively. While Ni, Cu, and particularly Mo additions are more effective than additions of Mn, their oxides are reducible during sintering in standard industrial conditions (1120°C, dissociated ammonia atmosphere, −30°C dew point). However, the powder metallurgy industry follows possibilities in order to develop

nickel-free sintered steels, which render mechanical properties as high as diffusion alloyed nickel-containing sintered steels and further fulfil the requirements of health protection [2].

During last 50 years sintered manganese steels have been the interest of scientists from all over the world. The main topics of the researches were concerned on:

- the effect of manganese content and other alloying elements on the mechanical properties of sintered structural parts [3-7],
- the effect of alloying elements, which in sintering temperatures create liquid phase, on the structure and mechanical properties of sintered manganese steels [7-8],
- elimination of expensive and cancerogenic nickel and heavy-recycled copper by introducing in sintered steels manganese and chromium causing to increase the mechanical properties of sintering manganese steels [9-10].

The first fully commercial PM steel with Mn in excess of 1% was patented in 1996 and produced by Canadian company Stockpole. Commercial exploitation of PM manganese ferrous alloys appears restricted to < 1.5% manganese at sintering temperatures < 1300°C. However, even these Mn contents require special processing procedures, e.g. comminuting ferromanganese under nitrogen to a mean particle size of 8μm to minimise the oxygen level of the starting powders. With a tensile strength of 600 MPa, and acceptable dimensional stability, manganese PM steels with density ~7g/cm^3 find applications in automotive industry. In Europe in recent years manganese has been introduced as an alloying element in iron-based structural parts on laboratory scale [11-12] and for pilot scale production [3], primarily in Germany, Slovakia, Poland and Bulgaria.

Following these research trends, the most important objective of this research work was to find both the satisfied mechanical properties of sintered manganese steels and the proper conditions to produce these sintered parts. This study is an attempt to evaluate common manufacturing techniques and sintering in a semi-closed container, determine their significance on the PM steel thermal history, and introduce an efficient approach to the generation of sintering process specifications based on actual material behaviour properties. The second object was to find an industrial applications of these steels which could be formed during sintering in low-hydrogen or hydrogen-free atmospheres with other constant industrial processing such as cooling rate.

The focus of alloy development was to utilise Mn alloying addition and carbon in combinations that optimise the synergistic effect of their presence on the hardenability of the alloy. Such steels as Fe-(3-4)%Mn-0.8%C are referred to as being "sinter-hardenable", since sintering furnaces equipped with enhanced cooling capacity have been produced for many years. There are a number of benefits of the sinter-hardening process. First of all the need for the secondary quench-hardening treatment is eliminated.

The powder metallurgy technique may allow sintered manganese steels to be made based on pure iron and ferromanganese powders with control over alloy microstructure. There are a lot of factors that contribute to the mechanical properties of sintered Fe-Mn-C steels, such as the based powders grade, chemical composition of the powder mixture, pressing and sintering conditions, tempering temperature, which have an influence on the structure and mechanical properties.

Because of it in this study, the data was treated in three groups. The first group pertained to the influence of iron and ferromanganese powders grade on the mechanical properties of steels and had to do with observed variations in mechanical properties caused by changes in sintering temperature and dew point of the sintering atmosphere. The second one dealt with the effect of cooling rate on the structure and mechanical properties of PM manganese steels. The third group of data was related to the influence of sintering atmosphere chemical composition and additional post-sintering heat treatment on the structure and mechanical properties of sintered manganese steels.

2. Main results

2.1. Powder used

Two iron powders have been used in the investigation: Höganäs sponge iron powder grade NC 100.24 and Höganäs atomised iron powder grade ABC 100.30. The manganese was added in the form of ferromanganese powder. Two types of ferromanganese powders were selected: HP III high-carbon ferromanganese powder, produced from Huta Pokój, milled in nitrogen atmosphere, and Elkem low-carbon ferromanganese powder provided by Huta Baildon. Additions of ultra fine graphite (Höganäs C-UF) were made to all materials. Commercial tin powder grade Sn-30GN-350 from Eckard-Poundmet was also employed.

2.2. Powder characterisation and testing

The most important parameters when evaluating the iron and ferromanganese properties were chemical compositions, hydrogen loss, the particle size and distribution, apparent and tap density, flowability and compressibility. Chemical composition of the ferromanganese powders was determined by conventional wet chemical method. Sieve analysis and sedimentation method were employed to determine the particle size of iron and ferromanganese powders, respectively. The results of these investigations are listed in earlier publications [6, 17, 19].

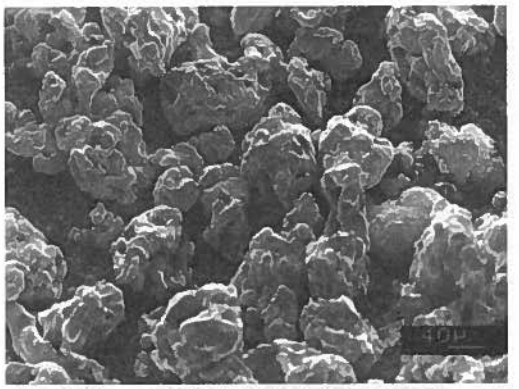

Fig. 1. NC 100.24 iron powder (SEM)

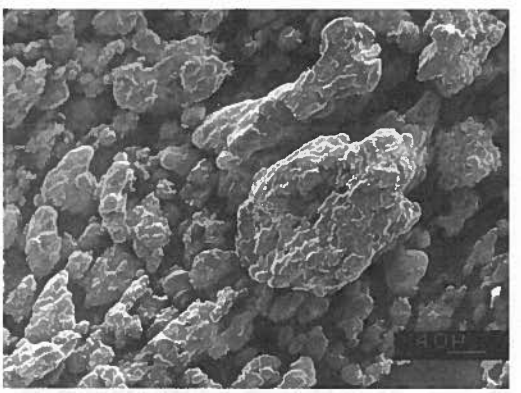

Fig. 2. ABC 100.30 iron powder (SEM)

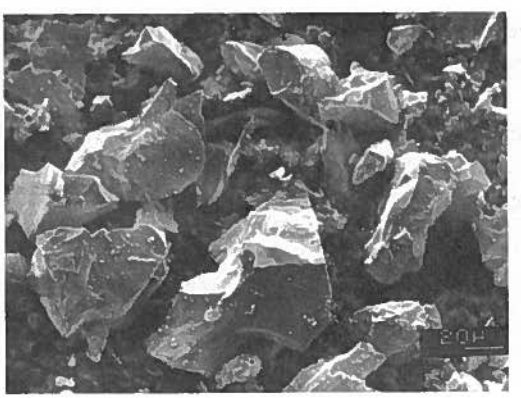

Fig. 3. HP III high-carbon ferromanganese powder (SEM)

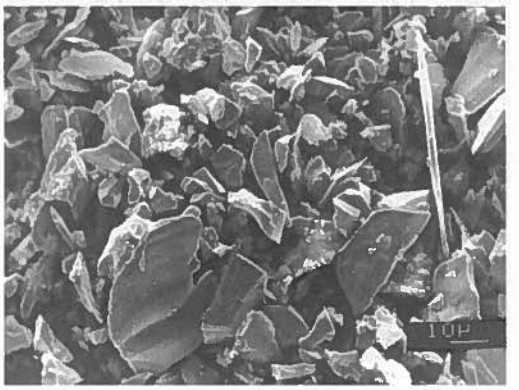

Fig. 4. Elkem low-carbon ferromanganese powder (SEM)

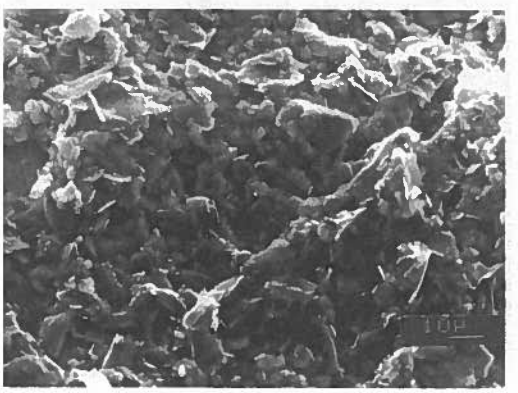

Fig. 5. Graphite C-UF powder (SEM)

Individual particle shape was investigated for iron, ferromanganese and graphite powder using scanning elcetron microscopy. The results of investigations are presented in Figs. 1-5.

Seventeen different compositions of powders were prepared by blending iron, ferromanganese, tin and graphite powders (table 1). The powders were mixed in a double cone laboratory mixer (60 min, 50 rev./min). No lubricant was added to the powder before mixing.

TABLE I

Summary of chemical composition, powder mixtures and specimens type

No	Iron powder	Ferromanganese powder	Tin powder	Chemical composition, wt.-%			Speciment type in work stage		
	Fe	Fe-Mn	Sn	Mn	C	Sn	First	Second	Third
1.	NC 100.24	Elkem	not used	3	0.8	0	3NCEL1	3NCEL2	3NCEL3, 3NCELATM
2.				4			4NCEL1	not used	not used
3.		HP III		3			3NCHP1		
4.				4			4NCHP1		
5.	ABC 100.30	Elkem		3			3ABCEL1		
6.				4			4ABCEL1		
7.		HP III		3			3ABCHP1		
8.				4			4ABCHP1		
9.	NC 100.24	Elkem	Sn-30GN-350	3	0.8	0.10	3NCELSN	not used	not used
10.						0.15			
11.						0.20			
12.						0.25			
13.						0.30			
14.						0.35			
15.						0.50			
16.						0.75			
17.						1.00			

2.3. Test bars preparation for all stages of this work

2.3.1. Compacting

The blended powders were pressed in steel dies with zinc stearate lubricated walls to achieve green density ~ 7 g/cm^3. Unaxial, single-action compacting with a stationary lower punch was used. Two types of compacts were pressed: 55×10×5 mm transverse rupture test bars and tensile strength test bars (ISO 2740). A summary of characteristic data of rectangular and ISO green compacts is presented in tables 2, 4-8.

TABLE 2

Green density of compacts; mean values

Specimen	d_0, g/cm^3		Specimen	d_0, g/cm^3		Specimen	d_0, g/cm^3		Specimen	d_0, g/cm^3	
	rect.	ISO		rect.	ISO		rect.	ISO		rect.	ISO
3NCEL1	6.88	6.67	3NCHP1	7.01	6.82	3ABCEL1	7.17	6.95	3ABCHP1	7.11	7.02
4NCEL1	6.91	6.70	4NCHP1	6.85	6.81	4ABCEL1	7.11	7.03	4ABCHP1	6.99	7.06

2.3.2. Sintering

Sintering was carried out in a horizontal laboratory furnace. The heat resisting steel tube furnace was equipped with water jacketed rapid convective cooling zone. Sintering conditions are summarised in table 3. To prevent oxidation, the specimens were set in a stainless steel semi-closed boat and were removed only after the boat had cooled to room temperature. To measure temperature inside the boat thermocouple NiCrNiAl with accuracy ± 0.1°C was employed. In tables 4-8 the density of sintered steels is summarised.

TABLE 3

Sintering conditions adepted during this work

Sintering parameter	First stage	Second stage	Third stage
Heating rate, °C/min	75	75	75
Isothermal sintering temperature, ST, °C	1120, 1150, 1180, 1200	1120, 1250	1120, 1250
Sintering time, τ, min	60	60	60
Sintering temperature control, °C	±2	±2	±2
Sintering atmosphere, ATM	hydrogen	hydrogen	hydrogen, mixture of H_2-N_2, nitrogen
Sintering atmosphere dew point, DP, °C	from -40 to -60°C	-60	below -60
Cooling rate, CR, °C/min	3.5 and 60	from 3.5 to 67	67
Control range of coling rate, °C	1100–550	from sintering temperature	from sintering temperature

TABLE 4

As-sintered density of 3NCEL1 and 4NCEL1 specimens; mean values

ST, °C	DP, °C	CR, °C/min	Specimen	d_1, g/cm^3		Specimen	d_1, g/cm^3	
				rect.	ISO		rect.	ISO
1120	-40	60	3NCEL1	6.78	6.72	4NCEL1	6.81	6.59
	-50			6.70	6.56		6.74	6.59
	-60			6.87	6.34		6.73	6.70
1150	-40			6.83	6.38		6.78	6.57
	-50			6.81	6.71		6.79	6.59
	-60			6.87	6.70		6.82	6.63
1180	-40			6.86	6.69		6.87	6.75
	-50			6.83	6.77		6.88	6.58
	-60			6.92	6.75		6.88	6.68
1200	-40			6.89	6.44		6.90	6.73
	-50			6.87	6.68		6.95	6.73
	-60			6.85	6.57		6.88	6.70

TABLE 5

As-sintered density of 3NCHP1, 4NCHP1, 3ABCEL1, 4ABCEL1, 3ABCHP1 and 4ABCHP1 specimens; mean values

ST, °C	DP, °C	CR, °C/min	Specimen	d_1, g/cm^3	
				rect.	ISO
1200	-60	60	3NCHP1	6.98	6.83
			4NCHP1	6.79	6.80
1180		1.5	3ABCEL1	7.03	6.91
		60		7.02	6.88
		1.5	4ABCEL1	6.91	6.96
		60		6.97	6.96
		1.5	3ABCHP1	6.98	6.94
		60		6.96	6.97
		1.5	4ABCHP1	6.74	6.90
		60		6.83	7.01

TABLE 6

Green and as-sintered density of 3NCEL2 PM specimens; mean values

Specimen	d_0, g/cm³		ST = 1120°C, DP = – 60°C			ST = 1250°C, DP = – 60°C		
			CR, °C/min	d_1, g/cm³		CR, °C/min	d_1, g/cm³	
	rect.	ISO		rect.	ISO		rect.	ISO
3NCEL2	6.93	6.95	5	6.96	6.97	5	7.05	7.03
			9	6.96	6.98	9	7.02	7.03
			16	6.93	6.98	20	7.03	7.04
			30	6.90	6.97	32	7.03	7.04
			47	6.88	6.96	41	7.04	7.03
			55	6.88	6.97	57	7.01	7.04
			67	6.89	6.97	64	7.00	7.04

TABLE 7

Green and as-sintered density of 3NCEL3 PM specimens; mean values

Specimen	TT, °C	ST = 1120°C, DP = – 60°C, CR = 67°C/min				ST = 1250°C, DP = – 60°C, CR = 64°C/min			
		d_0, g/cm³		d_1, g/cm³		d_0, g/cm³		d_1, g/cm³	
		rect.	ISO	rect.	ISO	rect.	ISO	rect.	ISO
3NCEL3	200	7.00	6.94	6.99	6.94	6.99	6.93	7.07	6.94
	300			6.97	6.94			7.07	6.93
	400			6.95	6.93			7.06	6.94

TABLE 8

Green and as-sintered density of 3NCELATM PM specimens; mean values

Specimen	Content of H_2 in N_2–H_2 mixture, %	ST = 1120°C, DP = – 60°C, CR = 67°C/min				ST = 1250°C, DP = – 60°C, CR = 64°C/min			
		d_0, g/cm³		d_1, g/cm³		d_0, g/cm³		d_1, g/cm³	
		rect.	ISO	rect.	ISO	rect.	ISO	rect.	ISO
3NCELATM	100	6.96	6.84	6.95	6.81	6.95	6.80	7.02	6.80
	75	6.98	6.85	6.97	6.83	6.97	6.84	7.03	6.85
	25	6.97	6.84	6.95	6.81	6.97	6.87	7.07	6.87
	5	6.97	6.85	6.93	6.82	6.99	6.83	7.02	6.82
	0	7.03	6.85	6.95	6.82	7.08	6.83	7.02	6.82

2.3.3. Post-sintering heat treatment

In the third stage of the work, after convective cooling, some of the specimens were tempered at 200, 300 and 400°C for 60 minutes in hydrogen and nitrogen atmospheres.

2.4. Testing of sintered specimens

2.4.1. Tensile test

The tensile properties were ascertained for as-sintered or sintered and tempered steels on dogbone tensile specimens according to PN–EN 10002–1 standard. A tensile test was carried out with MTS 810 testing machine at a crosshead speed of 0.5 mm/min. The load applied and the strain were recorded continuously throughout the test. The resulting stress-strain curves were analysed to identify the 0.2% offset yield strength ($R_{0,2}$ offset), tensile strength (UTS) and tensile elongation at fracture (A). In addition to the tensile and elongation testing, failed specimens underwent metallographic examination. Testing was performed on between 10 and 20 specimens per material. The results of the tensile test are shown in tables 9-13.

2.4.2. Bend test

Transverse rupture strength (TRS) was determined by three-point bend testing with stress at fracture evaluated used simple beam theory, i.e. assuming elastic behaviour, according to PN–EN ISO 3325 standard. The fixture had two support cylinders mounted parallel with the 28.6 mm distance between the centres. The load cylinder was mounted midway between the support cylinders. The testing equipment provided a static condition of loading. The value at which the load suddenly dropped to the first crack was recorded. The transverse rupture strength, in MPa, was calculated from the Navier formula. This procedure is only truly applicable to brittle specimens. It was used in this study as a routine measure to quickly distinguish between the apparent bend strength of the investigated alloys. However, some specimens involved in this study were optically found capable of being bent and an attempt was made to take into account plasticity and to convert some results to true bend strength [13-18]. The results of bend tests are presented in tables 9-13.

2.4.3. Impact test

Impact test (KC) was carried out using 55x10x5 mm specimens and a 15 J Charpy bar impact tester according to the PN–EN 10045–1 standard. Samples were placed on supports with a distance of 25 mm. The results of impact tests are presented in tables 9-13.

2.4.4. Apparent surface and cross-sectional hardness

The apparent hardness, as well as cross-sectional hardness of the test specimens (HV_{10}), was determined by means of Vickers hardness tester, according to the PN–EN ISO 3878. The results of hardness are presented in tables 9-13.

TABLE 9

Mechanical properties of 3NCHP1, 4NCHP1, 3ABCEL1, 4ABCEL1, 3ABCHP1 and 4ABCHP1 PM manganese steels; sintering atmosphere – 100%H_2; mean values

ST, °C	DP, °C	CR, °C/min	Specimen	UTS, MPa	TRS, MPa	HV_{10} app.	HV_{10} cross.	KC, J/cm^2	$R_{0,2}$ off-set, MPa	A, %
1200	-60	60	3NCHP1	421	919	184	211	5.56	290	0.35
			4NCHP1	312	597	215	160	3.75	280	0.26
1180		1.5	3ABCEL1	467	1176	148	134	10.06	313	1.76
		60		320	799	242	289	2.99	ND	0.18
		1.5	4ABCEL1	479	1136	151	163	7.39	343	1.21
		60		256	646	341	233	1.90	ND	0.11
		1.5	3ABCHP1	456	880	153	134	6.97	318	1.48
		60		340	795	195	205	4.07	ND	0.31
		1.5	4ABCHP1	491	922	157	147	2.80	335	1.09
		60		286	459	227	183	2.66	ND	0.28

TABLE 10

Mechanical properties of 3NCEL1 and 4NCEL1 PM manganese steels; sintering atmosphere – 100%H_2; mean values

ST, °C	DP, °C	CR, °C/min	Specimen	UTS, MPa	TRS, MPa	HV_{10} app.	HV_{10} cross.	KC, J/cm^2	$R_{0,2}$ offset, MPa	A, %
1120	-40	60	3NCEL1	452	1036	150	203	8.17	400	0.66
	-50			492	1189	150	147	8.23	380	1.24
	-60			433	1291	179	214	7.36	330	0.47
1150	-40			385	1253	179	216	5.82	ND	0.37
	-50			490	1161	156	132	8.27	395	0.62
	-60			427	1312	181	183	8.15	410	0.40
1180	-40			401	845	157	132	2.72	ND	0.25
	-50			423	1046	184	169	4.46	470	0.29
	-60			583	1354	166	196	6.78	490	0.74
1200	-40			469	1280	211	351	3.01	ND	0.39
	-50			527	1186	217	185	4.87	ND	0.60
	-60			445	1194	187	266	3.43	ND	0.39
1120	-40		4NCEL1	341	1147	205	284	3.31	ND	0.36
	-50			432	1157	151	230	5.80	360	0.61
	-60			369	994	184	222	3.98	330	0.43
1150	-40			328	919	223	264	2.09	ND	0.24
	-50			374	854	234	251	3.87	400	0.31
	-60			346	854	220	298	2.82	ND	0.37
1180	-40			298	840	259	331	2.30	ND	0.11
	-50			327	749	245	318	2.30	350	0.29
	-60			306	787	290	351	1.77	ND	0.15
1200	-40			322	835	264	288	2.39	ND	0.15
	-50			385	959	228	327	3.95	ND	0.17
	-60			289	788	242	372	2.12	ND	0.14

TABLE 11

Mechanical properties of 3NCEL2 PM manganese steels; sintering atmosphere – 100%H_2; mean values

Specimen	ST = 1120°C, DP = – 60°C							
	CR, °C/min	UTS, MPa	TRS, MPa	HV_{30} app.	HV_{30} cross.	KC, J/cm^2	$R_{0,2}$ offset, MPa	A, %
3NCEL2	5	478	1272	174	224	17.22	380	3.04
	9	506	1230	183	217	10.86	414	3.08
	16	568	1195	185	248	11.06	461	3.26
	30	557	1124	197	272	8.22	516	2.76
	47	559	1100	202	276	5.84	478	2.51
	55	535	954	213	292	5.24	518	2.01
	67	475	1066	206	301	4.68	528	1.90
	ST = 1250°C, DP = – 60°C							
	CR, °C/min	UTS, MPa	TRS, MPa	HV_{30} app.	HV_{30} cross.	KC, J/cm^2	$R_{0,2}$ offset, MPa	A, %
	5	595	1327	189	254	11.50	461	3.80
	9	614	1311	189	239	9.92	477	2.87
	20	583	1210	192	265	7.66	511	2.42
	32	586	1193	204	282	9.38	545	2.22
	41	521	1080	218	328	4.59	442	1.96
	57	491	1087	229	335	4.92	404	1.62
	64	458	1060	210	301	5.04	477	1.46

TABLE 12

Mechanical properties of 3NCEL3 PM manganese steels; sintering atmosphere – 100%H_2; mean values

Specimen	ST, °C	CR, °C/min	DP, °C	TT, °C	UTS, MPa	TRS, MPa	HV_{30} app.	HV_{30} cross.	KC, J/cm^2	$R_{0,2}$ offset, MPa	A, %
3NCEL2	1120	67	-60	200	740	1745	250	227	12.08	412	3.91
				300	740	1507	238	219	10.40	430	3.43
				400	744	1462	233	216	11.51	460	3.45
	1250	64		200	830	1479	247	278	10.10	474	3.69
				300	798	1448	252	274	4.87	472	3.03
				400	854	1755	257	245	15.69	499	3.71

TABLE 13

Mechanical properties of 3NCELATM PM manganese steel; mean values

ST = 1120°C, DP = -60°C										
Specimen	CR, °C/min	TT, °C	Content of H_2 in N_2-H_2 mixture, %	UTS, MPa	TRS, MPa	HV_{30} app.	HV_{30} cross.	KC, J/cm^2	$R_{0,2}$ off-set, MPa	A, %
3NCELATM	67	200	100	642	1279	196	236	4.68	386	1.87
			75	640	1291	195	247	5.09	400	1.79
			25	650	1299	201	226	7.44	420	1.78
			5	657	1234	197	186	7.27	421	1.82
			0	655	1259	212	202	14.31	410	1.93
ST = 1250°C, DP = -60°C										
Specimen	CR, °C/min	TT, °C	Content of H_2 in N_2-H_2 mixture, %	UTS, MPa	TRS, MPa	HV_{30} app.	HV_{30} cross.	KC, J/cm^2	$R_{0,2}$ off-set, MPa	A, %
3NCELATM	64	200	100	717	1296	212	315	5.04	426	1.60
			75	749	1343	212	295	13.30	443	1.71
			25	778	1411	222	298	10.83	459	1.82
			5	725	1420	221	266	12.45	451	1.67
			0	776	1458	228	260	13.23	464	2.00

2.4.5. Metallographic examinations

The examination included light-optical microscopy, microhardness using the H a - n e m a n n method and scanning electron microscopy equipped with energy dispersive X-ray spectrometer.

Metallographic sections used for microhardness measurement were polished carefully to avoid hardening surface layers which would have distorted the measured microhardness values and then 3% nital etched. The method of measurement microhardness was based on the Vickers method with load 20×10^{-2} (μHV_{20}). Figures 6-12 and 15-17 show etched sections of the specimens. To observe the fracture of sintered manganese steels, SEM was employed. Figures 13-14 and 18-23 show the most representative fractures of these steels. In tables 14-16 structural constituents of sinter-hardened manganese steels are listed. Table 17 presents microhardness of structural constituents observed in manganese steels.

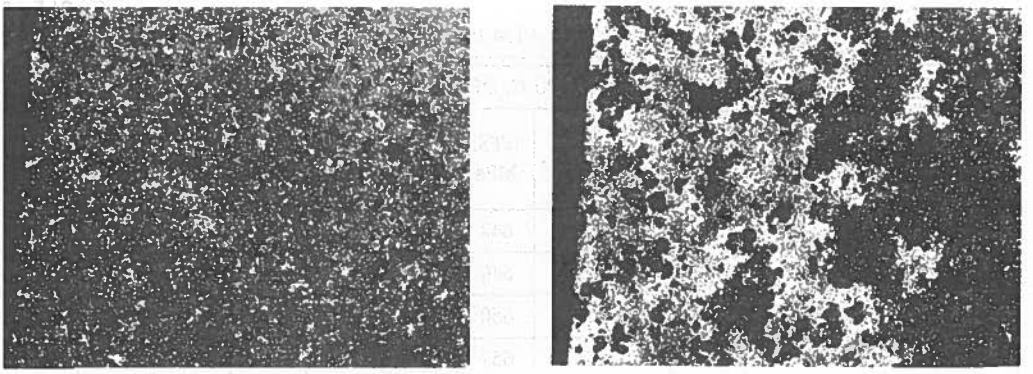

Fig. 6. Photomicrograph of surface layer of manganese steel
ST = 1120°C, ATM = 100%H_2, DP = – 60°C, CR = 60°C/min, mag. 45×, ferrite + pearlite
a) 3NCEL1 steel b) 4NCEL1 steel

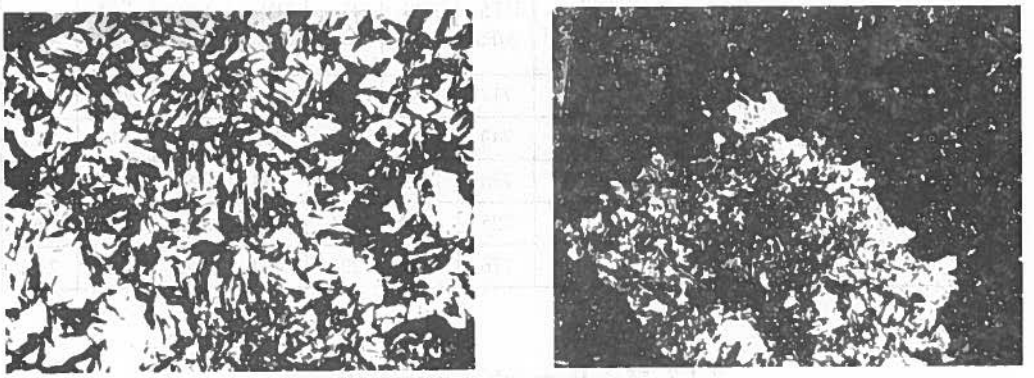

Fig. 7. Photomicrograph of manganese steel
ST = 1200°C, ATM = 100%H_2, DP = – 60°C, CR = 60°C/min, mag. 430×
a) 3NCHP1 steel – austenite, martensite b) 4NCHP1 steel – austenite + martensite, pearlite

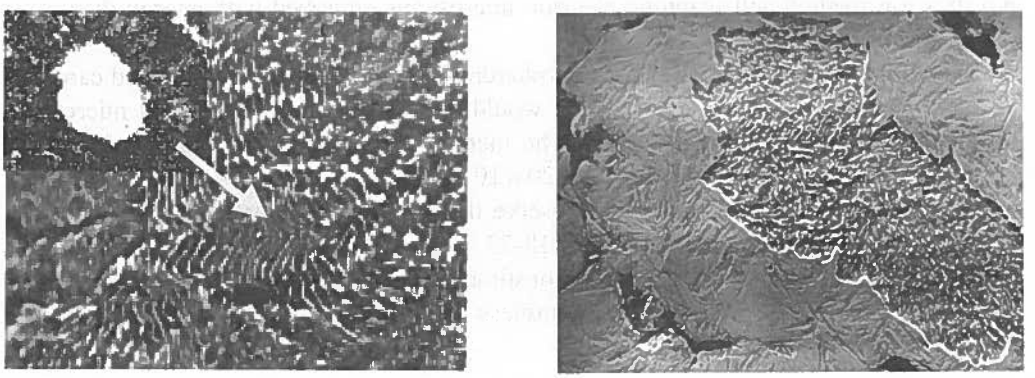

Fig. 8. Photomicrograph of manganese steel
ST = 1180°C, ATM = 100%H_2, DP = – 60°C,
a) 4ABCEL1 steel; CR = 1.5°C/min, mag. 2500× – pearlite (in the left bottom corner – ferrite with pearlite rim)
b) 4ABCEL1 steel; CR = 60°C/min, mag. 1000x – pearlite and retained austenite

TABLE 14

Structural constituents of PM maganese steels presented in the second stage of work

Microstructure			
CR, °C/min	ST = 1120°C	CR, °C/min	ST = 1250°C
5	Pearlite	5	Pearlite + proeutectoid ferrite
9		9	
16	Fine pearlite (troostite)	20	Fine pearlite + feathery bainite
30	Feathery bainite + fine pearlite	32	Acicular bainite + martensite
47	Acicular bainite + martensite + Mn-rich austenite	41	Acicular bainite + martensite + retained austenite
from 55	Acicular bainite + martensite + retained austenite	from 57	

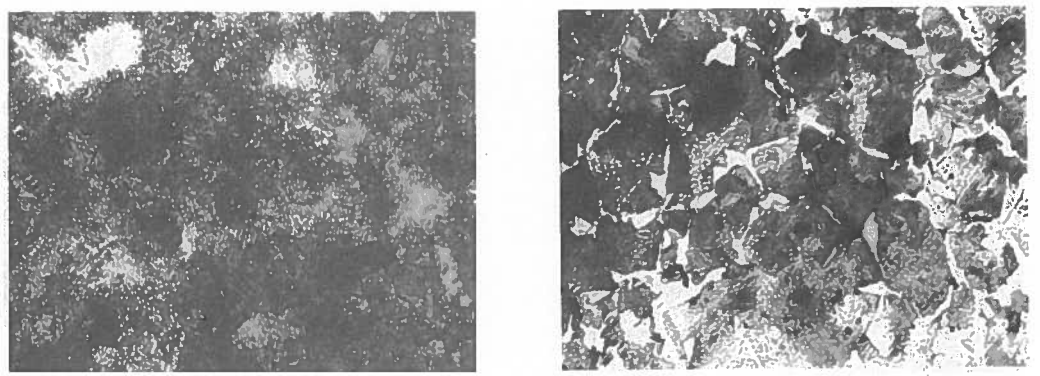

Fig. 9. Photomicrograph of 3NCEL2 PM steel
ATM = 100%H_2, DP = – 60°C; CR = 5 and 9°C/min, mag. 430×
a) ST = 1120°C – pearlite b) ST = 1250°C – pearlite and ferrite

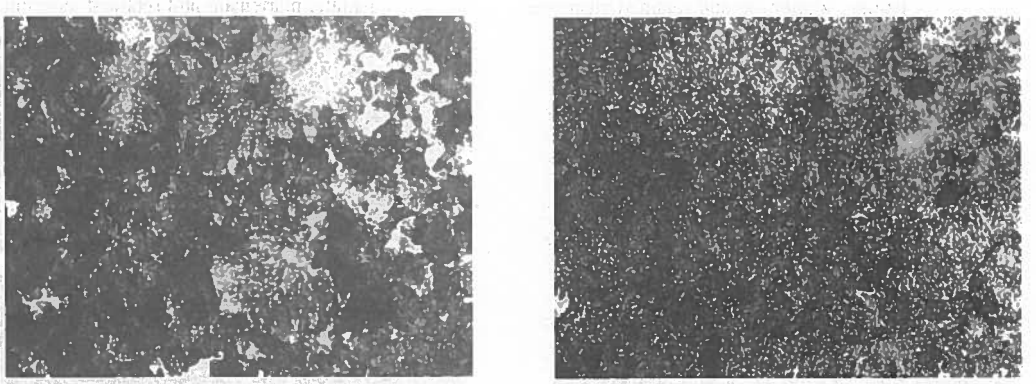

Fig. 10. Photomicrograph of 3NCEL2 PM steel
ATM = 100%H_2, DP = – 60°C, mag. 430×
a) ST = 1120°C, CR = 16°C/min – fine pearlite (troostite)
b) ST = 1250°C, CR = 20°C/min – fine pearlite (troostite) and ferrite

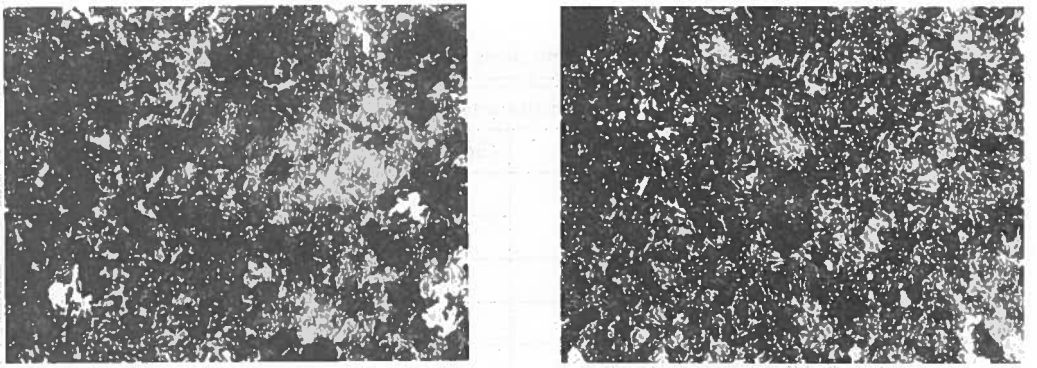

Fig. 11. Photomicrograph of 3NCEL2 PM steel
ATM = 100%H_2, DP = – 60°C, mag. 430×
a) ST = 1120°C, CR = 30°C/min – feathery bainite and pearlite
b) ST = 1250°C, CR = 3°C/min – bainite and martensite

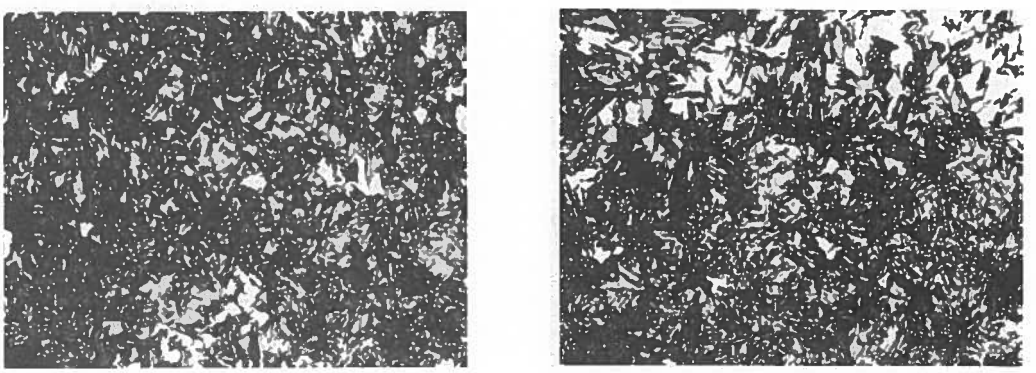

Fig. 12. Photomicrograph of 3NCEL2 PM steel
ATM = 100%H_2, DP = – 60°C, mag. 430×
a) ST = 1120°C, CR > 55°C/min – bainite, martensite and retained austenite
b) ST = 1250°C, CR > 57°C/min – bainite, martensite and retained austenite

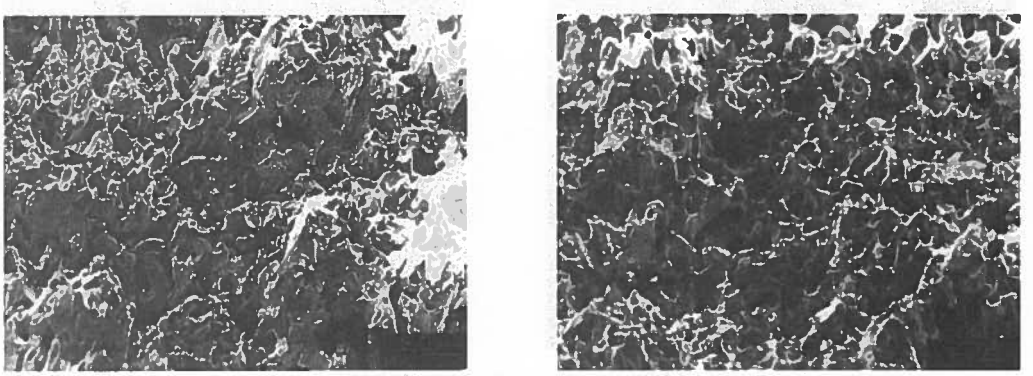

Fig. 13. Ductile fracture of 3NCEL2 PM steel
ATM = 100%H_2, DP = – 60°C, CR = 5°C/min
a) ST = 1120°C
b) ST = 1250°C

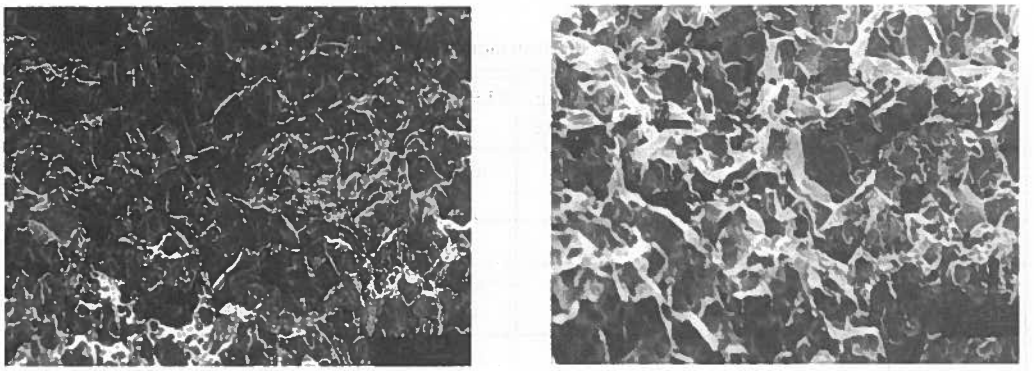

Fig. 14. Brittle fracture of 3NCEL2 PM steel
ATM = 100%H_2, DP = – 60°C, CR > 55°C/min
a) ST = 1120°C b) ST = 1250°C

TABLE 15

Structural constituents of PM maganese steel presented in the third stage of work

Specimen	TT, °C	ST = 1120°C, CR = 67°C/min	ST = 1250°C, CR = 64°C/min
3NCEL2	NT	martensite + retained austenite + bainite	
3NCEL3	200	martensite + retained austenite	
	300	sorbite	
	400	sorbite + ferrite	

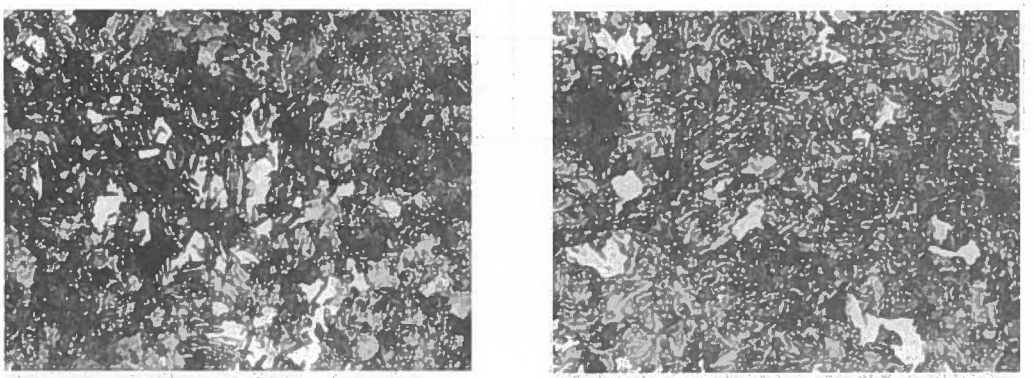

Fig. 15. Photomicrograph of 3NCEL3 PM steel
ATM = 100%H_2, DP = – 60°C, TT = 200°C, mag. 830×
a) ST = 1120°C, CR = 67°C/min – martensite and retained austenite
b) ST = 1250°C, CR = 64°C/min – martensite and retained austenite

TABLE 16

Effect of processing parameters on the structural constituents of PM manganese steels

Specimen	Sintering atmosphere	TT, °C	Tempering atmosphere	ST = 1120°C, DP = – 60°C CR = 67°C/min	ST = 1250°C, DP = – 60°C CR = 64°C/min
3NCEL1	100%H_2	NT	–	martensite + retained austenite	–
3NCEL2	100%H_2	NT	–	martensite + retained austenite + bainite	
3NCEL3	100%H_2	200	H_2	tempered martensite + retained austenite	tempered martensite + retained austenite
	100%H_2	300	H_2	tempered martensite	sorbite
	100%H_2	400	H_2	sorbite + ferrite	sorbite + ferrite
3NCELATM	100%H_2	200	N_2	coarse pearlite + bainite	tempered martensite + retained austenite
	75%H_2		N_2	pearlite; small amount of martensite	bainite + tempered martensite + retained austenite; small amount of ferrite
	25%H_2		N_2	troostite + pearlite; small amounts of ferrite, tempered martensite and bainite	tempered martensite + retained austenite; small aomount of ferrite
	5%H_2		N_2	troostite; small amounts of tempered martensite and retained austenite	tempered martensite + fine pearlite
	100%N_2		N_2	tempered martensite + retained austenite + bainite + troostite	tempered martensite + retained austenite + bainite

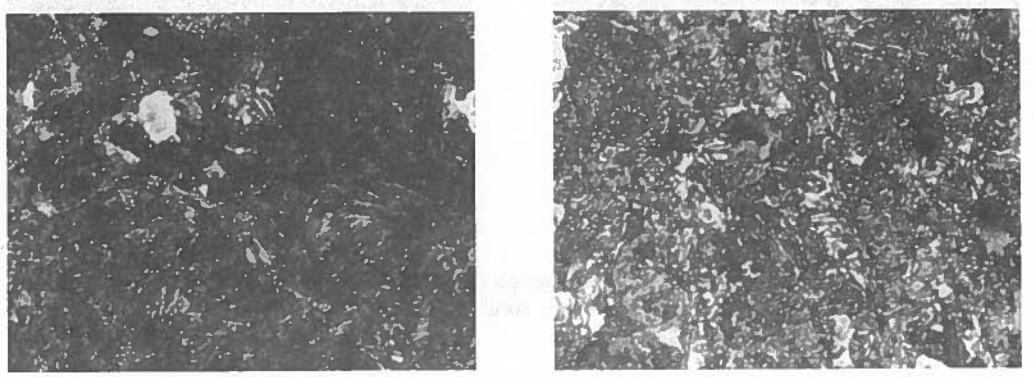

Fig. 16. Photomicrograph of 3NCEL3 PM steel
ATM = 100%H_2, DP = – 60°C, TT = 300°C, mag. 830×
a) ST = 1120°C, CR = 67°C/min – tempered martensite b) ST = 1250°C, CR = 64°C/min – sorbite

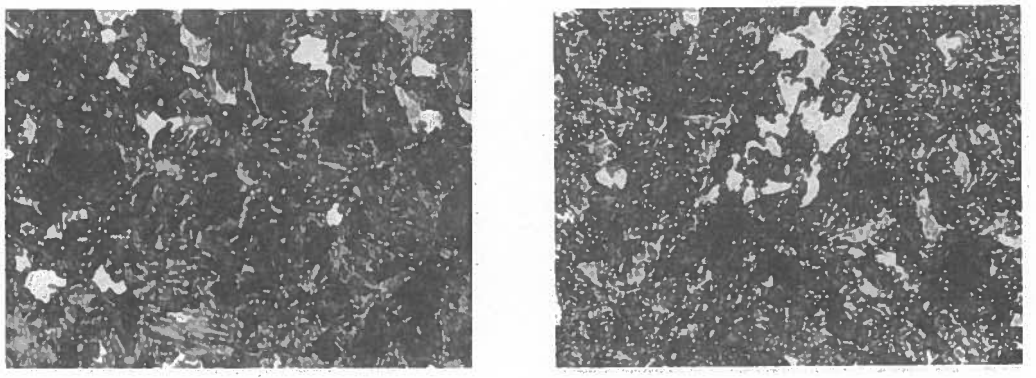

Fig. 17. Photomicrograph of 3NCEL3 PM steel
ATM = 100%H_2, DP = – 60°C, TT = 400°C, mag. 830×
a) ST = 1120°C, CR = 67°C/min – sorbite and ferrite b) ST = 1250°C, CR = 64°C/min – sorbite and ferrite

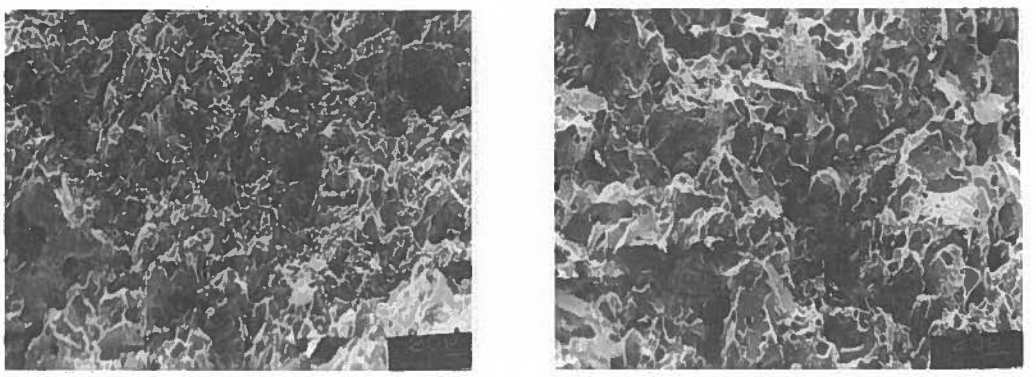

Fig. 18. Ductile fracture of 3NCEL3 PM steel
ATM = 100%H_2, DP = – 60°C, TT = 200°C
a) ST = 1120°C, CR = 67°C/min b) ST = 1250°C, CR = 64°C/min

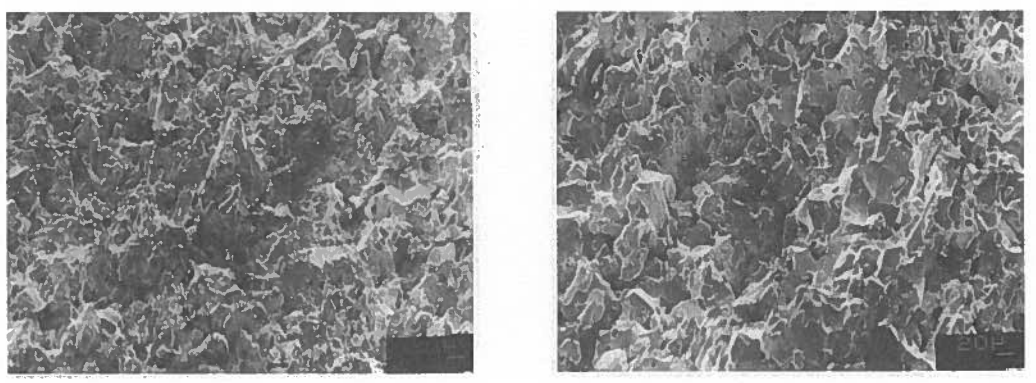

Fig. 19. Brittle fracture of 3NCEL3 PM steel
ATM = 100%H_2, DP = – 60°C, TT = 300°C
a) ST = 1120°C, CR = 67°C/min b) ST = 1250°C, CR = 64°C/min

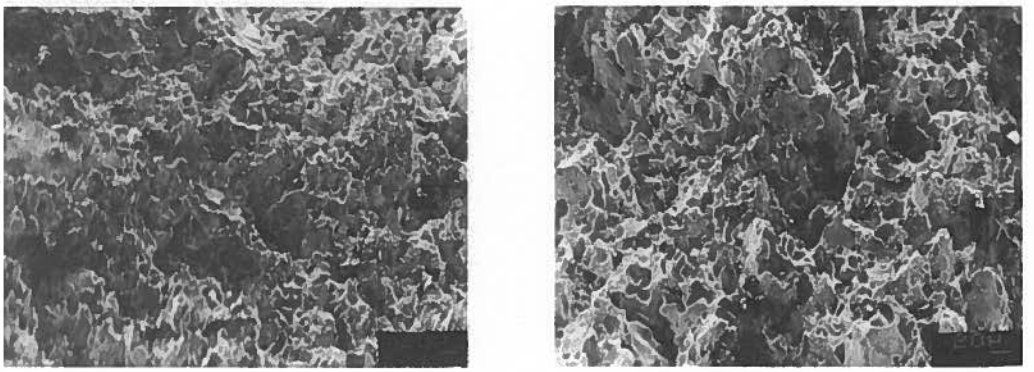

Fig. 20. Ductile fracture of 3NCEL3 PM steel
ATM = 100%H_2, DP = – 60°C, TT = 400°C
a) ST = 1120°C, CR = 67°C/min b) ST = 1250°C, CR = 64°C/min

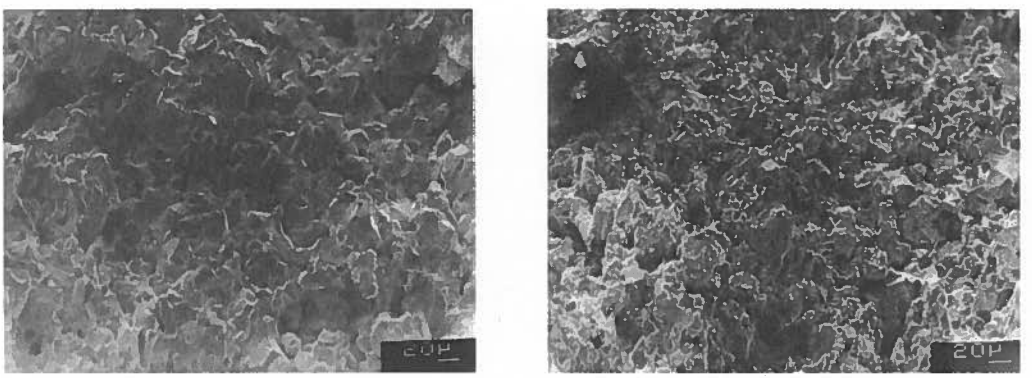

Fig. 21. Ductile fracture of 3NCELATM PM steel
ATM = 75%H_2-25%N_2, DP = – 60°C
a) ST = 1120°C, CR = 67°C/min b) ST = 1250°C, CR = 64°C/min

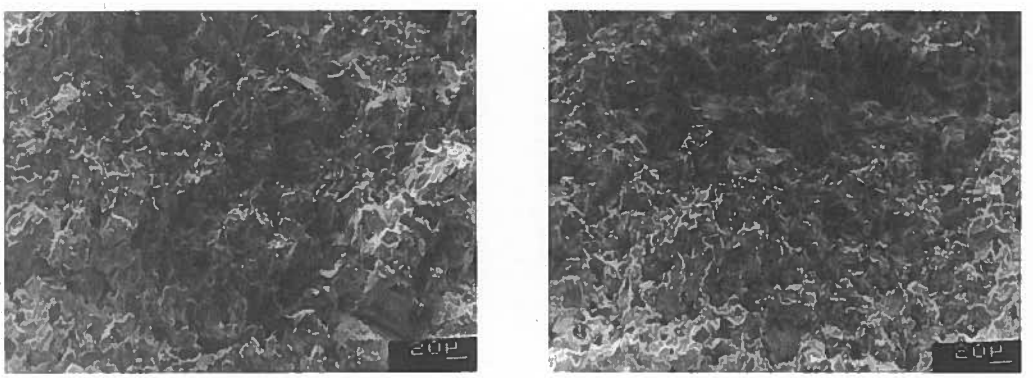

Fig. 22. Fractures of 3NCELATM PM steel
ATM = 25%H_2-75%N_2 and 5%H_2-95%N_2, DP = – 60°C
a) ST = 1120°C, CR = 67°C/min – brittle b) ST = 1250°C, CR = 64°C/min – ductile

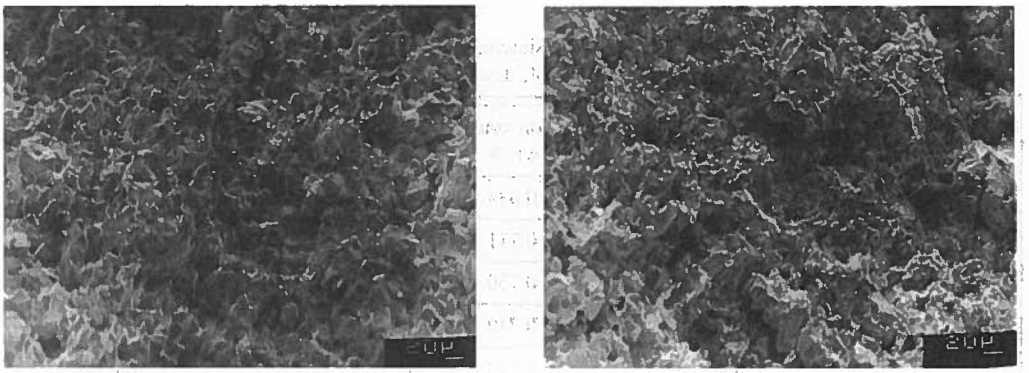

Fig. 23. Ductile fracture of 3NCELATM PM steel
ATM = 100%N_2, DP = – 60°C
a) ST = 1120°C, CR = 67°C/min b) ST = 1250°C, CR = 64°C/min

TABLE 17

Microhardness of structural constituents present in manganese steel

Structural constituent	Microhardness range, μHV_{20}
Ferrite	95–160
Pearlite	210–260
Pearlite + bainite/bainite	280–440
Austenite	450–570
Martensite	580–690

2.4.6. Chemical analysis of PM steels

Randomly chosen samples were examined using Leco CS-125 and Leco TS-336 analysers for the presence of carbon, oxygen and nitrogen. The results of investigations are presented in tables 18-19.

TABLE 18

Chemical analysis of manganese steels sintered in different temperatures in hydrogen atmosphere with a dew point – 60°C; mean values for 9 measurement

ST, °C	Carbon content, wt.-%	Oxygen content, wt.-%
Fe-3%Mn-0.8%C compact	0.766	0.229
1120	0.616	0.216
1150	0.537	0.146
1180	0.507	0.144
1200	0.469	0.117
1250	0.522	0.150

TABLE 19

Chemical analysis of manganese steels sintered in different temperatures in hydrogen, nitrogen and mixtures thereof, dew point – 60°C; mean values

ST, °C	Sintering atmosphere	Carbon content, wt.-%	Oxygen content, wt.-%	Nitrogen content, wt.-%
1120	100% H_2	0.634	0.310	0.0036
	75% H_2 – 25% N_2	0.711	0.452	0.0130
	25% H_2 – 75% N_2	0.730	0.497	0.0253
	5% H_2 – 95% N_2	0.749	0.489	0.0297
	100% N_2	0.714	0.593	0.0332
1250	100% H_2	0.519	0.148	0.0032
	75% H_2 – 25% N_2	0.580	0.325	0.0263
	25% H_2 – 75% N_2	0.569	0.325	0.0256
	5% H_2 – 95% N_2	0.620	0.283	0.0328
	100% N_2	0.619	0.344	0.0324

2.5. Dilatometric investigations of Fe-Mn-C compacts

Dilatometric investigations of Fe-Mn-C compacts were carried out in a horizontal dilatometer Netzsch 402E. Two types of mixtures were prepared:

- iron powder NC 100.24 with addition of 3% Mn provided from Elkem low-carbon ferromanganese,
- iron powder NC 100.24 with addition of 3% Mn and 0.8%C provided from low- and high carbon ferromanganese and graphite powders.

Unaxial, single-action compacting with a stationary lower punch was used to prepare rectangular 40×5×5 mm dilatometric test bars. Compacts were heated to the isothermal temperature with heating rate 10°C/min. Sintering was carried our at 1120, 1240 and 1300°C in hydrogen atmosphere with dew point – 60°C, then cooled with a range 20°C/min. The results recorded during this investigations were described in [24].

2.6. Additional test of sintered manganese steels

2.6.1. Wear resistance test

To investigate the wear resistance of sintered manganese steels a special set proposed by Cias et al. [20] was employed. The force 15,45 N was used to load the 10×10×5 mm test specimens to the rotating rim. Time of test was 10 minutes. As a wear resistance the width of erasion, in mm, was admitted. The results of wear resistance tests are summarised in table 20.

TABLE 20
Width of erasion as a wear resistance of sintered manganese steels; sintering atmosphere 100%H_2, mean values for 10 specimens

ST, °C	3NCEL1			4NCEL1		
	DP, °C					
	-40	-50	-60	-40	-50	-60
1120	3.16	3.04	3.10	3.14	2.84	2.34
1150	3.12	3.16	3.16	2.56	2.74	3.04
1180	2.90	2.70	2.86	2.92	2.88	2.78
1200	2.96	2.26	3.16	3.08	3.22	2.82

2.6.2. The effect of tin additions on the structure and mechanical properties of PM manganese steels

Having established processing parameters for manganese containing PM steels, the effect of tin additions was studied. A first step to achieving these aims would be to reduce the alloy inhomogeneity, and minimise hardenability scatter, using wetting agents and diffusion activators such as tin admixed with the ferromanganese powder. The compositions of tin-manganese intermetallic compounds formed during heating period are possibly variable since several intermetallics exists in the tin-manganese system [21] and the homogenisation process for such a compounds could considerably enhance the diffusion rate of iron between particles [22, 23]. The experiments were not limited on maintaining of conventional sintering temperature 1120-1150°C, which is the maximum allowable temperature in industrial wire-mesh belt furnaces. Manganese steels with tin addition were also investigated at sintering temperature 1180°C to improve their homogeneity, hardenability and strength. Sintering was carried out in the same horizontal laboratory furnace, in a hydrogen atmosphere with a dew point – 60°C. Heating and cooling rates were 75°C/min and 67°C/min, respectively.

The results of investigations of Fe-Mn-Sn-C samples were widely presented during EUROMAT 2001 Conference [7].

2.6.3. The effect of sintering time on the tensile properties of PM manganese steels

To check how sintering time influences the tensile properties of PM manganese steels, 30-minutes isothermal sintering was also employed. The results of investigations are presented in table 21.

As is shown in table 21, the shorter sintering time does not any influence on UTS of manganese steels sintered at 1120°C.

TABLE 21

The effect of sintering time on the tensile strength of sintered manganese steels

Specimen	ST, °C	CR, °C/min	τ, min	
			30	60
			UTS, MPa	
3NCEL2	1120	9	493	505
	1250		563	614

2.6.4. X-ray chemical analysis of PM manganese steels

X-ray chemical analysis was carried out in the University of Bradford, UK. Randomly chosen specimens after tempering at 200°C were checked to estimate manganese and iron concentration in sintered steels. The results show that after sintering at 1120°C average content of manganese in steels is about 2.5 wt.-%, except manganese-rich regions such as not fully dissolved particles of manganese. The minimum of manganese was recorded for steels sintered in 75%N_2 – 25%H_2 atmosphere.

3. Main results

The following section will compare the effect of sintering temperature, sintering atmosphere chemical composition and the sintering atmosphere dew point on density, hardness, UTS, TRS, tensile elongation, and impact energy with the various materials (the iron and ferromanganese powders) and processing techniques. The test program examined two principles: alloying with manganese to improve hardenability of the steel and processing to attain high sintered mechanical properties.

The analysis was performed by sorting the steels into 17 processing groups (table 1). It can be noticed, as was shown in [19], that ABC 100.30 iron powder has better compactibility (ISO 3927) than NC 100.24 iron powder. It influenced density before sintering of the specimens. It appears that low-carbon ferromanganese powder additions favour higher green density. In most cases, the density involved in tensile testing did not exactly match the density of the transverse rupture specimens. When this was the case, the tensile properties reported were extrapolated from the available data to ensure that the two set of data (UTS and TRS) were as comparable as possible. The specimens made of ABC 100.30 and Elkem or HP III powder mixtures reached the green density 7.17 g/cm^3 for rectangular and 6.99 g/cm^3 for ISO specimens. The specimens made of NC 100.24 and Elkem or HP III powder mixtures had green density not exceeding 7.01 g/cm^3 for rectangular and 6.82 g/cm^3 for dogbone tensile specimens.

Tables 9-13 present the results of mechanical investigations for Fe-3%Mn-0.8%C and Fe-4%Mn-0.8%C steel specimens. In general, the UTS and TRS of the Fe-(3-4)%Mn-0.8%C PM steel slightly increase with the decreasing dew point of the sintering atmosphere, which is presented in table 9. Decreasing atmosphere sintering dew point increases also impact energy and in some cases apparent surface hardness. The data (tables 10 and 11)

indicate that the effects of manganese, sintering atmosphere dew point and cooling rate on the mechanical properties of the investigated alloys are relatively predictable.

The cooling rate has a strong effect on the UTS, TRS, impact energy and apparent surface hardness. Decreasing the cooling rate to 3.5°C/min in some cases increases mechanical properties by a factor of up to ~ 2. Slow cooling rates favoured plasticity, which ceased to be significant for cooling rates above ~ 40°C/min. When slow cooling is employed, the plasticity of the specimens increases, and tensile elongation is up to 3.8% (table 11). Elongation increased with increasing sintering temperature and density, and decreasing the sintering atmosphere dew point and cooling rate. Higher manganese concentration, as well as lower sintering temperature increase plasticity in PM manganese steels.

The effect of increasing cooling rate appears to be complex. In both cases – sintering at 1120 and 1250°C then cooling with different cooling rates, the specimens with highest tensile properties are found for the alloys cooled with cooling rates 9-30°C/min. The highest UTS and TRS values are not found in those specimens exhibiting the highest hardness values but in the moderately cooled specimens.

Specimens cooled at 65°C/min were also tempered at 200, 300 and 400°C. Significant improvement in properties was attained as a result of the 200°C stress relief, e.g. 830 MPa tensile strength with 3.7% ductility for the 1250°C sintering temperature. Results were similar for the 400°C temper and there was an indication of temper embrittlement at 300°C (fig. 19), more severe for the specimens sintered at 1250°C.

The results of tensile and bend tests show (table 13) that it is possible to achieve high properties of manganese steels during sintering in nitrogen atmosphere. For this atmosphere the highest values of UTS and TRS were recorded.

The higher sintering temperature resulted also in more rounded porosity and a slight improvement in mechanical properties. For higher manganese content this trend wasn't observed so clearly. Although tensile strength and tensile elongation were higher for lower sintering temperature, bend strength was lower, and this is to the contrary to the 4 wt. -% Mn specimens sintered at 1250°C.

The impact properties of these steels are shown in tables 9-13, and it is seen that the toughness is high particularly in view of the strength level involved. As might be expected the impact toughness in slowly (3.5°C/min) cooled condition is superior to that of the convective cooled condition. The impact strength of the −40°C dew point atmosphere sintered specimens is somewhat lower, probably because of oxides introduced during alloy preparation.

Microhardness of the various phases observed in the specimens is recorded in table 17. The structure differences are connected with the different manganese content. Higher manganese concentration move CCT curves towards longer times. Also changes in the proportion between characteristic features in 4 wt.-% Mn specimens cooled slowly – 5 and 9°C/min – and with the cooling rate ~ 40°C/min were recorded.

The microstructures of the specimens, whose main microstructural constituents are summarised in tables 14-16, sintered at the lower temperature had finer grain size, but also reflected the compositional inhomogeneity contrary to the specimens sintered at 1250°C. Therefore the characteristic features described in tables 14-16 are not a complete microstructural description.

The Fe-3%Mn-0.8%C alloy differs from the classical eutectoid iron-carbon system regarding transformation to "pearlitic" and "martensitic" structures. Pearlitic transformation is slower in this alloy, and manganese austenite is far more stable with respect to transformation to martensite. Convective cooling resulted in much higher (cross sectional) hardness. In the convective (faster) cooled condition (60°C/min) the microstructure of sinter-hardened steel consisted of a bainite/martensite matrix containing some retained austenite. Furnace cooling (3.5°C/min) from sintering temperature produced a significant decrease in hardness and increase plasticity. The lamellar pearlitic microstructure then present was usually initiated at pores present during sintering. The convectively cooled specimens showed a very heterogeneous microstructure consisting of martensite, upper and lower (coarse and fine) bainite, retained austenite and in some cases ferritic cores of the iron powder particles. This is due to the poorly distributed manganese that decreased in concentration towards the centres of the powder particles. Carbon was retained in the Mn-rich areas, and interiors of the particles were thus mainly ferritic. Faster manganese diffusion and thus better microstructural homogeneity was achieved by sintering at higher temperature and using tin addition. In Fe-3%Mn-0.8%C inhomogeneous alloys, sintered at temperature 1120°C, bainitic/martensitic rims were found around the iron particles.

For sinter-hardened and tempered bainite/tempered martensite manganese PM steels, tempering transformations inducted plasticity has been examined as a means of obtaining a better balance of strength and ductility at more economically viable cost levels. It is now recognised that a not significant amount of manganese, non-expansive alloying element, which is required plus tight process control to enable the phenomenon to be used in a cost-effective manner and makes it possible to introduce PM manganese steels into practical production. Treatments (cooling rate 10-15°C/min) which will be compatible with a continuous sintering industrial line are designed to produce bainite in Fe-3%Mn-0.8%C steel. The amounts of bainite and martensite present in steels are increased significantly with the higher cooling rate thus resulting in increasing apparent cross-section hardness values. On the other hand the microstructure of Mn steels contains a significant portion of pearlite in the slow cooled (1.5-4.5°C/min) state.

The consequent contrast in mechanical behaviour of these heat treatment products will now be considered. The stress-strain curves of these alloys in both the sinter-hardened and tempered condition were examined. The curves for sinter-hardened alloy, which transforms to bainite/martensite on convective cooling, and the sorbitic alloy tempered at 400°C represent two extremes observed. The uniform plastic elongation of the tempered alloy is much larger than that of the sinter-hardened alloy. The former is typical for annealed material whereas the latter is more typical of a hardened structure. The difference in stress-strain behaviour between these two alloys is a manifestation of the striking difference in their fracture microstructures. Sinter-hardened alloy fractured in a brittle manner with very little plastic deformation and tensile elongation approximately 0.1%. Most brittle fractures in these alloys were transgranular. However, brittle fracture in sinter-hardened alloys occurred also in an intergranular manner because the grain boundaries contained a brittle film of oxides. In tempered alloys ductile typical fracture occurred in a transgranular manner after some plastic deformation (figs. 18, 20, 21, 22b, 23) and tensile elongation was 3.03-3.91%. The fact that tempering improves the tensile properties as well

as TRS of the Fe-3%Mn-0.8%C alloy is obvious. Martensitic transformation that is inducted upon cooling wherein parent and products phases have different densities develop internal residual stresses. These stresses may be eliminated by a stress relief annealing – tempering at 200°C. The stress relief annealing temperature is relatively low that effects resulting from martensite transformation are essentially not effected.

In Fe-3%Mn-(0.1-1.0)%Sn-0.8%C alloys the manganese alloyed zones grow into the iron particles and bainitic/martensitic rims include most of the particles. Small amounts of ferrite could be seen in the microstructures of specimens only when no tin addition was used. In the case of manganese steels contained tin and graphite powders and sintered at 1150 and 1180°C, it was evident that the distribution of manganese is less inhomogeneous. The effect of sintering temperature was only moderate. It is suggested that successful industrial sintering at 1150°C may be achieved. The mechanical properties (hardness, transverse rupture strength and tensile strength) show the effect of tin addition and the optimal tin concentration is 0.15-0.25%. Dimensional changes on sintering were acceptable, generally less than 1% and densities were in the range 6.8-7.0 g/cm^3.

4. Conclusions

The results indicate that processing of the Mn alloy steels achieved its objectives. The benefits of improved hardenability are shown if comparing the properties of Fe-(3-4)%Mn-0.8%C steels with those of commercial sintered nickel steels. Their properties were explained by the processing parameters in a relatively predictable manner. Thus it should be possible to design Mn steel structural parts to meet strength requirements.

The various experimental facts relating to mechanical properties described in the present paper can be summarised as follows.

1. The optimum combination of mechanical properties appeared to be obtained with a total 3% manganese addition at 0.8% carbon level. The test data indicate that the tensile strengths of Fe-(3-4)%Mn-0.8%C compare well with those previous published for as-sintered and rapidly cooled PM Mn steels. The results showed that UTS and TRS of the 3%-0.8%C and 4%-0.8%C steels were increased significantly by using lower dew point sintering atmosphere.
2. The optimised chemical composition, alloying technique and processing of PM manganese steels result in high mechanical properties of the material, which can be improved by increasing sintering temperature and/or applying sinter-hardening. The need for a secondary quench-hardening treatment is eliminated.
3. Improved processing of low alloy steels containing manganese resulted in mechanical properties – UTS 500 MPa and elongation up to 2% for furnace cooled specimens – equal or superior to those of many conventional PM steels. The properties of the investigated PM steels, which were determined following laboratory sintering in semi-closed containers are surprisingly good and belong to the best data available on comparable materials. The characteristics of this new class of steels suggest potential application in areas where high strength and hardness are desired, for example in the manufacturing of sintered gears.

4. It is possible to produce PM manganese steels in other than a hydrogen-rich atmosphere without decreasing their mechanical properties.

Acknowledgements

The financial support of the Polish Science Research Committee under the contract no 11.11.110.491 is gratefully acknowledged.

REFERENCES

[1] R.M. G e r m a n, Powder metallurgy science, MPIF, Princeton, New Jersey, 1984.
[2] EU Cancerogenic Directives 90/394/EEC and 91/322/EEC.
[3] S.C. M i t c h e l l, A.S. W r o n s k i, A. C i a s, M. S t o y t c h e v, Proc. of PM²TEC on the „Advances in powder metallurgy and particulate materials", MPIF, Vancouver **3** (1999), 7-129.
[4] S.C. M i t c h e l l, A.S. W r o n s k i, A. C i a s, Inżynieria Materiałowa **5** (124) Rok XXII, Wrzesień – Październik 2001, 633.
[5] A.S. W r o n s k i e t a l., Tough, fatigue and wear resistance sintered gear wheels. Final Report on EU Copernicus Contract no ERB CIPA-CT94-0108, European Commission, 1998.
[6] M. S u l o w s k i, A. C i a s, Inżynieria Materiałowa **4** (105), Lipiec – Sierpień 1998, 1179.
[7] A. C i a s, M. S u l o w s k i, M. S t o y t c h e v, Proc. of 7th European Conf. on Advanced Materials and Processes – EUROMAT 2001, Rimini, Italy, June 2001.
[8] R. K e r e s t i, M. S e l e c k á, A. Š a l a k, Proc. of Int. Conf. DFPM'99. Pieštany **2**, 108, September 1999.
[9] S.C. M i t c h e l l, B.S. B e c k e r, A.S. W r o n s k i, Proc. of. 2000 Powder Metallurgy World Congress, Kyoto **2** 923.
[10] A. C i a s, M. S t o y t c h e v, A.S. W r o n s k i, Proc. of 2001 Int. Conf. on Powder Metallurgy and Particulate Materials, MPIF, New Orleans 10, 131 (2001).
[11] A. Š a l a k, Powder Metallurgy International 16, 6 (1984).
[12] A. Š a l a k, G. Leitner, W. Hermel, Powder Metallurgy International **13**, 1 (1981).
[13] A. C i a s, S.C. M i t c h e l l, A. W a t t s, A.S. W r o n s k i, Powder Metallurgy **42**, 3, 227 (1999.
[14] A. C i a s, S.C. M i t c h e l l, A.S. W r o n s k i, Proc. of 1998 PM World Congress and Exhibition, Granada, Spain, 3-PM Steels, 179, (1998).
[15] A. C i a s, M. S u l o w s k i, S.C. M i t c h e l l, A.S. W r o n s k i, Proc. of European Congress on Powder Metallurgy Euro PM 2001, Nice, **4**, 246 (2001).
[16] A. C i a s, S.C. M i t c h e l l, K. P i l c h, H. C i a s, M. S u l o w s k i, A. W r o n s k i, Powder Metallurgy 46, 165 2 (2003).
[17] A. C i a s: Development and properties of Fe-Mn-(Mo)-(Cr)-C sintered structural steels. Wyd. AGH 2004, in press.
[18] A.S. W r o n s k i, A. C i a s, Powder Metallurgy Progress **3**, 3 (2003).
[19] M. S u l o w s k i, Archives of Metallurgy and Materials 49, 1, 58 (2004).
[20] A. C i a s, J. F r y d r y c h, T. P i e c z o n k a, Metalurgia Proszków **3**, 91 (1988).
[21] B. M a s s a l s k i, Binary alloys phase diagrams, ed. ASM Int., The Met. Inf. Soc, Materials Park, Ohio **3**, 2607 (1990).
[22] W.J. H u p p m a n n, W. K a y s s e r, H.E. E x n e r, F.I. E s p e r, Proc. of the 4th Symposium on "Powder Metallurgy", May 1975, Grenoble.
[23] S.K. C h a t t e r j e e, C. A. Mackay, Powder Metallurgy **4**, 183 (1980).
[24] M. S u l o w s k i, Rudy i Metale Nieżelazne, in press.

Received: 10 Marz 2004.

A R C H I V E S O F M E T A L L U R G Y A N D M A T E R I A L S
Volume 49 2004 Issue 3

B. GARBARZ *, J. MARCISZ*

PHASE TRANSFORMATIONS IN Fe – (1÷8)% Al – 0.1% C STEELS

PRZEMIANY FAZOWE W STALACH Fe – (1÷8)% Al – 0,1% C

Structural Al-bearing steels offer some special service properties not attainable for carbon or standard low-alloyed steels. Another reason for development of Al and other non-ferrous (mainly Cu) metals bearing steels is to increase recycling of steel scrap containing those metals. In this paper results of investigation of phase transformation and microstructure of phase constituents formed in experimental steels based on Fe – (0÷8)% Al – 0.1% C – 0.5% Cu – 0.05% Sn composition have been reported.

Using results of investigation of phase transformations in the experimental steels the pseudo-binary metastable phase diagram for Fe – (0÷8)% Al system, at constant concentration of 0.1% C and impurity elements, has been determined.

Stale konstrukcyjne zawierające jako pierwiastek stopowy Al charakteryzują się specjalnymi właściwościami użytkowymi, nieosiągalnymi dla stali węglowych lub standardowych niskostopowych. Inną przyczyną rozwoju stali zawierających Al i inne pierwiastki nieżelazne (głównie Cu) jest dążenie do zwiększenia stopnia recyklingu złomu stalowego zawierającego te metale. W niniejszym artykule przedstawiono wyniki badań przemian fazowych w eksperymentalnych stalach o składach bazujących na układzie Fe – (0÷8)% Al – 0,1% C – 0,5% Cu – 0,05% Sn. Wykorzystując wyniki badań przemian fazowych zachodzących w eksperymentalnych stalach opracowano pseudo-podwójny metastabilny układ fazowy Fe – (0÷8)% Al, przy stałej zawartości 0,1% C i pierwiastków domieszkowych.

1. Introduction

Aluminium addition to unalloyed and low-alloyed structural steels is widely used as deoxidizer and as microalloying element causing grain refinement and preventing ageing as a result of its high affinity to nitrogen. In recent years a new class of structural steels containing aluminium in the range of 0.5÷10 mass % as the main alloying element has became a subject of investigation.

* INSTITUTE FOR FERROUS METALLURGY, 44-100 GLIWICE, UL. K. MIARKI 12

Structural Al-bearing steels can offer some special properties not attainable for carbon structural steels: increased corrosion resistance in some environments, high vibration dumping performance, reduced density up to 10% in comparison with steels not containing Al. Research work aimed at development of production technology of sheets and shapes made of carbon-free steel containing Al in the range of 5÷8.5 mass % as the only alloying element has been undertaken [1, 2]. The main goal of the work has been to reduce specific weight of steel products used in car construction without deterioration of properties of the products. Carbon-free Fe-8.5 mass % Al steel was shown to have properties meeting requirements of the automotive industry [1, 2].

Other classes of steel containing Al and used in automotive industry are the TRIP grades (TRansformation Induced Plasticity) containing typically 0.15% C, 1.5% (Si + Al) and 1.5% Mn. It was found that substitution up to 1.2% Al for Si produced better technological properties of the steel and improved final properties of sheets [3]. Japanese NKK company developed a steel grade containing 3.5% Al and 0.5% Si having the dumping factor 15÷25 times larger than traditional carbon steel [4]. Addition of Al to standard unalloyed or low-alloyed structural steel results in increased corrosion resistance in environment containing chlorine ions [5]. Alloying with Al could also improve high-temperature corrosion behaviour of structural steels in some environments [6].

Another reason for increasing interest in research and development of Al-bearing structural steels is an ecological aspect of production and recycling of steel products. A very important issue of recycling technology in steel industry is how to utilize steel scrap containing increasing quantity of non-ferrous metals, amongst them aluminium. Some non-ferrous metals present in steel scrap can deteriorate quality of steel products. These are so called tramp elements of which the most common are Cu and Sn.

In this paper results of investigation of phase transformations and microstructure of phase constituents formed in experimental steels based on Fe-(0÷8)% Al – 0.1% C – 0.5% Cu – 0.05% Sn composition have been reported. The main aim of the work was to provide fundamental data describing evolution of microstructure during thermal and deformation treatment of a new class of low carbon Al-bearing structural steels. Until now only few original results concerning phase transformations in Fe-Al-C system have been published [7, 8, 9].

2. Experimental procedures

Experimental steels were melted in a vacuum induction furnace and cast as 25 kg ingots. Chemical composition of the steels prepared for investigation are given in the Table. Contents of the elements are given in mass per cent if not stated otherwise. Steel 921 is a reference material containing no Al and low level of Cu and Sn impurities.

To prepare experimental material for investigation the ingots were hot forged at temperature range of 950÷1200°C into 10 mm, 15 mm and 40 mm diameter round bars followed by cooling in a still air.

TABLE

Chemical composition of experimental steels

No of steel	mass %								ppm	
	C	Mn	Si	P	S	Al	Cu	Sn	N	O
922	0.097	0.48	0.26	0.010	0.011	0.004	0.52	0.050	23	30
912	0.082	0.54	0.35	0.013	0.009	1.06	0.52	0.054	42	18
914	0.068	0.51	0.22	0.010	0.009	4.12	0.50	0.052	18	15
926	0.107	0.52	0.22	0.012	0.005	7.91	0.50	0.050	10	23

Phase transformations were investigated using a deformation dilatometer DIL 805 Bähr Thermoanalyse and a simulator of metallurgical processes Gleeble 3800. In the Gleeble 3800 simulator programmed heating – deformation – cooling multi-stage cycles were carried out.

Microstructures of transformed in the dilatometer and in the Gleeble 3800 simulator specimens were analysed using optical microscopes, a scanning electron microscope Philips XL30, a transmission electron microscope JEM 2000FX and a X-ray diffractometer Siemens D5005. For X-ray diffraction analysis bulk specimens were applied and in transmission electron microscope thin foils of the investigated specimens were used. Both the electron microscopes were equipped with EDS attachments for chemical microanalysis.

3. Results

3.1. Fe-Al-0.1% C phase diagram

A part of the pseudo-binary metastable phase diagram Fe-Al(+0.1% C + additions and impurities Mn, Cu, Sn, Si, P and S) is shown in Fig. 1. The Fe-Al-0.1% C diagram in Fig. 1 has been determined using results obtained in the present work and any applicable published data. Metastable character of the diagram means that the phases shown in particular fields of the diagram has been identified after comparatively short times of isothermal heating, comparable with the times used in an industrial thermal and thermo-mechanical treatments. Therefore positions of some lines in the diagram, notably "b-c" and "e-f", should not be considered as definite and to improve accuracy of the diagram further research work is needed.

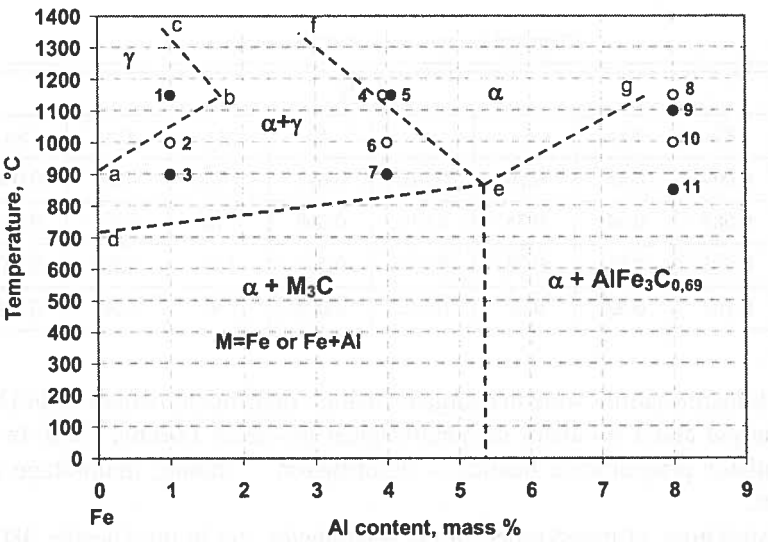

Fig. 1. A part of pseudo-binary metastable phase diagram Fe – Al (+0.1% C + impurities of Mn, Cu, Sn, Si, P, S) prepared as a result of investigation of phase transformations in experimental steels given in the Table 1. Points in the diagram indicate samples of given composition subjected to thermal or thermo-mechanical treatment

In the following sections of the paper microstructures of the experimental steels from the Fe-Al-0.1% C phase diagram are described and illustrated. Points in the diagram in Fig. 1 designated by numbers from 1 to 11 indicate samples of given composition subjected to thermal treatment and microstructural examinations. Open points represent treatments carried out in the deformation dilatometer. After the specimens reached the prescribed temperature they were heated during 5 minutes at the temperature, deformed by compression by 50%, kept at the temperature during 5 minutes and then cooled with various rates in the range $1°Cs^{-1}$ to $80°Cs^{-1}$. Closed points represent treatments carried out in the Gleeble 3800 simulator. After the specimens reached the prescribed temperature they were held at the temperature during 5 minutes and then two consecutive compressions by 50% each were applied followed after 1 minute holding at the temperature by cooling with various rates.

3.2. Experimental steel Fe – 1% Al – 0.1% C

Experimental steel Fe-1%Al-0.1%C contains deliberately introduced 0.5% Cu and 0.05% Sn and its complete chemical composition is given in Table 1 under number 912. It is seen from the phase diagram in Fig. 1 that during heating complete transformation to one-phase austenitic structure occurs in Fe-Al-0.1% C alloys containing up to about 1.8%Al. For such steel, including experimental steel 912, a standard continuous cooling transformation (CCT) diagram could be prepared. The CCT diagram prepared for steel 912 is shown in Fig. 2.

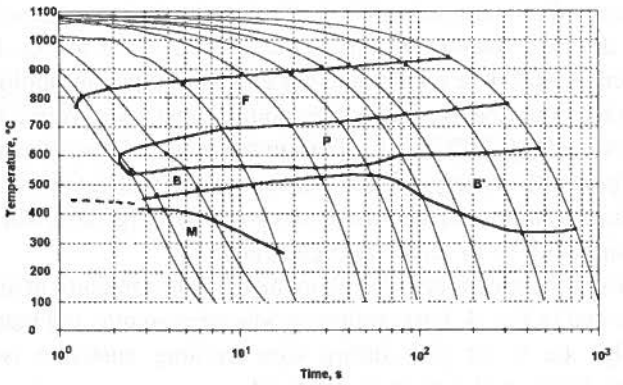

Fig. 2. CCT diagram for steel 912
Austenizing temperature: 1090°C
Austenizing time : 10 minutes
F – ferrite, P – pearlite, B, B' – bainites, M – martensite

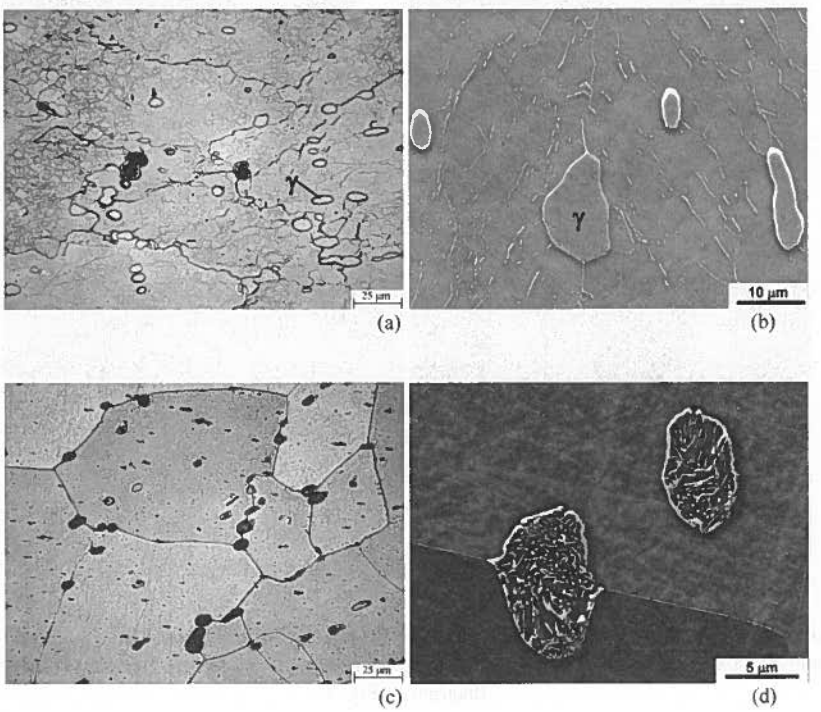

Fig. 3. Microstructures of steel Fe – 1% Al – 0.1% C (No 912) produced after fast cooling (a – optical microscopy, b – electron scanning microscopy) and after slow cooling (c – optical microscopy, d – electron scanning micriscopy) from point 2 in the diagram in Fig. 1

As a result of slow cooling from the one-phase austenite filed (point 1 in Fig. 1) ferrite-pearlite and ferrite-pearlite-bainite mixed microstructures were observed. Increase

in cooling rates resulted in increased amount of bainite and appearance of martensite, as it can be seen from the CCT diagram in Fig. 2. At points 2 and 3 in Fig. 1 two phase $\alpha+\gamma$ microstructures occur. Austenite constituent has an island-type morphology. Proportion of the austenite islands in the field designated by points 2 and 3 was found to be 4÷5 volume per cent. After fast cooling (80°Cs^{-1}) to room temperature of the specimen deformed by 50% at 1000°C (point 2) unrecrystallised ferrite matrix with untransformed and partly transformed austenite islands microstructure was produced, Fig. 3a-d. The austenite islands transformed to martensite or to ferrite and cementite.

Microstructures of the specimens treated in the Gleeble simulator at temperature 900°C (point 3) are presented in Fig. 4. Fast cooling produced austenite and martensite islands in ferrite matrix (Fig. 4a, b, c) and during slow cooling austenite islands underwent decomposition into ferrite and cementite (Fig. 4d).

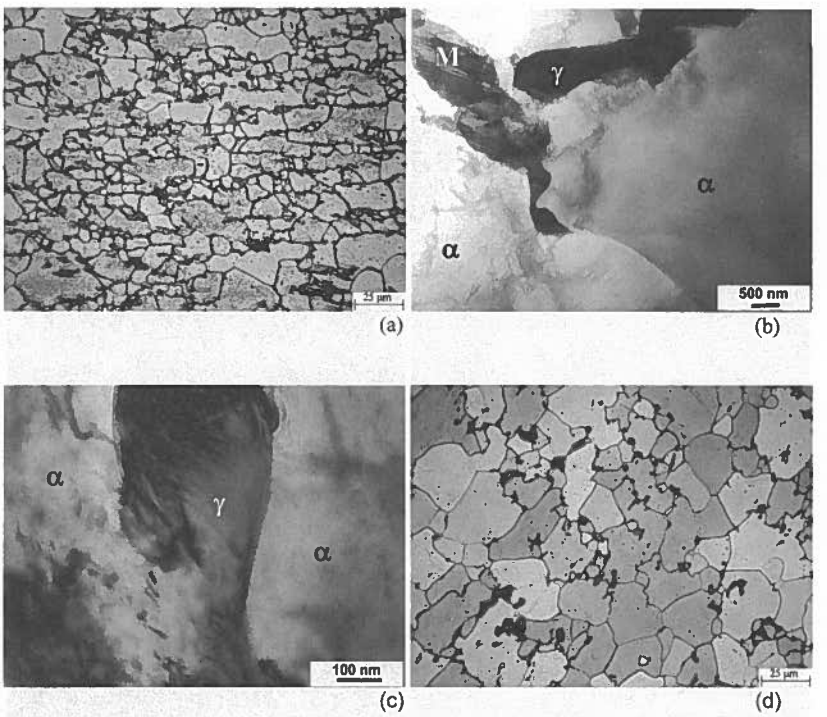

Fig. 4. Microstructures of steel Fe – 1% Al – 0.1% C (No 912) produced after fast cooling (a – optical microscopy, b nad c – transmission electron microscopy) and after slow cooling (d – optical microscopy) from point 3 in the diagram in Fig. 1

3.3. Experimental steel Fe – 4% Al – 0.1% C

Chemical composition of the experimental steel Fe-4% Al-0.1% C is given in Table 1 under number 914. Equilibrium phase composition of steel 914 in the temperature range 830÷1120°C consists of ferrite and austenite and above the "e-f" line (Fig. 1) one-phase

ferritic structure exists. After fast cooling from above the "e-f" line (points 4 and 5 in Fig. 1) a one-phase ferritic microstructure is produced. Slow cooling from the α– field above "e-f" line causes precipitation of carbides at grain boundaries of ferrite and inside the grains. Cooling after treatment in the two-phase $\alpha+\gamma$ field produces microstructure comprising ferritic matrix and islands of austenite or transformed austenite, depending on cooling rate applied. Examples of such microstructures are given in Figs. 5 and 6.

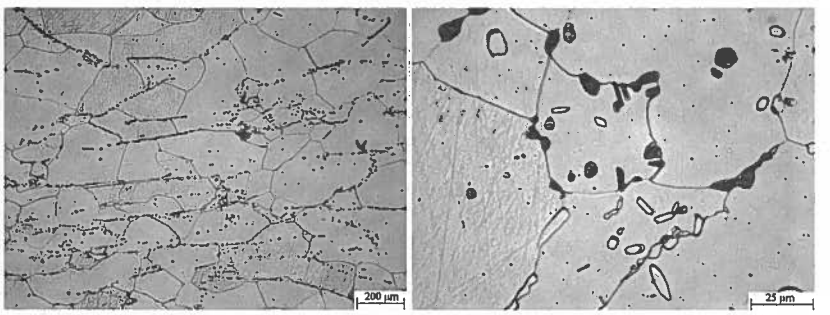

Fig. 5. Microstructures of steel Fe – 4% Al – 0.1% C (No 914) produced after slow cooling from point 6 in the diagram in Fig. 1; optical microscopy

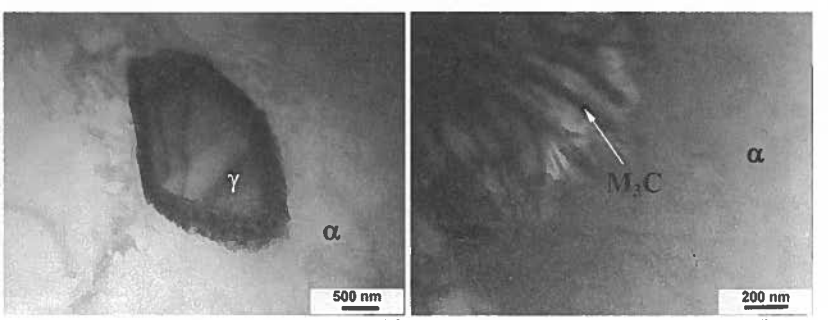

Fig. 6. Microstructures of steel Fe – 4% Al – 0.1% C (No 914) produced after slow cooling from point 7 in the diagram in Fig. 1; transmission electron microscopy, thin foils

3.4. Experimental steel Fe – 8% Al – 0.1% C

Experimental steel Fe-8% Al-0.1% C is designated by number 926 and its chemical composition is given in the Table 1. Over wide range of temperature steel 926 has a one-phase ferritic matrix (Fig. 1). Microstructures of all specimens investigated held at temperature range of 850÷1150°C (points 8÷11 in Fig. 1) and then cooled with various rates show particles of carbides. Carbides were analysed using X-ray diffraction and transmission electron microscopy and identified as $AlFe_3C_{0.69}$ carbide with crystallographic

parameters given by M o r r a l [10]. No diffraction maxima typical of Fe_3Al phase were found. Because experimental heat treatment cycles used in this study did not produced one-phase supersaturated ferritic structure of Fe-8% Al-0.1% C composition further research is needed to draw accurately the "e-g" line in the phase diagram.

Morphologies of $AlFe_3C_{0.69}$ carbide particles identified in the investigated specimens are shown in Figs. 7÷9.

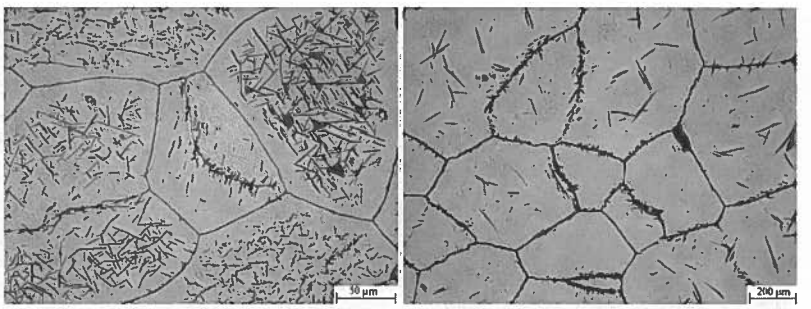

Fig. 7. Microstructures of steel Fe – 8% Al – 0.1% C (No 926) produced after fast cooling (a) and after slow cooling (b) from point 8 in the diagram in Fig. 1; optical microscopy

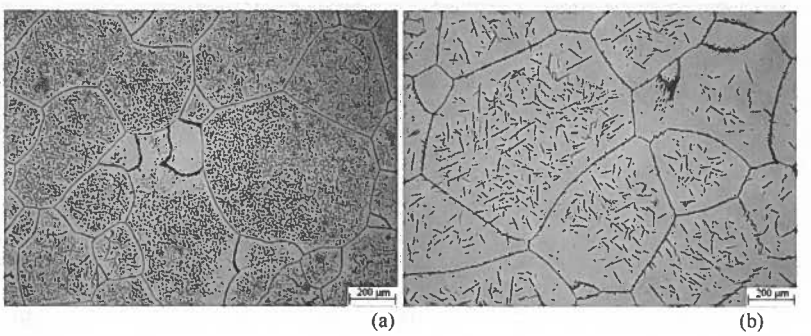

Fig. 8. Microstructures of steel Fe – 8% Al – 0.1% C (No 926) produced after fast cooling (a) and after slow cooling (b) from point 9 in the diagram in Fig. 1; optical microscopy

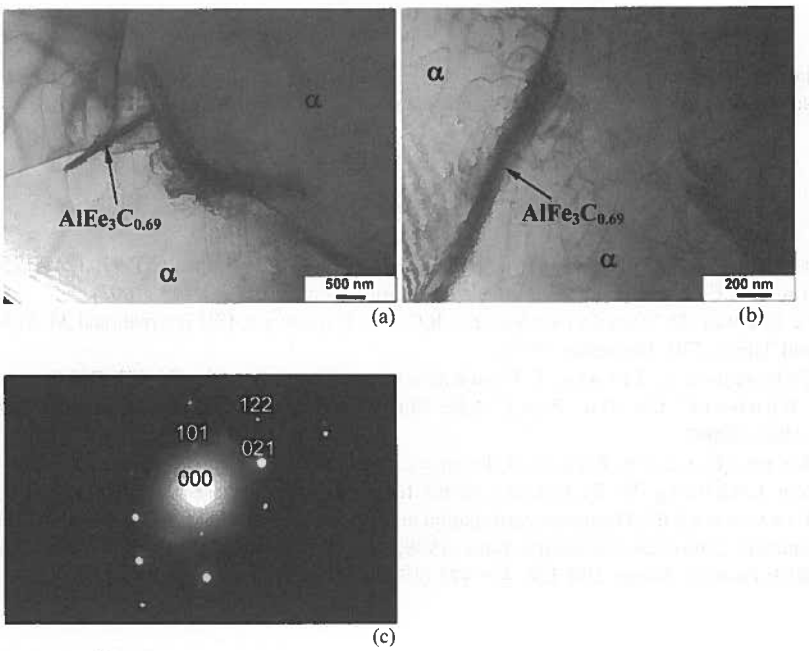

Fig. 9. Microstructures of steel Fe – 8% Al – 0.1% C (No 926) produced after fast cooling from point 9 in the diagram in Fig. 1 and an example of electron diffraction pattern obtained from the particle seen in (a); transmission electron microscopy, thin foils

3. Conclusions

Using results of investigation of phase transformations occurring during heating, deformation and holding at specific temperature and during cooling with various rates the pseudo-binary metastable phase diagram for Fe-Al(+ 0.1% C + impurity elements) system up to 8% of Al has been determined.

The established diagram is a part of a section through ternary Fe-Al-C phase diagram at constant carbon content of 0.1% and with given impurities level. Such diagram has not been found in the literature but the results obtained in this study are in agreement with published data concerning constitution of Fe-Al-C phase diagram.

Microstructures of the phases occurring in particular fields of the diagram were characterised.

Analysis of the phase transformation parameters and features of the microstructures obtained leads to the conclusion that from technological application point of view the most interesting are Fe-Al-0.1% C steels containing up to 5.5 mass % of Al subjected to thermo-mechanical treatment in the two-phase $\alpha+\gamma$ field.

Acknowledgment

Financial support of the reported above research by the Polish State Committee for Scientific Research under grant No 4 T08A 033 23 is gratefully acknowledged.

REFERENCES

[1] G. Frommeyer, E.J. Drewes, B. Engl, La Revue de Metallurgie–CIT **97**, 1245-1253 (2000).
[2] U. Brüx, G. Frommeyer, J. Jimenez, Steel Research **73**, 543-548 (2002).
[3] M. De Meyer, D. Vanderschuern, B.C. De Cooman, ISIJ International **39**, 813-822 (1999).
[4] (-) Steel Times, 570 (December 1992).
[5] T. Nishimura, A. Tahara, T. Kodama, Mater. Trans. JIM **42**, 478-483 (2001).
[6] S.W. Banovic, J.N. Du Pont, A.R. Marder, Metallurgical and Materials Trans. A **31A**, 1805-1817 (2000).
[7] A.S. Kenneford, V.E. Rance, S. Turner, Journal of the Iron and Steel Inst. **205**, 665-667 (1967).
[8] K. Von Löhberg, W. Schmidt, Archiv für das Eisenhittenwesen **11**, 607-614 (1938).
[9] L.A. Pietrowa (ed.), Diagrammy sostojanija mietalliczeskich sistem, WINITI, Moskwa, 1994, 260-267.
[10] International Centre for Diffraction Data (1998), original source – Morral F.R.: The Constitution of Iron-Rich Fe-Al-C Alloys, JISI **130**, 419-428 (1934).

Received: 10 February 2004.

A R C H I V E S O F M E T A L L U R G Y A N D M A T E R I A L S
Volume 49 2004 Issue 3

K. SOŁEK *, A. BIAŁOBRZESKI**

MODELLING OF THIXOCASTING PROCESSES OF MAGNESIUM ALLOYS

MODELOWANIE TIKSOTROPOWEGO PROCESU ODLEWANIA STOPÓW MAGNEZU

The purpose of this work is to demonstrate numeric model of magnesium alloy forming on the basis of pressure die casting technology. First section of the work discusses thixotropic casting process characteristics, process technological grounds and methods applied to obtain globular structure in magnesium alloys. Second section of the work constitutes a description of thixotropic casting process numeric model. Demonstrated method includes modelling of a whole range of phenomena, which take place during the casting process. Particular attention is focused on the construction of rheological model for material in solid-liquid state. A power-law model dependent on temperature, which describes material shear-thinning phenomenon, has been applied in order to do that. The applied model takes into account an internal variable, which describes phase proportion in the material being formed. During thixotropic forming the material goes through the phase change, progress of which strongly depends on temperature. In connection with this, the modelling of phase change thermal effect phenomenon has been introduced in the applied method. Computer program FORGE3®, in which both mechanical problem and thermal problem have been solved using finite element method, has been used for computing. As a result of performed analysis, three-dimensional simulations of die casting process have been obtained. They constitute a source of information on casting process parameters, including also that on material flow during mould filling.

Keywords: metals and alloys, phase change, thixocasting, rheology, computer simulation

Celem niniejszej pracy jest przedstwienie numerycznego modelu kształtowania stopów magnezu w oparciu o technologię odlewania ciśnieniowego. W pierwszej części pracy została opisana charakterystyka procesu odlewania tisotropowego, podstawy technologiczne procesu oraz metody uzysiwania struktury globularnej w stopach magnezu. Druga część pracy jest opisem modelu numerycznego procesu odlewania tisotropowego. Prezentowana metoda obejmuje modelowanie szeregu zjawisk jakie mają miejsce w trakcie procesu odlewania. Szczególna uwaga została zwrócona na budowę modelu reologicznwgo materiału w stanie stało-ciełym. Wyorzystano w tym celu model potęgowy, zależny od temperatury, który opisuje zjawisko rozrzdzania

* FACULTY OF METALLURGY AND MATERIALS SCIENCE, AGH UNIVERSITY OF SCIENCE AND TECHNOLOGY, 30-059 KRAKÓW, AL. MICKIEWICZA 30, POLAND
** RESEARCH INSTITUTE OF FOUNDRY, 30-418 KRAKÓW, UL. ZAKOPIAŃSKA 73, POLAND

ścinaniem materiału. Zastosowany model uwzględnia zmienna wewnętrzna, która opisuje propozyję faz w formowanym materiale. Materiał podczas formowania tisotropowego znajduje się w trakcie przemiany fazowej, której postęp bardzo mocno zależy od temperatury. W związku z tym w zastosowanej metodzie wprowadzono modelowanie zjawiska efetu cieplnego przemiany fazowej. Do obliczeń wykorzystano komputerowy program FORGE3®, w tórym zarówno problem mechaniczny, jak również termiczny został rozwiązany przy pomocy metody elementów sończonych. W wyniu przeprowadzinej analizy otrzymano trójwymiarowe symulacje procesu odlewania ciśnieniowego. Są one źródlem informacji o parametrach procesu odlewania, w tym również o przepływie materiału podczas wypełniania formy.

1. Introduction

After almost twenty years of stagnation, when casting technology of alloys in semi-solid state had been protected by patent protection, it became more popular in the nineties of the last century. The deformation of the material in partly liquid state might be executed using high pressure die casting machines and forging presses (or another machines designed for metal-forming processes), in order to produce elements made e.g. of aluminium and magnesium alloys in semi-solid technology, often called thixoforming. In the thixoforming processes material has to be in semi-solid state (in solidification range between liquidus and solidus temperature). The thixoforming processes are applied in processing of light alloys. The main advantage of light alloy application is the reduction of element weight, which consequently allows for energy saving and cost-effective production. At present thixoforming technology probably holds shares in 2% of total world production of elements made of light alloys and it is developed within the confines of both fundamental research and applications in Asia, Europe and the United States.

The forming of material in partly liquid state proceeds in the solidification range between liquidus and solidus temperature. In formed material, coexistence of liquid and solid phase, as well as the globular microstructure are assumed. The coexistence of liquid and solid phase in the magnesium alloy is caused by the aluminium impurity, which creates low-melting eutectic mixture. This situation is illustrated on Mg-Al alloy phase diagram in Fig. 1. The globular microstructure results from thixotropic change in the material. These features determine material consistency, which is characterized by low viscosity. It is the main advantage of this technology.

Better mechanical properties of products as compared to conventional casts, lower deformation forces in comparison with classical metal-forming and possibility of low plasticity alloys deformation by means of metal-forming technology constitute other advantages of this technology. Moreover, magnesium alloys are suitable for thixocasting due to not large volume of liquid phase, and thus lower alloy ignition risk.

Since the mid-nineties of the last century, development as regards modelling and optimisation of different stages of semi-solid state material forming technology has been achieved. Among other things – the ways of preparing globular microstructure in the alloys [1], the heating of the billets [2] and the die filling with material in partly liquid state. Production of the billets with different diameters has been started on commercial scale. New alloys have been designed especially for the

thixocasting process. A new magnesium alloy (MgAl5Si2) – A-G552, which is characterized by large elongation (without necessity of application of the heat treatment), has been designed for casting in semi-solid state [1].

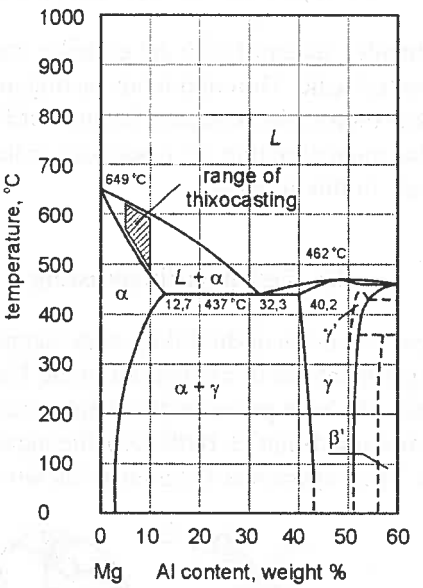

Fig. 1. Phase diagram of Mg-Al alloy

According to data contained in literature, several processes involving production of the billets with globular microstructure made of magnesium alloys exist in the world. Several variants of the globular microstructure receiving technology are developed for magnesium alloys. One of them is the P.I.D. process (Pressure Ingots Die Casting). This process consists of two stages. In the first stage, billet is received from liquid state on the pressure casting machine. Then in the second stage this billet is put into special pressing chamber of pressure casting machine. In the pressing chamber the globular microstructure is obtained using quick heating and induction stirring. Then, the billet is pushed into the die using pistons of high pressure die casting machines, where thixotropic casting is being formed. The whole process (including heating and filling the die) takes about 80 seconds [3]. Another one is the GIRCAST process, in which mechanical stirring of the alloy in vacuum or in protective atmosphere is applied. However, the process exactly connected with magnesium alloy thixocasting is THIXOMOLDING. THIXOMOLDING requires special, designed only for this process, high pressure die casting machines and suitable instrumentation. This process has been developed e.g. by Dow Chemical and Thixomat. The initial material in the form of granulated product is forced through the elongated chamber by spiral stirrer. During forcing through the alloy is heated to a temperature value within the solidus-liquidus temperature range (for magnesium alloys it is approximately 580°C). The end of the stirring chamber is at the same time the gating system. Therefore this technology is an integrated process of receiving the globular microstructure and moulding of the material.

2. Experiment

2.1 Input material preparation

Nowadays magnesium alloy material with the globular microstructure is not manufactured in Poland on commercial scale. The continuous casting machine with electromagnetic and mechanical stirring was built in the Research Institute of Foundry in Krakow (Poland), in order to obtain globular microstructure on laboratory scale. The machine was used to obtain thixotropy materials in this research.

2.2. Test part thixocasting

In this research the real processes of die filling with magnesium alloys (AM60, AZ91) were carried out. The experiments were carried out in the Research Institute of Foundry. The casting stand consisted of a high pressure die casting machine (it was a Swiss vertical cold-chamber hydraulic machine Bhler H-160B-D2), the measuring device (Data Process) and a resistance furnace. The experiment diagram is shown in Figure 2.

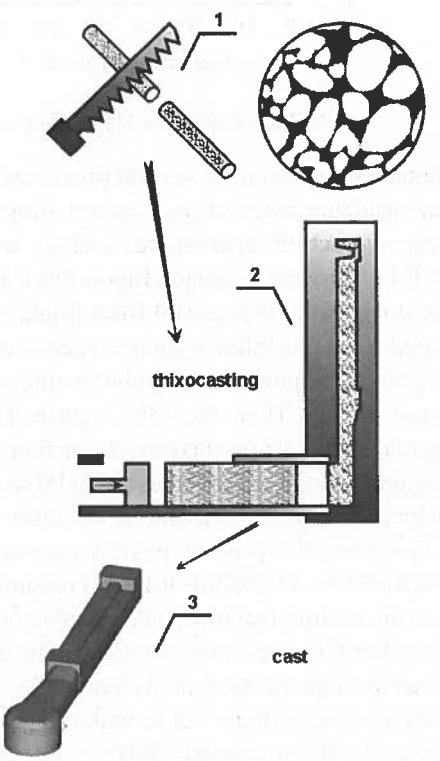

Fig. 2. The scheme of experiment, which was made in The Research Foundry Institute in Krakow. 1-cuting billet which has rheocast microstructure, 2-adapted high pressure die casting machine to thixocating, 3-cast

The die filling and hydraulic pressure control systems were modified, so that the pressure acting on the material could have been maximum. Generally, high pressure makes the thixocasting experiments possible.

Pressure value determined the cast overall dimensions and weight. However, expected experimental conditions of casting determined the gating system location and shape. The experimental cast, due to the conditions of the die filling with semi-solid state alloy, must be thick-walled (more than classical pressure casts made of liquid state). Moreover, the shape of the casts allows cutting out tensile test pieces, as well as the die filling validation. The shape has feather and rounded edges and the core, which is distant from gating system. The gating system is very massive and its shape overall dimensions are close to the cast thickness. The weight of the cast with the gating system is about 0.23 kg (the same cast made of aluminium A356 alloy weighs 0.34 kg). The shape of the experimental cast with basic dimensions is shown in Figure 3. The lowest possible piston diameter (40 mm) was applied in the gating system in order to get the largest forcing-through pressure of the material in semi-solid state.

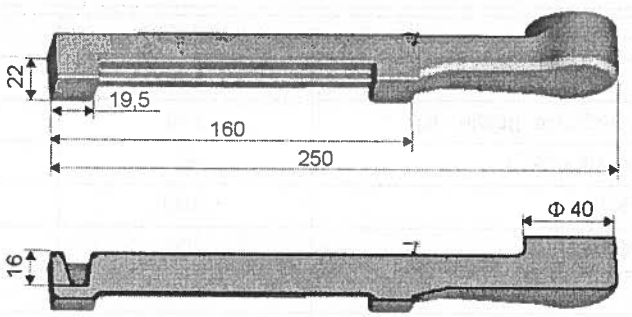

Fig. 3. Drawings of the cast. All dimension are given in mm

The range of casting process variable values for the magnesium AZ91 alloy is shown in Table 1. There are the range of the piston velocity and the initial temperature of the material and the mould, measured before the process.

TABLE 1

Range of values of technological parameters in the forming process

Factor/Level	Low level (–)	High level (+)
Pressing piston velocity in the first stage of injection [m/s]	0.5	1.0
Ingot temperature [°C]	560	580
Modul temperature [°C]	160	210

In practice, the issue of process optimisation, which depends on many variables, is being analysed. In this case the basic task is to identify the influence of individual variables on the process and then to optimise the values of these variables. In case of this research, the basic variables of the process, which can be controlled, are:

- piston velocity in the first stage of injection,
- initial temperature of the material in semi-solid state,
- initial temperature of the mould.

Acceptable range of the casting process variable values was established using a series of test casts. The ranges of these variable values for AZ91 alloy are shown in Table 1.

The aluminium billets were heated in the electrical furnace. Protective gas was composed of nitrogen (about 98% vol.) and sulphur fluoride (about 2% vol. sulphur hexafluoride) in order to prevent possible billet ignition. The gas was delivered periodically after the billets had reached the temperature of about 320°C, and it was delivered continuously after the billets had reached the temperature of about 380°C.

This work provides the analysis of real die filling with magnesium alloys AZ91 and AM60. Some physical properties of these alloys [4] are shown in Table 2.

TABLE 2

Selected physical properties of magnesium alloys AM60 and AZ91

Property	AM60	AZ91
Density [kg/dm^3]	1.80	1.81
Thermal expansion coefficient [μm/m · K]	25.6	25.2
Thermal conductivity [Wm^{-1}K^{-1}]	62	72
Specific heat [Jkg^{-1}K^{-1}]	1050	1050
Young's modulus [GPa]	45	17
Melting point [°C]	540–615	470–595
Brinell hardens number	62	75

2.3 Segregation of the cast chemical composition and mechanical properties

The chemical composition segregation proceeds during the casting mould filling. The differences between chemical composition in different parts of the cast result from the phase segregation process. The mechanics of this process is based on the flow of low-melting eutectic through porous zone of the solution α (Figure 1) under the influence of the pressure difference. The results of magnesium alloys AM60 and AZ91 chemical analysis, which was carried out in three different sections of the cast for three different pressure values during the die filling, are shown in Tables 3 and 4. The location of points of chemical analysis and cutting out of the specimens for mechanical properties analysis is shown in Figure 4. The segregation of chemical composition in direction of the die filling is clearly seen in Table 3 and 4. The magnitude of segregation results from different specific gravity of individual chemical elements. Segregation of the alloy chemical composition determines the difference of mechanical properties in particular sections of the cast. Mechanical and plastic properties of magnesium alloy AM60 in two different sections of the cast are shown in Table 5. The main alloying element described in magnesium alloys is aluminium. The aluminium content up to 6% increases cast alloy strength

and elongation. The aluminium content up to 10 % increases strength and elongation of plastically worked magnesium alloys. These properties can be observed as a result of the AM60 alloy analysis described in Tables 3 and 5. Point 3 has the highest Al content, which gives better mechanical properties ($R_{0,2}$ – apparent yield point, R_m – tensile strength) and plastic properties (A_5 – elongation) of the specimen cut out on side of this point. The values of the percent reduction of area Z equal zero because there are not differences between original D_0 and final D_u diameters of the samples. In Table 5 there are the results of the measurment; $F_{0,2}$ – the force at which the amount of the plastic deformation is 0.002 strain, F_m – the maximum load, L_0, L_u – original and final length of the samples. Chemical composition segregation is connected with the phase segregation in the material during filling of the mould. The two-phase dispersion mixture, where the grains of the solid solution α (Figure 1) are disperse phase and molten eutectic mixture is the dispersion medium, exists in the solidification range in the state of equilibrium. The microstructures of AM60 and AZ91 alloys in chemical analysis points are shown in Figures 5 and 6. The location of solid solution α (light grains) against the background of the eutectic mixture (the dark zone) are shown in the above-mentioned Figures. These microstructures are in conformity with measured chemical composition, which can be observed on the basis of Tables 3 and 4 analysis.

TABLE 3

Chemical analysis results in particular sections of thixotropic casts of alloy AM60 at mould cavity filling speed of 0.5 m/s

Section	Alloy chemical content in particular sections of cast, %							
	Al	Mn	Zn max	Si max	Cu max	Ni max	Fe max	Mg
1	5.55	0.260	0.045	0.006	0.007	0.003	0.008	94.121
2	5.35	0.027	0.041	0.007	0.011	0.003	0.006	94.555
3	5.60	0.260	0.045	0.007	0.008	0.003	0.005	94.072
Alloy initial composition	6.15	0.230	0.070	0.023	0.008	0.002	0.005	93.512

TABLE 4

Chemical analysis results in particular sections of thixotropic casts of alloy AZ91 at mould cavity filling speed of 0.5 m/s

Section	Alloy chemical content in particular sections of cast, %							
	Al	Mn	Zn max	Si max	Cu max	Ni max	Fe max	Mg
1	8.3–9.7	0.15–0.5	0.35–1.0	0.100	0.03	0.002	.005	88–91
2	8.1	0.17	0.59	0.010	0.12	0.003	0.015	90.99
3	8.4	0.17	0.68	0.026	0.13	0.003	0.004	90.65
Alloy initial composition	9.45	0.17	0.72	0.031	0.016	0.025	0.002	89.61

TABLE 5

Mechanical properties of AM60 alloy casts

Sample	D_0 mm	S_0 mm^2	L_0 mm	$F_{0,2}$ kN	$R_{0,2}$ MPa	F_m MPa	R_m MPa	L_u mm	A_5 %	D_u mm	Z %
1	15	176.6	75	13.9	78.7	31.8	180	79.5	6.0	15.0	0
2	15	176.6	75	14.8	83.8	36.8	208	82.1	9.5	15.0	0
Average					81.25		194		7.75		

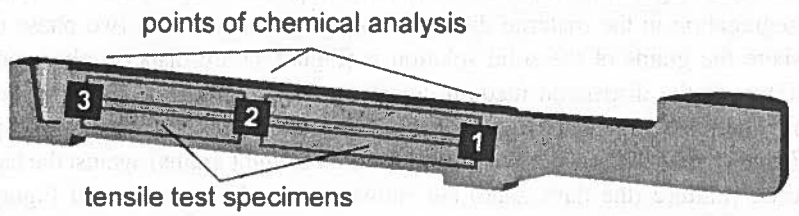

Fig. 4. Intersection of the shape of the cast. Three points, where chemical analysis were made, and places, where tensile test specimens were cut out, are shown

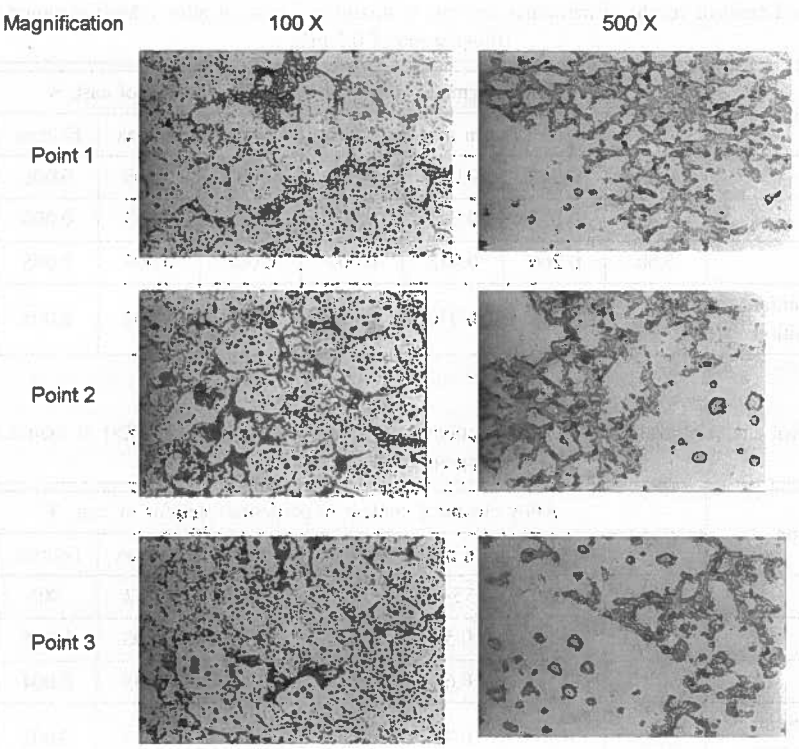

Fig. 5. Microstructure of the cast, which was made of AM60 alloy

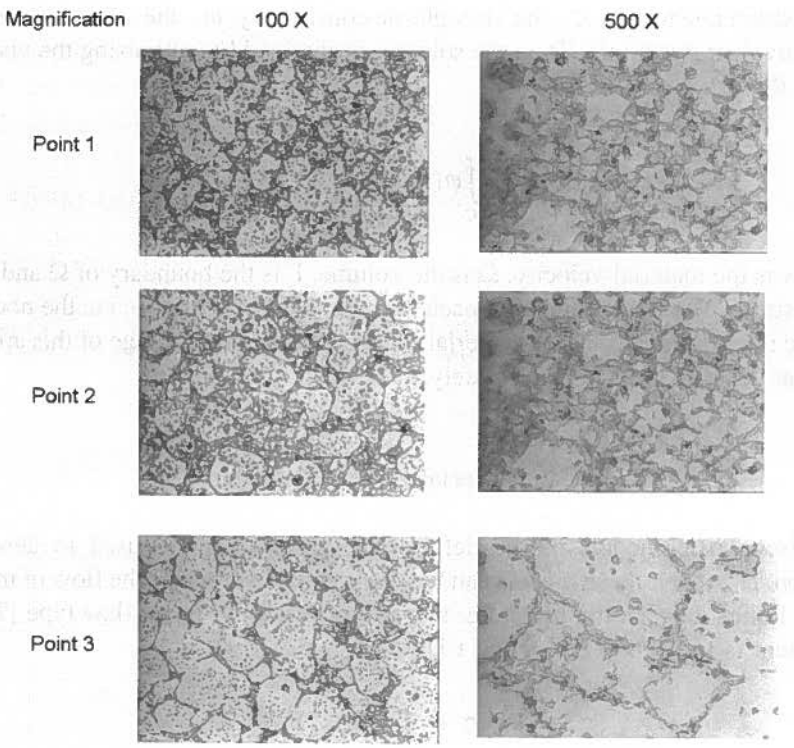

Fig. 6. Microstructure of the cast, which was made of AZ91 alloy

3. Numerical modelling

3.1 The mechanical model of semi-solid material deformation

The theoretical analysis was carried out with the help of terminology used in metal forming [5]. Experiments described in Section 2 were numerically simulated using the viscoplastic N o r t o n - H o f f l a w (1) implemented in the software FORGE®. The finite element method was used to solve the thermal and mechanical equilibrium equations at each process time step. FORGE® was initially designed for hot, warm and cold forging simulations. Namely, the viscoplastic potential of the stress field in the material is described as follows [6,7]:

$$\varphi(\dot{\varepsilon}) = \frac{K}{m+1} \cdot (\sqrt{3}\ \dot{\bar{\varepsilon}})^{m+1}, \qquad (1)$$

where: $\dot{\boldsymbol{\varepsilon}}$ – strain rate tensor, K – the viscoplastic consistency, m – the strain rate sensitivity, $\dot{\bar{\varepsilon}}$ – the equivalent strain rate. Then the solution is obtained by optimising the viscoplastic functional $\Phi(\mathrm{v})$:

$$\Phi(\mathrm{v}) = \int_{\Omega} \varphi(\dot{\boldsymbol{\varepsilon}})\,\mathrm{d}V - \int_{\Gamma} \mathbf{T}^d\,\mathrm{v}\,\mathrm{d}S, \tag{2}$$

where $\mathbf{v}$ is the material velocity, Ω is the volume, Γ is the boundary of Ω and $\mathbf{T}^d$ is the tangential stress. The Lagrangian approach is employed in FORGE®, i.e. the nodes of the mesh move in a similar manner as material points. The main advantage of this approach is the fact that the free surface is accurately tracked.

3.2. Material flow modelling

The viscoplastic models of the deformed body are usually used to describe hot deformation. However, these models can be also applied to describe the flow of material in a partially liquid state. In the literature, they are generally of power-law type [7, 8]. The most frequent is the N o r t o n - H o f f law:

$$\mathbf{s} = \boldsymbol{\sigma} + p\mathbf{I} = 2\eta_{app}\,\dot{\boldsymbol{\varepsilon}}, \tag{3}$$

where: $\mathbf{s}$ – the stress deviator, $\boldsymbol{\sigma}$ – the stress tensor, p – pressure, η_{app} – the semi-solid viscosity, and $\dot{\boldsymbol{\varepsilon}}$ is the strain rate tensor. In this work η_{app} is a function of the equivalent strain rate $\dot{\bar{\varepsilon}}$:

$$\dot{\bar{\varepsilon}} = \sqrt{\frac{2}{3}\sum_{ij} \dot{\varepsilon}_{ij}\,\dot{\varepsilon}_{ij}}. \tag{4}$$

In order to account for the shear-thinning behaviour of alloys in semi-solid state, a modified power-law relationship between η_{app} and $\dot{\bar{\varepsilon}}$ is supposed.

$$\eta_{app} = K(T)(\sqrt{3}\dot{\bar{\varepsilon}})^{m(t)-1}, \tag{5}$$

where K means the viscoplastic consistency and m means the strain rate sensitivity coefficient. As stated before, the viscosity is also strongly dependent on the volume fraction of solid f_s, and hence on the temperature of the material. To account for such dependency, the viscosity K and the strain rate sensitivity m were made f_s – dependent through the empirical relationship:

$$K = K_{liquid} \exp(Bf_s) \tag{6}$$

$$m = \frac{1 - m_{\min}}{2}\left[1 - \tanh\left(\frac{2\alpha\,(f_s - f_{s0})}{1 - m_{\min}}\right)\right] + m_{\min}, \tag{7}$$

where: m_{min} means minimum strain rate sensitivity and f_{s0} means critical fraction of solid. The strain rate sensitivity m may be taken with the following values:

- m = 0.2 for hot solid state,
- m = 1.0 for liquid state, which corresponds to the pure Newtonian behaviour,
- $m \in (0.2;1.0)$ for semi-solid state.

The exponent m value – approximately 0.2 means lack of liquid phase, and the exponent m value equal to 1.0 means no solid phase. The viscoplastic model described by the Norton-Hoff law does not include many parameters. It is the advantage of this model. The thixotropic behaviour of semi-solid material is strongly related to structural evolutions occurring during deformation, namely agglomeration and disagglomeration of solid particles. Agglomeration and disagglomeration of grains probably does not take place over the short injection time characteristics of thixocasting processes [9, 10]. Therefore, a change of the strain rate is most likely not to modify the degree of agglomeration. The lack of thixotropic behaviour was assumed in demonstrated rheological model.

3.3. The phase change thermal effect

The flow of material in semi-solid state is very sensitive to temperature. This is why temperature distribution should be determined very precisely. However, the temperature distribution in particular depends on the phase change [11,12]. The thixocasting processes proceed during solidification of the alloy with globular microstructure. Solidification is accompanied by the release of latent heat at the solid-liquid interface. When a conventional alloy or an impure metal, is cooled down from a liquid state, it begins to solidify at the liquidus temperature (T_l) and solidifies completely at the solidus temperature (T_s). There is no clear demarcation between the solid and liquid phases. The two phases are separated by two-phase mixture region, termed as the mushy zone. Pure metals and eutectic alloys undergo phase change isothermally, i.e. solidification occurs at a constant temperature, T_m, the melting (or freezing) point. The ratio of the sensible heat to the latent heat (L) is defined as the Stefan number (*Ste*):

$$Ste = \frac{C\Delta T}{L}, \tag{5}$$

where C is specific heat, and (ΔTT) is a reference temperature interval. The Stefan number is also a measure of solid-liquid interface velocity. Lower *Ste* value indicates that the interface movement will be slower due to large latent heat amount. The various methods

differ in the way that the latent heat release is handled, and may be broadly classified as *front tracking methods* and *fixed grid methods*. In front tracking methods, the solid-liquid interface is tracked continuously. The solid and liquid domains are treated as two separate domains. These methods can be used for pure metals and eutectic alloys. The fixed grid methods treat both solid and liquid regions as one continuous region and phase boundary is never explicitly determined. These methods can be used for conventional alloys or impure metals. One fixed grid method type is the *enthalpy method*. For the enthalpy method, the following equation is introduced:

$$\frac{\partial H}{\partial t} = \nabla \cdot (k \nabla T), \tag{6}$$

where: H – the enthalpy function, k – thermal conductivity, t – time. For the phase change occurring in a temperature interval between T_s to T_l the enthalpy function can be defined as follows:

$$H(T) = \int_{T_{ref}}^{T} \rho \cdot C(T)\,\mathrm{d}T + \rho(1 - f_s(T))\,L, \tag{7}$$

where: T_{ref} – reference temperature below T_s, ρ – density, f_s – solid fraction volume. The latent heat for AZ91 magnesium alloy is 373 kJ/kg [4]. The apparent specific heat, C*, can be calculated by differentiation of the temperature-dependent enthalpy H.

$$C^*(T) = \frac{\mathrm{d}H}{\mathrm{d}T} = C(T) - \frac{\mathrm{d}f_s}{d\mathrm{T}}\,L. \tag{8}$$

Moreover, the amount of solid fraction f_s as a function of temperature can be obtained from the S c h e i l equation:

$$f_S^{Scheil} = 1 - \left[\frac{T_M - T}{m_L C_0}\right]^{-\frac{1}{1-k}}, \tag{9}$$

where: T_M – pure component melting point, m_L – liquidus line slope, k – partition coefficient, C_0 alloying content. The enthalpy H and the apparent specific heat calculated for AZ91 magnesium alloy are shown in Figure 7.

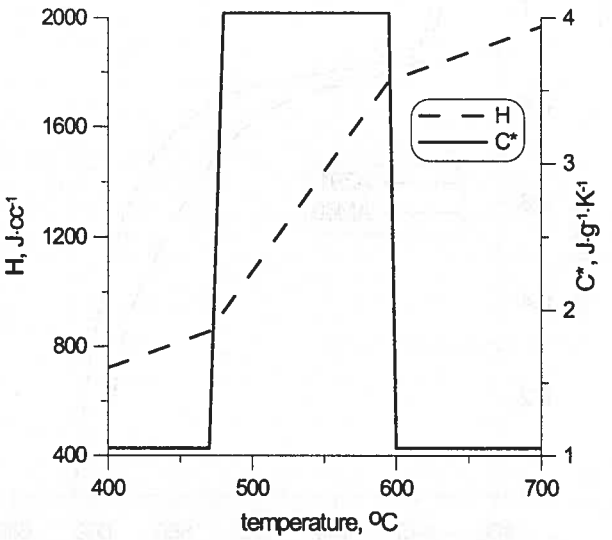

Fig. 7. The enthalpy and the apparent specific heat for AZ91 magnesium alloy

4. Results of simulations

The aim of the numerical work carried out in the Akademia Górniczo-Hutnicza in Krakow (Poland) was to learn about different aspects of die filling. The rheological models were created on the basis of data contained in literature [13]. Figure 8 shows the fraction solid versus the temperature for AZ91 and AM60 magnesium alloys [14]. These dependences were determined by means of Differential Thermal Analysis (DTA). Next rheological parameters values were assumed in simulations: $B = 24.6$, $K_{liquid} = 10^{-3}$ Pa · s, $\alpha = 2.0$, $m_{min} = 0.25$, $f_{s0} = 0.35$. The flow stress values are equal to the equivalent stress values, which is calculated as the second invariant of the stress tensor.

$$\bar{\sigma} = \left(\frac{3}{2} \sum_{ij} S_{ij} S_{ij} \right)^{1/2} . \tag{10}$$

The flow stress dependence in respect to the temperature and the strain rate for AZ91 alloy is shown in Figure 9.

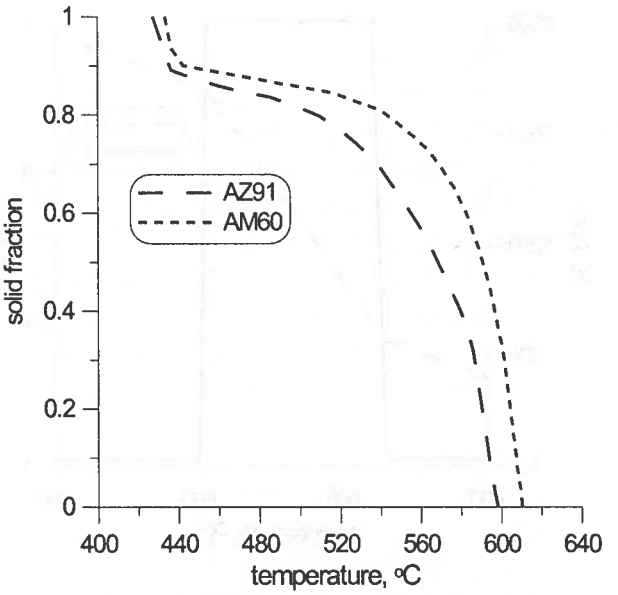

Fig. 8. The fraction solid versus the temperature for AZ91 and AM60 magnesium alloys

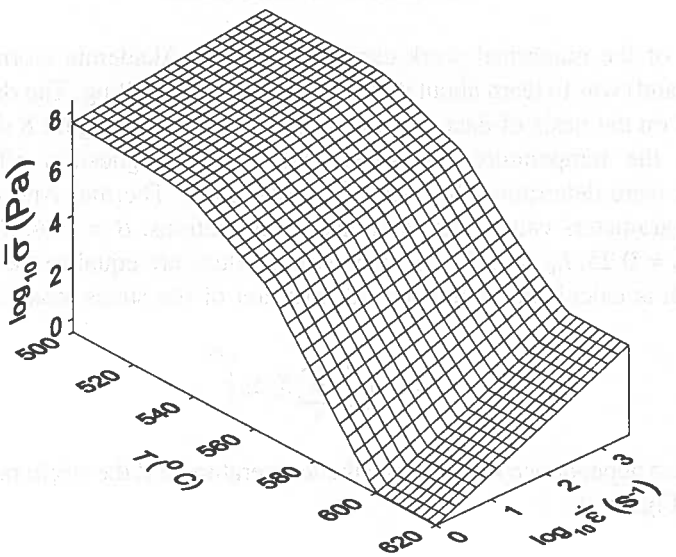

Fig. 9. The dependence of the flow stress with respect to the temperature and the strain rate for AZ91 magnesium alloy

The mesh of nodal points used in the simulations in comparison with real cast is shown in Figure 10. We see that all the cast fine details are shown very precisely.

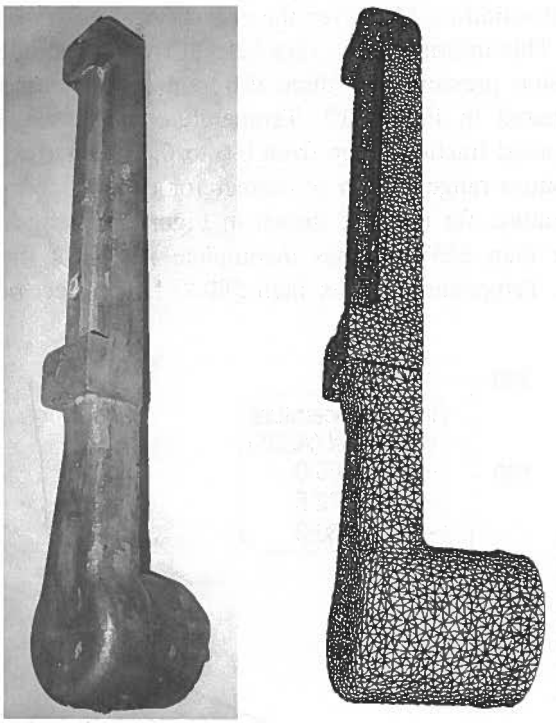

Fig. 10. Comparison of the simulated image (the mesh of the finite elements) with a photograph of the experimental cast made of AZ91 magnesium alloy

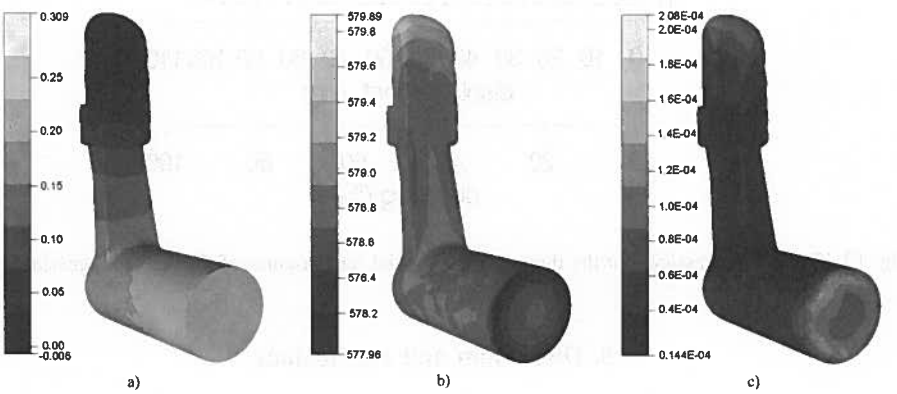

Fig. 11. Simulation of the experiment with FORGE3®: (a) pressure distribution (MPa), (b) temperature distribution (°C), (c) apparent viscosity distribution (MPa-s)

The temperature distributions, pressure and viscosity values are shown in Figure 11. While pressure distribution confirms expectations, the information about the thermal field is also quite useful. Namely, one can learn in detail how material is being cooled down and,

consequently, how it solidifies. Moreover, the viscosity value very strongly depends on the temperature value. This information is very helpful from technological point of view.

Finally, the piston pressures for three different initial temperatures of the AZ91 alloy are demonstrated in Figure 12. Temperature range between 565 and 580°C corresponds to the solid fraction range from 0.6 to 0.4. Numerical simulations allow to predict the temperature range, which is correct for a given form of the cast. Correct AZ91 alloy temperature, for the cast shown in Figure 10, ranges from 565 to 580°C. Temperature lower than 565°C causes incomplete filling of the die because of the alloy solidification. Temperature higher then 580°C is incorrect because liquid fraction is too high.

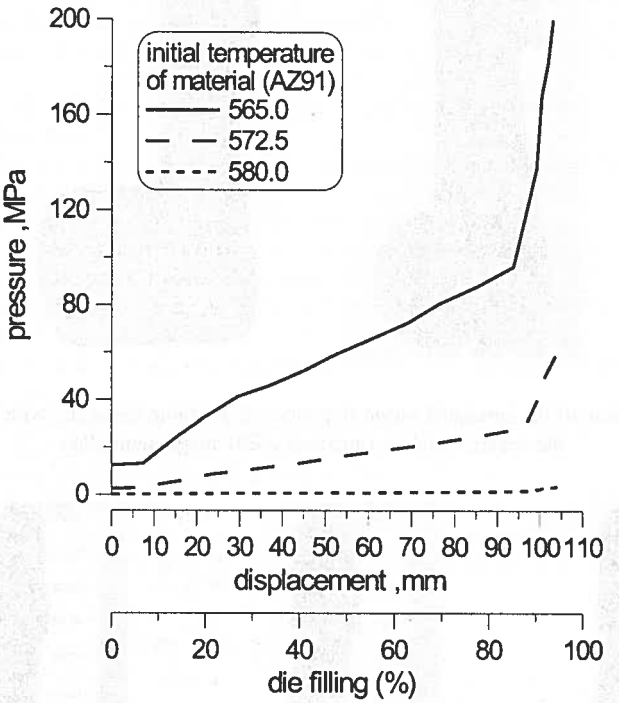

Fig. 12. The piston pressures for the three different initial temperatures of the AZ91 magnesium alloy

5. Discussion and conclusions

The N o r t o n - H o f f law allows to get correct description of behaviour of material in semi-solid state. Moreover this approach allows to calculate the value of process technological parameter, like for example piston forces. This single-phase viscoplastic model does not include many parameters. This is the advantage of this model.

The experiments allow to establish technological parameters of high pressure die casting of Mg alloy in semi-solid state. The initial material temperature and the die

temperature are of great importance. Piston velocity in the die filling first stage is less important.

This paper shows possibility to use the Lagrangian formulation in the finite element method, proving that thixocasting computations with the mesh of nodal points moving with the material are an important alternative to computations with a fixed mesh.

Recently it occurred to be possible to carry out three-dimensional simulations of industrial processes [6]. Such simulations are now available due to latest improvements in computer hardware and as a result of many years of research work carried out by scientists dealing with numerical solution of partial differential equations. However, even visual comparisons quite often allow to observe existence of discrepancies between numerical and experimental results. It seems that today researchers should focus on the development of precise mathematical models of physical phenomena, which occur in deformed material, in order to make computer simulations fully realistic. For thixocasting one may point out two sources of occurrence of discrepancies, which require further research work: the existence of special effects due to the microscopic nature of semi-solid processing, for example segregation of the phase composition, and the lack of reliable input data for simulations for arbitrarily selected material. In fact one can propose how to investigate these problems. Namely, the segregation of the phase composition can be described using formulation of fluid flow through porous media, or using the two-phase models [11,12]. Furthermore, missing data can be obtained from extra test measurements, using inverse analysis.

To summarise, the three-dimensional modelling of die filling for thixocasting, employing numerical methods used in the analysis of solid state forming processes, has been successfully demonstrated. The first successful tests to obtain these casts made of Mg alloys in partly-liquid state suggest that research involving the development of thixocasting technology should be continued.

Acknowledgements

The research was supported by the Polish State Committee for Scientific Research, project No 4 T08B 007 23.

REFERENCES

[1] M. Garat, L. Maenner, Hommes et Fonderie **288**, 37-49 (1998).
[2] M. Garat, S. Blais, L. Maenner, G. Laslaz, Hommes et Fonderie **298**, 37-49 (1999).
[3] J. Collot, Hommes et Fonderie **290**, 12-30 (1999).
[4] ASM Handbook: Properties and Selection: Nonferrous Alloys and Special-Purpose Materials **02**, The Materials Information Society (1991).
[5] R.H. Wagoner, J.L. Chenot, Fundamentals of Metal Forming, John Wiley & Sons, Inc. (1997).
[6] R.H. Wagoner, J.L. Chenot, Metal Forming Analysis, Cambridge University Press (2001).
[7] J.L. Chenot, M. Bellet, Numerical Modelling of Material Deformation Processes, Springer-Verlag, 179-224 (1992).

[8] L. Orgéas, J.-P. Gabathuler, Th. Imwinkelried, Ch. Paradies, M. Rappaz, Modelling Simul. Mater. Sci. Eng. **11**, 553-574 (2003).
[9] C.L. Martin, P. Kumar, S. Brown, Acta Metall. Mater. **42**, 3603-3614 (1994).
[10] M. Modigell, J. Koke, J. Petera, Proc. 5th Int. Conf. On SS Processing of Alloys and Composites, 317-326 (1998).
[11] J.N. Reddy, D.K. Gartling, The Finite Element Method in Heat Transfer and Fluid Dynamics, CRC Press (2001).
[12] R.W. Lewis, K. Ravindran, Int. J. Numer. Meth. Engng. **47**, 29-59 (2000).
[13] Y. Chino, M. Kobata, H. Iwasaki, M. Mabuchi, Acta Materialia **51**, 3309-3318 (2003).
[14] P.J. Uggowitzer, A. Wahlen, Proc. 6th Int. Conf. On SS Processing of Alloys and Composites, 429-435 (2000).
[15] C.G. Kang, Y.J. Chung, Proc. NUMIFORM 2001, A.A. Balkema Publishers, 1079-1085 (2001).
[16] M. Kiuchi, J. Yanagimoto, H. Yokobayashi, Cirp. Annals-Manufacturing Technology **50/1**, 157-160 (2001).

Received: 16 April 2004.

ARCHIVES OF METALLURGY AND MATERIALS
Volume 49 2004 Issue 3

M. DZIARMAGOWSKI *

INVESTIGATION ON THE CONVERTER SLAG REDUCTION

BADANIA PROCESU REDUKCJI ŻUŻLA KONWERTOROWEGO

Recently, new methods for utilization of converter slg have been sought. One possible method is the reduction of slag in an electric arc furnace. This leads to two phase: one metallic and the other non-metallic. The composition of the non-metallic phase can be adjusted to produce Portland clinker. The investigations were carried out in the 7,5t electric are furnace.

Od kilu lat poszukuje się nowych sposobów zagospdarowania żużla konwertorowego. Jedną z możliwych metod jest redukcja żużla w elektrycznym piecu łukowym. Otrzymuje się wówczas dwie fazy: metaliczną i niemetaliczną. Skład fazy niemietalicznej umożliwia wykorzystanie jej do produkcji klinkieru portlandzkiego. Badania przeprowadzono w elektrycznym piecu łukowym o pojemności 7,5 t.

1. Introduction

The increasing amount of converter slag volume requires continuous searching for the methods of its utilization. Magnetic separation of the pre-granulated converter slag is commonly used. The obtained non-metallic fraction is applied for road making, in production of building materials, to erect dams and levees and even it serves as the filling material in mining industry. The metallic fraction obtained at the same time is utilized as the charge material in metallurgical processes.

The existing converter slag utilization methods are considered as insufficiently effective and new methods are searched for. The slag reduction process in electric-arc furnace is one of these methods. Also, the research on the slag reduction in the induction furnace is being carried out. However, the number of related papers is small despite the 25-year period of research; the results obtained do not allow for wide application of the process under industrial conditions.

* FACULTY OF METLLURGY AND MATERIALS SCIENCE, UNIVERSITY OF SCIENCE AND TECHNOLOGY, 30-059 KRAKÓW, AL. MICKIEWICZA 30

2. The research on the converter slag reduction process in the world

The first attempts of converter slag reduction in the electric-arc furnace were carried out in Japan in 1979. The reduction process was run at the temperature of 1800°C and began from the intense and short-lived foaming of the slag under reduction. Based on the research made, it was found that to obtain the clinker for the production of Portland cement it is necessary to run the process for 15 minutes beginning from the moment the foaming ends. The heats carried out produced metal and non-metallic phases.

The non-metallic phase was utilized for production of Portland cement. The final adjustment of the chemical composition of the phase was made in the muffle furnace using CaO or SiO_2 additives. Metallic phase was utilized in converter processes [1].

In 1984 the news was issued about the erection of a slag processing plant with the output of 250000 Mg/year planned by the Belgian CBR group. The converter slag was planned to be processed by the reduction method in the arc furnace into clinker and materials for desulphurising mixtures, and the metallic phase. The tests were made in a 2-Mg electric arc furnace. Based on these tests, it was found that it was possible to obtain clinker from the mixture of converter slag and the carriers of aluminium oxides added to lower the temperature of the process. The investment costs were assessed at about 1 million Belgian francs. The predicted yearly production costs were estimated at 506 million Belgian francs. The costs covered first of all the costs of power (61%), costs of final products (13%) and remuneration. The 5-year amortization period was predicted [2].

Tests on the reduction of converter slag mixed with graphite reducer were also made in the induction furnace in China in 2003. The reduction was carried out at the temperature of 1650°C and 1800°C in a graphite crucible. Iron and manganese were totally reduced. The phosphorus content was reduced by 95.5%, 62.7% of which was reduced to the metallic phase, and the remaining part were evaporation losses. It was also observed that free CaO reacted with carbon at the temperature of 1800°C producing carbide CaC2 [3].

It is a disadvantage of the abovementioned methods of slag reduction that the reduction process is aimed mainly at the Portland clinker production. With fluctuating slag chemical composition, it is not possible to get the required chemical and mineralogical composition and properties of clinker. This is the reason why adjustments to the chemical composition of the obtained non-metallic phase by adding lime and silica after the melt are necessary.

3. The author's own research

The attempts made earlier were the premise for carrying out tests on converter slag reduction under laboratory conditions. The aim of the tests was to determine the range of chemical composition corrections to the non-metallic phase designed for Portland clinker, and also to determine the conditions of the reduction process when utilizing non-metallic phase as the Ca-Mg fertiliser [4-7].

The tests showed that the converter slag reduction process begins from the moment the slag is being added. The process generates intense slag foaming resulting from the

occurrence of the CO gas bubbles in the forming liquid. The most important factors that stabilise the foam include the viscosity of the liquid slag, the presence of the dispersed particles of the reducer and the forming metal phase and the formation of adsorption layers at the separation boundary of slag–metal drop or slag–CO gas bubble [8]. When slag adding is stopped, a spontaneous disintegration of the foam follows as the result of the coalescence of gas bubbles and metal drops falling down.

A slag amount to be reduced should be previously mixed with the reducer. The mixed material may be fed into the furnace as a single charge or be added continuously. The foaming of the slag increases its volume very quickly. For this reason, when adding a single charge under laboratory conditions, a crucible of sufficient height should be used. Likewise, under industrial conditions, the boiler of the furnace should have sufficient height. If the material is added continuously, the process can be run without increasing the height of the appliance used. Because the tests were made under laboratory conditions, and the verification of the obtained results was planned to be made under industrial conditions, it was decide to apply continuous adding of converter slag mixed with the reducer. This allowed to avoid the costs of building an industrial arc furnace.

The slag reduction tests were carried out in a 1-kg crucible. To assess the suitability of the non-metallic phase for application as a Ca-Mg fertiliser, greater amounts of the material were necessary for testing. For this reason the volume of the crucible was increased to 5 kg. Verification of the results obtained were made based on the melt made under industrial conditions in an electric-arc furnace.

Based on the tests made under laboratory conditions, it was found that the slag reduction level should depend on the application of the non-metallic phase. If the phase is planned to be utilized as Portland clinker, the reduction level should be such that the phase does not disintegrate autogenously because of the transition of the $\beta CaO.SiO_2$ form into the γ form and the hydraulic bonding properties are lost. If the non-metallic phase is to be used as a Ca-Mg fertiliser, the reduction level should be increased accordingly. The produced phase should not disintegrate autogenously and contain heavy metals.

A stabilised non-metallic phase can be obtained with reducer fraction of 4%. The slag reduction level will the be lower than 21% and the P_2O_5 content will exceed 0.3% mol, which will stabilize calcium silicate and makes the non-metallic phase autogenous disintegration impossible. The phase such produced can be used as Portland clinker after CaO additive is added to change the mineralogical composition such as to increase the fraction of alite $3CaO.SiO_2$ and decrease the fraction of belite $2CaO.SiO_2$. The adequate mineralogical composition can be used by reducing the mixture of converter slag, reducer and the pure CaO additive in quantity of 1–2% of the slag mass.

The non-metallic phase that disintegrates autogenously can be obtained when the reducer fraction in the charge is increased to 5% and the total reduction level exceeds 22%.

The fraction of non-metallic phase smaller than 0.5 mm in size is suitable for soil liming. The phase of larger sizes should not be used because of excessive amounts of iron oxides. It may be used as an addition to the sinter in the blast-furnace process. About 70% of fraction not exceeding 0.5 mm in size was obtained during the tests.

After laboratory investigations were finished, a test was made on converter slag reduction in a 7.5 Mg electric arc furnace. The furnace refractory lining was basic and was made of magnesite profiles and of working layer of burnt dolomite. For reduction, an amount of 500 kg of slag divided into 5 portions 100 kg each was designed. Each portion was mixed with 6 kg of milled carburite. More slag amount could not be reduced because of the basic character of the lining, and replacing the lining for the carbon one for a single tests was not possible due to the costs. Before the slag was added, 4 Mg of scrap was melted in the furnace as the slag mass was too small compared with the furnace volume.

The slag formed during melting the charge was removed from the furnace. The metal bath was deoxidised with ferrosilicon. Then a metal sample was taken, three slag portions mixed with carburite were fed and the current was turned on. After 15 minutes elapsed, the fourth, slag portion was added, and after next 10 minutes, the fifth portion. The process was stopped after 10 minutes from adding the last portion despite the fact that the foaming of the slag did not end. This resulted from the fear of the total local destruction of the refractory lining. After the process was stopped, a metal sample was taken and the slag was drained into the prepared box that was then left aside for cooling off. About 600 kWh of electric energy was used for the slag reduction.

The non-metallic phase obtained in the process was kept for 2 days in the box. The total mass of the phase was ca. 2 Mg. About 46 kg of the non-metallic phase disintegrated autogenously. The remaining part did not disintegrate and was in a lumped form. The chemical composition of the non-metallic phase and the changes of the metal bath chemical composition are presented in Table.

The autogenous disintegration of about 10% of the non-metallic phase occurred due to the transition of the allotropic form $\beta 2CaO.SiO_2$ in the form $\gamma 2CaO.SiO_2$. The transformation of β into γ taking place at the temperature of 675°C is a slow transformation of the structure. A significant ion shifting occurs then together with the disintegration of the lattice and decomposition of the phase accompanied by about 12% volume increase. The formation of the γ form can be counteracted by building foreign atoms into the silicate lattice. The amount of the foreign oxides necessary for stabilization of the β phase depends on the size of silicate crystals. The following compounds are listed most frequently as stabilizers: As_2O_3, P_2O_5, Al_2O_3, B_2O_3, Cr_2O_3, Mn_2O_3, BaO, FeO, MgO, MnO, SrO, alkalis, fluorides, sulfates and sulfides. Fast cooling off the non-metallic phase to fix the $\beta 2CaO.SiO2$ form is also one of the efficient methods.

The non-metallic phase not undergoing the autogenous disintegration was obtained under laboratory conditions at the total reduction level did not exceed 22% and the P_2O_5 content exceeding 0.3% mol. Under industrial conditions, a higher content of FeO and Cr_2O_3 and, at the same time, a lower content of P_2O_5 were obtained in non-metallic phase. The higher content of FeO and Cr_2O_3 resulted from the too early stop of the reduction process, while the lower content of P_2O_5 resulted from its lower content in the slag. This points at the more strongly stabilizing influence of P_2O_5 than FeO and Cr_2O_3. Under such conditions, a stabilized non-metallic phase can be obtained by its fast cooling by compressed air or water.

TABLE

Comparison of chemical composition of the obtained non-metallic phase with the chemical composition of the clinker obtained in the CBR group

No.	Component	Chemical composition, %			
		Converter slag	Phase not undergoing the autogenous disintegration	Phase undergoing the autogenous disintegation	Clinker from CBR plants
1	C	–	0.17	0.15	–
2	CaO	41.53	52.51	52.82	53.20
3	SiO_2	14.62	21.34	21.63	21.40
4	MgO	5.13	6.85	8.69	4.90
5	FeO	22.39	6.22	8.09	4.11
6	Fe_2O_3	6.43	4.48	1.96	–
7	MnO	6.70	4.84	4.03	2.20
8	Cr_2O_3	0.87	0.48	0.19	–
9	Al_2O_3	1.04	1.67	1.04	11.10
10	P_2O_5	0.82	0.53	0.45	0.70
11	S	0.08	0.16	0.10	–

The chemical composition of the non-metallic phase not undergoing the autogenous disintegration was similar to the chemical composition of the clinker manufactured by this method according to the Belgian license [2]. The same content of CaO and SiO_2 was obtained as well as the MgO content increased by about 2% which resulted from high wear of the refractory lining. The content of iron and manganese oxides doubled because of too early stopping of the reduction process. At the same time the content of Al_2O_3 was smaller by ca. 10%, which favorably influences the clinker properties. The contents of P_2O_5 and sulphur were similar to those in Belgian clinker.

4. Conclusions

The reduction process in an electric-arc furnace may be applied to both liquid and solid converter slag. The liquid slag may be that coming from the current production, the solid one can be that from slag dumps. Because in the initial phase of the reduction the intense foaming of slag occurs and its volume increases, the process should be run in a furnace with its walls heightened or the material should be added divided into small portions. Also, continuous adding of the material should be taken into consideration. The metallic and non-metallic phases are the outcomes of the process of which the non-metallic phase can be utilized as Portland clinker or Ca-Mg fertiliser.

A test made under industrial conditions in a 7.5 Mg electric-arc furnace showed that the converter slag reduction can be run without heightening the furnace. However, because of the quick wear of the basic lining of the furnace, it is necessary to replace it for the carbon lining. The intense foaming during reduction requires that the charge material be divided into several portions charged subsequently at a-few-minute time intervals. If the non-metallic phase is designed for Portland clinker, compressed air or water for cooling should be applied during tapping. Fast cooling prevents the obtained non-metallic phase from autogenous disintegration, especially at low content of P_2O_5 in the converter slag and the lack of other stabilizers.

The reduction process with slag added in small portions has been described in several authors publications [4-7]. The processes of slag reduction in the furnace with heightened walls and that with continuously added slag still require explanations. During such investigations the optimum current conditions should be determined, reducer type and its form should be selected, as well as the conditions of modification of the non-metallic phase chemical composition should be given. The continuation of investigations under laboratory conditions is necessary for designing the converter slag reduction industrial installation and technology.

REFERENCES

[1] S. Kubodera, T. Koyama, R. Ando, R. Kondo, Transactions of the Iron and Steel Institute of Japan **19**, 7, 419-427. (1979).
[2] J. Piret, A. Dralants, Stahl und Eisen **104**, 16, 774-778. (1984).
[3] G.A. Li, F. Zhang, L. Zhang, Z.T. Sui, Journal of Materials and Metallurgy **2**, 3, 167-172. (2003).
[4] M. Dziarmagowski, M. Karbowniczek, M. Pyzalski, J. Okoń, Ironmaking and Steelmaking, **19**, 1, 45-49. (1992).
[5] M. Dziarmagowski, Archives of Metallurgy **47**, 3, 287-295 (2002).
[6] M. Dziarmagowski, Archives of Metallurgy **48**, 2, 201-207 (2003).
[7] M. Dziarmagowski, Archives of Metallurgy **49**, 1, 73-81 (2004).
[8] M. Karbowniczek, Pienienie żużla w procesach stalowniczych, Rozprawy Monografie, Kraków 1998.

KBN, grant nr. 4T08B02825

Received: 7 Marz 2004.

A R C H I V E S O F M E T A L L U R G Y A N D M A T E R I A L S
Volume 49 2004 Issue 3

K. PIEŁA *

HIGH-TEMPERATURE INHOMOGENEOUS PLASTIC FLOW OF ZINC SINGLE CRYSTALS WITH SOFT ORIENTATION

WYSOKOTEMPERATUROWE NIEHOMOGENEICZNE PLASTYCZNE PŁYNIĘCIE KRYSZTAŁÓW CYNKU O MIĘKKIEJ ORIENTACJI

The work presents results of investigation of the influence of experimental conditions (temperature and strain rate) on the high-temperature mechanisms of plastic deformation of zinc single crystals with soft orientation. The performed experiments allow to state, that crystals show the tendency toward macroscopic localization of plastic flow: in basal slip systems, in mechanical twins and in kink bands. It has been proved the existence and the reasons for temperature anomaly of the strain-hardening and temperature anomaly of the plasticity of the tested crystals as well as close relation between the parabolic stage C and twinning. It has been also confirmed that persistent necking, leading to cracking during the tensile test, is preceded by one of two forms of strain localization: twinning or kink band formation.

W pracy przedstawiono wyniki badań nad wpływem warunków odkształcenia (temperatury i prędkości) na mechanizmy wysokotemperaturowego odkształcenia plastycznego kryształów cynku o miękkiej orientacji. Stwierdzono, że badane kryształy wykazują skłonność do makroskopowej lokalizacji odkształcenia w systemie podstawy, bliźniakach i pasmach ugięcia. Udokumentowano istnienie i wskazano przyczyny temperaturowej anomalii umocnienia i temperaturowej anomalii plastyczności jak również związek parabolicznego stadium C z bliźniakowaniem. Potwierdzono także pogląd, iż formowanie uporczywej szyjki, prowadzące do rozerwania kryształu cynku w próbie rozciągania, jest zawsze poprzedzone jedną z dwu form lokalizacji odkształcenia, tzn. bliźniakowaniem lub formowaniem pasm ugięcia.

1. Introduction

It has been known since a long time, that the course of the tension curves of zinc and cadmium (as well as magnesium) single crystals with soft orientation depend essentially on

* DEPARTMENT OF STRUCTURE AND MECHANICS OF SOLIDS, UNIVERSITY OF SCIENCE AND TECHNOLOGY-AGH, 30-059 KRAKÓW, AL. MICKIEWICZA 30, POLAND

the temperature test. Three-stage curve of the $\tau - \gamma$ is registered only in a narrow range of temperature 0.40 – 0.55 T_m (T_m – melting temperature) and with increasing temperature of the test to about 0.7 T_m it is replaced by a two-range curve. This change is accompanied by rapid decrease of work-hardening rate to values close to zero – at two first stages (*A* and *B*) – and the increase of the length of the stage of easy glide *A*, as well as, successive gradual reducing of the stage B and final decay of the parabolic stage *C* [1–7].

In the above mentioned studies, concentrated on the problems of thermal activation of the deformation processes, the mechanical characteristics of crystals were interpreted on the base of dislocation mechanisms. In the opinion of the authors of these studies, the strain-hardening rate at the stage *A* results from the interaction of the slip dislocations of the basal system $(0\,0\,0\,1)\langle 1\,1\,\bar{2}\,0\rangle$ with the coplanar dislocations (from other basal systems) and with the forest dislocations (sessile and pyramidal systems), as well as with subboundaries – both those present in the virgin crystal (mosaic) as well as those "building" in the course of deformation derived from the so-called "polygonal slip" [8–24]. Since the interactions of the coplanar basal dislocations are very weak [25], a decisive contribution to work hardening originates from the interaction of the basal dislocations with the forest ones – in particular, from the agglomerates of slip dislocations, formed around the forest dislocations [10]. At the stage A the dislocations motion and their propagation are in principle limited to the basal system and the density of the forest dislocations remains stable.

At a far advanced stage of easy slip the stress concentration at the front of the agglomeration causes either the "breaking through" of the forest dislocations or initiates a shear in the 2-nd order pyramidal systems $\{1\,1\,\bar{2}\,2\}\langle\bar{1}\,\bar{1}\,2\,3\rangle$ [10]. The appearing "new" pyramidal dislocations induce local relaxation of stress in the basal systems, but simultaneously they lead to the increase of the density of forest dislocations. Beginning of stage *B* corresponds to the penetration of the whole cross-section of the crystal by the lines of the pyramidal slip. Distribution of dislocations in the crystals is then highly inhomogeneous [9], and gradual "filling" of the crystals by the forest dislocations causes the increase of the work-hardening coefficient [e.g. 26]. The structure of the crystals undergoing tension becomes unstable and there take place the nucleation of twins [9, 27–29]; with other modes of load, deformation is localized in thick basal slip bands and is manifested as the effect of "jerky" flow or with distinctly marked "yield point" [16, 19, 22, 30]. Thus, it can be said that the work-hardening rate and the mode of plastic behavior of crystals at stage *B* are determined by the density of the forest dislocations.

The parabolic stage *C* of the stress – strain curve, since the publication of the studies by Seeger et al. [e.g. 31], was usually connected (by analogy to RSC metals) with intensification of the cross slip and such interpretation was also proposed by majority of the above cited studies [1–7]. However, neglecting the discussions and the critical remarks found in several papers concerning RSC metals (a detailed discussion can be found in the study [32]), attention should be given to the significant fact, that– in the case of zinc and cadmium – it has never been precisely stated which of the two types of dislocations: <a> or <a+c>, operating at the stage *B* would determine such behavior, and that there has never been presented a convicting experimental evidence for the activity of such mechanism of deformation.

With an increase of the deformation temperature to above 0.4 T_m, at least a part of the slip dislocations becomes annihilated, overcoming of the forest dislocations is strongly supported by thermal activation, the newly formed network of slip dislocations becomes thermally unstable (or never formed at all), and part of the dislocations forms low-energy arrangements of polygonal walls. These phenomena, defined commonly as "dynamic" recovery, refer, however, mainly to the basal dislocations. Such a conclusion is suggested by the results of the investigations of the thermal stability of the dislocation structure of zinc crystals, subjected to strain and, subsequently, to static annealing [15]. In this study it has been demonstrated that while, according to the predictions, the density of the basal dislocations is quickly decreasing with increasing temperature and annealing time, the stability of the forest dislocation is also greatly affected by the preceding basal slip. This slip leads to "sweeping-up" of the pyramidal dislocations as a result of reorganization of the pyramidal forest dislocations, consisting, successively, in their transformation into slip dislocations and subsequent annihilation. Great stability both as regards the influence of the temperature and the plastic strain, is demonstrated by the small density of forest dislocations.

The results of this experiment may suggest that high-temperature mechanical characteristics of zinc crystals is determined by processes reducing the density of the basal dislocations. These may account for the signaled decrease of the work-hardening rate at the stages *A* and *B*, and these processes should become more intense with the test temperature rise. However, it is difficult to explain why in such conditions, facilitating the cross-slip of the screw segments of dislocations, the parabolic stage *C* vanishes.

On the other hand, there exists a number of dispersed information, which bring to a different approach to the process of high-temperature deformation of zinc and cadmium crystals. Already the early experiments, presented in the work by Schmid and Boas [33], have shown that the maximal plasticity of zinc crystals is observed at the temperature 523 K, and its drop at the temperature 573 K was connected with the "decomposition of the crystal into grains". The suggestion about the existence of an anomaly of plasticity in these crystals seems to be confirmed by Kajbyshev at all. [34], demonstrating simultaneously that the decrease of plasticity is accompanied by the increase of the "mean" work-hardening coefficient and structurally connected with the appearance of "spatially misoriented areas". The dimensions of these areas were estimated at about 1 mm and the dislocations tangles, observed under these conditions were interpreted as a result of the activity of nonbasal systems.

What is more, it is known that plastic flow of zinc single crystals at elevated temperatures is inhomogeneous. Investigations of the initial (up to about 40%) stage of zinc crystals with soft orientation, carried by Regel and Govorkov [35] have shown that the slip in the matrix occurs in a homogeneous way only at ambient temperature whereas at higher temperatures there can be distinguished two forms of inhomogeneous flow: in a single, strongly localized neck (at 473 K) or multinecking (at 573 K). In each case the oscillation of loading was observed. Similar effects have been observed later in pure and alloyed zinc crystals [36, 37]. Results of tension tests of zinc single crystals with various orientations, carried out in the temperature range 293–573 K, tend to suggest that the temperature anomaly of the work-hardening at stage A can be the result of a changes in the

form of strain localization, and the transition from a rectilinear stage *B* to a parabolic stage *C* should be associated with intensification of the processes of mechanical twinning [28].

Homogeneous twinning shear is accompanied by transformation of dislocation substructure. Y o o and W e i [38, 39] proved that twinning in the system $\{1\ \bar{1}\ 0\ 2\}$ transforms most of the matrix dislocations into a high-energy dislocations in twin. As a consequence, the twinned volume is much more harder than surrounding matrix; this was clearly demonstrated already by S c h m i d and W a s s e r m a n n [40] and B e l l and C a h n [27] as a 2-3-fold increase of critical resolved shear stress for basal slip.

However, the stability of such dislocation structure is restricted only to a relatively low homologous temperatures and – at elevated temperatures – the twinned volumes are preferred sites for the processes of structural regeneration. Two observations confirm this supposition, i.e. the considerable "acceleration" of static recrystallization within the twin as well as the high plastic strain in twinned volumes [33]. Moreover, it is well known that the processes of static recovery and of static recrystallization are faster in the case when the metallic specimen undergoes the stress [41]. In the opinion of D y b i e c and K o r b e l [42], similar effect takes place during the continuous mechanical test, when the area of localized strain is "temporarily" inactive. It seems than that the experimental conditions can influence the behavior of twinned volumes of zinc single crystals (possibility of slip on 'alien' dislocation distribution, "dynamic" recovery and "dynamic" recrystallization) and thereby the disappearance of parabolic hardening stadium *C* at elevated temperatures.

The present work:

- shows that the high-temperature mechanical characteristics of zinc single crystals of soft orientation are determined mainly by the tendency toward the macroscopic localization of plastic flow: in basal slip system, in twins and in kink bands;
- proves the existence and reasons for the temperature anomaly of work-hardening and the temperature anomaly of plasticity;
- indicates the close relation between twinning and the occurrence of the parabolic stage of work-hardening curves and
- confirms the opinion that the macroscopic strain localization precedes formation of a persistent neck.

2. Experimental

The experiment was carried out on zinc single crystals of 99.995% purity, obtained by Bridgman method (of vertical gradient of temperature) and the initial orientation $\chi_o = 52°$, $\lambda_o = 38°$ (where: χ_o, λ_o – angle between the crystal axis and the normal to the plane (0 0 0 1) and the direction <1 1 $\bar{2}$ 0>, respectively). The crystals were subjected to a tension test in a wide range of temperature (373–673 K) and deformation rate ($8 \times 10^{-4} - 8 \times 10^{-2}$ s^{-1}). Recorded mechanical characteristics are presented in Fig.1 in a form of dependence: tensile force-elongation, while the plasticity indices of the crystals are shown in Figs. 2 and 3. Deformed crystals were subjected to macro- and microscopic (deformation traces) observations and their results are shown in Figs. 4 and 5.

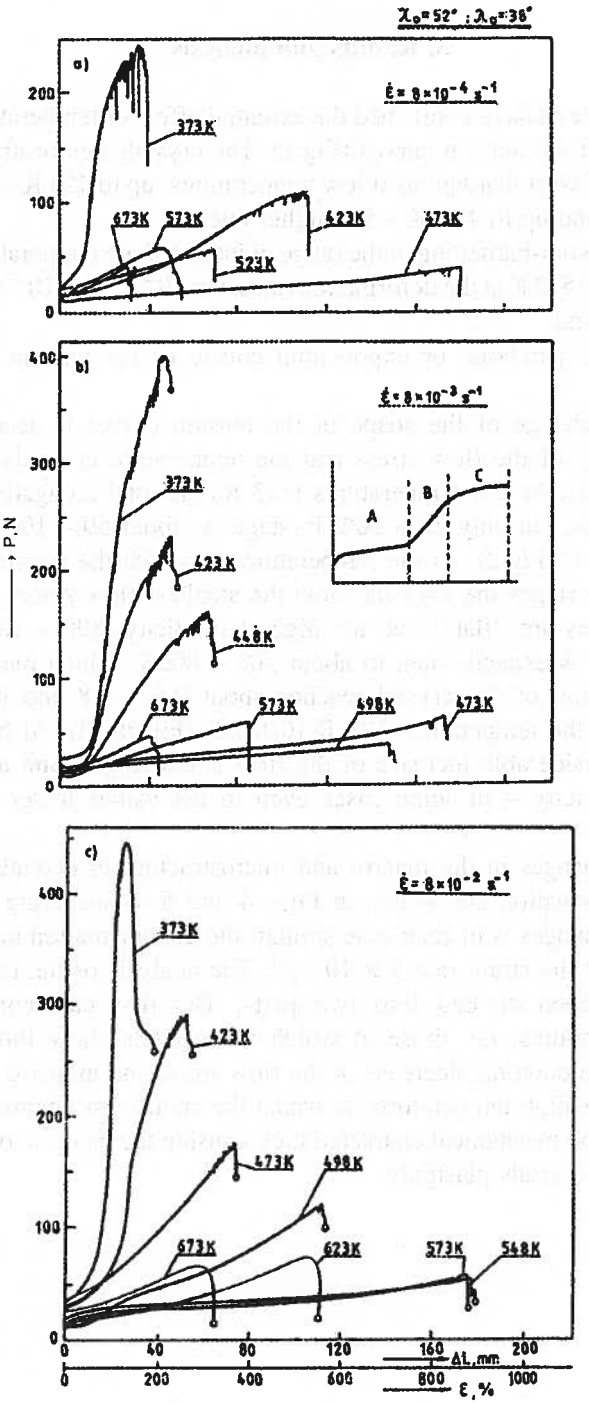

Fig. 1. Tensile curves of zinc single crystals with soft orientation. Initial strain rate: a) 8×10^{-4} s^{-1}; b) 8×10^{-3} s^{-1}; c) 8×10^{-2} s^{-1}

3. Results and analysis

The mechanical tests have confirmed the essential effect of temperature and the strain rate on the course of the tension curves (Fig.1). The crystals demonstrate:

- three stages of work-hardening at low temperatures: up to 423 K – for the strain rate 8×10^{-4} s^{-1}) and up to 448 K – for higher ones;
- two stages of work-hardening in the range of intermediate temperatures: up to 473 K, to 523 K and to 573 K at the deformation rates: 8×10^{-4} s^{-1}, 8×10^{-3} s^{-1} and 8×10^{-2} s^{-1}, respectively, and
- the rectilinear, parabolic or exponential course of the tension curves at higher temperatures.

The sequential change of the shape of the tension curves is accompanied by the temperature anomaly of the flow stress and the temperature anomaly of the plasticity of crystals (Fig.1; 2a). At low temperatures (373 K) the total elongation of the crystals amounts 150 – 225%, but only 25 – 50% in stage A, about 50 – 100% in stage B and 25 – 125% in stage C (Fig.2). At the temperatures at which the tensile curves has only two work-hardening stages the crystals show the smallest flow stress, the lowest strain hardening (the curves are "flat") and the highest plasticity, 800 – 1000% (Fig.1; 2a). The length of stage A expands then to about 500 – 800%, which means that its share in the total elongation of the crystal reaches about 0.6 – 0.8 and it is considerably greater than that at the temperature 373 K (0.1-0.2) (Fig.2b; 3). At high temperatures there take place considerable increase of the flow stress (Fig.1) and a drastic decrease of the crystals plasticity – in some cases even to the values lower than that at 373 K (Fig.2a).

Characteristic changes in the macro- and microstructure of crystals with increasing temperature of deformation are shown in Figs. 4 and 5. Considering the fact that the sequence of these changes is in each case similar, the documentation has been limited to crystals deformed at the strain rate 8×10^{-3} s^{-1}. The analysis of the results of structure investigations has been divided into two parts. The first part comprises low and intermediate temperatures, i.e. those at which the crystals show three or two work-hardening stages, a monotonic decrease of the flow stress and increase of plasticity. The second part concerns high temperatures at which the another mechanism of plastic flow leads to changes in the mechanical characteristics, causing the increase of work-hardening and decrease of the crystals plasticity.

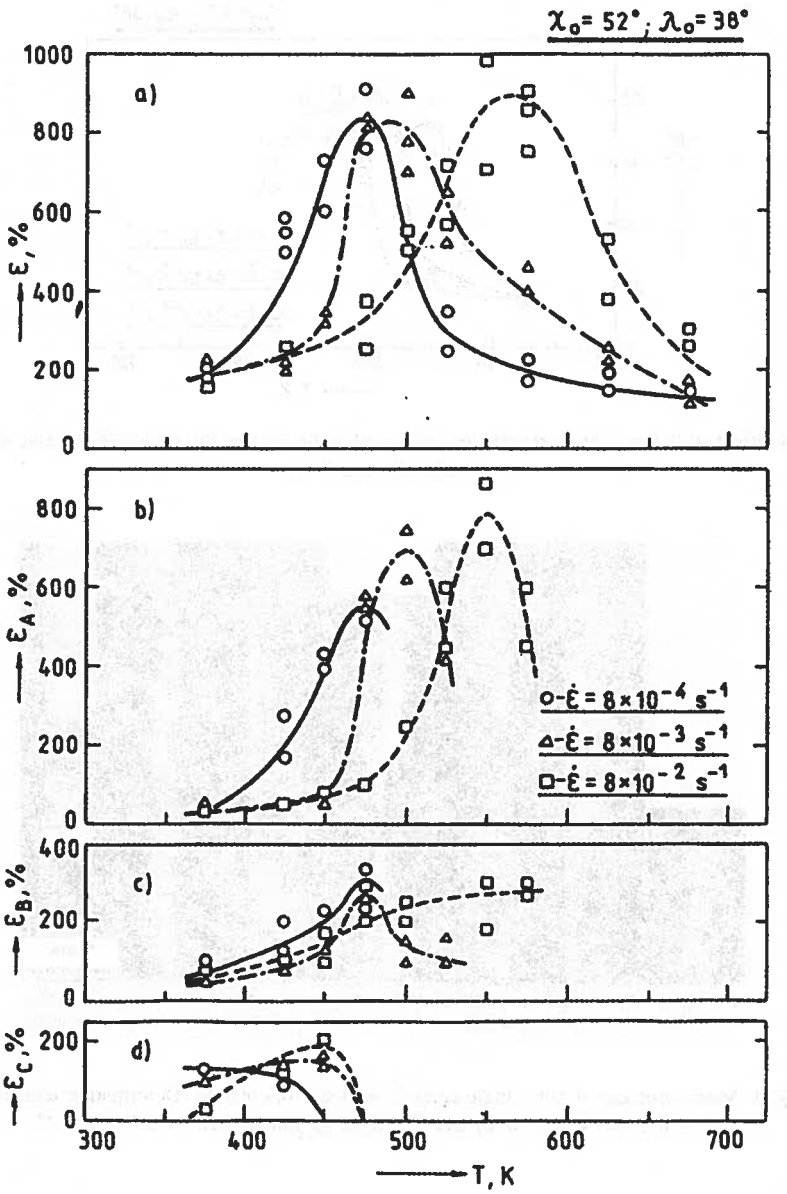

Fig. 2. The effect of deformation temperature and initial strain rate on plastic indices of zinc single crystals with soft orientation: a) total tensile elongation; b-d) elongation in stage A, B and C, respectively

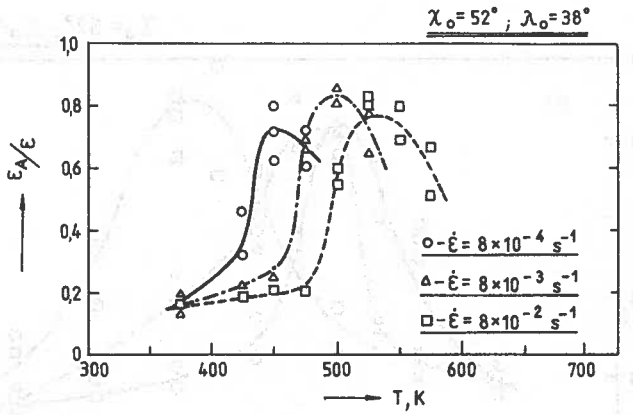

Fig. 3. The effect of deformation temperature and initial strain rate on the ratio $\varepsilon_A/\varepsilon$ for zinc single crystals with soft orientation

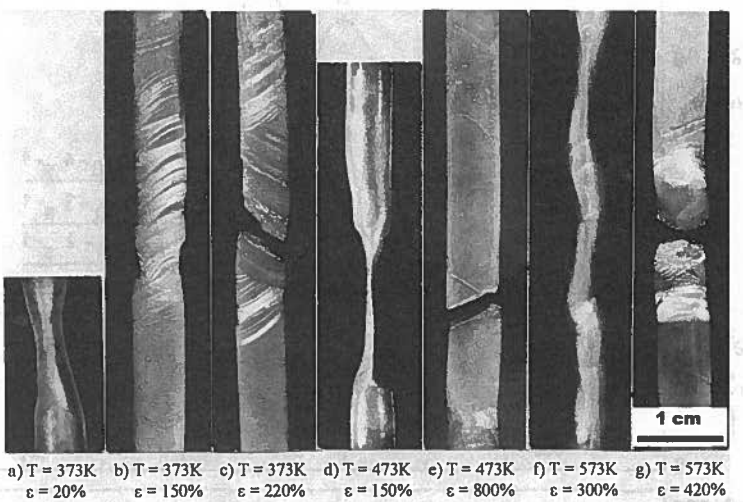

Fig. 4. Macrostructure of zinc single crystals with soft orientation. Deformation temperature: 373 K (a-c); 473 K (d, e) and 573 K (f, g). Initial strain rate 8×10^{-3} s^{-1}

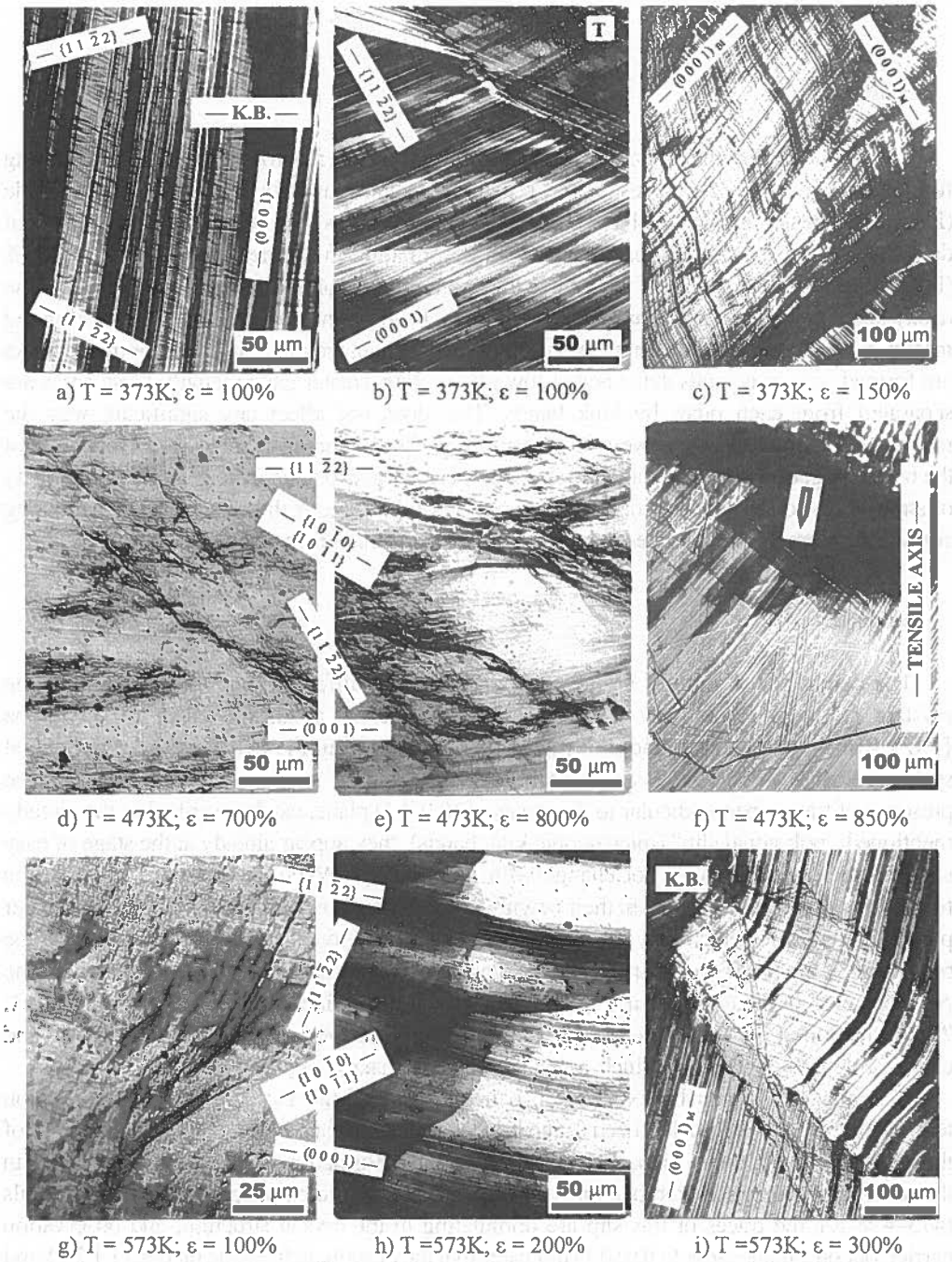

a) T = 373K; ε = 100% b) T = 373K; ε = 100% c) T = 373K; ε = 150%

d) T = 473K; ε = 700% e) T = 473K; ε = 800% f) T = 473K; ε = 850%

g) T = 573K; ε = 100% h) T =573K; ε = 200% i) T =573K; ε = 300%

Fig. 5. Deformation traces on the surfaces of zinc single crystals with soft orientation. Deformation temperature: 373 K (a-c); 473 K (d-f) and 573 K (g-i). Initial strain rate 8×10^{-3} s^{-1}. Plane of observation: {1 0 $\bar{1}$ 0} (a, i) and – (0 0 0 1) (b-h). (M – matrix; T – twin; K.B. – kink band)

3.1. Temperatures 373 – 498 K

Stage A

The plastic flow of the crystals is initiated by formation of a macroscopic neck which, during further deformation, propagates to the remaining, almost undeformed part of the sample (Fig.4a,d). The tendency to the basal slip localization increases with increasing temperatures of deformation, and in crystals tested at 473 K, deformation in the neck reaches 400 – 500% (Fig.4d), and the propagation of the neck to the remaining part of the crystals ("spreading" of the neck) takes place at almost constant load (Fig.1). In the transition area: neck / undeformed matrix, only the bending of basal planes is observed, while in the case when two (or more) necks are formed, e.g. in crystals deformed at low rate or with greater gauge length, these areas are separated from each other by kink bands. This does not affect any significant way the mechanical characteristics, however it is responsible for shortening of stage A and reduction of the total elongation of the crystals (Fig. 2a,b; 3). As it is easy to notice, the great inhomogeneity of strain leads to the conclusion, that a description of the stage A through the work-hardening coefficient cannot be associated with a particular deformation mechanism.

Stage B

The conditions of the test are also responsible for a different topological pattern of the crystals at stage *B*. At low temperatures (373 K), on a surface close to the plane $\{1\ 0\ \bar{1}\ 0\}$there can be seen traces of fine slip originating from the two 2-nd order pyramidal systems, well visible in the areas between thick slip bands in the basal systems (Fig.5a). The presence of traces, perpendicular to the traces of (0 0 0 1) plane, can be ascribed to the already mentioned "polygonal slip" (microscopic kink bands); they appear already at the stage of easy slip and their position does not change with deformation. When, at advanced stage B, the formation of twins takes place, in their neighbourhood there are activated additional 2-nd order pyramidal systems, which play the role of the accommodation slip (Fig.5b). In each case the beginning of the process of twinning, accompanied by rather small drops of load, precedes the parabolization of the tension curve and, in this way, it determines the length of stage *B* (Fig.1; 2c). Reduction of the strain rate leads to the decrease of the work-hardening of the crystal and causes a delay of twinning, which as a consequence makes stage *B* longer (Fig.2c).

A similar effect can be expected also in the case of the increase of the deformation temperature, however, as it has been found by topological investigations, in 3–4 fold increase of the length of stage *B* there can participate an additional deformation mechanism – a wavy slip in the secondary systems. At temperatures corresponding to the maximal plasticity of the crystals (473–498 K), the traces of this slip are dominating in the crystal structure, and observation carried out on a plane close to (0 0 0 1) indicates that they originate from the planes $\{1\ 1\ \bar{2}\ 2\}$ and $\{1\ 0\ \bar{1}\ 1\}$ and / or $\{1\ 0\ \bar{1}\ 0\}$, which have a common slip direction $<\bar{1}\ \bar{1}\ 2\ 3>$ (Fig.5d,e). It cannot be excluded that this slip is an alternative deformation mechanism with respect to twinning – it reduces the level of local stress so that it makes the nucleation of twins difficult.

An unambiguous evaluation of the role of the wavy slip in secondary systems, however, is difficult on account of the fact that in these temperature conditions of the test, nucleation of a few twins leads to almost immediate cracking of the crystals (Fig. 1). Within the twins – besides slip traces in the basal system – there appear dynamically recrystallized grains; this is evidenced by the presence of "new" slip traces indicated by an arrow in Fig. 5f. The recrystallization processes favor persistent localization and are responsible for quick cracking of the crystal in the volume of the twin and in the neighbouring crystals matrix (Fig. 4e). This observation leads to the conclusion that sufficiently high (preventing recrystallization) stability of structure of twins may be – at lower temperatures or higher deformation rates – a condition determining the existence of stage *C*. This explains also the cause of the differentiated effect of the deformation conditions on the length of stage *B*, i.e. the presence of a distinct maximum of plasticity at the temperature 473 K – at small tension rates and monotonic increase with temperature – in the case of a test realized at a strain rate 8×10^{-2} s^{-1} (Fig. 2c).

Stage C

Structural observations and the course of the tension curves have shown that plastic deformation of zinc crystals at stage *C* is realized mainly by twinning and has a mechanically unstable character (Fig. 1; 4b,c). Considering that deformation takes place at increased temperatures, the strain localization is accompanied by processes of "dynamic" recovery – both in the matrix and, first of all, in twinned volumes – the time of unloading of the crystal as a result of twin formation (measured to the moment of reaching again the primary level of stress) is equal to about few (or even more) seconds. These processes may be responsible for the fact that the rather small activity of basal system inside the newly formed twins (and its absence in crystals subjected to tension at high rate), gradually increases with increase of deformation (as well as with increase of the temperature). Since the nucleation of the twins takes place in crystals in which the lattice underwent considerable rotation to the direction $<1\ 1\ \bar{2}\ 0>$, the basal slip in the macroscopic twins may occur in conditions of "geometrical softening" [43]. The shear strain, occurring by such slip, often exceeds the value 1 (Fig. 4b,c; 5c), and the described effects are responsible for the decrease of the work-hardening rate at stage C, especially in crystals deformed at lower strain rates (Fig. 1).

Twinning as well as localized basal slip occurring in the twins volume, lead to considerable "misalignement" of the crystal (Fig. 4b). The occurring "geometrical defects" generate great bending stresses, which are initially easily accommodated by successive twins and slip in 2-nd order pyramidal systems. Both the gradual fragmentation of structure – caused by twinning and work-hardening of the matrix due to slip limit the possibilities of twinning and unavoidably lead to slip fracture along the basal plane in one of the twins (Fig. 4c).

At somewhat higher temperatures (423–448 K) or lower deformation rates at 373 K, a neck is often formed in the area of the crossing twins, and the gradual rotations of the basal planes in these twins enable considerable deformation in the neck until the "point-shaped" shear failure (Fig. 6). In none of the considered cases there have been observed any effects of recrystallization, and it can be definitely stated that the cracking of zinc crystals at stage C has a character of shear failure and takes place in a twinned volume [44].

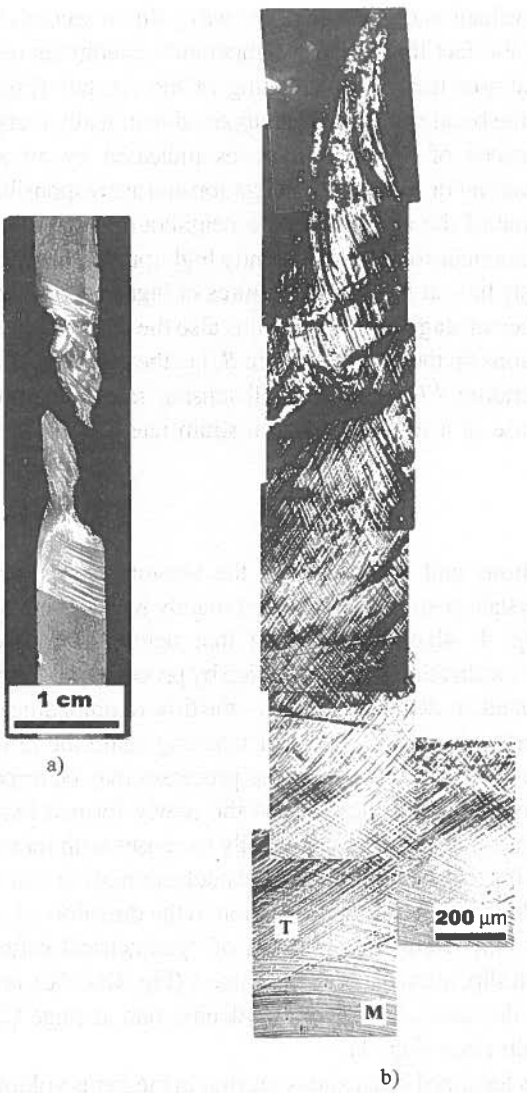

Fig. 6. Macro- (a) and microstructure (b) in the neck area of zinc single crystals with soft orientation. Deformation temperature 448 K; initial strain rate 8×10^{-3} s^{-1}. (M – matrix; T – twin)

3.2. Temperatures above 498 K

At high temperatures, instead of strongly localized necking (typical for lower temperatures), there appears the tendency to multinecking and deformation in the neighbouring necks is accommodated by kink bands (Fig. 4f). This process takes place along the whole length of the crystal and leads to its macroscopic fragmentation into blocks, separated by high-angle boundaries. Continuation of the tension test causes the increase of the misorientation of the neighbouring blocks

as a result of opposite rotation of the lattice and formation a "bamboo" structure. Inside the block, on the crystal surface close to (0 0 0 1), besides the basal slip traces, there appear corrugated traces, originating from the 1-st order prismatic systems (and / or 1-st order pyramidal systems) and, only locally, traces of the 2-nd order pyramidal systems (Fig. 5g). This slip contributes to the microfragmentation of the structure, and the newly formed fragments show a clear tendency to fast misorientation (Fig. 5h).

Simultaneous macro- and microscopic fragmentation of the structure and activity of the secondary systems suppress the development of the particular neck and increase of the strain-hardening of crystals in the range of high temperatures. It can be assumed that the results of the described processes have been treated as the above mentioned "decomposition of the crystal into grains", or interpreted as the effect of the formation of "spatially misoriented areas" [33, 34].

The final (persistent) neck is then always formed in the area of the kink bands, and after cracking – it assumes semi-circular form, "imitating" the course of a kink band (Fig. 4g). The cracking is preceded by recrystallization processes induced either on high-angle boundaries or in rather small twins, penetrating only into the tensioned part of the cross-section of the crystal (Fig. 5i) [44].

4. Conclusions

1. High-temperature mechanical characteristics of zinc single crystals with soft orientation are influenced by the processes of macroscopic localization of deformation: in basal system, in the twin bands and in the kink bands.
2. The change of the localization form: from strongly localized neck at stage A and the wavy slip in the secondary systems at stage B into crystal fragmentation, both in the macro- scale (formation of multineck and kink bands) and in micro-scale (as a result of slip in secondary systems) is responsible for the temperature anomaly of work-hardening and the temperature anomaly of plasticity.
3. The twinning begins at advanced stage B and it directly precedes the parabolic stage C, in which the dominating deformation mechanism is twinning and the basal slip taking place in the volume of twins.
4. Stage C disappears when the structure of twins nucleated at stage B becomes thermally unstable and the processes of "dynamic" recrystallization occur in them.
5. The persistent necking, leading to cracking of the crystal undergoing to tension was always preceded by strain localization – twinning or kink band formation; the direct cause of cracking is either shear failure in the twins (at lower temperatures) or the processes of "dynamic" recrystallization in twins and kink bands (at higher temperatures).

Acknowledgements

The Polish State Committee for Scientific Research supported this work under grant No. 11.11.180.134.

REFERENCES

[1] M. Boček, G. Hötzsch, Phys. Stat. Sol. **6**, 777 (1964).
[2] M. Boček, G. Hötzsch, Phys. Stat. Sol. **7**, 373 (1964).
[3] M. Boček, G. Hötzsch, B. Simmen, Phys. Stat. Sol. **7**, 833 (1964).
[4] M. Boček, V. Kaśka, Phys. Stat. Sol. **4**, 325 (1964).
[5] M. Boček, P. Lukáč, B. Smola, M. Švábová, Phys. Stat. Sol. **7**, 173 (1964).
[6] K. Lücke, G. Masing, K. Schröder, Z. Metallkunde **46**, 792 (1955).
[7] A. Seeger, H. Träuble, Z. Metallkunde **51**, 435 (1960).
[8] Z.S. Basinski, S.J. Basinski, Phil. Mag. **9**, 51 (1964).
[9] P.B. Hirsch, J.S. Lally, Phil. Mag. **12**, 595 (1965).
[10] F.F. Lavrentev [in]: Fizika deformacionnowo uprocznienia monokristałlow. Izd. Naukowa Dumka, 107, Kiew 1972.
[11] F.F. Lavrentev, Mat. Sci. Eng. **46**, 191 (1980).
[12] F.F. Lavrentev, Ju.A. Pochil, Mater. Sci. Eng. **18**, 261 (1975).
[13] F.F. Lavrentev, Ju.A. Pochil, O.P. Salita, FMM. **37**, 529 (1974).
[14] F.F. Lavrentev, O.P. Salita, Ju.G. Kazarov, FMM. **26**, 348 (1968).
[15] F.F. Lavrentev, O.P. Salita, S.V. Sokolski, Mat. Sci. Eng. **33**, 199 (1978).
[16] F.F. Lavrentev, O.P. Salita, S.V. Sokolski, Phys. Stat. Sol. a **54**, 145 (1979).
[17] F.F. Lavrentev, O.P. Salita, W.I. Starcev, FMM. **21**, 97 (1966).
[18] F.F. Lavrentev, O.P. Salita, G.W. Zjabrev, FMM. **29**, 1088 (1970).
[19] F.F. Lavrentev, W.L. Vladymirowa, Mater. Sci. Eng. **30**, 141 (1977).
[20] F.F. Lavrentev, W.L. Vladymirowa, FMM. **31**, 162 (1971).
[21] F.F. Lavrentev, W.L. Vladymirowa, FMM. **29**, 150 (1970).
[22] F.F. Lavrentev, W.L. Vladymirowa, A.L. Gajduk, FMM. **27**, 732 (1969).
[23] J.D. Livingston, Acta Met. **10**, 229 (1962).
[24] N. Nagata, T. Vreeland Jr., Phil. Mag. **25**, 1137 (1972).
[25] E.H. Edwards, J. Washburn, Trans. AIME. **200**, 1239 (1954).
[26] P. Lukáč, Czech. J. Phys. **B35**, 275 (1985).
[27] R.L. Bell, R.W. Cahn, Proc. Roy. Soc. **A239**, 494 (1957).
[28] K. Pieła, Arch. Metall. **36**, 311 (1991).
[29] N.R. Risebrough, E. Teghtsoonian, Canad. J. Phys. **45**, 591 (1967).
[30] J-P. Michel, G. Champier, Mater. Sci. Eng. **52**, 63 (1982).
[31] A. Seeger, [in]: Dislocations and mechanical properties of crystals. ed. J.C. Fischer, W.G. Johnston, R. Thompson, T. Vreeland Jr., John Wiley and Sons, 243, N. York 1957.
[32] M. Niewczas, AGH Kraków 1992, dissertation.
[33] E. Schmid, W. Boas, Kristallplastizität, ed. Springer Verlag, 93, Berlin 1936.
[34] O.A. Kajbyshev, W.W. Astatin, R.Z. Valijew, FMM. **46**, 1297 (1978).
[35] W.R. Regel, W.G. Govorkov, Kristallografia **1**, 64 (1958).
[36] A. Łatkowski, K. Pieła, A. Dziadoń, J. Wesołowski, Z. Metallkunde **80**, 26 (1989).
[37] K. Pieła, J. Wesołowski, Z. Metallkunde **10**, 758 (1992).
[38] M.H. Yoo, Trans. AIME., **245**, 2051 (1969).
[39] M.H. Yoo, Phil. Mag., **14**, 573 (1966).
[40] E. Schmid, G. Wassermann, Z. Phys., **48**, 370 (1928).
[41] P.H. Thornton, R.W. Cahn, J. Inst. Metals **89**, 455 (1960-61).
[42] H. Dybiec, A. Korbel, Mat. Sci. Eng., **A117**, L31 (1989).
[43] K. Pieła, to be published.
[44] K. Pieła, A. Korbel, Proc. Seventh JIM Int. Symp. (JIMIS-7): Aspects of high temperature deformation and fracture in crystalline materials. 91, Nagoya 1993.

Received: 10 April 2004.